Sedimentology and Geochemistry of Gas Hydrate-rich Sediments from the Oregon Margin (Ocean Drilling Program Leg 204)

Sedimentologia i Geoquímica de Sediments rics en Hidrats de Gas del Marge d'Oregon (Ocean Drilling Program Leg 204)

Elena Piñero Melgar

Doctoral Thesis
Barcelona, May 2009

Cover: Photograph of a sample of massive gas hydrate recovered from 2.69 meters below seafloor near the summit of Hydrate Ridge during Leg 204 (Sample 204-1250D-1H-CC, 12–14 cm). The photograph is by ODP Photographer John Beck.

Portada: *Fotografia d'una mostra d'hidrat de gas massiu recuperada a 2.69 metres sota el fons marí a prop del cim de southern Hydrate Ridge durant el Leg 204 (Mostra 204-1250D-1H-CC, 12–14 cm). La fotografia es del fotògraf d'ODP John Beck.*

Memòria de Tesi Doctoral presentada per
Elena Piñero Melgar
per a optar al títol de Doctora per la Universitat de Barcelona

Tesi realitzada en la Unitat de Tecnologia Marina (UTM),
Centre Mediterrani d'Investigacions Marines i Ambientals (CMIMA)
del Consell Superior d'Investigacions Científiques (CSIC),
Barcelona

La doctoranda:

Elena Piñero Melgar

Les directores de la tesi:

Dra. Eulàlia Gràcia i Mont
Unitat de Tecnologia Marina (CSIC)

Dra. Francisca Martínez-Ruiz
Insituto Andaluz de Ciencias de la Tierra (CSIC / UGR)

El tutor de la tesi:

Dr. Mariano Marzo Carpio
Departament d'Estratigrafia, Paleontologia i Geociències Marines
Universitat de Barcelona

Departament d'Estratigrafia, Paleontologia
i Geociències Marines
Universitat de Barcelona
Programa de Doctorat en Ciències de la Terra
Bienni 2003-2005

Sedimentology and Geochemistry of Gas Hydrate-rich sediments from the Oregon Margin (Ocean Drilling Program Leg 204)

Sedimentologia i Geoquímica de Sediments rics en Hidrats de Gas del Marge d'Oregon (Ocean Drilling Program Leg 204)

Elena Piñero Melgar
Maig de 2009

Agraïments

Aquesta tesi va començar com un cartell penjat a una paret. Des d'aquell dia moltes coses han passat, i en cadascuna d'elles m'he trobat acompanyada per uns i d'altres.

En primer lloc, vull agrair a les co-directores de la tesi, Eulàlia Gràcia i Paqui Martínez-Ruiz, la confiança que han dipositat en mi durant tot aquest temps. A l'Eulàlia vull agrair-li el saber transmetre la seva energia i la seva gran capacitat d'aprenentatge. A la Paqui li vull agrair la capacitat de treure importància als més variats problemes i ser capaç de projectar part de la seva serenitat. A part de les dues co-directores, aquesta tesi ha comptat amb l'ajut de'n Juan Cruz Larrasoaña, que ha estat com un company "avançat" de feina.

La M. Torres, en M. Canals, en C. Hensen, en A. Camerlenghi, en J.P. Foucher i en J.C. Larrasoaña han acceptat amablement formar el tribunal que jutjarà aquest treball. En M. Marzo ha exercit perfectament el seu paper de tutor de la tesi, fent de nexe amb la universitat sempre que els tràmits administratius han estat necessaris.

Aquesta tesi s'ha realitzat a la Unitat de Tecnologia Marina del CSIC, on tots els seus membres m'han acollit la mar de bé durant aquests cinc anys. En especial recordaré els esmorzars de taula quilomètrica, així com les converses filosòfico-científiques sobre la orientació de la unitat. Però a part dels esmorzars, hi ha hagut moltes altres coses, com xerrades científiques, discussions, mudances, dinars a la platja, patxarans, gozziles i gairebé algun dinar... el que arriba a ser tota una convivència.

Durant aquest temps, he realitzat diverses estades a l'*Instituto Andaluz de Ciencias de la Tierra* de Granada, on hem realitzat gran part de les anàlisis químiques de la tesi. Vull tenir una menció especial per al seu equip tècnic que, a més, sempre em van fer sentir com a part del grup. La major part de les anàlisis granulomètriques de la tesi es van realitzar al laboratori de sedimentologia de l'Institut de Ciències del Mar del CSIC, on les noies sempre van estar disposades a donar-me un cop de mà i facilitar-me la feina feixuga. Una menció especial mereix la feina de la M. Auleda que, com a part del seu treball de final de carrera (dirigit per la E. Gràcia i A. Calafat), va fer anàlisis granulomètriques al Laboratori de Sedimentologia del Departament d'Estratigrafia, Paleontologia i Geociències Marines de la Facultat de Geologia. Les anàlisis de TOC i S per aquest estudi s'han portat a terme a l'Institut de d'Investigacions Químiques i Ambientals de Barcelona, dins del grup dirigit per en J. Grimalt.

En George von Knorring, li haig d'agrair el gran esforç que va suposar fer les correccions gramaticals de la tesi amb el poc temps del que disposàvem. Crec que amb la seva ajuda, ara començo a utilitzar bé les preposicions...

A més, he realitzat estades a la Bremen Universität (Alemanya), la Scripps Institution of Oceanography (USA) i al Centre of Oceanic and Atmospheric Sciences (USA). Vull agrair als caps dels tres grups on he estat (G. Bohrmann, M. Kastner i M. Torres) per haver-me donat la possibilitat d'anar a aprendre noves tècniques però, sobretot, altres maneres de treballar i d'enfocar la vida científica. En tots aquests llocs, sempre he fet uns quants amics: companys de despatx, de pis, de nacionalitat o fins i tot de partida de mus, cosa que m'ha fet sentir una mica més a prop de casa.

Durant aquests anys he pogut participar en els millors congressos científics de la matèria (EGU, AGU, International Conference in Gas in Marine Sediments, etc.), el que m'ha fet conèixer la "gas-hydrate family" i sentir-me una més del grup; en especial, s'inclouen l'A. Tréhu i en G. Borhmann, co-chiefs de la campanya ODP Leg 204, en M. Riedel and T. Collett co-chiefs de la Expedition 311 de l'IODP, i tants d'altres...

A més, vull agrair al grup de D-Recerca i la FJI/Precarios haver-me fet aprendre tantes coses sobre el funcionament del sistema científic. D'aquí han sortit molt bons amics que d'alguna manera heu fet que pogués arribar aquest dia.

Ja en l'àmbit més personal, vull agrair a la meva família haver-me fet costat durant tots aquests anys, donant-me ànims en els moments més difícils però compartint també totes les bones emocions. Per acabar, vull agrair a tots els amics que han anat i vingut durant aquests anys l'haver deixat la seva petjada en la meva vida. En especial vull agrair la seva paciència en la meva gran inconstància i durant les meves fugides espirituals, que tots han patit en un moment o altre.

The samples analysed in this study were provided by the Ocean Drilling Program (ODP) that is sponsored by the U.S. National Science Foundation (NSF) and participating countries under management of the Joint Oceanographic Institutions, Inc. in which Spain is included as part of the European Consortium for Ocean Research Drilling (ECORD). This work was supported by the Spanish Ministry of Science and Innovation (*Ministerio de Ciencia e Innovación*) through *Acciones Especiales* REN 2001-5262-E and BTE 2002-11698-E especially devoted to the Spanish participation (pre-cruise and post-cruise) in the ODP Leg 204. Funding was also complemented by National Projects IMPULS (REN 2003-05996-MAR), EVENT (CGL2006-12861-C02-02), MARCAL (CGL2006-13327-C04-04 CLI), MARM (200800050084447) and European Science Foundation EuroMargins SWIM Project (REN2002-11234-E-MAR). The *Acción Complementaria* SUMATRA (CTM2006-27159-E) allowed the participation of Elena Piñero in a coring cruise, in which a protocol similar to ODP was applied. Elena Piñero benefited of the MEC FPU Ph.D. fellowship 2003-2872 from year 2004 to 2008.

Contents

PARTII

PART IV

Abstract

Gas hydrates have been recently recognized as a key factor affecting a number of global processes such as the climatic change, sea floor stability, etc. In this thesis we present the multidisciplinary study of gas hydrate rich sediments recovered during ODP Leg 204 "Drilling gas hydrates at Hydrate Ridge". The main objective of this thesis is to study how the textural characteristics of marine sediments can affect the main pathways and intensity of fluid flow and how fluid flow determines the distribution of gas hydrates in the continental margins, as well as the main geochemical processes that occur during early diagenesis.

To reach these objectives, a complete sedimentary and geochemical study of 581 sediment samples from southern Hydrate Ridge was carried out. The methods and techniques that were applied include: complete textural analyses (grain size, granulometric distribution curve, statistical parameters, identification of the coarse-grained particles, carbonate content…), mineralogy (bulk sediment and clay minerals), physical properties (magnetic susceptibility) and geochemistry (major and trace elementary composition, total organic carbon).

The southern Hydrate Ridge sediments are mainly made up of four lithofacies defined as: hemipelagites, turbidites, ash layers and debrites. Mass-transport deposits such as turbidites and debrites are more abundant in Lithostratigraphic Unit III and II, as well as in Lithostratigraphic Unit IA in the slope basin of southern Hydrate Ridge. Some increasing trends with depth can be observed in the smectite content in the clay mineral assemblages of southern Hydrate Ridge sediments. These features suggests that the transport in suspension of fine sediments through the California Current was more effective during the Pliocene and early Pleistocene period. Bedload transport of coarse material from local and distal areas was more effective during the middle Pleistocene and Holocene due to the tectonic reactivation of the southern Hydrate Ridge uplift. During the Pleistocene and owing to the pervasive fluctuation of sea-level, gas hydrate dissociation together with the seismic movements in the Oregon margin seems a plausible triggering mechanism for mass-movements. Thus, the results presented here confirm that the sedimentation patterns in the Hydrate Ridge region are controlled by climate and tectonic parameters such as the regional intensity of the California Current or the local tectonic movements that lead to the uplift of the Ridge. These parameters mainly control the clay mineral distribution as well as the sedimentary facies that are produced.

The sedimentary fabric of gas hydrate-rich intervals is disturbed during core recovery due to gas hydrate dissociation. The two main disturbance fabrics generated through this process are

mousse-like and soupy. The gas hydrate –rich sediments analyzed for this thesis are coarser-grained in respect to the hemipelagite sediments. The coarse-grained layers such as turbidites and ash layers could act as conduits for fluids in the southern Hydrate Ridge region because of their higher porosity and permeability. In this context, methane-rich fluids migrate through these layers from deep in the sedimentary sequence and into the gas hydrate stability zone.

A number of barium fronts have been identified in southern Hydrate Ridge sediments and interstitial waters. Barite fronts were formed as a result of the barite recycling process during early diagenesis, which is controlled by the availability of methane–rich fluids, *in situ* decomposition of organic matter and the sulphate gradient. Modelling of these data shows that these processes were active at southern Hydrate Ridge for a period of up to one thousand years. A number of geochemical and sedimentological processes are proposed in this thesis as plausible mechanisms to allow the survival of the barite fronts during diagenesis.

As in southern Hydrate Ridge sediments, the sedimentary texture plays an important role in controlling the major fluid flow pathways in the continental margins. The temporal evolution of the fluid flow can be studied in a given area through the distribution of the mineral phases that form during early diagenesis, as well as the interstitial water composition.

Resum expandit de la tesi

Presentació i objectius

Aquesta tesi integra els resultats obtinguts d'un conjunt d'anàlisis sedimentològiques i geoquímiques de sediments marins rics en hidrats de gas perforats durant la campanya *Leg* 204 del programa internacional de perforació oceànica científica *Ocean Drilling Program* (ODP) en el marge d'Oregon (EUA). Espanya forma part d'aquest programa de perforació com a membre de l'*European Consortium for Ocean Research Drilling* (ECORD). La participació d'Eulàlia Gràcia, co-directora d'aquesta tesi, en la campanya ODP *Leg* 204: "*Drilling gas hydrates at Hydrate Ridge"*, va fer possibilitar l'oportunitat única de tenir accés a mostres de sediment d'una excel·lent qualitat científica, així com a totes les dades recollides a bord del vaixell de recerca oceanogràfica *Joides Resolution* durant la campanya.

El coneixement científic sobre el hidrats de gas ha millorat de forma molt significativa durant les darreres dècades, després del reconeixement de la seva important influència en diversos processos d'abast global com són: el canvi climàtic, l'estabilitat dels fons submarins, l'extracció de gas com a recurs econòmic, la injecció o segrest de CO_2, la biosfera profunda, etc.

Els objectius principals de la tesi inclouen:

(1) Caracteritzar les principals litofàcies sedimentàries que formen *southern Hydrate Ridge*.

(2) Analitzar els processos climàtics i tectònics que controlen el transport de sediment i la seva sedimentació en el marge continental d'Oregon, així com la seva evolució durant els darrers 1.5 milions d'anys.

(3) Discutir la dissociació dels hidrats de gas com a possible mecanisme desencadenant de moviments de massa en la regió de *Hydrate Ridge* i en el marge d'Oregon en general.

(4) Avaluar la distribució d'hidrats de gas a *southern Hydrate Ridge* i la seva relació amb les propietats texturals i físiques del sediment. Estudiar la textura sedimentària com a factor determinant en la distribució dels hidrats de gas.

(5) Quantificar la concentració de Bari en els sediments de *southern Hydrate Ridge* en comparació amb la composició de les aigües intersticials, i com a conseqüència dels processos geoquímics que hi tenen lloc durant la diagènesi inicial.

(6) Presentar un nou model de formació i preservació dels fronts de barita en el sediment, quantificant el temps necessari per a la seva formació.

(7) Estudiar el flux de fluids a través dels sediments de *southern Hydrate Ridge*, controlat per la textura i l'arquitectura sedimentària, mitjançant l'estudi de la distribució dels hidrats de gas així com d'alguns minerals d'origen diagenètic.

La tesi s'estructura en tres parts. La Part I inclou els Capítols 1 i 2, començant per una revisió sobre l'estat de l'art dels coneixements més significatius sobre els hidrats de gas i la seva recerca (formació, estabilitat, origen, quantitat, etc.). El Capítol 2 descriu breument el marge de Cascadia i *southern Hydrate Ridge*. Els resultats més significatius obtinguts durant la campanya ODP *Leg* 204 s'exposen a la Part II (Capítol 3), incloent la descripció dels mètodes utilitzats per detectar hidrats de gas. El Capítol 4 presenta la descripció de les principals metodologies i tècniques analítiques utilitzades per a aquest estudi, així com els criteris per a mostrejar els sediments. La Part III inclou els principals resultats així com la seva discussió. Està estructurada en quatre capítols. El Capítol 5 tracta sobre la descripció sedimentològica de *southern Hydrate Ridge*, definint les principals litofàcies i discutint la seva reconstrucció paleoambiental. Les principals àrees font així com els mecanismes de transport dels sediments són avaluats durant els darrers 1.5 milions d'anys. La descripció detallada dels sediments rics en hidrats de gas es presenta al Capítol 6, suggerint que aquests s'acumulen preferentment a les capes de major mida de gra. El Capítol 7 presenta un avanç sobre la geoquímica dels sistemes marins rics en hidrats de gas, introduint un nou model sobre els processos diagenètics que donen lloc a la formació de fronts de barita ($BaSO_4$) i com evolucionen en el temps en *southern Hydrate Ridge*. Finalment, el Capítol 8 comprèn la breu integració de tots els temes tractats en aquesta tesi, proposant unes conclusions precises. A més, s'inclou una descripció de les principals tasques a realitzar per completar aquest estudi. Les referències, figures, taules així com els principals acrònims utilitzats es llisten al final de la tesi.

1. Introducció: Els hidrats de gas

Els hidrats de gas són substàncies naturals semblant al gel, formades per molècules d'hidrocarburs de baix pes molecular que queden incloses en una xarxa de molècules d'aigua, enllaçades per forces de *van der Waals*, també anomenades clatrat (Sloan, 1998). La inclusió de molècules d'hidrocarbur en les molècules d'hidrat de gas els proporciona la capacitat de combustió, tot i la seva semblança al gel i la seva baixa temperatura. Els hidrats de gas metà, els més abundants a la natura, són l'objecte d'aquest estudi.

Els hidrats de gas han estat recentment inclosos com a prioritat en els programes més importants per a la recerca oceànica, com són el *U.S. Margins* de la *National Science Foundation* o el *Deep Sea Frontier* de la Comunitat Europea.

Sir Humphrey Davy (Davy, 1811) va ser el primer químic en sintetitzar una molècula d'hidrat de clor. Diferents avanços es van produir durant les primeres dècades del segle XX, després que els hidrats de gas fossin identificats com la matèria que produïa la obstrucció de les

canonades de gas en diversos camps de perforació de gas i petroli. Durant la dècada dels seixanta es va suggerir l'existència dels hidrats de gas en grans quantitats a la natura. Durant els anys setanta la recerca sobre els hidrats de gas va ser liderada per la comunitat científica russa. Va ser durant aquest període quan Makogon (1971) va fer el primer descobriment dels hidrats de gas presents a les àrees de permafrost de Sibèria. Alguns anys després, els hidrats de gas van ser recuperats inclosos en sediments profunds del Mar Caspi i del Mar Negre (Yefremova i Zhizhchenko, 1974). A partir d'aquesta data, la recerca en hidrats de gas ha anat molt lligada al desenvolupament de noves tecnologies geofísiques o de mostreig capaces de detectar els hidrats de gas *in situ* i de poder-los recuperar sense perdre les seves propietats. Des d'aleshores els hidrats de gas han estat presents com a objectiu principal o secundari de les principals campanyes i programes oceanogràfics del món. L'interès científic pels hidrats de gas ha estat acompanyat per la publicació de diverses novel·les de ciència ficció o *eco-thrillers* (e.g. Barnes, 1994; Irvine, 2004; Schätzing, 2006).

Cristal·lografia dels hidrats de gas

Els hidrats de gas poden incloure diferents tipus de molècules, que s'encaixen en 3 tipus diferent d'estructures moleculars: a) l'estructura I es forma en el sistema cúbic, i està constituïda per 46 molècules d'aigua formant dues caixes pentagon-dodecaedrals i dues caixes tetradecaedrals; b) l'estructura cúbica II està constituïda per 136 molècules d'aigua formant setze pentagon-dodecaedres i vuit hexadecaedres; i c) l'estructura hexagonal H és la ménys freqüent i està constituïda per 34 molècules d'aigua que formen tres tipus de caixes diferents.

L'estructura d'hidrat de gas resultant depèn de la relació entre la mida de la molècula d'hidrocarbur i la cavitat formada. Per això, l'estructura I és la més freqüent, ja que és la que pot incorporar les molècules més petites (p.ex. metà).

Camp d'estabilitat i origen dels hidrats de gas

Els hidrats de gas només són estables sota condicions de baixa temperatura i alta pressió. A més, la seva formació està influenciada per la disponibilitat de molècules de gas. Les condicions d'estabilitat dels hidrats de gas es troben de forma natural a àrees de permafrost i llacs d'altes latituds en l'àmbit continental, així com en els marges continentals sota profunditats d'aigua majors de 300 metres en l'àmbit oceànic (Kvenvolden, 1988). En aquest ambient, la intersecció entre la corba d'estabilitat dels hidrats de gas amb la corba de temperatura en els sediments (geoterma) defineix el que es coneix com la Zona d'Estabilitat dels Hidrats de Gas (GHSZ: *Gas Hydrate Stability Zone*).

La base de la GHSZ representa el límit entre el camp d'estabilitat dels hidrats de gas i el del gas (Henry et al., 1999), de tal manera que l'hidrat de gas es dissociarà en aigua i gas quan superi aquesta profunditat degut a l'enterrament sedimentari progressiu al llarg del temps, que bàsicament està controlat per l'índex de sedimentació. La variació en el nivell del mar pot fer variar la potència de la GHSZ degut al canvi de pressió exercit per la columna d'aigua sobre el sediment. Un altre paràmetre que pot impedir la formació d'hidrats de gas és la salinitat, que afecta la força iònica de la solució.

La major part dels marges continentals es troben sota les condicions d'estabilitat dels hidrats de gas. En aquest context, la presència de suficient quantitat de molècules de gas representa el factor limitant més important per a la distribució d'hidrats de gas en els fons oceànics (e.g. Schulz i Zabel, 2006). El metà, que és l'hidrocarbur que es troba de forma més freqüent com a constituent d'hidrats de gas a la natura, pot tenir un origen termogènic o biogènic o una barreja de tots dos. L'estudi de la seva composició isotòpica dóna idea del seu origen.

Evidències de la presència d'hidrats de gas

Durant les darrers dècades s'han desenvolupat diverses tècniques geofísiques per a l'estudi i quantificació de la presència d'hidrats de gas en els sediments marins. Algunes d'elles seran explicades al Capítol 3, mentre que en aquesta secció ens centrarem en l'evidència sísmica, que ha estat la més utilitzada.

El reflector que simula el fons marí (BSR: *Bottom Simulating Reflector*) és un reflector fàcilment identificable en els perfils sísmics, degut a que és paral·lel al del fons marí, però de polaritat inversa. La seva profunditat coincideix amb la profunditat teòrica de la base de la GHSZ. Tanmateix, s'ha recuperat hidrat de gas en zones on havia esta impossible identificar un BSR, mentre que si ha estat identificat en àrees on no s'han recuperat hidrats. Aquests fets evidencien que la formació d'aquest reflector està influenciada per altres paràmetres com la distribució dels hidrats dins de la GHSZ, la quantitat total d'hidrats, la seva fàbrica, la distribució de gas sota la GHSZ, etc.

Distribució dels hidrats de gas

Els hidrats de gas es distribueixen per les àrees de permafrost i grans llacs a altes latituds en l'àmbit continental i en els marges oceànics de més de 300 metres de profunditat dels oceans Atlàntic, Pacífic, Índic i Antàrtic, arribant a profunditats de fins a 1.100 metres en la columna sedimentària, depenent del gradient geotèrmic de l'àrea. Durant les darreres dècades, els hidrats de gas han estat recuperats en més de 40 regions i la seva presència ha estat proposada en més

de 100 àrees en base a evidències sísmiques, geofísiques o geoquímiques (Lorenson and Kvenvolden, 2007).

Quantitats estimades d'hidrat de gas

La mida del reservori d'hidrats de gas està poc definida, especialment pel que fa a la quantitat d'hidrats contingut en els sediments dels marges continentals. Durant els darrers anys s'han publicat diferents estimacions globals fins a arribar a un volum estimat de 1-5 x 10^{15} m^3 (Milkov, 2004). Les quantitats recentment presentades fan entreveure que l'explotació econòmica dels hidrats de gas només serà possible en els ambients més rics o allà on es troben de forma més localitzada.

Per què és important la recerca sobre els hidrats de gas?

A part de l'interès econòmic que suposa l'explotació comercial de l'hidrocarbur contingut com a hidrat de gas en els fons oceànics, darrerament s'ha proposat la influència dels hidrats de gas en diverses àrees com són: a) el segrest de CO_2; b) el paper del hidrats de gas en el cicle del carboni; c) l'activitat biològica profunda; c) el canvi climàtic; d) el canvi climàtic durant el màxim tèrmic Paleocè-Eocè (PETM: *Paleocene-Eocene Thermal Maximum*); i e) l'estabilitat dels marges continentals.

El segrest de CO_2 en els sediments marins s'ha proposat com una solució possible per mitigar l'efecte hivernacle de l'emissió d'aquest gas a l'atmosfera. Per això, diversos estudis en fase de desenvolupament i implementació plantegen la possibilitat d'injectar CO_2 en àrees on els hidrats de gas estiguin en fase d'explotació (e.g. Wallmann, 2007). Els hidrats de gas juguen un paper dins del cicle del Carboni. Degut a la seva abundància i a les seves delicades condicions d'estabilitat, ha estat proposat el seu paper com a "condensador". Així, els hidrats de gas s'anirien acumulant en el fons del mar fins que un canvi més o menys sobtat en les seves condicions de pressió i temperatura (p.ex. degut a una baixada del nivell del mar o a un increment en la temperatura de l'aigua del mar) produiria el seu alliberament cap a l'aigua i l'atmosfera. Un mecanisme similar hauria produït l'alliberament de grans quantitats d'hidrats de gas durant el PETM. L'alliberament sobtat d'hidrats de gas també podria actuar com a factor desencadenant de moviments de massa, degut a la pèrdua de cimentació que això produiria. A més, els hidrats de gas juguen un paper important en el desenvolupament de les comunitats biològiques que viuen en les àrees de surgència de fluids i gasos en els fons marins.

2. Marc geològic

El marge de Cascadia: Prisma d'acreció

Hydrate Ridge és un alt estructural del marge occidental de Nord Amèrica, també conegut com el marge de Cascadia. Aquest marge es divideix en el marge de Columbia Britànica a Canadà i el de Washington, Oregon i Nord de Califòrnia als Estats Units. El prisma d'acreció de Cascadia es forma a mida que la Placa de Juan de Fuca subdueix obliquament sota la Placa de Nord Amèrica. La zona de subducció de Cascadia està limitada a Nord i Sud per punts triples, formats per la intersecció de la Falla *Queen Charlotte* amb *Explorer Ridge* i per la Falla de *Sant Andreas* i la de Mendocino, respectivament. L'índex de subducció de Cascadia s'ha estimat en ~4.5 cm/a (e.g. DeMets et al., 1990) i juntament amb la jove edat de la placa que subdueix fan de Cascadia un marge actiu capaç de generar grans terratrèmols amb una recurrència d'entre 300 i 600 anys (Goldfinger et al., 1992). El prisma d'acreció de Cascadia s'estén fins a 150 km en la seva porció nord, davant de la Península de Washington, on els ventalls submarins d'Astoria i Nitinat estan sent incorporats al marge continental. Aquesta és una àrea d'elevada activitat de transport de sediments i amb alta pressió de fluids, ja que els sediments que són subduïts contenen gran quantitat d'arenes grolleres. Els encavalcaments actius del talús inferior de Cascadia es caracteritzen per la seva vergència cap al mar en la seva porció més al Nord (Vancouver Island), que canvia a una vergència cap a terra en la porció central del marge (British Columbia, Washington i Nord d'Oregon). En la porció Sud del marge d'Oregon, els encavalcaments presenten vergència cap a mar, tot i que és variable en el marge de Califòrnia. La definició d'aquests segments es correspon amb dades de ruptures de terratrèmols durant l'Holocè (e.g. Witter et al., 2003).

La circulació oceànica superficial al marge d'Oregon està governada pel Gir d'Alaska, del que forma part el corrent Nord-Pacífic i el corrent d'Alaska; i el Gir Subtropical, del que forma part el corrent de Califòrnia. El corrent de Califòrnia recorre bona part del marge d'Oregon i Califòrnia cap al Sud, mentre que el corrent d'Alaska recorre el marge d'Oregon i Washington en direcció Nord.

Hydrate Ridge

Hydrate Ridge es troba en el talús del marge d'Oregon, a uns 80 km de Newport i a una profunditat de 1500 metres. Aquest talús connecta el marge continental amb la Plana Abissal de Cascadia. La major part del marge està format per alts estructurals similars a *Hydrate Ridge* que conformen petites conques sedimentàries que s'omplen de material hemipelàgic i turbidític (Carlson and Nelson, 1987). Es distingeixen dos cims en *Hydrate Ridge*, el cim Nord a 600 m de profunditat, i el cim Sud a 800 m. El cim Nord representa un estadi més madur en l'evolució

d'aquests alts estructurals, amb un extens paviment carbonatat en la seva superfície. En canvi, el cim Sud només presenta una petita zona amb paviment carbonat.

El patró de falles presents a *southern Hydrate Ridge* és relativament ben conegut (e.g. Kulm et al., 1986; MacKay et al., 1992) i és conseqüència de la compressió resultant de la subducció obliqua (Johnson et al., 2003). El límit entre la zona dominada per la vergència cap a terra al Nord i una altra dominada per la vergència cap a mar al Sud es troba a *Hydrate Ridge*, generant una zona de vergència mixta en aquesta àrea. *Hydrate Ridge* es troba limitat al Nord per la falla de Daisy Bank i al Sud per la Falla d'Alvin Canyon, que provoquen una rotació del bloc en el sentit de les agulles del rellotge (Johnson et al., 2000).

Existeix una relació directa entre els hidrats de gas i els paviments carbonatats a *Hydrate Ridge*, com a d'altres alts submarins localitzats en complexes d'acreció. L'estudi del paviment carbonatat del cim Nord i Sud de *Hydrate Ridge* evidencien la dissociació d'hidrats de gas com a possible procedència de les surgències de metà detectades en el fons marí. El descobriment d'aquestes surgències de metà així com l'aflorament d'hidrats de gas en el fons marí de *Hydrate Ridge* van possibilitar el reconeixement d'aquesta zona com una de les més riques del món en hidrats de gas (Suess et al., 2001). Nombroses campanyes oceanogràfiques s'han dut a terme en aquest emplaçament, com ara el *Leg* 146 d'ODP, el *Leg* 204 d'ODP, la campanya 110 del RV Sonne, campanyes americanes de mostreig de sediment, sísmica, etc.

3. ODP *Leg* 204

El *Leg* 204 d'ODP va ser el primer estrictament dedicat a la recerca sobre hidrats de gas en els complexos d'acreció, utilitzant les tècniques disponibles més avançades, així com l'equipament de mostreig més desenvolupat (Shipboard Scientific Party, 2002). L'àrea d'estudi va ser *Hydrate Ridge*, una àrea on s'havia estimat una elevada quantitat d'hidrats de gas. Durant la campanya es van perforar més de tres kilòmetres de sediment en nou estacions (*Sites* 1244 a 1252), superant la profunditat del BSR en la majoria dels *Sites*. Els *Sites* es van situar en una àrea de quatre per onze kilòmetres, en base a les dades de sísmica multicanal 3D adquirides prèviament a la campanya.

En la sísmica multicanal 3D de la zona de *southern Hydrate Ridge* destaquen diversos reflectors sísmics. L'Horitzó A és un reflector que mostra una amplitud deu vegades més gran que els altres nivells sismo-estratigràfics. Va ser perforat en diverses localitats (*Sites* 1245, 1247, 1248, 1250) per a estudiar la seva possible implicació en el transport de fluids i el seu alt contingut en gas. Els Horitzons B i B' són dos reflectors d'alta amplitud i estan fracturats per

nombroses falles, possiblement associades a la formació d'un anticlinal (Anticlinal A). Els horitzons B i B' *downlapen* sobre l'horitzó AC que va ser interpretat com el límit superior del material del prisma d'acreció. Els *Sites* 1244 i 1246 van ser planejats per a estudiar la seva implicació en el transport de fluids. L'objectiu principal dels *Sites* 1248, 1249 i 1250, situats al cim de *southern Hydrate Ridge*, va ser avaluar les característiques sedimentològiques de la fàcies sísmica transparent que s'identifica en aquesta zona, a més d'estudiar la presència d'un doble BSR en el registre sísmic. El *Site* 1251 es va situar a la conca de talús adjacent al *southern Hydrate Ridge* per tal d'estudiar la presència de dipòsits de moviment de massa en aquesta zona. El *Site* 1252 va ser plantejat com a estudi dels materials del prisma d'acreció de Cascadia que es troben a menys profunditat en la zona de la conca de talús.

Principals resultats del Leg 204 d'ODP

Els principals resultats obtinguts durant el *Leg* 204 d'ODP són:

- Existeix una gran quantitat d'hidrats de gas des del fons marí fins a uns 30 metres de profunditat sota del cim de *southern Hydrate Ridge*. Les dades de clorinitat en aquesta zona demostren que la formació d'aquests hidrats de gas ha estat recent i ràpida.

- Des de 45 metres de profunditat i fins a la base de la GHSZ els hidrats de gas es distribueixen en acumulacions lenticulars en les capes. La seva concentració a la conca de talús és relativament baixa.

- Les diferents dades geofísiques, geoquímiques i sedimentològiques utilitzades durant la campanya per a deduir la distribució dels hidrats de gas a la zona d'estudi van donar resultats similars. Les anomalies tèrmiques registrades sistemàticament a la recepció dels testimonis de sediment van proporcionar un registre coherent amb la distribució d'hidrats de gas.

- Les noves tecnologies de mostreig HYACE i HYACINTH es van utilitzar durant la campanya per a mantenir els testimonis de sediment en les seves condicions originals de pressió i temperatura per tal de conservar els hidrats de gas i evitar la seva dissociació.

- La base de la GHSZ representa una discontinuïtat en les dades geoquímiques de composició de les aigües intersticials. Aquest fet suggereix que la formació dels hidrats de gas està íntimament lligada a les variacions en la composició geoquímica dels sediments.

- Diverses capes d'alt contingut en cendres volcàniques, juntament amb capes de turbidites i àrees d'elevada fracturació funcionen com a conductes preferents per al flux de fluids.

A més, la descripció visual dels testimonis de sediment feta durant la campanya va ser sintetitzada en una correlació estratigràfica, definint cinc unitats litoestratigràfiques en funció de les característiques sedimentològiques, i tenint en compte també les dades de sísmica multicanal. Posteriorment a la campanya i com a part del *Scientific Results Volume*, Chevalier et al. (2006) va presentar una nova correlació sismoestratigràfica un cop acabat el processat de

totes les dades sísmiques 3D. A més, va proposar un model de seqüència deposicional per a *southern Hydrate Ridge*.

La presència d'un doble BSR en les dades sísmiques de *southern Hydrate Ridge* va ser interpretada per Bangs et al. (2005) com a corresponent a una pujada de 120 metres en el nivell del mar ocorreguda fa 18.000 anys, com a conseqüència de l'últim màxim glacial. Aquesta pujada del nivell eustàtic va ser contrarestada per un increment en la temperatura del fons del mar d'entre 1.7 i 2.2 ºC. Aquest canvi en la posició de la base de la GHSZ hauria provocat la dissociació massiva d'hidrats de gas a la zona de *Hydrate Ridge*.

Proxies per a la detecció dels hidrats de gas

Durant la campanya *Leg* 204 d'ODP van ser utilitzats diversos *proxies* per a la detecció d'hidrats de gas, en base a les diferents propietats físico-químiques dels hidrats de gas en relació a les dels sediments que els contenen. Entre ells es troben:

Resistivitat elèctrica mesurada pel sistema de mesura-mentre-es-perfora (LWD: *logging while drilling*): Degut a la menor resistivitat elèctrica dels hidrats i del gas respecte de l'aigua intersticial, la seva presència produeix una anomalia de baixa resistivitat.

Clorinitat: Els hidrats de gas exclouen les sals de la seva estructura en formar-se. D'aquesta manera, la seva dissociació produeix un descens en la clorinitat degut a l'alliberament d'aigua dolça que produeix una dilució de l'aigua intersticial.

Anomalia de temperatura: La dissociació dels hidrats de gas és una reacció endotèrmica; és a dir, que consumeix calor. Durant la campanya, els testimonis tot just arribats a coberta, es van fotografiar mitjançant una càmera d'infrarojos per tal de detectar les zones on el procés de dissociació d'hidrats de gas era més evident, per les anomalies de baixa temperatura.

Volum de gas: Per tal d'evitar que el gas contingut en el sediment s'escapi, es va utilitzar un dispositiu d'autoclau capaç de recuperar testimonis de sediment a la seva pressió original.

Fàbriques sedimentàries pertorbades: La dissociació dels hidrats de gas continguts en el sediment produeix l'alliberament de gran quantitat d'aigua que produeix la pertorbació de la fàbrica sedimentària original. Les fàbriques sedimentàries resultants de la dissociació d'hidrats de gas es van definir com a "mousse" i de sopa (*mousse-like* i *soupy*, respectivament).

Els hidrats de gas a *southern Hydrate Ridge* es presenten sota diferents fàbriques: disseminada, venes, capes, nòduls i massiva.

Distribució dels hidrats de gas al southern Hydrate Ridge

En base als diferents *proxies* utilitzats durant la campanya *Leg* 204 d'ODP, es va deduir la distribució dels hidrats de gas a *southern Hydrate Ridge*. Els *proxies* estudiats indiquen una alta

concentració d'hidrats de gas sota el cim de *southern Hydrate Ridge* fins als 20-40 metres de profunditat, amb una concentració del 30-40 % estimada en el *Site* 1249 i concentracions menors (~5 %) sota aquesta profunditat. Als flancs de *southern Hydrate Ridge*, la concentració d'hidrats de gas va ser estimada en ~5 %. Grans quantitats d'hidrats van ser trobats en la profunditat corresponent a l'Horitzó B, que està format per dues capes de mida de gra relativament grollera. En la conca de talús de *southern Hydrate Ridge* l'extensió i distribució dels hidrats de gas és més limitada que a la zona del cim o als flancs, amb una concentració propera a l'1%.

La distribució heterogènia dels hidrats de gas a la zona de *southern Hydrate Ridge* va ser atribuïda als dos règims del gas per assolir la GHSZ: a) el règim produït mitjançant reaccions; i b) el règim dominat pel transport. El règim dominat per les reaccions químiques es produeix majoritàriament per la metanogènesi i és actiu a tota la zona. En canvi, el règim dominat pel transport subministra gas metà cap a la zona del cim a través dels conductes preferents dels fluids. Aquests dos règims es superimposen de tal manera que una gran quantitat de gas metà és subministrat a la zona del cim de *southern Hydrate Ridge*.

4. Dades i mètodes

En aquesta tesi s'han aplicat diverses metodologies de sedimentologia, geoquímica i propietats físiques dels sediments. Els sediments analitzats es van mostrejar amb una resolució de dues mostres per testimoni (normalment a la secció 2 i 5), excepte en creuar horitzons característics, que es van mostrejar a una resolució d'una mostra per secció. En cada profunditat es va prendre una mostra pels estudis sedimentològics i geoquímics i una altra pels anàlisis de propietats magnètiques dels sediments, de tal manera que totes les dades són directament correlacionables (Gràcia et al., 2006).

Anàlisis texturals

L'anàlisi textural complet de les 581 mostres del cim, flancs i conca de talús de *southern Hydrate Ridge* inclou l'anàlisi de la mida de gra, paràmetres texturals, contingut en carbonat i caracterització de les partícules grolleres.

Les anàlisis de mida de gra de les mostres de sediment provinents dels *Sites* 1244 a 1250 van ser realitzades al laboratori de sedimentologia de l'Institut de Ciències del Mar (CSIC) mitjançant un SediGraph (Micromeritics, 1978). Després d'un atac en H_2O_2 per eliminar la matèria orgànica, les mostres van ser tamisades a 50 μm. La fracció grollera va ser tamisada en columna a obertures de malla de 2, 4 i 6 mm, i les partícules individuals van ser identificades

amb una lupa binocular. La fracció més fina (< 50 μm) va ser analitzada amb el SediGraph, que mesura l'atenuació dels raigs X que travessen una solució on les partícules es troben en suspensió i les intensitats enregistrades es converteixen en pes en funció de la densitat i la Llei de Stoke's (Bianchi et al., 1999). La fracció més grollera (> 50 μm) va ser analitzada en el tub de sedimentació. El tub de sedimentació mesura els canvis de pressió que es produeixen en l'aigua degut a la caiguda de les partícules. Tota la informació sobre la mida de gra va ser integrada en una única corba granulomètrica mitjançant el programa "Integració" desenvolupat pel Grup de Geologia Marina de l'Institut de Ciències del Mar (CSIC). La mida de gra de les 176 mostres dels *Sites* 1251 i 1252 van ser analitzades mitjançant el sistema Coulter al Departament d'Estratigrafia, Paleontologia i Geociències Marines de la Universitat de Barcelona. El coulter analitza la intensitat del raig laser difractat per les partícules de sediment.

Tant el SediGraph com el tub de sedimentació es basen en la llei de Stokes, mentre que el Coulter es basa en la llei de la refracció. Per aquest motiu les dades obtingudes per ambdós mètodes no són directament comparables. Degut a la discrepància entre ambdues tècniques, els resultats dels *Sites* 1251 i 1252 a la conca de talús de *southern Hydrate Ridge* només es consideraran com a tendència general i no seran integrats en l'anàlisi dels paràmetres granulomètrics. Els paràmetres estadístics de les granulometries obtingudes pel mètodes del SediGraph i tub de sedimentació van ser calculats mitjançant el programa "Integració" desenvolupat pel Grup de Geologia Marina de l'Institut de Ciències del Mar (CSIC), incloent-hi resultats de desviació estàndard, moda, mitjana, asimetria i angulositat de la corba granulomètrica.

La identificació de les partícules grolleres es va realitzar mitjançant una lupa binocular (x 100) del Grup de Geologia Marina de l'Institut de Ciències del Mar (CSIC). El programa informàtic "Compta 98", desenvolupat en el mateix grup, va ser utilitzat per quantificar les partícules de cada classe.

El contingut en carbonat total va ser analitzat mitjançant el calcímetre de Bernard del Laboratori de Sedimentologia de l'Institut de Ciències del Mar (CSIC).

Anàlisis mineralògiques

La composició mineralògica total de les mostres, així com la composició de les argiles va ser analitzada mitjançant la difracció de Raigs X (XRD: *X-Ray Diffraction*) en l'*Instituto Andaluz de Ciencias de la Tierra* (UGR / CSIC) de Granada. Les escombrades del difractòmetre Phillips PW 1710 van ser ajustades a 2º-64º 2θ per mostra de sediment total i a 2º-

30º 2θ per mostres de la fracció argila. Aquestes mostres havien estat tractades prèviament amb àcid acètic per eliminar els carbonats i les argiles van ser centrifugades per a la seva separació. Les mostres van ser analitzades abans i després del seu tractament en etililenglicol per a produir l'inflament dels minerals de l'argila. La composició total i de la fracció argila van ser semi-quantificades mitjançant el programa informàtic X-Powder (Martín-Ramos, 2004). L'error absolut d'aquest mètode és de ±5 % per a la mineralogia total i del 10 % per a la mineralogia de les argiles. Degut a l'alt error d'aquesta semi-quantificació, el tractament dels resultats sobre la mineralogia de les argiles serà en forma de tendència i no en valors absoluts.

Microscopi electrònic de rastreig

El microscopi electrònic de rastreig (SEM: *Scanning Electron Microscopy*) va ser utilitzat al *Centro de Instrumentación Científica* de la *Universidad de Granada*, així com un analitzador d'energia retrodispersada de raigs X (EDAX: *Energy Dispersive X-Ray Analyser*), per a estudiar la morfologia i composició de les partícules grolleres dels sediments (> 50 μm).

Propietats físiques

La susceptibilitat magnètica de les mostres va ser mesurada al Laboratori de Paleomagnetisme (CSIC-UB) de l'Institut de Ciències de la Terra "Jaume Almera" (CSIC) de Barcelona (Larrasoaña et al., 2006). Les dades van ser normalitzades pel pes total de la mostra, per a unificar la seva intensitat.

Anàlisis geoquímiques

Es van realitzar diverses anàlisis geoquímiques de les mostres, incloent-hi: contingut en carboni orgànic total, elements majoritaris i traça i extracció seqüencial de barita en sediments. A més, el programa informàtic CoTReM va ser aplicat per obtenir un model geoquímic en base als resultats de composició i a dades de composició de l'aigua intersticial obtingudes durant la campanya *Leg* 204 d'ODP.

El contingut en carboni orgànic total (TOC: *Total Organic Carbon*) va ser analitzat al Servei de Microanàlisi Elemental de l'Institut d'Investigacions Químiques i Ambientals de Barcelona (CSIC). Les anàlisis de carboni es van realitzar després d'un atac àcid en HCl al 7 % durant 12h i la neutralització del pH de les mostres.

La composició elemental dels elements majoritaris en el sediments de *southern Hydrate Ridge* es va obtenir mitjançant un espectròmetre de masses amb flama de plasma (ICP-MS: *inductively coupled plasma-mass spectrometry*) del *Centro de Instrumentación Científica* de la *Universidad de Granada*, amb Re i Rh com a estàndards interns. Les mostres s'havien tractat

prèviament amb una solució de HNO_3 + HF i es van realitzar diverses rèpliques de les anàlisis. L'error d'aquest mètode s'ha establert en Bea (1996).

La composició dels elements majoritaris en les mostres de sediment (Al, Ca, K, Mg, Fe i Mn) es va analitzar mitjançant espectrometria d'absorció atòmica (AAS: *Atomic Absorption Spectrometry*) al *Centro de Instrumentación Científica* de la *Universidad de Granada*. L'error d'aquest mètode s'estima en el 2 % i el seu límit de detecció és de 0.1 ppm.

El procediment descrit per Paytan et al. (1993) per a l'extracció seqüencial de la barita va ser aplicat sobre algunes mostres de sediment de *southern Hydrate Ridge*, seleccionades en funció del seu contingut en Ba. Les extraccions es van realitzar al Laboratori de Geoquímica de l'*Instituto Andaluz de Ciencias de la Tierra* (CSIC / UGR). El procediment inclou l'atac seqüencial dels diversos minerals que composen el sediment, fins a arribar a un residu de barita. El contingut en Bari del residu de l'atac per a destruir els minerals carbonatats del sediment es va dur a terme en un ICP-MS dels Serveis Cientificotècnics de la Universitat de Barcelona. L'anàlisi morfològica de les partícules de barita es va realitzar per SEM.

Els resultats geoquímics de composició del sediment dels flancs de *southern Hydrate Ridge* (*Sites* 1244 a 1247), així com algunes de les dades de composició d'aigua intersticial d'aquests mateixos *Sites*, obtingudes durant la campanya *Leg* 204 d'ODP, van ser utilitzades per a aplicar el programa CoTReM (CoTReM: *Column Transport and Reaction Model*) per obtenir un model geoquímic de la formació de fronts de barita durant la diagènesi inicial. La velocitat d'enterrament del sediment està controlada per la taxa de sedimentació, metre que els ions en dissolució es transporten per difusió molecular. El model es va aplicar fins a una profunditat de 50 metres.

5. Sedimentologia i mineralogia dels sediments de *southern Hydrate Ridge*: Implicacions en àrea font, ambient deposicional i distribució dels hidrats de gas

La distribució de sediment en una àrea determinada està afectada per moltes variables. Aquestes variables resulten interactives i inclouen: tipus i mida del sediment, canvis del nivell del mar, tectònica, aport de sediment, circulació oceànica, etc. (e.g. Stow i Piper, 1984). Per aquest motiu, en àrees on la transformació dels minerals de l'argila durant la diagènesi inicial es pot considerar mínima, es pot traçar la procedència i transport del sediment mitjançant l'estudi de l'evolució de la composició i textura del sediment al llarg del temps.

Textura, propietats físiques i mineralogia dels sediments de southern Hydrate Ridge

Cim: Els sediments del *Site* 1248 en el cim de *southern Hydrate Ridge* poden ser classificats com a argiles llimoses, amb una mida de gra mitjana de 8.3ϕ, amb una distribució granulomètrica mitjana de 55% argila, 41% llim i 4% arena. El contingut en carbonat total varia entre el 3 i el 17%. La seva composició mineralògica mitjana és: 45-50% quars, 25-30% argiles, 15-20% feldspats i 5-10% calcita. La composició mitjana dels minerals de l'argila és: 40-50% mica detrítica, 20-30% esmectita, 15-25% clorita i 5-15% caolinita. Els sediments del *Site* 1249, al cim de *southern Hydrate Ridge* tenen mides de gra entre 8 i 9ϕ. El contingut en carbonats de les mostres és relativament alt (8%). La seva composició mineralògica és de 45-55% quars, 25-35% feldspat i <5% calcita. Els seus minerals de l'argila es distribueixen en 45-55% mica detrítica, 15-25% esmectites, 10-20% clorita i 5-15% caolinita. La mitjana de la mida de gra dels sediments del *Site* 1250 és 8.4ϕ, corresponent a argiles llimoses. La seva distribució granulomètrica mitjana és de 57% argiles, 40% llims i 3% arenes. El contingut en carbonat varia entre el 2 i el 9.5%. Els resultats sobre mineralogia total mostren una composició mitjana de 46 % argiles, 31% quars, 17% feldspats i 5% calcita. En quant a la composició dels minerals de l'argila, els més abundants són els detrítics (44%), seguits per les esmectites (23%), clorites (21%) i caolinita (13%).

Flanc Oest: Els sediments del *Site* 1245, al flanc oest de *southern Hydrate Ridge* tenen una mida de gra mitjana de 8.4ϕ (argiles llimoses), amb una distribució mitjana de 56% argiles, 41% llims i 3% arenes. El contingut en carbonat varia entre 4 i 11%, i la composició mineralògica total està formada per 51% quars, 28% miques, 15% feldspats i 6% calcita. La composició mineralògica de l'argila és de 45% mica detrítica, 26% esmectites, 20% clorites i 10% caolinita. Al *Site* 1247 la mida mitjana dels sediments és de 8.4ϕ. La seva distribució granulomètrica mitja és de 57% argila, 40% llim i 3% arena. El contingut en carbonat varia entre 3 i 11%. La seva composició mineralògica total és de 45-50% argiles, 25-30% quars, 15-20% feldspats i 2-7% calcita. La mineralogia d'argiles és de 40-50% mica detrítica, 15-25% esmectites, 15-25% clorites i 10-20% de caolinites.

Flanc est: Els sediments del *Site* 1244 mostren una mitja de la mida de gra de 8.4ϕ, amb continguts de carbonat entre el 4 i el 11%. La composició mineralògica total és de 45-50% argiles, 28-33% quars, 18-23% feldspats i 3-8% calcita. En quant a la mineralogia d'argiles, la seva composició és: 40-50% mica detrítica, 20-30% clorita, 15-25% caolinita i 10-20% esmectites. Els sediments del *Site* 1246 tenen una mitja de mida de gra de 8.5ϕ, amb continguts en carbonat de fins al 26%. Mineralògicament, els sediments estan formats per argiles (45-

55%), quars, (28-33%), feldspats (18-23%) i calcita (2-7%). En quant a la mineralogia de les argiles, són 40-50% mica detrítica, 18-28% esmectites, 10-20% clorites i 8-18% caolinita.

Conca de talús: Els sediments analitzats del *Site* 1251 mostren una mida de gra mitjana de 6ϕ, amb un contingut mitjà de carbonat de calci del 6%. La seva composició mineralògica és e 50-55% argiles, 25-30% de quars, 10-15% de feldspats i <5% de clacita. Les argiles, estan formades per mica detrítica (65-75%), esmectites (15-25%), caolinita (10-20%) i clorita (5-15%). Els sediments del *Site* 1252 tenen una mitja de mida de gra de 6.2ϕ, amb carbonat de calci de fins al 13% (mitja de 5%). La seva composició mineral mitjana és de 50-55% de mica detrítica, 30-35% quars, 15-20% feldspats i <5% de calcita. La composició dels minerals de l'argila és de 65-75% mica detrítica, 15-25% esmectites, 5-15% clorita i 5-15% caolinita.

Litofàcies de southern Hydrate Ridge

Els resultats sedimentològics de totes les mostres analitzades, juntament amb l'anàlisi les fotografies dels testimonis de sediment, van permetre definir les 4 litofàcies característiques de *southern Hydrate Ridge* com:

- Hemipelagita: és la litofàcies més abundant i està formada per argiles llimoses (mitja 58 % argila, 41% llim i 1% arena), relativament poc seleccionades, amb corbes granulomètriques unimodals i gran quantitat de conquilles de foraminífers tant bentònics com planctònics.

- Turbidita: 190 mostres es van classificar dins d'aquesta fàcies. Es tracta de mostres relativament grolleres (mitja de mida de gra entre 6.6ϕ i 8.9ϕ), molt poc seleccionades, amb corbes granulomètriques bimodals i una gran quantitat de fragments terrígens en la seva fracció grollera. Dins d'aquesta litofàcies es van poder distingir mostres corresponents a les diferents posicions de la seqüència de Bouma (base, cua) i mostres corresponents a turbidites biogèniques.

- Cendres volcàniques: disset de les mostres analitzades contenen una gran quantitat de fragments de cendres i vidres volcànics a la seva fracció grollera. La seva mida de gra és relativament grollera (6.2ϕ a 8.7ϕ), són sediments molt poc seleccionats i la seva distribució granulomètrica és clarament bimodal.

- Debrites: vuit mostres analitzades corresponen a aquesta litofàcies. Són argiles llimoses (mitja de mida de gra de 8.5ϕ) que contenen clasts argilosos i estructures de deformació plàstica. La seva distribució granulomètrica és semblant a les hemipelagites, amb un contingut relativament alt en fragments de conquilles de foraminífers.

Distribució de fàcies a southern Hydrate Ridge

L'estudi de la distribució de les litofàcies a l'estructura de *southern Hydrate Ridge* ha permès la definició i caracterització de sis noves unitats litoestratigràfiques (LU: *Lithostratigrafic Unit*).

La LU VI està formada per sediments hemipelàgics més antics de 1.6 milions d'anys, on s'intercalen alguns dipòsits de moviments de massa. Degut a la compactació dels sediments que formen aquest unitat, algunes de les estructures internes no s'han preservat. Aquests dipòsits corresponen majoritàriament a turbidites. Al sostre de la LU VI s'han identificat nivells de contingut relativament elevat en glauconita. La LU V és una seqüència de més de 300 metres de potència, composta per sediments hemipelàgics que inclouen nombrosos dipòsits de moviments de massa, majoritàriament turbidites, però també amb algunes debrites. Aquesta unitat es va formar durant el període d'entre 1.6 i 1 milió d'anys i el seu límit superior es correspon amb l'Horitzó A. La LU IV és una unitat relativament potent (fins a 130 metres), que es va dipositar al flanc Est i a la conca de talús. Està formada per dipòsits hemipelàgics amb baix contingut en partícules biogèniques i una gran quantitat de partícules terrígenes. Es va dipositar simultàniament a les LU III i II. La LU III està formada per hemipelagites, amb freqüents turbidites intercalades. La LU III es troba sobre la LU V al cim i flanc Oest de *southern Hydrate Ridge*. El seu límit superior coincideix amb l'Horitzó Y identificat als perfils sísmics. La formació de la LU III es va produir durant el periode entre 1 i 0.5 milions d'anys, en relació amb la formació del plec F (veure figures sobre l'evolució de *Hydrate Ridge* al capítol 5). La LU II està formada per hemipelagites on s'intercalen un gran nombre de turbidites, especialment en ambdós flancs de *southern Hydrate Ridge*. Els Horitzons B i B' formen part d'aquesta LU, que es va formar ara fa entre 0.5 i 0.3 milions d'anys. La LU I es subdivideix en les subunitats IB i IA. La LU IB s'acomoda per sobre la LU IV a la conca de talús. Està formada principalment per hemipelagites amb poques turbidites. Aquesta LU te una edat entre 0.3 i l'actualitat i es va dipositar durant l'aixecament de *Hydrate Ridge*. La LU IA es troba sobre la LU IB en la conca de talús de *Hydrate Ridge*. Conté nombroses turbidites i un parell de *debris flows* i representa la sedimentació més recent (< 0.2 milions d'anys) en la conca de talús.

Reconstrucció paleoambiental de southern Hydrate Ridge

Analitzant les dades sedimentològiques de *southern Hydrate Ridge*, les seves LU es poden agrupar en dos grups: un primer grup (LU VI a LU IV) d'unitats amb poques turbidites i un segon grup (LU IV a I) amb nombroses turbidites. A més, s'ha realitzat un càlcul aproximat de l'edat de les primeres turbidites del registre sedimentari a cada *Site* (la més somera) en base a l'índex de sedimentació calculat durant la campanya *Leg* 204 d'ODP segons dades bioestratigràfiques i micro-paleontològiques.

Respecte a la incorporació dels sediments al marge continental, els factors hidrodinàmics primaris que governen el transport de sediment afecten tant al transport en suspensió del material fi com al transport de fons del material més groller. Els processos que afecten la meteorització i el transport en suspensió del material argilós inclouen: els corrents superficials, les capes nefelítiques, el clima, l'índex d'erosió, l'enllaç entre les capçaleres dels canyons submarins amb zona costanera durant les fluctuacions del nivell del mar, els fluxos hiperpícnics generats pels rius o pel desglaç, etc. Pel que fa al transport de fons de les partícules grolleres, inclou les corrents de terbolesa i altres fluxos gravitatius a través dels canyons principals, el subministrament directe de sediment des del marge continental proper i els processos locals de re-treballament.

En el cas concret del marge d'Oregon, les vies de subministrament a través de rius, canals i canyons, així com els corrents oceànics superficials i de fons són relativament ben coneguts (e.g. Karlin, 1980; Underwood i Torres, 2006). Aquests estudis demostren que les esmectites arriben al marge principalment a través del riu Columbia, mentre que les clorites i les miques detrítiques són més típiques dels monts de Klamath. De tota manera, la composició mineralògica de les argiles es veu altament influenciada pels patrons de dispersió de sediment al marge, bàsicament controlats pels corrents oceànics. En aquest sentit, el corrent de Califòrnia ha estat exposat a fluctuacions durant el Pleistocè, en funció dels cicles glacials d'aquesta època (Herbert, 2001). Desgraciadament, la cronostratigrafia de la zona de *southern Hydrate Ridge* no ha estat ben definida, dificultant l'estudi de l'evolució d'aquests paràmetres. Per aquest motiu, només tindrem en compte una visió simplificada de les oscil·lacions del nivell del mar durant el Pleistocè, sense arribar a considerar estadis isotòpics individuals. Respecte al transport de fons en el marge d'Oregon, els tres processos principals són: a) els esdeveniments turbiditics provinents del riu Columbia a través dels canyons d'Astoria i Willapa; b) el subministrament directe de sediment des dels monts de Klamath; i c) processos locals de re-movilització del sediment.

Respecte a la composició dels minerals de l'argila, es pot veure un descens en el contingut d'esmectites amb el temps en els *Sites* 1245 i 1247. Aquests resultats suggereixen que durant el Pleistocè Inferior, quan la LU V va ser formada, els processos de transport en suspensió eren més efectius transportant materials fins en direcció Sud des del Riu Columbia i cap a la zona de *southern Hydrate Ridge*. En canvi, el transport en suspensió va veure reduïda la seva competència durant el Pleistocè Mitjà i Superior, amb el descens del nivell del mar.

El factor més important que afecta el subministrament de sediment des del riu Columbia cap al marge d'Oregon és l'extensió i intensitat de la meteorització. Com que durant el Pleistocè es

va produir un descens relatiu del nivell del mar, podem considerar que l'àrea afectada per la meteorització i l'erosió es va fer més gran, fent més important els factors que afecten la meteorització com a control per a la sedimentació en aquesta àrea. Altres factors que afecten el subministrament a la zona de *southern Hydrate Ridge* estan relacionats amb la circulació oceànica, que està controlada pel corrent de Califòrnia. La disminució gradual del contingut en esmectites durant el Pleistocè suggereix que el corrent de Califòrnia era molt eficient durant el Pleistocè Inferior, mentre que el marge d'Oregon actuava de trampa del material més groller 2-20μm (Krissek, 1984). A mida que el nivell del mar va anar descendint, el transport en suspensió del material del riu Columbia va anar reduint, a mida que el corrent de Califòrnia perdia competència. A partir del Pleistocè Mitjà el transport de fons de material provinent dels monts de Klamath va guanyar importància i, per això, hi ha més dipòsits grollers (turbidites) en les LU més joves.

L'aixecament tectònic de *southern Hydrate Ridge* ha estat datat com a Pleistocè Superior (Chevalier et al., 2006). La reactivació tectònica del marge continental, els canvis en el nivell del mar i el moviment de subducció de la Placa de Juan de Fuca podrien actuar com a desencadenants dels moviments de desestabilització durant el Pleistocè Superior.

El transport de fons des dels Monts de Klamath i del material re-treballat van esdevenir processos predominants durant l'Holocè. En aquest context, les turbidites descrites en els darrers metres de la seqüència sedimentària als *Sites* 1244, 1245 i 1252 corresponen amb el darrer període de baix nivell del mar (i.e. últim màxim glacial). Per altra banda, diversos moviments de massa s'han descrit durant l'Holocè en els *Sites* 1246 i 1252 del flanc Est i conca de talús de *southern Hydrate Ridge*, suggerint que la sedimentació en aquestes dues zones segueix activa. En els *Sites* 1248, 1249 i 1250 del cim de *southern Hydrate Ridge*, no s'hi han trobat dipòsits de transport en massa durant els darrers 40-100 milers d'anys, suggerint que aquesta àrea està principalment essent erosionada.

En conclusió, els sediments de les LU VI i V van ser dipositats durant estadis de nivell del mar alt en un ambient de plana abissal. Aquestes unitats contenen grans quantitats d'esmectites que preferentment provenen del riu Columbia i van ser transportades pel corrent de Califòrnia. Els moviments de massa generats per fenòmens de re-treballament local i de material provinent dels monts de Klamath es van anar fent més importants durant el Pleistocè Mitjà (LU IV a II), mentre els moviments tectònics iniciaven l'aixecament de *Hydrate Ridge*. El corrent de Califòrnia va anar perdent competència gradualment mentre el nivell del mar baixava fins a l'últim màxim glacial, produint un descens en el contingut d'esmectita dels sediments. Durant l'Holocè i sota condicions de nivell del mar estable, l'aixecament de *Hydrate Ridge* va anar

produint moviments de massa locals, generant marques d'erosió al cim i dipòsits de turbidites en els flancs i en la conca de talús.

Fluxos gravitatius a southern Hydrate Ridge

Nombrosos dipòsits de fluxos gravitatius (500 comptabilitzats) com a resultat de moviments de massa i corrents de terbolesa han estat identificats a *southern Hydrate Ridge*. Altres evidències dels processos d'inestabilitat inclouen marques erosives, cicatrius, discordances, fàcies sedimentàries, etc. Els moviments de massa es formen per un increment en la càrrega, per la pèrdua de resistència del sediment o per la combinació de les dues causes. Donat que el marge d'Oregon és un marge sísmicament actiu i que *Hydrate Ridge* és un alt estructural aixecat tectònicament, cal considerar els fenòmens sísmics com a causes del desencadenament dels fenòmens gravitatius. Però també és sabut que una gran quantitat d'hidrats de gas està present en els sediments de tot el marge de Cascadia. Per aquest motiu i, donada l'alta fluctuació del nivell del mar durant el Pleistocè, la dissociació dels hidrats de gas ha de considerar-se també com un probable mecanisme desencadenant de moviments de massa en aquesta regió. En aquest sentit, l'alta freqüència de turbidites en les LU III i II i la seva coincidència amb períodes de baix nivell del mar, corroboren aquesta hipòtesi.

6. Distribució dels hidrats de gas en relació a la textura sedimentària

Textura dels sediments rics en hidrats de gas de southern Hydrate Ridge

Per a estudiar com la textura sedimentària influeix en la distribució dels hidrats de gas a la zona de *southern Hydrate Ridge*, es van analitzar vint mostres de sediment seleccionades en base a la seva fàbrica (*soupy* o *mousse-like*) i quatre intervals sedimentaris en base al seu contingut en hidrats de gas. Aquest contingut en hidrats de gas havia estat deduït a partir de imatges de tomografia computeritzada de Raigs X, mesurada en els intervals de sediment preservats a -80ºC.

Les vint mostres de sediment de fàbrica *soupy* i *mousse-like* analitzades per aquesta tesi mostren una mida de gra mitjà entre 7.7 i 8.8ϕ, amb continguts d'arena de fins al 8.9 % (55 % argila, 41 % llim i 3 % arena). Tot i que la seva estructura interna es troba pertorbada degut a la dissociació dels hidrats de gas, la seva corva granulomètrica mostra característiques similars a les de la fàcies de turbidita. Dels quatre intervals analitzats, només tres van desenvolupar textures *soupy* o *mousse-like* després de la dissociació dels hidrats de gas. Precisament el quart interval era el que contenia menys quantitat d'hidrats segons les imatges de tomografia computeritzada obtingudes prèviament a la dissociació (Abegg et al., 2006, 2007). Els resultats

de l'anàlisi de les mostres de sediment riques en hidrat de gas mostren una mida de gra més grollera que el sediment hemipelàgic present a *southern Hydrate Ridge*.

Textura sedimentària com a factor determinant de la distribució d'hidrats de gas

La mida de gra pot donar informació sobre la porositat disponible i, per tant, permeabilitat per al transport de fluids o espai on formar hidrats de gas (e.g. Soloviev i Ginsburg, 1997; Weinberger et al., 2006).

Les fàbriques sedimentàries *soupy* i *mousse-like* han estat identificades en relació amb la presència d'hidrats de gas en marges continentals actius i passius, en zones de volcans de fang, etc. (e.g. Paull et al., 1996b; Soh, 1997; Pinheiro et al., 2003). Aquestes fàbriques es van generar espontàniament en mostres de sediment on la presència de sediment havia estat deduïda a través d'imatges de tomografia computeritzada de Raigs X, després de provocar la dissociació dels hidrats de gas que contenien. Aquesta evidència demostra l'ús de les fàbriques *soupy* i *mousse-like* com a *proxy* per a demostrar la presència d'hidrats de gas en una zona. Si comparem aquesta evidència amb altres *proxies* geofísics que evidencien la presència d'hidrats de gas, aquestes mostres corresponen a intervals amb anomalies tèrmiques negatives detectades en imatges d'infraroig i amb intervals de baixa resistivitat elèctrica.

La major part de les mostres pertorbades i riques en hidrats de gas analitzades per aquest estudi tenen una mida de gra més grollera que la mitjana de mida de gra de les mostres de fàcies hemipelàgica definida en aquesta tesi. Així, es pot deduir que els hidrats de gas es formen preferentment en les capes de sediment més groller, que corresponen a intervals de major porositat. Així, el gas migraria aprofitant les capes de mida de gra més gran, formant hidrats de gas un cop assolida la GHSZ.

Només dues mostres pertorbades mostren una mida de gra més fina que la mitjana de mida de gra de la fàcies hemipelàgica. Aquests sediments es van mostrejar a poca fondària sota el cim de *southern Hydrate Ridge*, precisament a la zona on es va trobar més quantitat d'hidrat de gas durant la campanya *Leg* 204 d'ODP. Aquesta evidència fa pensar que en la zona del cim hi ha prou metà disponible en les zones intersticials com per a arribar a formar hidrats de gas fins i tot en les capes de menor mida de gra.

Dues mostres localitzades sota la profunditat del GHSZ també mostraven una fàbrica pertorbada. Tot i que la diferència de profunditat (10 metres) està dins del rang d'incertesa del càlcul de la profunditat del BSR a partir dels models de velocitat sísmica, una altra explicació

possible per al desenvolupament de fàbriques pertorbades sota la GHSZ seria l'ex-solució del gas del fluid intersticial.

7. Processos geoquímics durant la diagènesi inicial

Els processos geoquímics de la diagènesi inicial inclouen els canvis sedimentaris que tenen lloc durant els primers estadis de l'enterrament, quan la temperatura és baixa i no hi ha sobre-pressió. En les àrees de gran contingut en hidrat de gas, les reaccions geoquímiques que tenen lloc durant aquesta etapa es veuen fortament influenciades per la presència de fluxos rics en hidrocarburs. En aquest sentit, la oxidació anaeròbica del metà (AOM: *Anaerobic oxidation of methane*) és una reacció que consumeix metà i sulfat i forma carbonat i sulfur sota l'acció de diversos organismes microbians. El flux de metà i el sulfat disponible, que bàsicament depèn de la concentració marina, defineixen la profunditat on té lloc que s'anomena zona de transició del metà i el sulfat (SMT: *sulphate – methane transition zone*).

La barita ($BaSO_4$), com a sulfat de Bari, forma part del cicle del Sofre. A més, es relaciona amb el cicle del carboni a través de la AOM i la oxidació de la matèria orgànica. El cicle de la barita durant la diagènesi inicial estableix que la barita s'acumula al fons del mar provinent de la columna d'aigua. Durant el seu enterrament i degut a l'esgotament del sulfat, la barita es dissol mentre el sulfat és consumit pel metà a través de la AOM i la oxidació de la matèria orgànica. El Bari dissolt es difon cap amunt a través de la columna sedimentària per a tornar a precipitar en forma de barita quan troba suficient sulfat disponible, formant un front d'acumulació (e.g. Torres et al., 1996b). Per això, la identificació i l'estudi dels pics de barita en el sediment pot donar informació sobre el flux de metà que hi ha en una regió. Si considerem un índex de sedimentació constant, la mida dels pics de barita pot donar informació sobre el temps que un flux de metà mínim ha estat operatiu en una àrea determinada.

Contingut en Bari en els sediments i aigües intersticials de southern Hydrate Ridge

Els continguts en Bari en els sediments i les aigües intersticials de *southern Hydrate Ridge* varien entre 454 ppm i 1021 ppm. En el cim de *southern Hydrate Ridge* no s'han trobat tendències o acumulacions significatives en els primers metres de la columna sedimentària. Les concentracions de Bari en els sediments dels flancs Est i Oest de *southern Hydrate Ridge* mostren continguts elevats en els primers metres sota el fons marí, amb altres pics de concentració algunes desenes de metres per sota. Alguns d'aquests pics profunds es relacionen amb pics en la concentració de Bari dissolt en les aigües intersticials. En la conca de talús de *southern Hydrate Ridge* la concentració de Bari en els sediments mostra una clara tendència

creixent a profunditat que es correspon amb valor elevats de Bari en la composició de les aigües intersticials.

Dades de Bari, Bari / Alumini i TOC a southern Hydrate Ridge

Per tal de comprovar que el contingut en Bari mesurat en els sediments correspon a la presència de minerals de Bari i no a la cristal·lització de sals de Bari des de l'aigua intersticial, les anàlisis de Bari en sediments van ser repetides en deu mostres seleccionades després de rentar-les repetidament amb aigua desionitzada. Els resultats obtinguts no difereixen gaire dels resultats de contingut de Bari originals, evidenciant que la cristal·lització de Bari des de l'aigua intersticial no és un fenomen destacable.

La presència en els sediments d'alts continguts en alumini-silicats rics en Bari podria produir un increment en el contingut en Bari. Per a descartar aquesta hipòtesi, es va estudiar comparativament les corbes de contingut total de Bari, respecte a les corbes de contingut en Bari normalitzat respecte l'Alumini. No s'observa cap diferència remarcable entre les dues corbes de cada *Site* evidenciant que la presència d'alumini-silicats no és la raó dels alts continguts en Bari en els sediments de *southern Hydrate Ridge*. Aquest mateix procediment comparatiu es va realitzar respecte a les corbes de TOC de cada *Site*. Les corbes de Bari i les de TOC no mostren tendències semblants.

Contingut de sulfat i metà en les aigües intersticials

Els continguts en sulfat i metà present en les aigües intersticials van ser analitzats sistemàticament durant la campanya *Leg* 204 d'ODP. Aquestes anàlisis van permetre calcular els respectius perfils de concentració i la profunditat de la SMT en els *Sites* dels flancs i conca de talús de *southern Hydrate Ridge*. Els perfils de concentració de sulfat no van poder ser calculats als *Sites* del cim de *southern Hydrate Ridge* degut al descens en la concentració en els primers centímetres de la columna sedimentària.

Controls sedimentològics i geoquímics dels continguts de Bari

La distribució en profunditat del contingut de Bari en els sediments i aigües intersticials de *southern Hydrate Ridge* mostra l'existència de diversos intervals amb alts continguts en Bari tant en la fase sòlida com en la líquida. Aquesta coincidència suggereix que el mineral de Bari en aquests sediments està sent dissolt. Altres vegades, els pics d'alt contingut en Bari en els sediments no es corresponen amb alts continguts en la fase líquida. Aquest fet podria ser degut a que el mineral de Bari és estable a aquelles profunditats o bé està sent dissolt, però el Bari resultant està sent ràpidament difós. Alguns d'aquests pics es troben per sota del nivell del SMT. En ocasions s'observen també pics d'alt contingut en Bari en les aigües intersticials que

no es corresponen amb pics en la fase sòlida. Aquest fet podria ser degut a l'existència de fluids rics en Bari, corresponents a fluxos de fluids transportats a gran profunditat.

Als *Sites* 1245 i 1247 s'observa un pic en la concentració de Bari en les aigües intersticials entre la profunditat de la base de la GHSZ i la profunditat de l'Horitzó A. Aquest pic no es correspon amb cap característica remarcable en la concentració de Bari en els sediments. L'Horitzó A ha estat reconegut com un dels principals conductes per al transport de fluids a la zona de *southern Hydrate Ridge* (Tréhu et al., 2004a). Aquestes dades evidencien el possible transport de fluids rics en Bari al llarg de l'Horitzó A. En arribar a *southern Hydrate Ridge*, aquests fluids quedarien atrapats entre la profunditat de l'Horitzó A i la base de la GHSZ. La base de la GHSZ actuaria com una barrera per als fluids, degut a la ocupació de la seva porositat pels hidrats de gas. Aquest procés d'acumulació de fluids sota de la GHSZ es corrobora amb dades disponibles sobre composició de gasos dissolts, que mostren un increment atípic en la proporció entre gas età i metà en aquesta mateixa profunditat (C_1/C_2; Tréhu et al., 2003).

Barita diagenètica

El Bari en els sediments marins acostuma a formar fases minerals com sulfats (barita $BaSO_4$), carbonat (whiterita $BaCO_3$), alumino-silicats (e.g. feldspats), òxids i hidròxids. Els residus de l'extracció seqüencial de barita i la següent aplicació de SEM i EDAX mostren que la barita és el mineral de Bari més freqüent en el sediments de *southern Hydrate Ridge*. Els cristalls de barita mostren formes poligonals i arestes afilades. Aquestes evidències suggereixen l'origen diagenètic dels cristalls de barita, descartant el seu origen biològic. La no correspondència amb les dades de TOC reforça aquesta idea. La comparació entre les dades de Bari i les de Bari normalitzat respecte l'Alumini suggereixen que els cristalls de barita no tenen un origen detrític. Totes aquestes evidències mostren que l'origen més probable dels cristalls de barita són els relacionats amb les reaccions geoquímiques que tenen lloc durant la diagènesi inicial. També s'hi ha detectat estructures de dissolució, que poden ser atribuïdes a la dissolució de la barita en el sediment, però també a la dissolució durant el procés d'extracció seqüencial.

Per comprovar si fases de carbonat de Bari han estat dissoltes durant el procés d'extracció de la barita, es van realitzar anàlisis de contingut de Bari en el residu de l'atac de carbonats de catorze mostres riques en Bari. Els resultats donen valors molt baixos (< 5ppm), demostrant que el carbonat de Bari no és un dels minerals presents en els sediments de *southern Hydrate Ridge*.

Temps necessari per a la formació dels pics de barita

Els índex de dissolució i re-precipitació de la barita estan controlats pel transport del Bari dissolt via difusió molecular. Per això, el procés pot ser modelitzat en base a la segona llei de

Fick. Varem aplicar el programa informàtic CoTReM per a quantificar el temps necessari per a formar les diferents acumulacions de barita detectades als dos flancs de *southern Hydrate Ridge*. El model va ser aplicat sobre una concentració de base estimada per a cada *Site*. Com a factor de control, es va utilitzar la porositat calculada per a cada *Site* durant el *Leg* 204 d'ODP. La porositat exerceix una gran influència sobre el transport en difusió i, per tant, sobre els resultats obtinguts. Per això, el temps necessari obtingut per a cada *Site* es considera només com una dada aproximada.

Es van obtenir resultats corresponents a períodes de temps d'entre 375 i 1000 anys, que semblen coherents amb d'altres aproximacions calculades en diferents ambients geològics (e.g. Riedinger et al., 2006).

Fronts de barita somers

La disminució en la concentració de sulfat en els primers metres de sediments marins està relacionada amb la presència de fluxos de metà. En el cas de *southern Hydrate Ridge*, la presència de fluxos de metà en el fons marí ja havia estat detectada prèviament (e.g. Suess et al., 2001).

Fronts somers de barita han estat detectats en les dades geoquímiques dels *Sites* 1244 a 1247 en ambdós flancs de *southern Hydrate Ridge*, sobre la profunditat del SMT. La seva evolució en el temps va ser modelitzada amb el programa informàtic CoTReM. Els resultats obtinguts mostren que el pic més som detectat en les dades de Bari en sediments serà dissolt gradualment durant els propers 1000 anys a mida que va sent enterrat. Aquests pics no es corresponen amb pics en la concentració de Bari en l'aigua intersticial, suggerint que una ràpida difusió del Bari dissolt acompanya la seva dissolució. Els pics somers d'acumulació de barita poden ser formats per dos processos: a) l'acumulació directa de barita en el fons marí per processos biològics o detrítics, o b) el cicle diagenètic de la barita en un ambient de flux de metà superior a l'actual. Els resultats del model CoTReM mostren que el front d'acumulació de barita actual es troba diversos metres per sota de l'actual profunditat del SMT i anirà enfonsant-se gradualment durant els propers mil anys, mentre que els pics de barita més profunds (> 20 mbsf) seran dissolts. La zona de major índex de reacció del Bari mostra una profunditat actual semblant a la del SMT, però amb una amplada molt superior. Aquesta zona també s'anirà enfonsant durant els propers mil anys. Aquests resultats demostren que la AOM i la oxidació de la matèria orgànica són processos actius no només en una estreta interfície, sinó al llarg de tot un ample interval. Resultats similars es van presentar per a la regió de *Blake Ridge* (Snyder et al., 2007).

Hi ha dos processos geoquímics capaços de generar un desplaçament en profunditat de la SMT: a) la reducció del flux de metà, i b) un increment en el sulfat disponible a la columna sedimentària superficial. El model considera un flux de metà constant. Els resultats suggereixen que els pics de barita més superficials dissolts actuen com a font de sulfat en la columna sedimentària, produint la profundització de la SMT. Una altra causa possible pel desplaçament de la SMT és un esdeveniment deposicional sobtat.

Fronts de barita profunds

Tal i com s'ha presentat a dalt, en els dos flancs de *southern Hydrate Ridge* s'han detectats pics de contingut de barita per sota del SMT, la zona on teòricament el sulfat està exhaurit i, per tant, la barita no és geoquímicament estable. Riedinger et al. (2007) va suggerir la formació d'una crosta carbonatada o de sulfur en les partícules de barita com una possible explicació per a la no dissolució d'aquest sulfat en profunditat. Tot i que el procés encara no es coneix prou bé, les dades de baix contingut en TOC i Bari en el residu de l'atac de carbonats durant el procés d'extracció seqüencial de barita, suggereixen que aquest no és un mecanisme present en els sediments de *southern Hydrate Ridge*. Tanmateix, l'anàlisi de SEM dels cristalls de barita i la seva composició analitzada per EDAX mostren continguts en Calci relativament elevats.

Un canvi abrupte en l'índex de sedimentació ha estat considerat com un factor que pot provocar la preservació del mineral barita en profunditat (e.g. Torres et al., 1996b). En aquest context, la sedimentació sobtada d'un gran moviment de massa (e.g. *debris flow*), produiria un enterrament sobtat dels fronts de barita, així com la migració de la SMT que canviaria cap a un altre interval. L'elevat nombre de moviments de massa identificats en els sediments de *southern Hydrate Ridge* suggereixen que aquesta podria ser una possible explicació per a aquest procés. Tanmateix, l'estudi de l'edat dels pics del Bari en funció de l'edat dels moviments de massa descrits a *southern Hydrate Ridge* seria necessari per tal de corroborar aquesta hipòtesi.

Altres autors han proposat l'advecció de fluids rics en sulfats des d'altes profunditats en la columna sedimentària com a mecanisme de formació de fronts d'acumulació de barita en profunditat. Les corbes de concentració de Bari en profunditat, mostren que en els *Sites* 1251 i 1252, a la conca de talús de *southern Hydrate Ridge*, sediments rics en Bari estan s'estan dissolent en la zona corresponent als materials del prisma d'acreció. Aquests materials actuarien com a font dels fluids rics en sulfat. El sulfat dissolt migraria a través dels conductes preferents per a la circulació de fluids i faria precipitar barita en trobar prou Bari disponible.

8. Conclusions i treball futur

Les principals conclusions assolides durant aquesta tesi són les següents:

- La major part dels sediments de *southern Hydrate Ridge* corresponen a hemipelagites, amb nombroses turbidites intercalades, juntament amb algunes debrites i capes riques en cendres volcàniques.

- El patró sedimentari en la regió de *southern Hydrate Ridge* estan controlades per paràmetres climàtics i tectònics, com la intensitat del corrent de Califòrnia i els moviments locals d'aixecament de *southern Hydrate Ridge*. Aquests paràmetres controlen la distribució dels minerals de l'argila al marge d'Oregon, així com les fàcies sedimentàries que s'hi produeixen.

- El transport en suspensió del material fi pel corrent de Califòrnia va ser més efectiu durant el Pleistocè Inferior. El transport de fons dels materials grollers d'abast local i regional va ser el procés predominants durant el Pleistocè Mitjà i l'Holocè degut a la reactivació de l'aixecament de *southern Hydrate Ridge*.

- Durant el Pleistocè Superior i degut a les fluctuacions del nivell del mar, la dissociació dels hidrats de gas, juntament amb els moviments sísmics produïts per moviments tectònics del marge de Cascadia són les causes més probables per generar els nombrosos moviments de massa del marge d'Oregon.

- Les fabriques *mousse-like* i *soupy* es produeixen per la dissociació dels hidrats de gas. La seva identificació durant la descripció sedimentològica dels testimonis de sediment és clau, especialment en àrees d'alt contingut en hidrats de gas com ara volcans de fang, àrees de surgències, etc.

- La majoria dels sediments pertorbats i rics en hidrats de gas de *southern Hydrate Ridge* tenen una mida de gra superior a la mida de les hemipelagites, i corresponen a la fàcies turbidita. Aquestes capes de major mida de gra actuarien com a conductes de transport de fluids sota la GHSZ i com a espai disponible per a la formació d'hidrats de gas a la GHSZ.

- Diversos fronts d'acumulació de barita es formen a *southern Hydrate Ridge* com a resultat de processos geoquímics durant la diagènesis inicial, relacionats amb els fluids rics en metà i la descomposició de la matèria orgànica. Aquests processos han estat actius a *southern Hydrate Ridge* durant un període de mil anys.

- La textura sedimentària juga un paper essencial controlant la trajectòria de migració dels fluids a *southern Hydrate Ridge*. L'evolució temporal del flux de fluids pot ser estudiada mitjançant les fases minerals que es formen durant la diagènesis inicial.

Perspectives de treball futur

Aquesta tesi correspon a l'estudi multidisciplinar d'un sistema sedimentari marí ric en hidrats de gas, on s'integren dades de sedimentologia, mineralogia i geoquímica, tal i com he resumit anteriorment. Tanmateix, com a tot treball de recerca, també ens hem trobat amb algunes dificultats remarcables. En aquest sentit, la incertesa en l'edat dels sediments ha representat el major handicap per aquest estudi, especialment a l'hora d'entendre l'evolució temporal dels factors climàtics i tectònics que controlen la sedimentació a la regió de *southern Hydrate Ridge*. Per a resoldre aquesta problemàtica es podrien aplicar diverses tècniques, com ara: la determinació directa de l'edat a través de datacions de ^{14}C per edats fins a 40-50 milers d'anys; l'anàlisi de la composició isotòpica de l'Oxigen (^{18}O) dels foraminífers presents al sediment hemipelàgic; l'anàlisi de la paleointensitat magnètica, els quals permeten arribar a tot el quaternari; etc.

Altres estudis que es podrien realitzar per a millorar aquest treball inclouen:

- El tractament estadístic de totes les dades. Les dades sedimentològiques, mineralògiques, geoquímiques i magnètiques utilitzades per a aquesta tesi són totalment relacionables, ja que provenen de mostres de sediment localitzades a la mateixa posició en la columna sedimentària. Per tal de determinar quines d'aquestes variables estan relacionades entre si i poder estudiar quins processos les afecten, proposem aplicar diversos mètodes d'estadística multivariant (e.g. mètode dels components principals, anàlisi de correspondència, etc.).

- Un estudi sedimentològic integrat de tot el marge de Cascadia permetria comprovar la influència dels paràmetres climàtics i tectònics a tota la regió. En aquest sentit proposaria fer un estudi comparatiu amb les dades obtingudes recentment durant la campanya *Expedition* 311 de l'IODP davant de la illa de Vancouver.

- Algunes tasques pendents per a completar l'estudi geoquímic de les dades presentades en aquesta tesi són: l'estudi de la distribució d'alguns elements químics, l'anàlisi isotòpic de Sofre als cristalls de barita, etc.

- Millores en el model geoquímic CoTReM serien molt útils per a modelitzar l'evolució dels fronts de Bari i dels flux de metà a la zona de *southern Hydrate Ridge*. Aquest mateix model podria ser aplicat també per estudiar l'evolució d'altres fases minerals durant la diagènesi inicial, com ara els sulfurs de Ferro com la greigita i la pirrotita, estudiats per Larrasoaña et al., (2007). La possible aplicació d'aquests minerals com a *proxies* per a l'evolució dels fluxos de metà també és un punt important a considerar.

Presentation and objectives

The knowledge on gas hydrate has been significantly improved during the last decade after the recognition of this topic as a key factor affecting a number of different global processes such as climatic change, seafloor stability, economic gas extraction, deep-sea biosphere, etc. The identification of the importance of gas hydrate has been translated into its inclusion as a priority in the most important worldwide programs for ocean research: the U.S. MARGINS of the National Science Foundation, the Deep Sea Frontier of the European Community, and the Initial Science Plan of the Integrated Ocean Drilling Program.

This study was launched during the Leg 204 of the Ocean Drilling Program (ODP): "Drilling gas hydrates at Hydrate Ridge" (7^{th} of July – 2^{nd} of September 2002). Eulàlia Gràcia was involved in this cruise as part of the shipboard scientific party and on behalf of the Spanish scientific community. Spain forms part of the ODP (actually IODP), as part of the European Consortium for Ocean Research Drilling (ECORD). Our participation in ODP Leg 204, funded through an *Acción Especial* REN 2001-5262-E of the Spanish Ministry of Science and Education, enabled us to access to the complete dataset analyses and interpretations made during the cruise, the first one completely dedicated to the exploration and systematic sampling of a gas hydrate-rich setting, such as Hydrate Ridge. After completing the ODP Leg 204, and due to the recognition of the valuable data acquired and the unique opportunity to continue this study, funding from a second *Acción Especial* BTE 2002-11698-E enabled us to start the analyses of our requested sediment samples.

A review of the state of the art in this topic shows that most of the recently published studies focus on single aspects of gas hydrate research, giving only a partial and incomplete view of the full story. Nevertheless, scientific knowledge demands more multidisciplinary studies in order to improve the understanding about the global processes that affect gas hydrate systems, e.g. how a change in gas hydrate stability could globally affect our planet. In this context, this thesis presents an integrated study of gas hydrate-rich sediments from southern Hydrate Ridge, recovered during ODP Leg 204 cruise involving three main aspects: 1) lithostratigraphic study of sediments from southern Hydrate Ridge; 2) characterization of the main gas hydrate-rich intervals; and 3) a geochemical study of the early diagenetic process and their influence on the formation and preservation of barite fronts within the sedimentary column.

Objectives of the thesis

The main objectives aimed in this thesis are as follows:

(1) To characterize the main sediment facies of southern Hydrate Ridge: The description of the sediment texture, bulk and clay mineralogy, magnetic susceptibility, carbonate content and coarse-grain mineralogy of sediment samples from the four environments of southern Hydrate Ridge: the summit, the western and eastern flanks and the slope basin. This will allow the detailed characterization of the main lithofacies that compose southern Hydrate Ridge, studying their distribution, abundance and evolution over time.

(2) To analyze the climatic and tectonic processes that control the sediment transport and deposition in the Oregon continental margin and their evolution during the last 1.5 M.a.: The determination of the main mechanisms for sediment transport (bedload or suspension) operating in the Oregon margin and providing sediment deposition in the Hydrate Ridge area. The study of the evolution of the main factors governing sediment transport over the last 1.5 million of years, including both climatic and tectonic processes.

(3) To discuss the gas hydrate dissociation as a plausible triggering mechanism of mass-transport deposits in the Hydrate Ridge region and on the Oregon margin: The determination of the main triggering mechanisms for mass-transport movements. Discussion of the relevance of the identified triggering mechanisms during the last 1.5 million of years in the Oregon margin.

(4) To evaluate the gas hydrate distribution at southern Hydrate Ridge and its relationship with textural and physical properties of the sediment. To study the sedimentary texture as a significant factor for gas hydrate distribution in southern Hydrate Ridge: The sedimentary characterization of selected disturbed sediment samples (mousse-like and soupy) and gas hydrate-rich samples from southern Hydrate Ridge. Physical properties as porosity will add valuable information about the permeability of the sediment. Available computer tomographic images will be used to quantify the gas hydrate content in the selected sediment intervals.

(5) To quantify the barium concentration in sediment samples and to compare it with the pore water concentration from southern Hydrate Ridge: Integration of this data with other textural and chemical parameters such as the content of total organic carbon or aluminium. Analysis of the main barium-rich minerals present in the sediment facies. Evaluation of the detrital, biogenic or diagenetic origin of the barite fronts at southern Hydrate Ridge.

(6) To elucidate the evolution of early diagenetic processes and the formation of barite fronts in a marine gas hydrate system with respect to the processes that govern fluid flow in an accretionary complex system: Modelling the barite front formation and preservation. Quantification of the time required to form the barite fronts in the sedimentary column through the application of the CoTReM software. Evaluation of the processes involved in their formation. Research into the future evolution of the barium profiles at southern Hydrate Ridge, and investigation of the main parameters affecting barite conservation at depth.

(7) To study fluid flow in the southern Hydrate Ridge sediments: Sedimentological properties control the main conduits for fluid flow. Fluid flow controls the methane availability for gas hydrate formation and barite front formation over time. The interpretation of the sedimentological, geochemical and gas-hydrate distribution results will enable us to undertake a preliminary study of the fluid flow in Hydrate Ridge.

Structure of the thesis

This Ph.D thesis is structured in three parts. Part I includes Chapter 1 and 2, which present the main basic concepts for gas hydrate research and establish the main characteristics of the Cascadia continental margin, the geological setting of this study. Chapter 1 starts with the state of the art in gas hydrate research for the last decades, following by the basic concepts about gas hydrate formation, stability and evidences. The main implications of gas hydrate research, such as its role as an energy source, climate change, as a special component of the carbon cycle, or slope instability in continental margins are also discussed. Chapter 2 includes a synthetic description of the Cascadia continental margin from a physiographic, tectonic and oceanographic point of view and, more specifically, of the study area: the Hydrate Ridge and its southern summit.

Part II describes the available data obtained during ODP Leg 204, as well as the specific data and methodologies used during this thesis. Chapter 3 focuses on the main results and highlights from ODP Leg 204, including sedimentary and tectonic approaches. The description of the main geophysical, sedimentological and geochemical parameters and tools applied or first used during the cruise are presented, as well as their capability to detect gas hydrates in the sedimentary column. Chapter 3 ends with a detailed description of the gas hydrate distribution in southern Hydrate Ridge. Some of these data such as the infrared thermal images, resistivity-at-the-bit, etc., has been used in this thesis to infer the gas hydrate presence in the analysed sediments. The main methodologies applied in this thesis are presented in Chapter 4, starting with the criteria used for sediment sampling. This chapter includes a description of all the

sedimentary, mineralogical and geochemical techniques applied on sediment samples, as well as some physical properties that were used for reference.

Part III of this thesis includes the main results and discussion of the sedimentological and geochemical analyses. This part includes four chapters (5 to 8). Chapter 5 deals with the lithological description of the sediments from southern Hydrate Ridge, describing and discussing the textural, mineralogical and magnetic susceptibility results of more than 550 analysed samples. All these analyses allow the recognition and description of the four main lithofacies that form southern Hydrate Ridge. The detailed study of the lithofacies distribution enables a palaeoenvironmental reconstruction for southern Hydrate Ridge, including a discussion of the most probable sediment sources and transport mechanisms in the area. The main climatic and tectonic controls for sediment distribution in the Oregon margin are also evaluated over the last 1.5 millions of years. The role of gas hydrate dissociation as a triggering mechanism for slope destabilization is also briefly discussed. The relationship between sediment texture and gas hydrate presence is evaluated in Chapter 6. The textural, mineralogical and magnetic susceptibility characteristics of discrete sediment samples rich in gas hydrates are analysed, leading to the conclusion that gas hydrates in southern Hydrate Ridge preferentially form in the coarse-grain layers. A new complete description of the sediment disturbance fabrics mousse-like and soupy is made, proving that these sedimentary fabrics are directly related to the dissociation of gas hydrates. Chapter 7 represents a further step on the geochemistry of marine gas hydrate systems. This chapter focuses on early diagenetic processes and barite distribution, describing the different geochemical and sedimentological factors that can affect its formation and preservation over depth. The use of the CoTReM modelling software allows further understanding on the evolution of the distinct barite enrichments over time, and lead to the presentation of a new model of barite formation and conservation in gas hydrate-rich environments located in accretionary complex systems. Finally, Chapter 8 comprises a brief integration of all the results presented in this thesis, summarizing a list of conclusions. A proposal of the further work needed to complete the present study is also included at the end of this chapter.

Part IV includes a list of all cited references. It also contains a list of the figures and tables captions, as well as the main acronyms used in the thesis. The thesis ends with a list of acronyms and its Catalan translation.

PART I

1. Introduction

Gas hydrates are naturally occurring ice-like compounds in which low molecular weight gases (methane, propane, etc.) are trapped within a lattice of water molecules, also known as clathrate or clathrate hydrate, linked by van der Waals forces (non polar) (Sloan, 1998). Methane hydrates, the most common gas hydrates (Rath, 2008), are chemical structures formed by methane molecules trapped in cages of water molecules that became unstable when they are empty. The inclusion of hydrocarbon molecules in gas hydrates gives them the capacity to burn even with their ice-like appearance and their low temperature (Figure 1.1). The principal conditions controlling the formation and preservation of gas hydrates in nature are temperature, pressure and availability of low molecular weight gases and water molecules.

Recently, gas hydrate research has been included as a priority in the most important programs for ocean research: the U.S. MARGINS of the National Science Foundation (Margins office, 2003), the Deep Sea Frontier of the European Community (Cochonat et al., 2007), and the Initial Science Plan of the Integrating Ocean Drilling Program (IODP Planning Sub-Committee, 2005). The different aspects that will be improved throughout these programs include: knowledge of the economic potential of gas hydrates, the geological hazards arising from hydrate destabilization and its impact on climate. Some of these aspects will be introduced below.

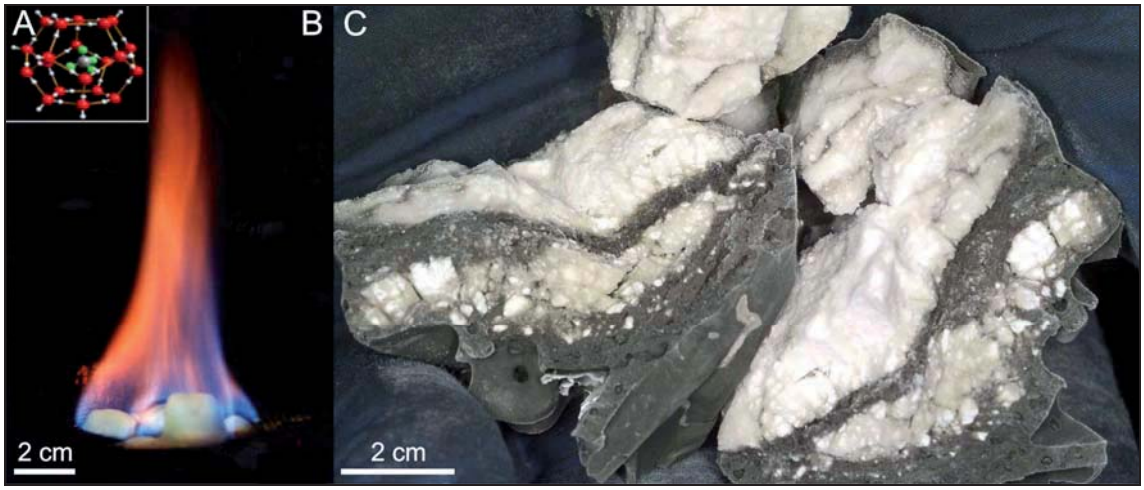

Figure 1.1. A. Clathrate structure (University of Göttingen, GZG. Abt. Kristallographie). **B.** When gas hydrate dissociates, the gas (mainly methane) released can be burned while water drips (from USGS webpage). **C.** Example of natural gas hydrate samples (white) recovered during Ocean Drilling Program Leg 204 from southern Hydrate Ridge, Cascadia margin (NE Pacific).

Sir Humphrey Davy (Davy, 1811) was the first chemist to synthesize a chlorine hydrate molecule and has therefore been regarded as the discoverer of gas hydrates. Following the

advances made in chemistry during the 1920s and 1930s, gas hydrates were identified as the solid substances that formed within the natural gas pipelines occasionally clogging them in permafrost areas (Hammerschmidt, 1934). After this discovery, the hydrocarbon industries funded research to gain insight into the formation of gas hydrates in order to avoid problems of gas transport over long distances (e.g. Hovland and Gudmestad, 2001). During the 1940s and 1950s the chemical studies on hydrates were continued by Powell, who first named the molecular structure *clathrate* (Palin and Powell, 1945; 1947). During the 1960s it was suggested that methane-rich gas hydrates existed in nature and in large quantities (Makogon, 1965). In the 1970s Russian scientists pioneered gas hydrate research with the first discovery of gas hydrates in a natural environment in the permafrost area of Siberia (Makogon, 1971). Some years later, gas hydrates were discovered in the Canada's MacKenzie Delta (Bily and Dick, 1974) and in sediments from the Caspian and the Black Sea (Yefremova and Zhizhchenko, 1974). During the 1970s and 1980s the development of new geophysical prospecting tools allowed the prediction of gas hydrate in large sediment areas of the Blake Ridge, in the American eastern continental margin (Atlantic Ocean) (Stoll et al., 1971) and elsewhere (Shipley et al., 1979). In 1979 hydrates were recovered during Leg 66 of the Deep Sea Drilling project offshore Mexico, in the Middle American Trench (Watkins and Moore, 1981), initiating modern gas hydrate research along the principal oceanic continental slopes (Kvenvolden, 1993). Parallel to these investigations and because of its direct relationship with the presence of cold seeps, pockmarks and gas in sediments, gas hydrate investigations have been complemented by studies in all these related topics (e.g. Mazurenko and Soloviev, 2003; Carson et al., 1995). Some of the beneficial applications of gas hydrates that have been tested include water desalination (Max, 2006), gas storage and transportation of methane (e.g. Sloan 2000; Gudmundsson et al., 2000; Chatti et al., 2005) and hydrogen (e.g. Mao et al., 2002), carbon dioxide sequestration (Lee et al., 2003), cold storage or air conditioning (Fournaison et al., 2004).

An analogous evolution in the number of publications and international conferences dedicated to gas hydrates has been observed in the past decades. The scientific interest in gas hydrate research comes from the recognition that methane hydrates might represent an important energy source for the future (e.g. Kvenvolden, 1988; Adam, 2002; Collett, 2002; Kennett et al., 2002) as well as an important carbon budget within the global carbon cycle (e.g. Dickens, 2003). In this regard, several studies have demonstrated that gas hydrates play an important role in past and present global warming periods since methane is one of the main atmospheric gases involved in the greenhouse effect (e.g. Dickens, 2001b). Another scientific topic that has been widely studied is the role of gas hydrate as a potential geohazard given that massive dissociation of gas hydrates could give rise to continental slope instability, i.e.

triggering sediment mass-movements and tsunamis (e.g. Bouriak et al., 2000; Haflidason et al., 2004).

Scientific interest in gas hydrates has been accompanied by a large number of science fiction books in recent decades. These eco-thrillers mainly focus on the capacity of gas hydrates to trigger several natural catastrophic phenomenona. The book *Mother of Storms* by John Barnes (1994) offers a fictional example of catastrophic climate change caused by a massive methane clathrate release. Another book is *The Life Lottery* by Ian Irvine (2004), in which unprecedented seismic activity triggers a release of methane hydrate, reversing global cooling. In the German bestseller *The Swarm (Der Schwarm;* by Schätzing, 2006) an undersea intelligent life known as *Yrr* heats methane hydrate deposits to cause tsunamis in the North Sea.

1.1. Gas hydrate crystallography

Gas hydrates can contain different types of gas molecules in separate cages (Figure 1.2). Methane hydrates are the most common hydrates occurring in nature, but other gases such as H_2S and CO_2 are also widely found in natural hydrate structures.

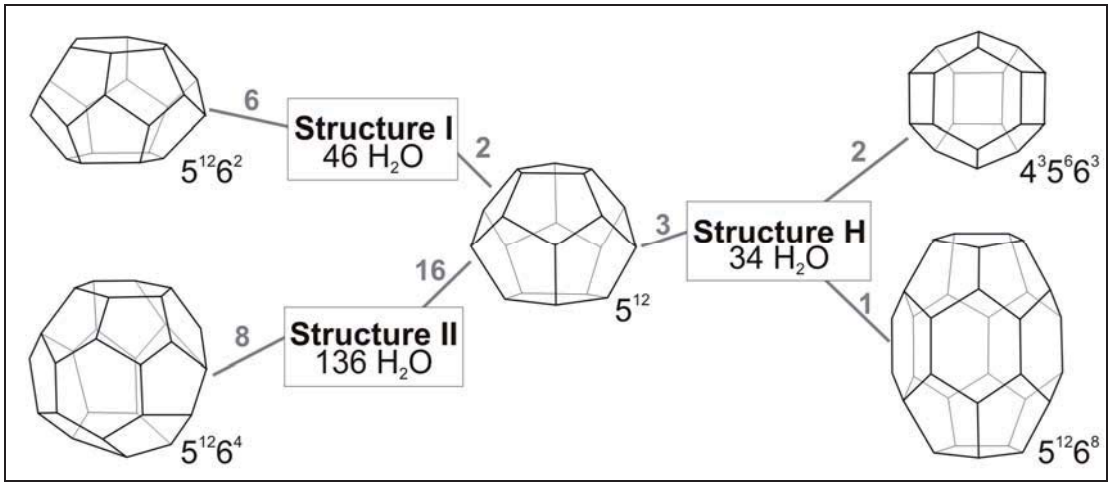

Figure 1.2. Types of clathrate hydrate structures and crystallographic structures of the cavities they form (e.g. 5^{12} is the cage formed by twelve pentagons). Numbers of H_2O molecules for each type are shown. The number of each cavity type is labelled in grey (modified from Schulz and Zabel, 2006).

Gas hydrates have been found naturally forming three different types of crystal structures (Sloan, 1998): Structures I, II and H (Figure 1.2). Cubic structure I consists of 46 water molecules forming two pentagonal-dodecahedron cages (5^{12}) and six tetradecahedron cages ($5^{12}6^2$) (Table 1.1). This is the most common structure and the typical gas molecules filling its cages are CH_4 and CO_2. Cubic structure II consists of 136 water molecules that form sixteen pentagonal-dodecahedrons (5^{12}) and eight hexadecahedrons ($5^{12}6^4$). Type II clathrates are

normally filled by O_2 or N_2 gases. Structural type H is hexagonal and the most infrequent in nature. It consists of 34 water molecules, forming three types of cages: three 5^{12}, two $4^3 5^6 6^3$ and one $5^{12}6^8$, which allow large hydrocarbon molecules to fit in (e.g. butane). Structural type H requires two guest-molecules to be stable.

	I		II		H		
Symmetry	Cubic		Cubic		Hexagonal		
Crystallographic group	$Pm\bar{3}n$		$Fd\bar{3}m$		P6 / mmm		
Cell constant (Å)	12.03		17.31		a= 12.26; c= 10.17		
Cavity	Small	Large	Small	Large	Small	Medium	Large
Description of cavity	5^{12}	$5^{12}6^2$	5^{12}	$5^{12}6^4$	5^{12}	$4^3 5^6 6^3$	$5^{12}6^8$
Number of cavities / cell unit	2	6	16	8	3	2	1
Cavity radius (Å)	3.8	4.33	3.91	4.73	3.9*	4.06*	5.71*
Coordination number	20	24	20	28	20	20	36
n H_2O / unit cell	46		136		34		

Table 1.1. Summary of the structural characteristics from the three crystal hydrate structures. * Estimates of structure H cavities from geometric models (from Sloan, 1998).

The occupied hydrate cage is a function of the size ratio of the guest molecule to the host cavity (Figure 1.3). Thus, because of clathrate configurations, molecules smaller than 3.5Å will not stabilize hydrates, and those over 7.5 Å are too large to fit in the most common cavities (hydrate structures I and II). For instance, if a propane molecule (C_3H_8) is found in the necessary pressure and temperature conditions hydrate structure II will form because this molecule is too large to fit in one cage of structure I.

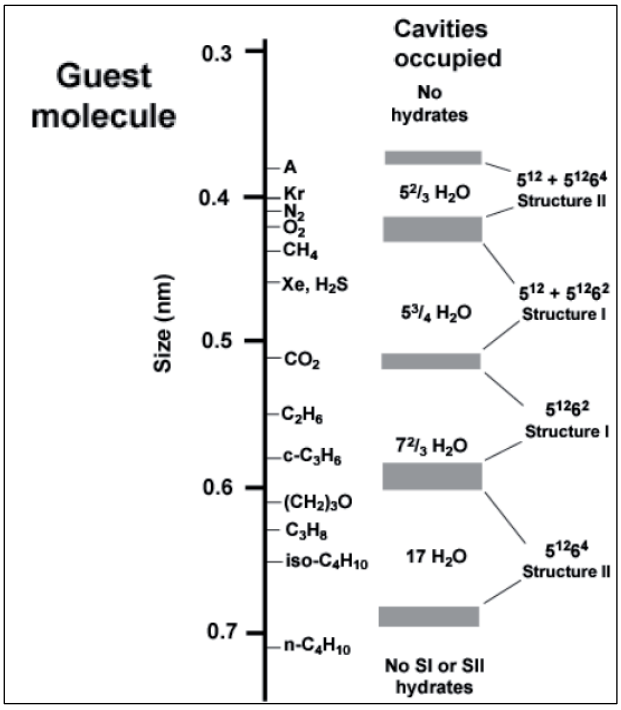

Figure 1.3. Guest molecules and hydrate cage size range of structures I and II (Sloan, 1998). Horizontal lines show the size of typical hydrate-forming guest molecules. The number of water molecules shown corresponds to single guest gas occupants listed on the left. The related types of structures formed are listed on the right.

As shown in Figure 1.3, structure I, the most frequent structure forming gas hydrates, contains small guest molecules, with a radius ranging from 4 to 5.5Å as CH_4, CO_2 or H_2S. The formation of these gases in marine sediments is normally related to biological activity and thus, gas hydrates of structure I are the ones usually found in seafloor sediments underlying areas of high productivity. Structure II generally occurs with guest molecules of 6-7Å radius, including gas mixtures. These gas hydrates are usually present in areas where gases are of thermogenic origin. Structure H, because of its big cages, may be formed in any environment, but only if a mixture of small and large molecular gases is found.

1.2. Gas hydrate stability field and origin

Gas hydrates are ice-like compounds, only stable at conditions of low temperature and high pressure. Besides pressure and temperature (P/T) conditions, gas hydrate formation is also controlled by the availability of water and gas molecules. The P/T conditions required for pure methane hydrate stability in marine sediments in a normal seawater salinity environment are illustrated (red line) in Figure 1.4

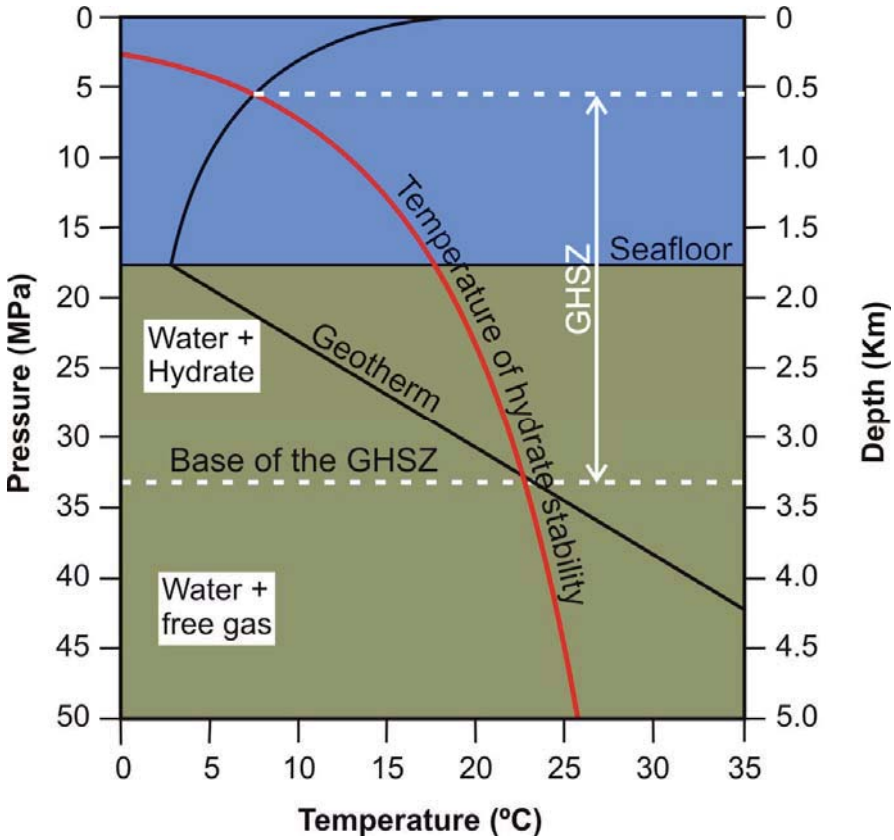

Figure 1.4. Stability diagram of gas hydrates in the deep sea (modified from Buffet and Archer, 2004). The stability temperature for clathrate increases with pressure/depth. The depth of the base of the gas hydrate stability zone (GHSZ) and its total extension is defined by the intersections of the geotherm and the temperature of gas hydrate stability.

The appropriate P/T conditions for gas hydrate formation are normally found in natural environments of permafrost areas and large lakes in high latitude continental areas and in continental margins with water depth exceeding 300 m in the oceans (Kvenvolden, 1988). Therefore, in marine sediments the main limiting factor for the existence of gas hydrates is the presence of a sufficient quantity of low molecular gases such as methane (Schulz and Zabel, 2006). In these environments, the intersections between the temperature curve of gas hydrate stability and the temperature profile within the sediments (geotherm) define the width of the gas hydrate stability zone (GHSZ) (Figure 1.4), which also depends on the bottom water temperature of the ocean (Bohrmann et al., 2003). In the entire interval of the GHSZ, gas hydrates will spontaneously form if enough gas is present. Given the hydrate lower density (0.913 g cm^{-3}; Sloan, 1998) with respect to seawater (1.030 to 1.050 g cm^{-3}), any gas hydrate formed in the water column will rise towards the sea surface, producing its dissociation once the P/T stability conditions are lost. However, gas hydrates formed within the GHSZ in the sediment pore space can be fixed and may remain stable over long periods of time.

The base of the GHSZ is a phase boundary between the gas hydrate and free gas fields (Henry et al., 1999). Gas hydrates would naturally dissociate when they exceed the limit of the temperature of stability of gas hydrates because of time and burial, which are mainly controlled in a specific geological setting by the sedimentation rate. The thickness of the GHSZ tends to be constant for a given water depth because the geotherm is relatively uniform over a broad region beneath the seafloor for a certain period of time (Schulz and Zabel, 2006). However, a variation in the water depth (i.e. change in sea level) would modify the pressure conditions on marine sediments, dramatically affecting the stability of gas hydrate deposits.

Another parameter that can avoid gas hydrate formation is water salinity, which affects the ionic strength of water (Schulz and Zabel, 2006; DingHui and WenYue, 2007). In a natural environment, the addition of ions to the water would shift the temperature curve of hydrate stability to the left (Figure 1.4) because they inhibit gas hydrate formation owing to the decreasing availability of water molecules. On the other hand, the presence of high-molecular hydrocarbons, such as CO_2, H_2S, etc., would shift the stability boundary to the right, thus increasing the P/T field where gas hydrates are stable.

Since most of continental margins present the suitable P/T conditions for gas hydrate formation, the presence of sufficient gas molecules seems to be the main limiting factor affecting gas hydrate distribution (Schulz and Zabel, 2006). Thus, gas hydrate forms only if the saturation limit for CH_4 in water is exceeded (Figure 1.5).

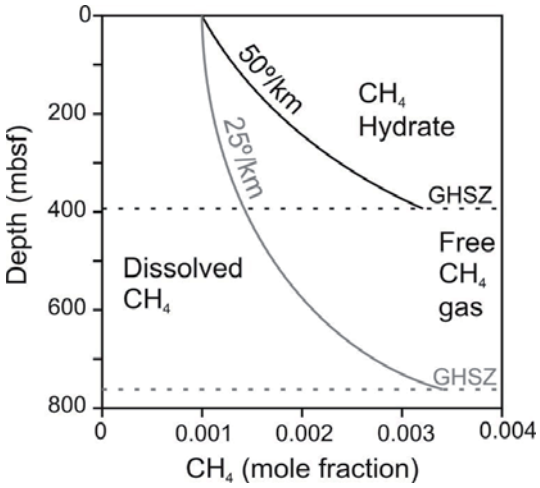

Figure 1.5. Theoretical solubility curves of methane gas as a function of depth in marine sediments based on thermodynamic functions and assuming two different geothermal gradients. The temperature affects the vertical gradient of methane solubility and the depth of the base of the GHSZ (discontinuous lines). Hydrostatic pressure for a water depth of 2000 m and a bottom water temperature of 2.5 ºC are assumed. mbsf = meter below sea floor (modified from Zatsepina and Buffett, 1997).

Methane, which is the most common hydrocarbon forming natural gas hydrates, may have a microbial origin, a thermogenic origin or a mixture of both (Figure 1.6) (Claypool and Kvenvolden, 1983). Microbial methane forms most of natural gas hydrates, and has a carbon-isotopic composition lighter than -60‰ (relative to the Peedee Belemnite – PDB – standard) (Kvenvolden and Lorenson, 2001). In this case, methane is formed by methanogenic organic processes that take place near the sediment surface, in which CO_2, from organic matter, is reduced to methane. Subsequently, the resulting methane may form hydrates in place, after migration over short distances or after recycling during the concomitant processes of hydrate formation and dissociation accompanying sedimentation (Paull et al., 1994).

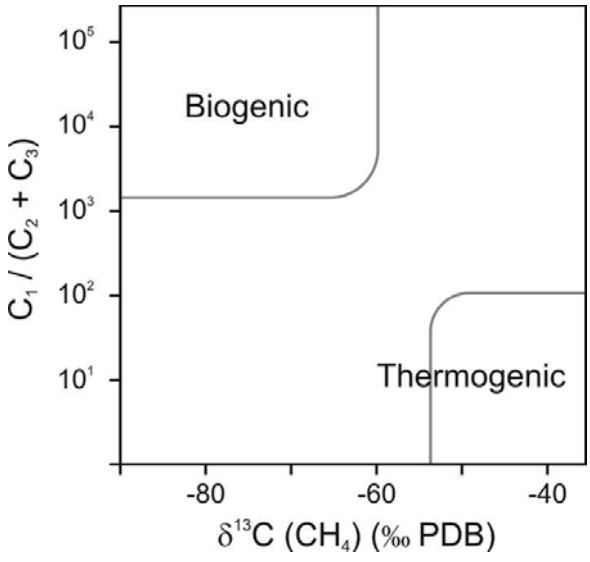

Figure 1.6. Origin of gas as a function of molecular gas composition and isotopic composition of methane. C_1= methane, C_2= ethane, C_3= propane, PDB= Peedee Belemnite (modified from Claypool and Kvenvolden, 1983).

On the other hand, methane with a carbon isotopic composition heavier than -60‰ has a thermal origin and is usually accompanied by significant amounts of other higher molecular weight gases, such as propane, ethane, etc. This mixture results from the decomposition of

organic matter at sediment depths greater than 1000 m and usually migrates long distances from deeply buried sediment and into the GHSZ, where it can form gas hydrates.

Thus, analyses of the isotopic composition of methane in combination with the molecular composition of gases can be used to infer the origin of the gas molecules forming gas hydrates. Recent studies in a number of marine sedimentary systems such as Blake Ridge (Dickens et al., 1997b), Hydrate Ridge (Suess et al., 2001), Nankai Trough (Takahasi et al., 2001), Congo-Angola basin (Charlou et al., 2004), and the Sea of Okhotsk (Ginsburg et al., 1993) show that most of the gas forming gas hydrate has a microbial origin. Furthermore, gas hydrates with a thermogenic origin have only been recovered at the Gulf of Mexico (Brooks et al., 1984) and the Caspian Sea (Ginsburg et al., 1992).

1.3. Evidence for gas hydrates

A number of geophysical techniques have been developed in the last decades in an attempt to deduce the presence of gas hydrates in the deep sea environment. Of the direct evidence available, outcropping of gas hydrates on the sea floor as well as explorations with ROVs (remotely operated vehicle) and driven submarines can be highlighted (Figure 1.7). The indirect evidence include the use of seismic data, electrical resistivity devices, chloride concentration of interstitial waters, infrared camera and sedimentary disturbance fabrics. In this chapter the use of seismic data will be briefly commented upon. Other indirect evidence will be discussed below (Chapter 3).

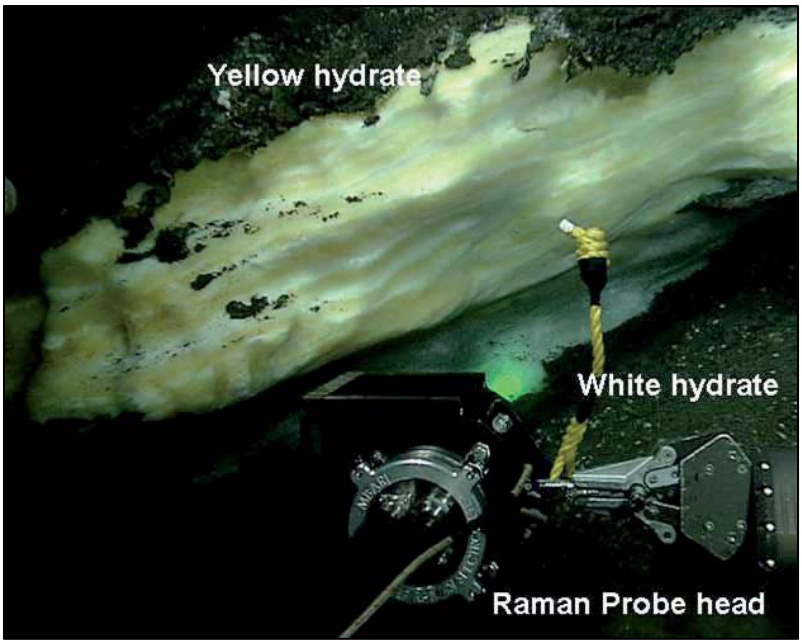

Figure 1.7. Yellow and white hydrates imaged at the Barkely Canyon, offshore Canada and sampled by a remotely operated vehicle (ROV) (modified from http://www.oar.noaa.gov/spotlite/2007/spot_gashydrates07.html).

1.3.1. Seismic evidence

During the 1970s, the presence of a prominent seismic reflector in several gas hydrate-rich environments was identified. Its position coincided with the thermodynamically defined depth of the base of the GHSZ. These new results deal with the extensive use of seismic data to detect new gas hydrate-rich deposits (e.g. White, 1977; Hyndmann and Spence, 1992; Shipley et al., 1979). This reflector can be easily recognized because it is parallel to the seafloor and has an inverse polarity, and is therefore referred to as "bottom simulating reflector" (BSR) (Figure 1.8).

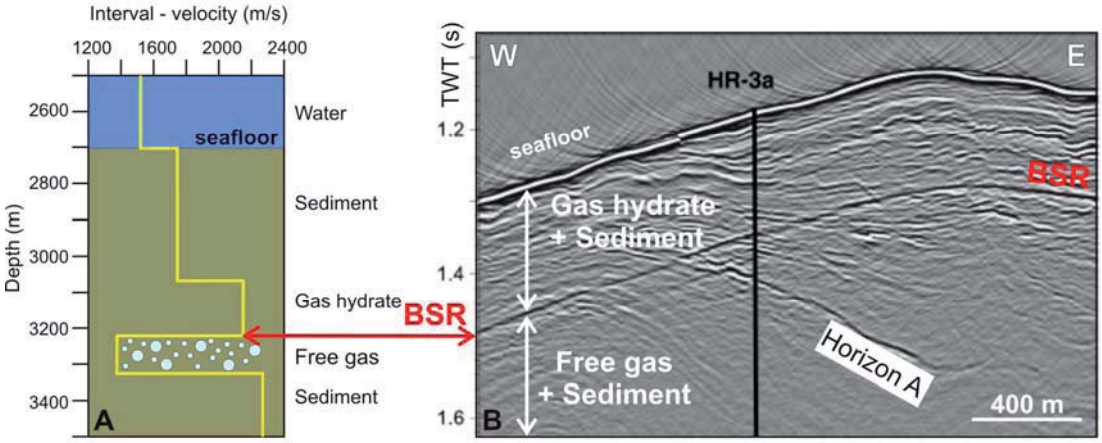

Figure 1.8. A. Seismic velocity model showing the strong contrast between gas hydrate-rich and gas-rich sediments in a continental margin (modified from Schulz and Zabel, 2006). **B.** Seismic record from Hydrate Ridge (Tréhu et al., 2002) showing the distinct reflection of the bottom simulating reflector (BSR) indicating the base of the gas hydrate stability zone (GHSZ). High amplitude reflections below the BSR are related to free gas filling pore spaces. Horizon A, a bright seismic reflector possibly acting as conduit for gas migration (Tréhu et al., 2004a) is also labelled. TWT = Two-way-traveltime.

The BSR usually crosses the stratigraphic horizons of the seismic profiles (Figure 1.8), because its position is controlled by the acoustic impedance between gas hydrate-rich sediments (above the BSR, in the GHSZ) and gassy sediments (below the BSR) rather than by the sedimentary architecture (e.g. Ewing and Hollister, 1972; Tucholke et al., 1977). Thus, the BSR is a reflector that mimics the seafloor topography and its depth as the GHSZ thickness depends on the P/T conditions that control gas hydrate stability.

However, a BSR is not always developed or observed in seismic profiles located in gas hydrate-rich environments. For instance, gas hydrates have been recovered at a number of localities without the presence of a BSR, as in the Gulf of Cadiz (e.g. Somoza, 2001; Pecher et al., 2001), providing evidence that other parameters such as gas hydrate distribution in the GHSZ, total gas hydrate quantity, gas hydrate fabric, gas distribution below the GHSZ, etc. control the formation of the BSR. At some localities, although a well developed BSR is

observed in the seismic records, only low quantities of gas hydrates are recovered during sediment coring (e.g. Holbrook, 2001; Kastner, 2001). Thus, BSR, as an indirect proxy of gas hydrate presence can be only used as valid evidence in studies that include other indirect and direct proxies.

1.4. Gas hydrate distribution

Gas hydrates are naturally found in high latitude continental areas from Russia (permafrost and large lake margins) as well as in active and passive margins in oceanic areas (Figure 1.9). In sub-aquatic sediments, including marine and large lakes in high latitudes, gas hydrates are found at water depths exceeding 300 m and bottom water temperatures near 0º C in the Atlantic, Pacific, Indian and Antarctic oceans (e.g. Lorenson and Kvenvolden, 2007). In these environments, gas hydrates can reach depths of up to 1100 m in the sediment column, depending on the geotherm gradient of the area. Thus, natural gas hydrates are substances naturally restricted to the shallow geosphere.

In recent decades, gas hydrates have been recovered in more than 40 regions, and their presence has been deduced in more than 100 geological settings from geophysical, geochemical and geological evidence (e.g. BSR detection, well logging, etc.) (Mazurenko and Soloviev, 2003) (Figure 1.9). A number of gas hydrate-rich localities have been studied on the Pacific and Atlantic margins. Nevertheless, exploration continues in other terrestrial areas such as the western African margin and the Antarctic margins (e.g. Ben-Avraham et al., 2002; Tinivella et al., 2002, respectively). The potential amount of gas hydrate in the Earth has been estimated at 10^4 gigatonnes of methane carbon (Lorenson and Kvenvolden, 2007).

Detailed studies on gas hydrate-rich areas in the Atlantic (Blake Ridge) and the Pacific (Hydrate Ridge) margin of North America have estimated the quantity of gas hydrate that fills the sediment pore space (e.g. Paull et al., 1996b; Tréhu et al., 2004b, respectively). Based on the combination of several proxies, an average between 1% and 2% of pore space in the GHSZ has been suggested as being filled with gas hydrates. Nevertheless, gas hydrate distribution within the GHSZ is not homogeneous, and gas hydrate-rich intervals seem to be restricted to a number of zones that are structurally and stratigraphically controlled (Tréhu et al., 2004a). In these zones gas hydrates are present as layers, compact nodules or disseminated patches, filling fractures, etc.

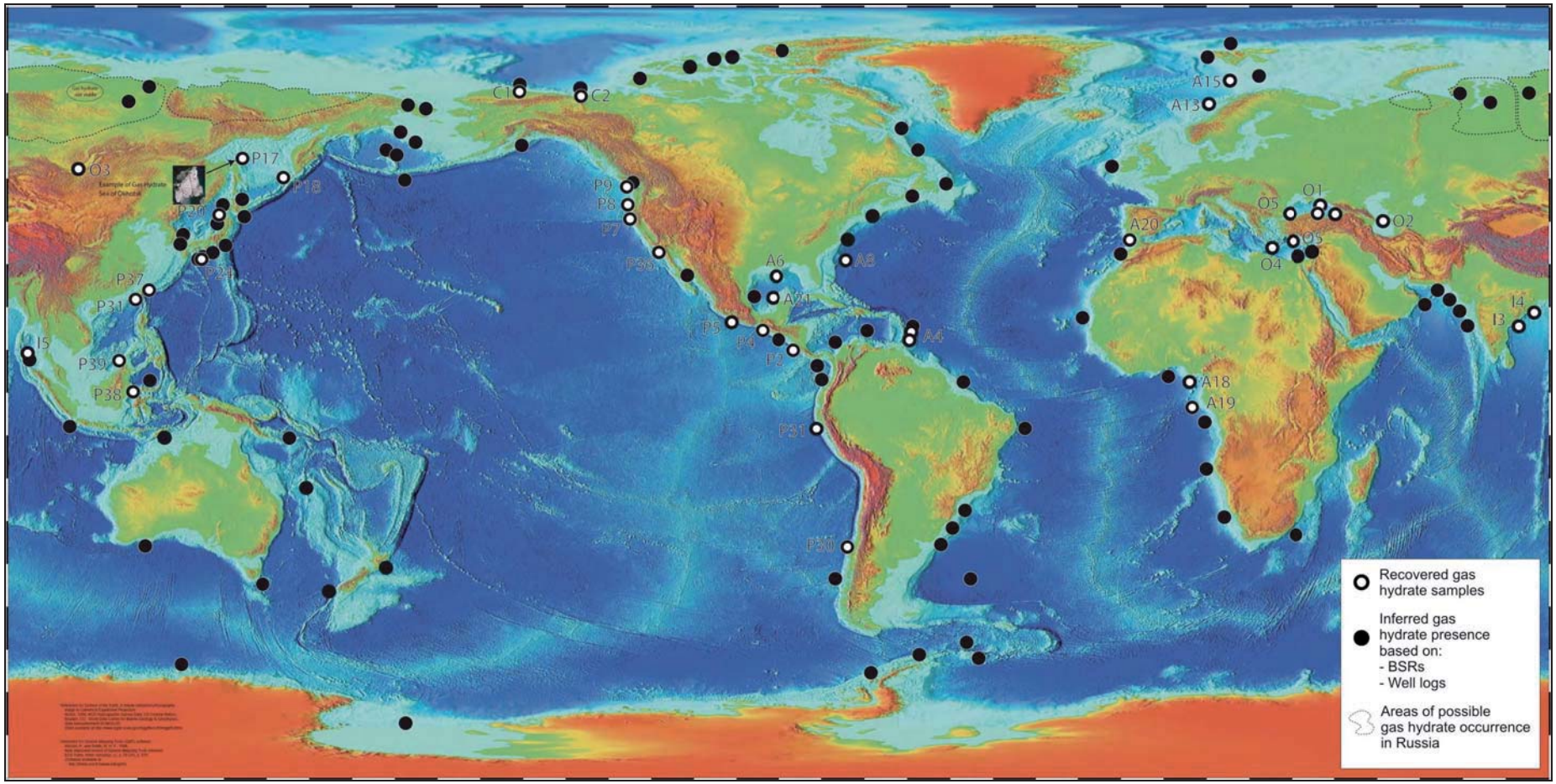

Figure 1.9. Topographic and bathymetric map showing natural gas hydrate deposits in the world deduced from recovered gas hydrates samples and inferred gas hydrates occurrences based on seismic evidence (bottom simulating reflector - BSR presence) and well logs. Areas of possible gas hydrate occurrence in permafrost regions in Russia are also indicated (modified from Lorenson and Kvenvolden, 2007). A= Atlantic ocean; P= Pacific ocean; I= Indian ocean; O= other locations (such as Mediterranean Sea, Black Sea, etc.).

1.5. Global estimates of gas hydrate

The size of the total gas hydrate reservoir is poorly known, especially the oceanic budget conserved in continental margin sediments. A number of estimates have been proposed during the last decades (e.g. Milkov et al., 2004), and the size of the submarine reservoir of gas hydrates seems to decrease in every new study (Table 1.2). The highest estimates (i.e. $3x10^{18}$ m^3) for gas hydrate reserves were based on the first assumption that fully dense clathrates filled the entire floor of the deep ocean (Dobrynin et al., 1981). Since then improvements in gas hydrate knowledge from direct measurements and more precise estimations based on geochemical and geophysical proxies have revealed that gas hydrates are restricted to a narrow range of depths controlled by the P/T conditions, and mainly form low concentrations (e.g. Kerr, 2004). Recent estimates calculated on the basis of direct sampling on natural environments suggest that the global inventory of gas hydrates ranges from 1 to 5 x 10^{15} m^3 (Milkov, 2004). This estimate represents an amount of 500-2,500 gigatonnes of Carbon (Gt of C). For comparison, the total amount of carbon stored in the atmosphere has been estimated at 700 Gt. These recent amounts are significantly smaller than the 10,000 to 15,000 Gt of C suggested in earlier studies (e.g. Kvenvolden, 1998) (Table 1.2).

Methane gas ($x10^{15}$ m^3)	**Reference**
5-25	Trofimuk et al., 1977
7,600	Dobrynin et al., 1981
3.1	McIver, 1981
40	Kvenvolden and Claypool, 1988
10	Makogon, 1981
21	Kvenvolden, 1988
21	MacDonal, 1990
26-140	Gornitz and Fung, 1994
23-91	Harvey and Huang, 1995
1	Ginsburg and Soloviev, 1995
7	Holbrook et al., 1996
15	Makogon, 1997
2-20	Dickens et al., 1997b
1-5	Milkov et al., 2004

Table 1.2. Global estimates of total volume of methane gas from gas hydrates in submarine environments (modified from Kvenvolden and Lorendson, 2001; Milkov et al., 2004).

The limited volume and concentrations recently proposed reduce the potential of using gas hydrates as hydrocarbon reservoir suitable for exploitation. Only the most gas hydrate-enriched

environments are economically viable as energy resources. In these environments, gas hydrate could serve as a possible source of methane, while migrated methane from deep below the GHSZ would be another potential source. However, the capacity of gas hydrate to act as a seal, has not been well established, and in various settings, gas transportation through the GHSZ has been reported (e.g. Tréhu et al. 2006).

1.6. Why is gas hydrate research important?

Apart from the obvious economic interest in gas hydrate exploration (methane is the major gas-hydrocarbon resource), the possibility of CO_2 sequestration in gas hydrate-rich areas has been recently studied and is currently in a testing phase at a number of onland localities (Wallmann, 2007). Other questions that will be discussed in this chapter include the actual behaviour of methane hydrate as part of the carbon cycle and its importance for deep sea biological activity and global warming. Recent studies on the role of gas hydrate in past climatic changes and in triggering large mass-movements will be also presented.

1.6.1. Gas hydrates as energy resource and CO_2 sequestration

The need for energy has generated a strong international expectation in the exploration for natural gas hydrates. Specific national hydrate programs have been developed recently in Canada, China, India, Japan, Taiwan and the United States. Technological progress and global economy will determine the future production of gas from submarine gas hydrate deposits (e.g. Bohannon, 2008; Hester and Brewer, 2009). The 2002 Mallik program, an international consortium of countries and energy companies, confirmed the technical feasibility of gas production from gas hydrate deposits in permafrost areas (Dallimore and Collett, 2005). The recent Indian Natural Gas Hydrate Project (NGHP) Expedition 01 discovered one of the world's richest gas hydrate deposits (Collett and Scientific Party, 2007). Production testing on deep sea deposits is planned for 2009 by the Indian NGHP, and the Japanese National Program set 2017 for commercial production of the gas hydrate deposits in the Nankai Trough (Sloan and Koh, 2007).

The future of gas hydrate exploitation as an energy resource depends on a number of factors including the geological studies to identify concentration sites and settings where methane can be effectively extracted from gas hydrate and the engineering studies to determine the most efficient means of dissociating gas hydrates *in situ* and extracting gas safely. In this regard, geo-mechanical studies are needed to assess the reaction of hydrate-bearing sediments to external disturbances such as overload due to pipelines and other production devices, shaking attributed to earthquakes, loss of sediment cohesion due to gas hydrate dissociation and porosity

inoccupation, etc. Furthermore, scientific and technological knowledge with respect to seismology, geochemistry, electromagnetics, heat flow, micro- and macrobiology, and drilling technology in marine sediments must also be addressed. In addition, economic analyses for the extraction of gas from conventional reservoirs and geopolitical issues related to energy security are other points that need to be taken into account. Thus, the successful use of gas hydrates as an energy resource mainly depends on government and industry investments in research and development (Hester and Brewer, 2009).

Another idea considered recently is the replacement of methane from natural gas hydrates deposits by carbon dioxide (CO_2) (Figure 1.10). With this new technique, the recovery of gas would be combined with CO_2 sequestration. This approach is advantageous in that CO_2 is trapped and not liberated to the atmosphere, but also in that hydrates are left in place, theoretically reducing the risk of slope instability. Although the exchange is thermodynamically favourable, its extension is limited by the transport of fluid CO_2 into the sub-seafloor sediment, producing some reduction in the CH_4 recovery, about 36 % for gas CO_2 and 60% for liquid CO_2 (Lee et al., 2003). Marine CO_2 sequestration is currently at an experimental stage, implying further research on transport limitations and exchange time rates (e.g. Graue et al., 2006, Zhou et al., 2008), CO_2 solubility (e.g. Aya et al., 1997; Uchida et al., 1997; Yang et al., 2000), CO_2-hydrate formation kinetics, CO_2-hydrate stability (e.g. Circone et al., 2003) and numerical modelling for spatial characterisation of gas hydrate deposits (Wallmann, 2007).

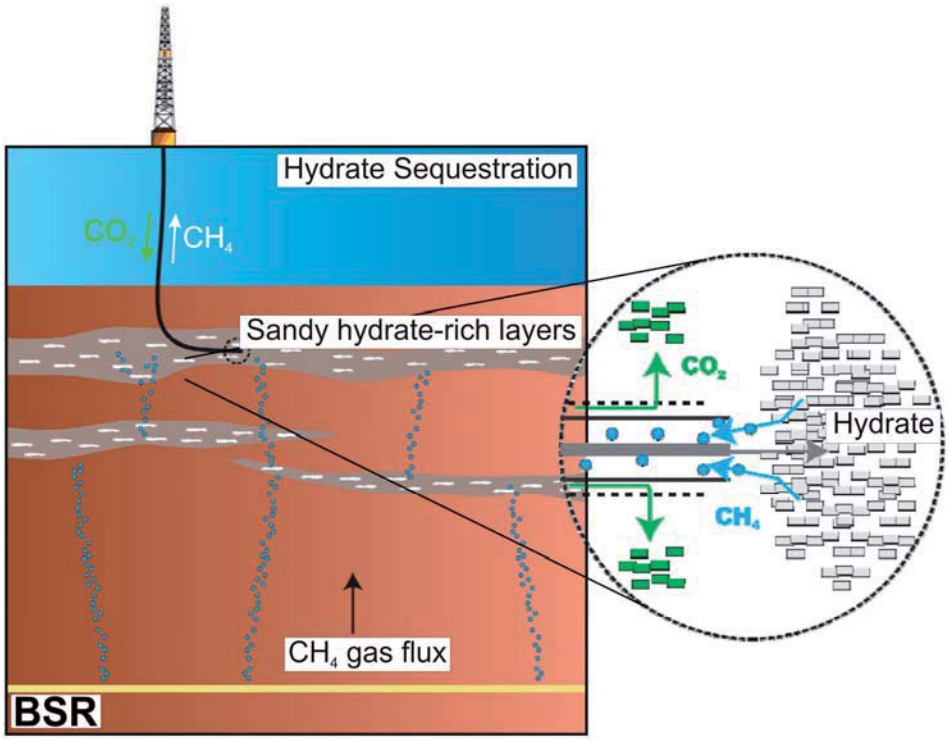

Figure 1.10. Scheme of CO_2 sequestration in the sandy layers of a hydrate-rich geological setting. Methane is produced, while CO_2 is stored. The bottom simulating reflector (BSR) and the methane flux are also indicated (modified from Wallmann, 2007).

1.6.2. The role of gas hydrates in the carbon cycle

Methane contained in gas hydrates forms part of the global carbon budget (Figure 1.11). The carbon cycle of the Earth corresponds to the biogeochemical cycle by which carbon is exchanged among the biosphere, pedosphere, geosphere, hydrosphere, and atmosphere (Dickens, 2001b). The cycle is usually represented as four major reservoirs of carbon interconnected by several exchange pathways. These reservoirs are: a) the atmosphere; b) the terrestrial biosphere, which usually includes fresh water systems and non-living organic material, such as soil carbon; c) the oceans, including dissolved inorganic carbon and living and non-living marine biota; and d) sediments including fossil fuels. The oceans contain the largest active pool of carbon near the surface of the Earth, although the deep ocean has a much slower exchange rate with the atmosphere. The movements of carbon between these reservoirs (exchanges) occur through various chemical, physical, geological, and biological processes. The global carbon budget corresponds to the balance of carbon exchanges (incomes and outputs) between the carbon reservoirs or within one specific loop of the carbon cycle (Figure 1.12).

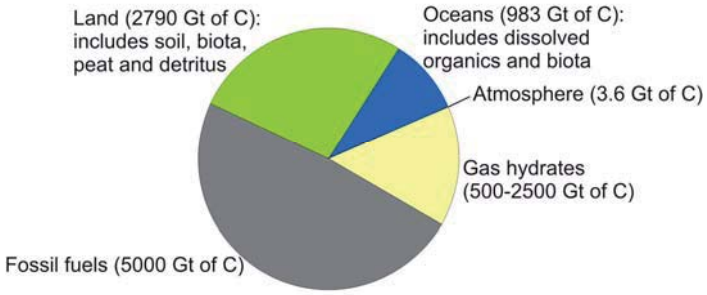

Figure 1.11. Distribution of organic carbon in Earth reservoirs (excluding dispersed carbon in rocks and sediments, such as kerogen and bitumen, which equals nearly 1000 times this total amount). Gt of C = gigatonne (10^{15} tons) of carbon (modified from Kvenvolden, 1993).

The exogenic carbon cycle includes all carbon in the ocean, atmosphere and biomass (Figure 1.12). Carbon is added to and removed from the exogenic carbon cycle through several external inputs, such as rivers, weathering and volcanoes, and outputs, such as carbonate precipitation and organic matter formation (Dickens, 2003). Variations in these external fluxes can thus change the mass and isotopic composition of the exogenic carbon fields through time (e.g. Sundquist, 1986; Sundquist and Broecker, 1985; Schmidt and Shindell, 2003; Berner et al., 1983). Recently published studies (e.g. Dickens 2001b; 2003) have suggested a new conceptual model for the global carbon cycle including a gas hydrate capacitor (Figure 1.12). Carbon forming gas hydrates is progressively stored in a capacitor until a triggering mechanism for its release appears (e.g. temperature rise in deep waters, sea-level change). Subsequently, this carbon budget is injected into the system. In this approach, the gas hydrate budget affects the global isotopic composition of the exogenic carbon cycle due to its massive release or confinement and as a function of the global P/T conditions at the sub-seafloor sediments.

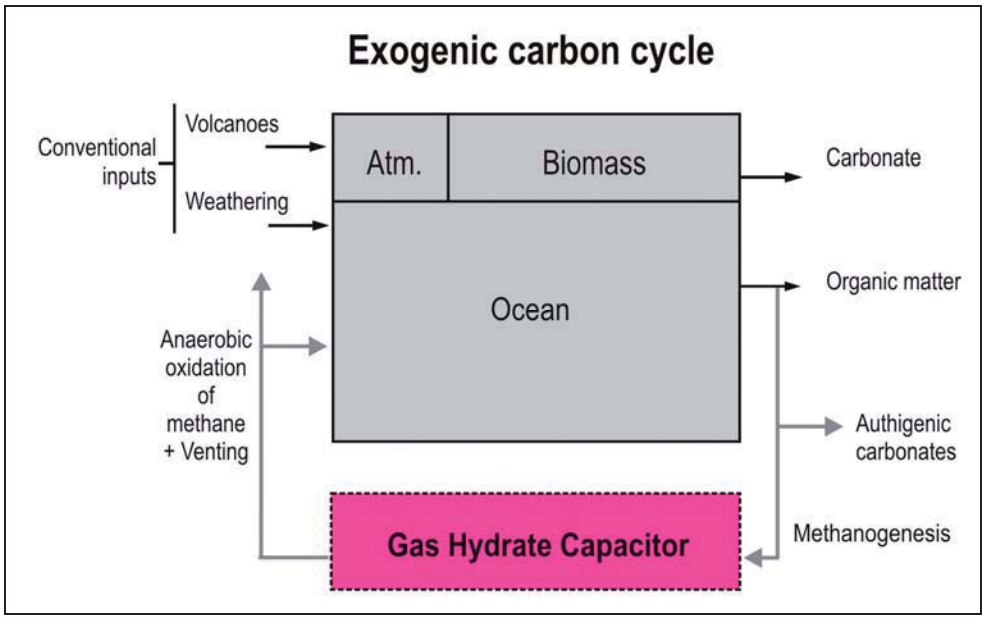

Figure 1.12. Exogenic carbon cycle at steady state conditions. Carbon enters through volcanism and weathering and exits as carbonate precipitation and organic matter formation. Some processes affecting methane availability to form gas hydrates are methanogenesis, anaerobic oxidation, methane venting and authigenic carbonate precipitation. Atm. = atmosphere (modified from Dickens, 2003).

1.6.3. Biological activity

As stated above, gas hydrates have been identified and sampled from the seafloor at several locations (e.g. Tréhu et al., 2003). Although methane at high water depth would be dissolved, these detections prove that gas hydrates can exist in direct contact with seawater. The only way of gas hydrate preservation on the seafloor is with a constant high flux of methane-saturated waters (Egorov et al., 1999). Therefore, methane-rich fluxes in gas hydrate-rich environments could reach the seafloor in two ways: gas hydrate dissociation and natural upward migration of gas. These processes produce a continuous supply of energy and carbon for the benthic environment in the form of methane molecules. The development of several biological communities in gas hydrate-rich and gassy environments has been described (Sahling et al., 2002). Recent studies have demonstrated that the colonization of seeps basically depends on the local H_2S gradient generated by anaerobic oxidation of methane (AOM) (e.g. Barry and Kochevar 1998, Sahling et al., 2002). AOM is mediated by a microbial consortium of methanotrophic archaea and sulphate reducing bacteria first identified in gas hydrate-bearing samples from Hydrate Ridge (Boetius et al., 2000). In the biological consortium, the archaea oxidize methane [1] while bacteria reduce sulphate through 2 different pathways [2 and 3] that are still under discussion.

[1] $$CH_4 + 2H_2O \rightarrow CO_2 + 4H_2$$

[2] $SO_4^{2-} + 4H_2 + H^+ \rightarrow HS^- + 4H_2O$

[3] $SO_4^{2-} + CH_3COOH + 2H^+ \rightarrow 2CO_2 + H_2S + 4H_2O$

The net reaction can be summarized as follows [4]:

[4] $CH_4 + SO_4^{2-} \rightarrow HCO_3^- + HS^- + H_2O$

The metabolic couple involved in AOM produces sulphide (HS^-) and dissolved inorganic bicarbonate (HCO_3^-) from methane (CH_4) and sulphate (SO_4^{2-}) (Masuzawa et al. 1992, Wallmann et al. 1997; Borowski et al., 2000). Gas hydrates and gas-rich fluids provide the methane while seawater is the natural supply of sulphate. The hydrogen sulphide produced by AOM constitutes the energy source for the chemoautotrophic organisms living on the seafloor, near gas hydrates or cold seeps (Fisher, 1990, Nelson and Jannasch, 1983; Bohrmann et al., 2002) (Figure 1.13). A number of studies suggest that in a specific gas hydrate setting, the local H_2S gradient generated by AOM controls the biological community that is developed on every area as a function of the intensity and concentration of the flux (e.g. Parkes et al., 2000; Sahling et al., 2002). Thus, the sulphide-oxidizing bacterium *Beggiatoa* is usually found forming mats in areas of very high sulphide flux; while *Calyptogena* clams typically colonize areas with lower sulphide concentrations and surround the *Beggiatoa* mats. *Acharax* clams live in burrows within the sediment, restricted to environments of very low sulphide concentration (e.g. Sahling et al., 2002) (Figure 1.14).

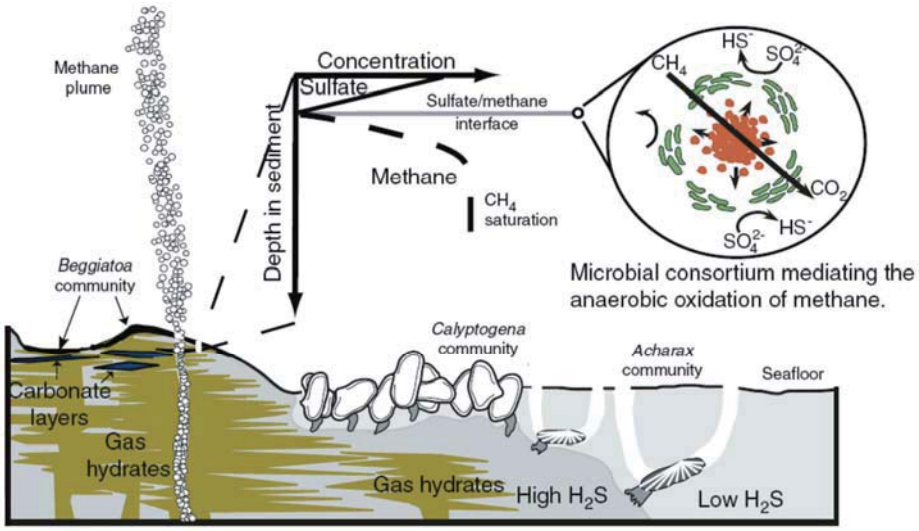

Figure 1.13. Schematic illustration of gas hydrate deposits and biogeochemical communities in near-surface sediments at southern Hydrate Ridge. Anaerobic oxidation of methane (AOM) is mediated by a microbial consortium producing hydrogen sulphide fluxes and gradients, which control the distribution of vent communities around gas seeps and gas hydrates exposures on seafloor as well as near surface carbonate precipitation (Sahling et al., 2002).

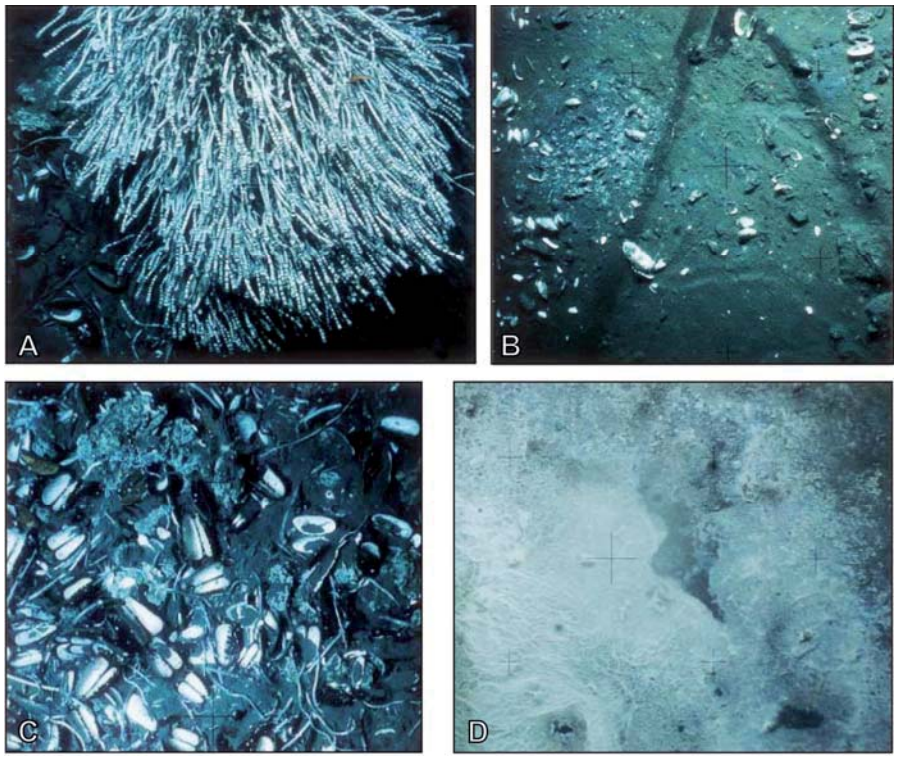

Figure 1.14. Seafloor images from active vent sites off Costa Rica indicated by the abundance and prolific colonies of chemosynthetic organisms. **A.** *Pogonophora* colony; **B.** Scattered bivalves, bacterial mat, and carbonate fragments; **C.** Bivalve cluster: vesicomyid clams (white shells), solemyid bivalves (black periostracum) and mytilid mussels (brown shells; left foreground); **D.** Large bacterial mat (thick individual strands recognizable) surrounding vent orifice (modified from Bohrmann et al., 2002).

In addition to sulphide production, AOM increases carbonate alkalinity in bottom seawater, which drives pervasive carbonate precipitation (e.g. Teichert et al., 2005a). The high concentrations of bicarbonate as a respiration product, the presence of microbial surfaces and the exudation of organic polymers that can bind calcium ions are all factors that stimulate authigenic carbonate precipitation in gas hydrate-rich environments (Iversen and Jørgensen, 1985; Teichert el at., 2005a) (Figure 1.15).

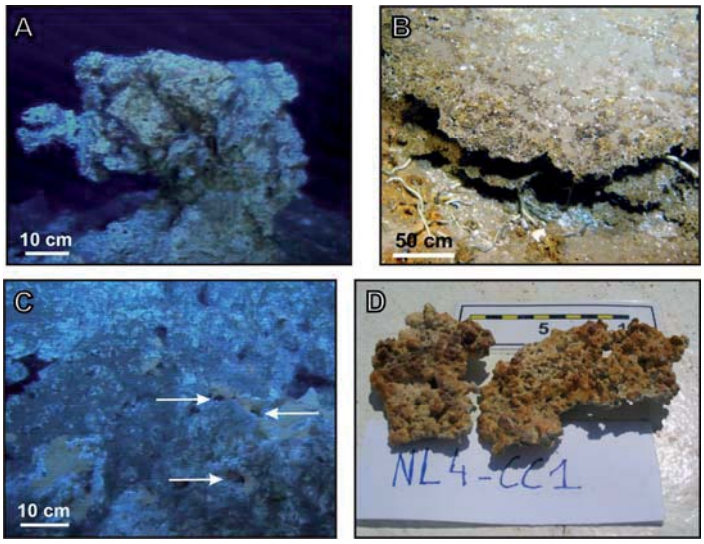

Figure 1.15. Seafloor photographs and detailed image of authigenic carbonates from Hydrate Ridge in the Cascadia margin (A and C) and the Nile deep sea fan (B and D). **A.** Carbonates with high porosity; **B.** Slabs of carbonate crust associated with tubeworms and bivalve shells; **C.** Opening of fluid channels (arrows) surrounded by bacterial mats (*beggiatoa*); **D.** Small porous slabs of carbonate crust (modified from Teichert et al., 2005a and Gontharet et al., 2007).

1.6.4. Global warming

Methane is an important component of the atmosphere, with about 4.9 x 10^5 g of methane carbon, which implies a concentration of 0.0001745% (Figure 1.16). Methane is a relatively important greenhouse gas with an estimated global warming potential in relation to CO_2 of 72 averaged over 20 years or 25 averaged over 100 years (Forster et al., 2007). This means that a methane emission will have 72 times the impact on temperature of a carbon dioxide emission of the same mass over the following 20 years and 25 times over the following 100 years. These rates show that methane has a large effect for a brief period (about 10 years), whereas carbon dioxide has a small effect for a long period (over 100 years). The Earth's methane concentration in the atmosphere has increased by about 150% since 1750, and it accounts for 20% of the total radiative forcing from all of the long-lived and globally mixed greenhouse gases (Forster et al., 2007).

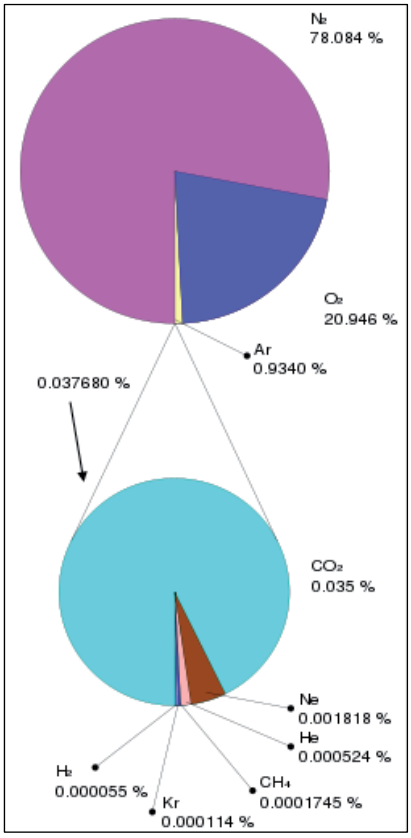

Figure 1.16. Composition of the Earth's atmosphere in December 1987. The lower pie represents the least common gases that compose 0.038% of the total atmosphere. Values are normalized on % volume (http://www.globalwarmingart.com/wiki/Wikipedia:Methane - _note-Technical_summary).

Because methane is radiatively a highly active gas, it is also considered a "greenhouse" gas. The Earth's atmosphere has a wide variety of sources and sinks of methane, in which gas hydrates, represent approximately 5% (Figure 1.17). As the permanence of methane trapped as gas hydrates on the seafloor or in permafrost areas is a function of pressure and temperature, a change in the environment conditions could lead to a large release of methane into the atmosphere. As a result of the presence of gas hydrates in deep ocean margins, some studies suggest that the actual release of methane to the atmosphere in response to the anthropogenic climatic warming could take place over time scales of millennia (Hester and Brewer, 2009). Nevertheless, this continuous methane release could have a chronic but significant impact on atmospheric composition, already detected in analyses from ice core records (Etiope et al., 2008).

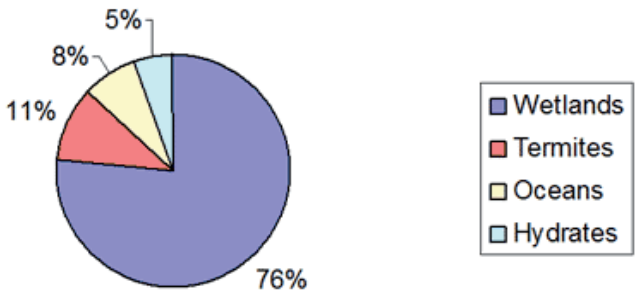

Figure 1.17. Natural sources of atmospheric methane, including gas hydrates (5%) (IPCC, 2001).

1.6.5. Past climatic changes: the Palaeocene-Eocene Thermal Maximum

About 55 million years ago, coinciding approximately with the Palaeocene-Eocene boundary, the $\delta^{13}C$ signature of carbon in the Atlantic and Pacific oceans and onland decreased abruptly by 2.5 to -5‰ on a time scale less than 10 kyr (e.g. Dickens, 2001b; 2003; Archer, 2007; Kennet and Stott, 1991; Roehl et al., 2000; Farley and Eltgroth, 2003). At the same time, the $\delta^{18}O$ of $CaCO_3$ from intermediate depths in the ocean analyzed in marine sedimentary records decreased by 2-3‰, suggesting a temperature warming of about 5º C. These trends were detected in marine records from different areas, highlighting the relative worldwide synchronicity of this event (Figure 1.18).

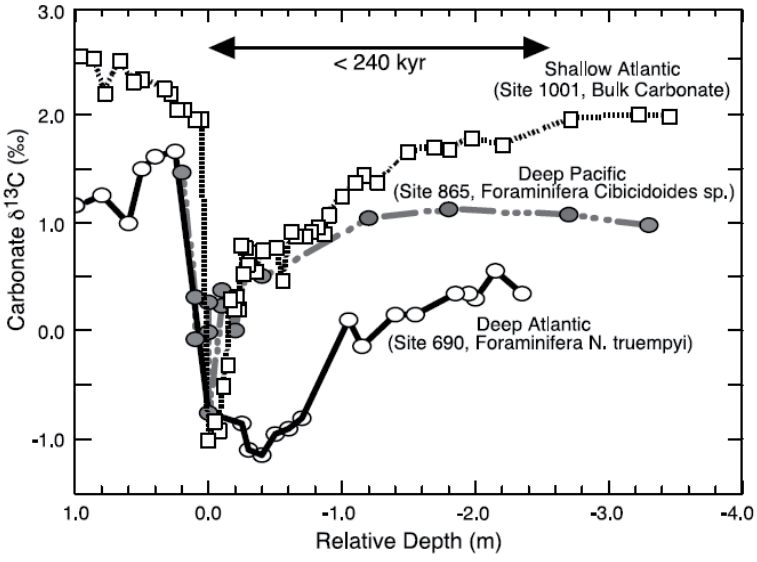

Figure 1.18. Carbon isotope records across the Paleocene-Eocene Thermal Maximum in different phases at three marine locations. Original records have been placed on a common depth scale with the $\delta^{13}C$ minimum at 0.0 m (Dickens, 2003). Note that the sedimentation rates vary between sites, giving different shapes to the excursion.

This climatic event has been called the Palaeocene-Eocene thermal maximum (PETM). Its coincidence with a prominent benthic foraminifer's extinction and an extraordinary terrestrial mammal diversification suggests that a mechanism for extreme environmental and global change altered the global carbon cycle during that time. In marine records, planktonic

foraminifera and terrestrial carbon records show a $\delta^{13}C$ perturbation slightly earlier than the benthic, suggesting that the deep ocean was invaded by a carbon amount from the atmosphere (Thomas et al., 2002). Other similar events have been reported during the Jurassic and the Mesozoic - Palaeogene transition (e.g. Hesselbo, 2000; Jenkyns, 2003).

Downhole logging data from the Caribbean Sea (ODP Leg 165) indicate an abrupt and distinct signature in the physical and chemical properties extending for tens of meters above and below the PETM (Röhl and Abrams, 2000). These observations indicate a rapid environmental change at the PETM, which persisted beyond the PETM anomaly. These continuous-depth series reveal that the PETM was a multiphase event with a nearly instantaneous onset followed by very different physical and chemical conditions of short duration succeeded by a longer transition to new, more permanent environmental circumstances. The estimated duration of these "phases" on the PETM are consistent with palaeontological studies of macro and micro fauna abundance (e.g. Tremolada and Bralower, 2004).

During the PETM, the rise in sea level produced by the glaciers and ice caps melting, would have raised the subsurface hydrostatic pressure, increasing the GHSZ thickness and, thus, stabilizing gas hydrates. On the other hand, the warming of bottom water would have converted massive amounts of marine gas hydrates into free methane gas, which was then added to the ocean. In contrast to the rise in sea-level, a regional uplift of hundreds of meters in the north Atlantic region has also been reported for this period (MacLennan and Jones 2006). This regional uplift favoured the gas hydrate dissociation by decreasing the GHSZ thickness and sustaining the sea-water temperature effect. After the methane dissolution in seawater, the release of carbon to the atmosphere enhanced warming through the greenhouse effect, acting as a feedback process.

1.6.6. Slope instability and triggering mechanism of mass movements

Marine gas hydrates cement sediment particles significantly modifying the sediment strength. Thus, its formation and eventual dissociation due to changes in P/T conditions (e.g. owing to a sea-level drop or an increase of seafloor temperature) may influence the occurrence and extent of submarine landslides (Figure 1.19) (e.g. Haq, 1998; Xu, 2004; Henriet and Mienert, 1998). The mechanism of destabilization is produced in two ways: first, a weakening of the sediment and a rise in pore pressure is produced owing to the increment in water content coming from gas hydrates; second, the gas released from gas hydrates alters significantly the behaviour and mechanical properties of the marine soils (e.g. Wheeler, 1988a, 1988b; Sultan et al., 2004b). In addition to the excess pore pressure and gas release resulting from hydrate melting, the presence of gas hydrate, which cements the grains filling the voids, may prevent the

normal sediment compaction processes in the GHSZ. In this case, gas hydrate dissociation may generate an under-consolidated soil with low resistance, i.e. a drop in sea level may reduce the pressure at the seafloor and cause the melting of methane hydrate. The sudden release of gas would trigger landslides and slumps, and also a gas plume rising to the ocean surface (Figure 1.19). In this particular case, in which gas hydrate dissociation is produced by a sea-level change, Paull et al. (1996a) demonstrated that turbidites and tsunamis in the sedimentary record are increased during low-stand periods, especially in gas hydrate-rich settings. The development of numerical and conceptual models of the U.S. Atlantic margin (e.g. Carpenter, 1981) and the European Atlantic margin (e.g. Sultan et al., 2004b) has reinforced the idea of gas hydrate dissociation as an important triggering mechanism of submarine mass movements, highlighting the relevance of gas hydrates in geological processes (McIver, 1977; Nisbet and Piper, 1998).

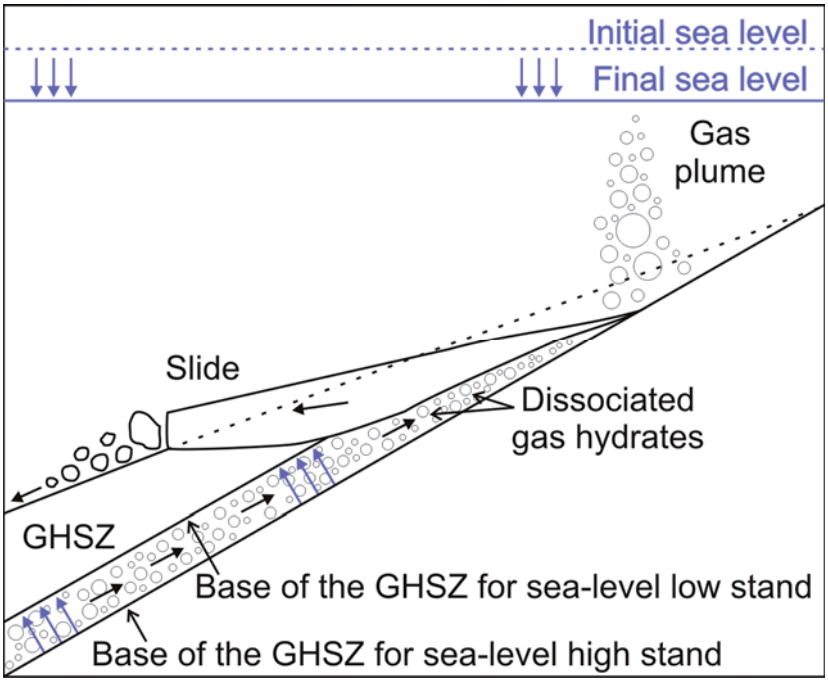

Figure 1.19. Theoretical cross section showing gas hydrate dissociation and related landslide and sudden gas release due to a drop in sea level. The change in sea level reduces the pressure on the seafloor and causes the melting of methane hydrate. The sudden release of gas can result in landslides and slumps. It can also result in a plume of gas rapidly rising to the ocean surface. GHSZ = Gas Hydrate Stability Zone (modified from Katz et al., 1999).

One of the largest exposed submarine landslides in the ocean is the Storegga Slide in the Norwegian continental margin. The slide excavated the top 250 m of sediment over a swath hundreds of kilometres wide affecting an area of c. 95,000 km^2 and a sediment volume of minimum 2,400 km^3 and maximum 3,200 km^3, stretching half-way from Norway to Greenland, which implies a runout distance of 810 km (Haflidason et al., 2004) (Figure 1.20).

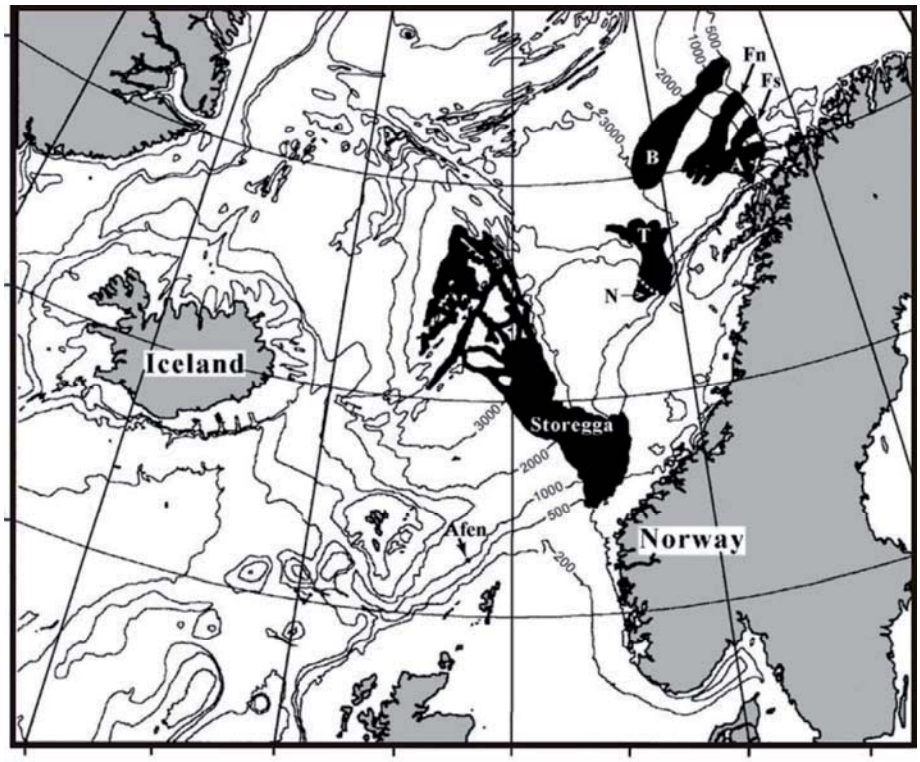

Figure 1.20. Bathymetrical map of the Norwegian–Greenland Sea with outline (in black) of large exposed submarine slides. The slides are either labelled as Storegga and Afen or with a letter such as N (Nyk), T (Trænadjupet), A (Andøya), Fs (Fugløy Bank south), Fn (Fugløy Bank north), B (Bjørnøyrenna) and M (Malenebukta) (Haflidason et al., 2004).

There have been comparable slides in the Norwegian margin approximately every 100 kyr, roughly synchronous with the glacial cycles (e.g. Canals et al., 2004; Solheim et al., 2005). The last slide, Storegga, occurred about 8150 years ago after deglaciation. It generated a tsunami that reached the British Isles and tsunami deposits have been identified also in North-East Scotland (Dawson and Smith, 2000; Dawson and Stewart, 2007; Driscoll et al., 2000; Smith et al., 2004; Dawson et al., 1988). The Storegga slide area contains methane hydrate deposits as indicated by a prominent BSR (Bunz and Mienert, 2004; Mienert et al., 2005; Zillmer et al., 2005a, b) corresponding to the base of the hydrate stability zone at 200-300 m, and pockmarks (Hovland et al., 2005) indicating gas expulsion from the sediment.

The slide was presumably triggered by an earthquake, but the sediment column was probably not stabilized because of rapid sediment accumulation and/or gas hydrate dissociation. The rapid accumulation during glacial periods of moraine sediments shed by the Fennoscandian ice sheet on the edge of the shelf (Bryn et al., 2005) produced an increase in pore pressure in the pre-existing clay-rich layers of the sediment column. After a specific load is exceeded, the clay-rich units fail and the whole margin collapses (Dugan and Flemings, 2000). This mechanism

explains why the Norwegian continental margin has landslides almost synchronous with the glacial cycles.

The other mechanism is dissociation of gas hydrate deposits because of an increase in ocean temperatures. The rise in sea level due to ice-caps melting would increase the thickness of the GHSZ. On the other hand, warming of the near-surface sediment would provoke hydrate dissociation by increasing methane solubility in seawater, and producing methane dissolution in seawater rather than gas bubbles towards the atmosphere (Sultan et al., 2004b). In any case, the gas hydrate dissolution would have decreased the cohesion of the sediment column, facilitating its failure.

The amount of methane released by the Storegga slide has been estimated at 1-2 Gt of C of methane in gas hydrates on the basis of the size of the landslide and the potential content of hydrate in the sediment column (10% of the pore water volume). As regards the methane radiative force in the atmosphere, the effect of the methane released during the Storegga landslide would have been comparable in magnitude to the CO_2 produced by the eruption of Mt. Pinatubo. However, the methane effect would have lasted at least five times longer than the eruption of a large volcano (Archer, 2007).

2. Geological setting

2.1. The Cascadia margin and accretionary complex

2.1.1. Physiography and tectonics

Hydrate Ridge is a structural high located in the western margin of North America, also known as the Cascadia continental margin. The Cascadia continental margin is formed from North to South, by the British Columbia, Washington, Oregon and the northern California continental margins (Figure 2.1).

The Cascadia accretionary prism is formed as the Juan de Fuca plate system obliquely subducts beneath the North American plate along the British Columbia, Washington, Oregon, and northern California continental margins. The Cascadia subduction zone is limited by triple junctions at its northern and southern ends (Figure 2.1). In the North just South of Queen Charlotte Island, it intersects the Queen Charlotte Fault and the Explorer Ridge. In the South, just off of Cape Mendocino in California, it intersects the San Andreas Fault and the Mendocino fault zone at the Mendocino Triple Junction (Figure 2.1).

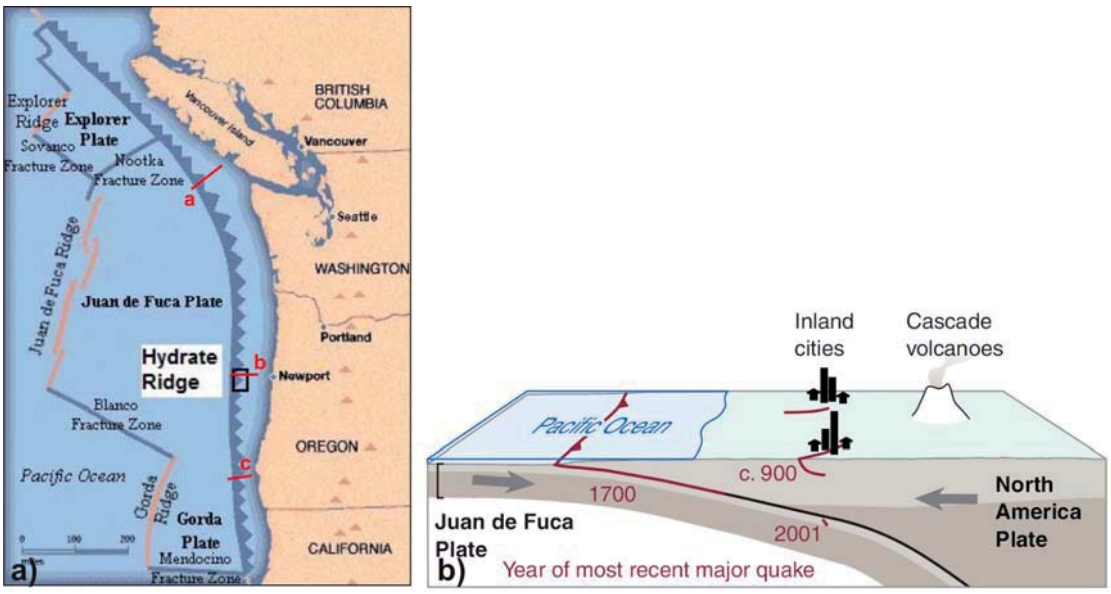

Figure 2.1. Plate tectonics map and diagram of the Cascadia accretionary complex area. **A.** Principal tectonic plates of the western American margin. Small square shows the location of Hydrate Ridge. Triangles show the location of the principal onland volcanoes of the region. Nootka Blanco and Mendocino fracture Zones and the principal Tectonic Ridges are also depicted. A, b and c label the seismic lines showed in Figure 2.3. **B.** Theoretical scheme of the Cascadia subduction zone, showing the two last major earthquakes (modified from Atwater et al., 2005).

The current subduction rate in Cascadia has been estimated at ~4.5 cm/yr (e.g. Silver 1971; Riddihough, 1984; Davis and Hyndaman, 1989; DeMets et al., 1990; Nedimović et al., 2003)

(Figure 2.1). The fast convergence rate as well as the young age of the subducting plate (10 Ma), characterizes Cascadia as an active margin able to generate great earthquakes (Magnitude ~8) with a recurrence period of 300 to 600 years (e.g. Goldfinger et al., 1992; Karlin et al., 2004). The last big earthquake in Cascadia was in 1700 with a magnitude of 8.7-9.2 (e.g. Atwater et al., 2005). The earthquake involved the Juan de Fuca Plate from mid-Vancouver Island in southwest Canada off British Columbia to northern California. The length of the fault rupture was about 1000 kilometers (600 miles) with an average slip of 20 meters (Atwater et al., 2005).

The Cascadia accretionary wedge extends from 60 km off southern Oregon to 150 km off northern Olympic Peninsula of Washington, where the thick Pleistocene Astoria and Nitinat fans are presently being accreted to the continental margin (e.g. Nelson, 1985) (Figure 2.2). This is an area of active fluid flow and high pore pressure (MacKay, 1995) since sediments on the subducting plates contain large volumes of sandy and silty turbidites (Tréhu et al., 2003). At present, most of this sediment is accreted to the continental margin either by offscraping at the deformation front or by underplating beneath the accretionary complex some 10 km east of the deformation front (MacKay, 1995; MacKay et a., 1992; Tréhu et al., 1994; Kelsey et al., 1996; Nedimovic et al., 2003; Johnson et al., 2006).

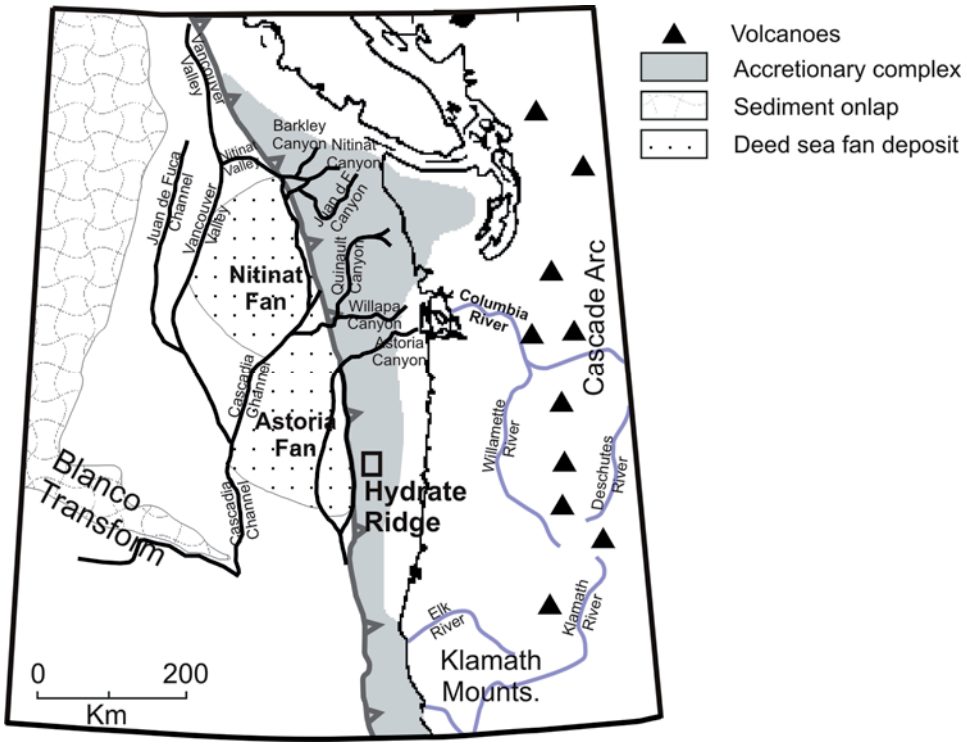

Figure 2.2. Physiographic map of the Oregon-Washington margin, showing the main rivers, canyons and channels operating in the system, as well as the main deep sea fans of the area: the Nitinat and Astoria fans. Blanco transform and the onlap sediment area are also depicted (modified from Underwood et al., 2005).

The active accretionary thrust faults of the lower slope of Cascadia are characterized by mostly seaward vergence offshore of the Vancouver Island (Davis and Hyndman, 1989; Hyndman et al., 1994; McNeill et al., 1997); landward-vergent thrusts in the British Columbia, Washington and northern Oregon margins (Seely, 1977; MacKay, 1995; MacKay et al., 1992; Flueh et al., 1998; Adam et al., 2004; Booth-Rea et al., 2008) (Figure 2.3) in relation of the subduction of the rapidly deposited and overpressured sediment from Astoria and Nitinat submarine fans (Seely, 1977; MacKay, 1995); seaward-vergent thrusts in the central and southern Oregon margin (MacKay, 1995; Goldfinger et al., 1992; 2000; MacKay et al., 1992); and offshore northern California, the structural vergence changes more frequently along strike (North to South) from dominantly seaward vergent to landward vergent back to seaward vergent (Gulick et al., 2002) (Figure 2.3). In addition to the seaward and landward thrust faults and folds that comprise the Cascadia accretionary wedge, nine WNW-trending left-lateral strike slip faults also cut across the lower slope of the wedge (Goldfinger et al., 1997). These faults form in the lower plate as a result of dextral shear of the forearc, owing to the oblique subduction, and propagate upward into the accretionary wedge through time.

Recent sedimentary evidence from estuarine systems and coastal lagoons in the Oregon coast reveal that the recurrence and spatial distribution of earthquakes in the Cascadia subduction zone during the Holocene period may best be explained by a variable rupture mode model, whereby giant earthquakes that rupture the entire margin may be followed by earthquakes of lesser extent that rupture segments of the subduction zone (e.g. Witter et al., 2003; Kelsey et al., 2002; Kelsey et al., 2005). Thus, segment boundaries may act as barriers to rupture propagation and limit the size of some earthquakes to Mw 8.5. (Witter et al., 2003). Data from the southern British Columbia coast reveal that large tsunamis had struck the Cascadia continental margin several times during the late Holocene. Tsunamis such as the one that caused about $10 Million damage in Vancouver Island in 1964 can be expected in the future, which represents a hazard to people and property in western North American coastal areas (Clague and Bobrowsky, 1994). The recognition of this geological risk and the identification of large amounts of gas hydrates in Cascadia continental margin justify the detailed study of this margin (e.g. Carson et al., 1995; Hyndmann et al., 2001; Tréhu et al., 2003; Riedel et al., 2006a, 2006b).

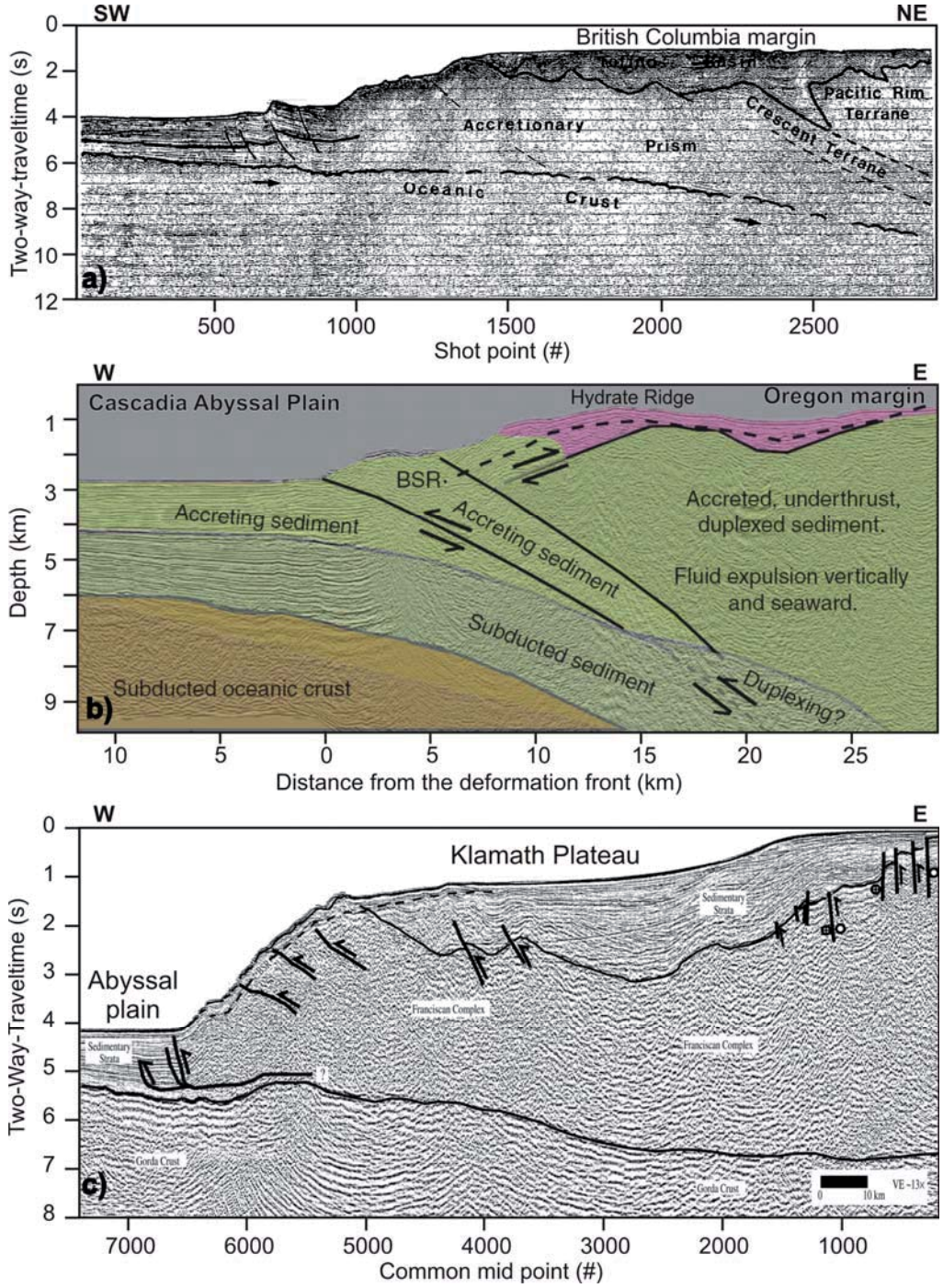

Figure 2.3. Linedrawings of three seismic sections across the Cascadia accretionary wedge in the British Columbia, Oregon and California margins. Location of the seismic profiles is shown in Figure 2.1. **A.** Migrated time section of multichannel line 85-01 off southern Vancouver Island. Major tectonic elements and sedimentary units are shown. Vertical exaggeration is 4:5:1 at water velocity and 1:1 at 6.7 km · s^{-1} (modified from Davis and Hyndmann, 1989). **B.** Linedrawing of seismic profile OR89_Line 2 through southern Hydrate Ridge (central Oregon margin) obtained during the site survey conducted for ODP Leg 146 (MacKay et al., 1992). Two-way-traveltime was converted into depth using the velocity model of Gerdom et al. (2000). Subducted oceanic crustal materials are shown in orange; abyssal plain and accreted sediments are shown in shades of green; slope basin sediments are depicted in pink (modified from Tréhu et al., 2006). **C.** Mendocino Triple Junction Seismic Experiment line MTJ-14. Profile shows the transition from the abyssal plain to the Klamath Plateau and continental shelf. Basin sediments were deposited above the Franciscan Complex of the accretionary prism. The subducting Gorda plate can also be observed. Notice the pattern of lower-angle thrust faults to the west and higher-angle thrust faults to the east with little deformation in the central syncline (modified from Gulick et al., 2002).

2.1.2. Oceanography

The main surface currents that govern the oceanic circulation of the Oregon-Washington margin form part of the Alaska Gyre and the North Pacific Subtropical Gyre. As part of this clockwise circular current, the California Current (Figure 2.4) is intimately linked to the atmospheric pressure systems over the North Pacific and western North America (Hickey, 1979; Emery and Hamilton, 1985). Thus, the cool northern waters are moved southwards along the western coast of North America to just south of the U.S.-Mexico border, making the coastal waters cooler than other coastal areas of comparable latitude (e.g. Herbert et al., 2001). Conditions favourable for coastal upwelling exist over most of the year, especially in the summer months, off northern California. The warmer, more saline, more oligotrophic waters of the central Pacific Gyre are located about 1000 km offshore (Figure 2.4). Much of the arid climate of the south-western North America responds to the atmospheric conditions that drive this near-surface oceanic system, which is only disrupted during the *El Niño* years, when sea surface temperatures increase along the California margin, upwelling diminishes (e.g. Simpson, 1983) and rainfall is more frequent onland (e.g. Ely et al., 1994).

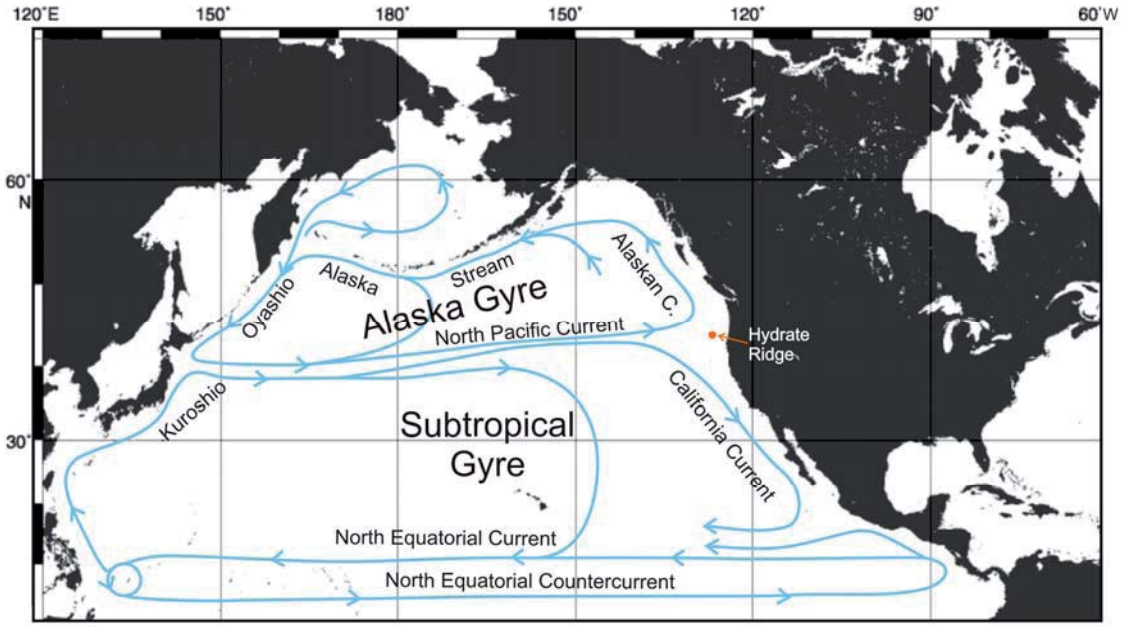

Figure 2.4. Schematic map of the principal oceanic surface currents affecting the North Pacific Ocean, including the North Pacific Subpolar gyre, or Alaska Gyre, and the North Pacific Subtropical Gyre. The situation of Hydrate Ridge in the Oregon-Washington continental margin is also shown (modified from Lyle et al., 2000).

The Alaska current, is the northward warm water current along the coast of British Columbia and the Alaska Panhandle, resulting from the northward diversion of part of the North Pacific Current. In contrast to typical sub-Arctic Pacific water, the Alaska Current water is characterized by temperatures above 4° C and surface salinities below 32.6 parts per thousand.

2.2. The Hydrate Ridge

2.2.1. Physiography

Hydrate Ridge is located on the slope of the Oregon margin (up to 1500 m depth), approximately 80 km offshore Newport and 15 km east from the current deformation front (Figure 2.1; Figure 2.2). The steep slope of the Oregon - Washington margin connects the continental shelf of western America with the Cascadia abyssal plain, which occupies an area of 35,000 km^2 (Weaver and Thomson, 1987). The Cascadia abyssal plain has a consistent slope to the south, parallel to the continental margin (Griggs and Kulm, 1970). Much of the slope of the Oregon margin consists of structural hills and ridges similar to Hydrate Ridge enclosed by small basins partially filled with hemipelagic sediments and turbidity-current deposits (e.g. Carlson and Nelson, 1987). In this geological setting, Hydrate Ridge is a 25 km long and 15 km wide ridge formed by two highs: the northern ridge at 600 m depth and the southern one at 800 m depth (Figure 2.5).

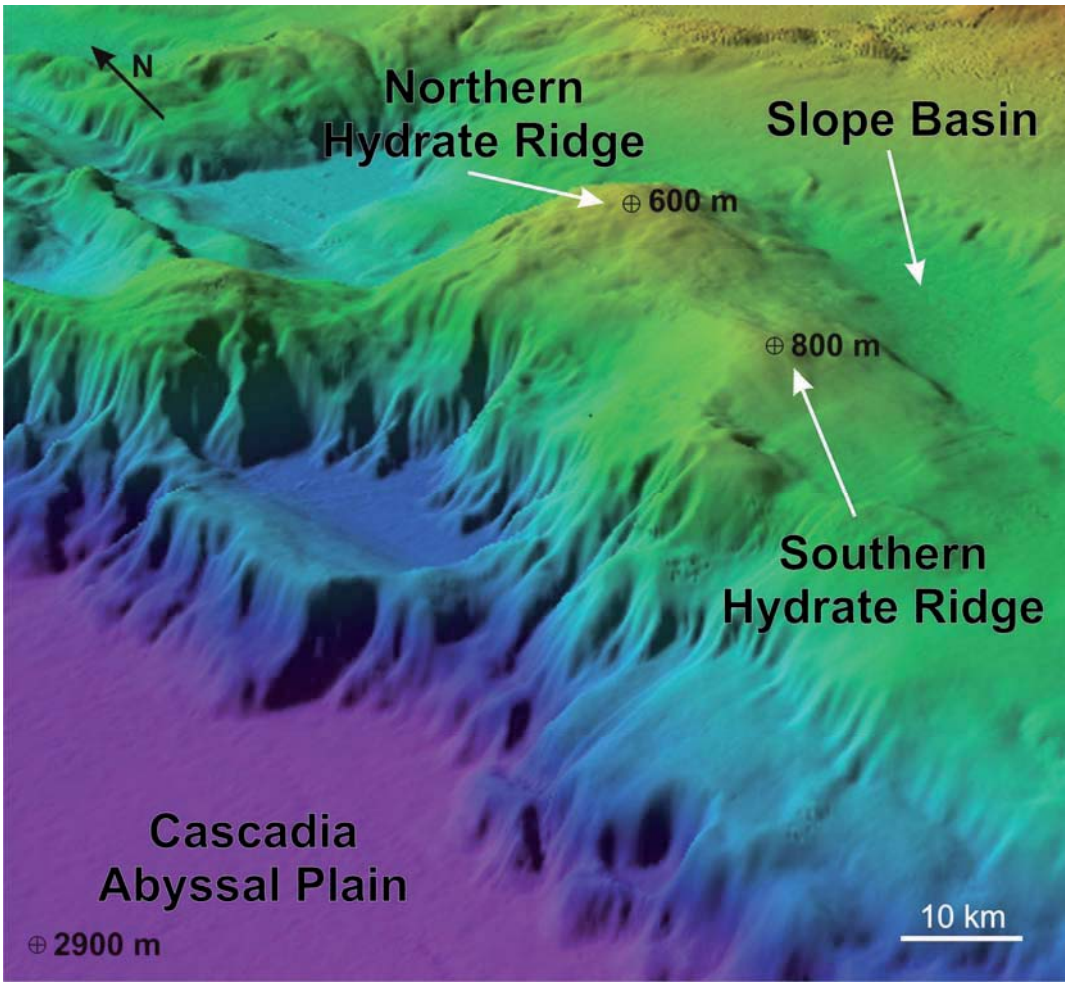

Figure 2.5. Bathymetric 3-D view of the Cascadia accretionary prism, showing the northern and the southern summit of Hydrate Ridge. The slope basin adjacent to Hydrate Ridge and the Cascadia Abyssal Plain are also indicated.

The northern summit of Hydrate Ridge represents a more mature stage in the evolution of these ridges (Tréhu et al., 1999), as evidenced by extensive carbonate pavement (Kulm et al., 1986; Greinert et al., 2001; Johnson et al., 2003) and upward deflection of the BSR related to a thrust fault (Westbrook et al., 1994; Kastner et al., 1995). In contrast, southern Hydrate Ridge is less evolved; it exhibits only limited and localized carbonate crusts and minor discrepancies in the BSR depth with respect to the predicted depth based on seawater/gas hydrate phase boundary (Torres et al., 2002).

2.2.2. Structural Setting

The major fault pattern on Hydrate Ridge, which provides a pathway for methane and fluid venting, is relatively well known (Kulm et al., 1986; MacKay et al., 1992; Tréhu et al., 1999). It is related to the evolution and growth of the Cascadia convergent margin. This is a highly deformed portion of the accretionary wedge that results from the oblique subduction-driven compression (Johnson et al., 2003).

In the central Oregon portion of the margin where Hydrate Ridge is localized, a transition zone exists between a northern landward vergent province (the Washington and northern Oregon margins) and the southern seaward vergent province (the southern Oregon margin), yielding a narrow zone of mixed vergence, both along and across strike, which is coincident with the location of two of the nine left-lateral strike slip faults (Johnson et al., 2000).

Hydrate Ridge appears to be bounded at its northern and southern ends by the left-lateral strike-slip Daisy Bank and Alvin Canyon faults, respectively (Figure 2.6). The geometry and slip direction of these faults imply a clockwise rotation of the block contained between them, with an overall right-lateral shear zone (Goldfinger et al., 1992; 1996). Thus, the oblique subduction-driven right-lateral shear of the Hydrate Ridge block is responsible for the apparent clockwise rotation of the ridge itself (Johnson et al., 2000) (Figure 2.6). The faults extend through the accreted sediments deep below the GHSZ up to several km (Figure 2.3). At depth, they tap a fluid reservoir, which contains free methane. The faults and fractures serve as conduits to channel methane up to the seafloor where it either escapes into the water column or forms secondary gas hydrates, as is the case on the summits of Hydrate Ridge (Johnson et al., 2000).

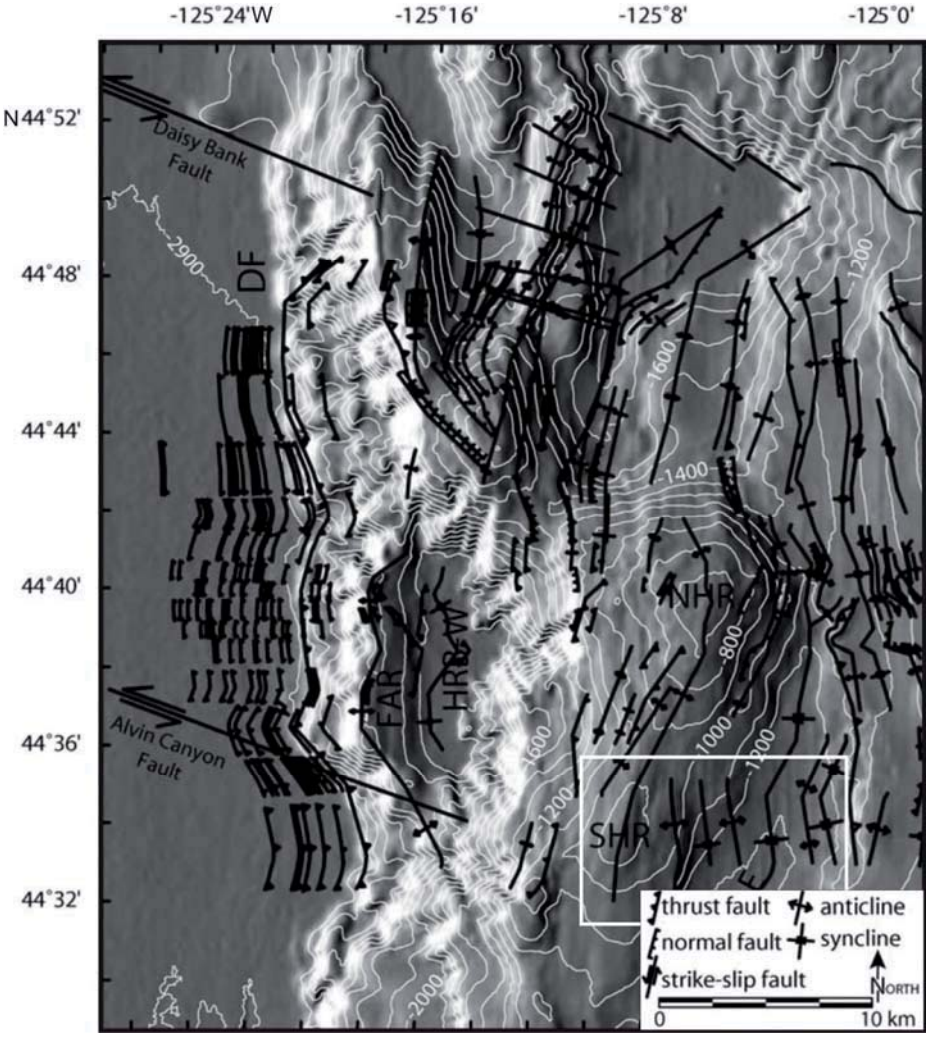

Figure 2.6. Structural map of the Hydrate Ridge region (interpreted from multichannel seismic reflection profiles collected during the site survey for ODP Leg 204, inset), overlain on 100 m contour shaded relief bathymetry. Daisy Bank and Alvin Canyon faults accommodate the deformation north and south of Hydrate Ridge and thrusts and fold belts are common in the region limited by the strike-slip faults. The major geologic and geographical features are labelled as follows: DF= deformation front; FAR= first accretionary ridge; HRB-W= Hydrate Ridge Basin-West; NHR= Northern Hydrate Ridge; SHR= Southern Hydrate Ridge; HRB-E= Hydrate Ridge Basin-East; DB= Daisy Bank. The outlined white box corresponds to the area depicted in Figure 2.6. (modified from Johnson et al., 2003).

A detailed study of the dipping of minor fractures at southern Hydrate Ridge reveals that fractures at the crest are typically high-angle (60º) with isotropically distributed strikes, whereas those on the ridge flanks have lower dips (20-60º) and strike parallel to the trend of Hydrate Ridge (Figure 2.7). In the eastern slope basin, no significant fracturing was found (Weinberger and Brown, 2006). These differences indicate that the minimum principal stress direction is horizontal at the ridge crest as a result of a topographically-driven extension and the relative gravitational collapse of southern Hydrate Ridge (Weinberger and Brown, 2006). Chaotic fracturing at the ridge crest (Figure 2.7) results from the interaction of the stress state and free

gas migration, which is confined to high permeability sediments and fractures. In contrast, on the ridge flanks, the well ordered fractures agree with stress orientations, which result from an obliquely dipping of principal stress direction and allows the predominance of aqueous flow.

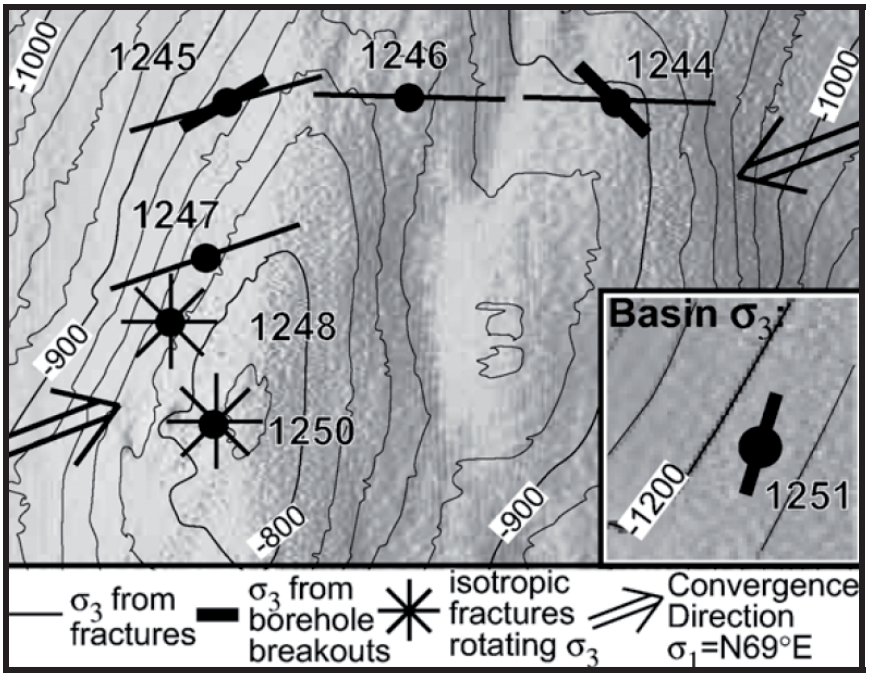

Figure 2.7. Map of principal stress orientations from ODP Leg 204 borehole breakouts (thick lines) and mean fracture directions on the flanks (thin lines) of southern Hydrate Ridge. Isotropic fracturing on the ridge crest indicates dominance of horizontal stress. The convergence vectors between the Juan de Fuca and North American plates are also shown (Weinberger and Brown, 2006).

The analysis of the 3-D high-resolution multichannel seismic data acquired in year 2000, allowed the characterization of two main seismostratigraphic units at southern Hydrate Ridge: an upper unit characterized by folded and uplifted stratified sediments that unconformably onlaps the unit below. This lower unit is characterized by a low frequency incoherent facies, interpreted as highly deformed accretionary complex material (Tréhu et al., 2002). The stratigraphic characterization of these units is discussed in Chapter 5.

2.2.3. Presence of gas hydrates

A close association between gas hydrates and carbonates exists on Hydrate Ridge and in other accretionary ridges within the GHSZ. This is mainly caused by dewatered fluids from the prism that supply methane to the GHSZ and also transfer heat to shallower depths. The heat can induce the destabilization of gas hydrates (Suess et al., 2001). At both, the northern and southern summits of Hydrate Ridge, authigenic carbonates, pore-water carbon and oxygen isotopes support this association by suggesting that the precipitation of carbonates is in part derived from methane coming from the destabilization of gas hydrate (Bohrmann et al., 1998;

Clague et al., 2001; Greinert et al., 2001). Thus, destabilized gas hydrate contributes to the total accumulation of authigenic carbonates precipitated by accretionary wedge dewatering and compaction (Bohrmann et al., 1998).

After more than a decade of research, the active fluid flow in the Cascadia convergent margin has been inferred, among others, from the identification of high active venting of fluids and gases and exposures of methane hydrates on the seafloor on the northern and southern peaks of Hydrate Ridge as well as on the Southeast Knoll (e.g. Suess et al., 2001; Heeschen et al., 2003) (Figure 2.8). Gas hydrates are under stable conditions on the seafloor in these three areas and, the presence of gas bubbles in the water column suggests a rapid transport of methane upwards through the sedimentary column (Tréhu et al., 2002). The detection of cold seeps and carbonate crusts in Hydrate Ridge propitiated the recognition of this area as one of the richest in gas hydrates in the world twenty years ago (Kulm et al., 1986). Since 1996, when massive hydrates were first discovered on the seafloor summit of southern Hydrate Ridge (Bohrmann et al., 1998), there have been numerous successive cruises to explore gas hydrates formation and distribution in this region. During the German RV Sonne Cruise 110 (1996), gas hydrates from the seafloor were for the first time sampled.

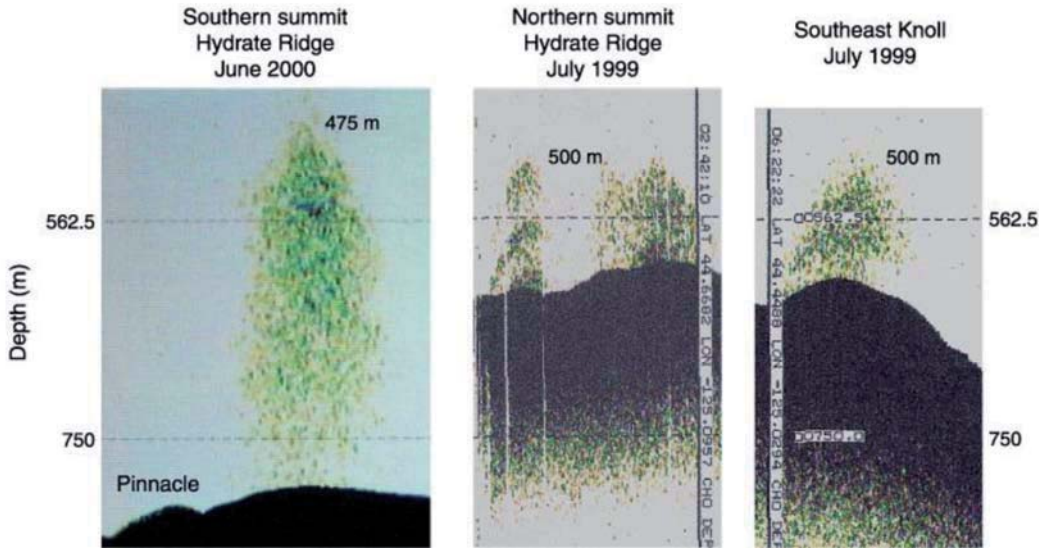

Figure 2.8. Echosounder records (12 kHz) from southern and northern Hydrate Ridge and Southeast Knoll in the Oregon continental margin, showing gas bubbles escaping to the water column (Tréhu et al., 2003).

During Leg 146 of the ODP (Westbrook, Carson and Musgrave, 1992), four sites were drilled at the Cascadia continental margin to investigate the tectonic dewatering within the accretionary prism. Sediments off and within the accretionary wedge were drilled (Carson et al., 1995). Based on the recognition of the potential presence of methane hydrates in the seismic reflection data (MacKay et al., 1994; Tréhu et al., 1999), Site 892 was drilled at the northern

Hydrate Ridge (Figure 2.9). At this Site, disseminated H_2S-rich methane hydrates were only recovered between 2 and 19 mbsf. Although pore water geochemical and temperature anomalies suggested the presence of disseminated gas hydrate near the BSR, no gas hydrate was recovered near its depth 75 mbsf (Kastner et al., 1995; Hovland et al., 1995). The environment of deposition of Site 892 sediments was interpreted as basin plain, taking into account the presence of deep water depositional features. Subsequent sedimentological analyses confirmed this interpretation and concluded that these sediments were deposited before the tectonic uplift of the continental slope caused by accretionary processes in the Cascadia wedge complex (e.g. Camerlenghi et al., 1995). Recently Leg 204 of the ODP has investigated the formation of gas hydrates and fluid migration mechanisms at southern Hydrate Ridge (Figure 2.9).

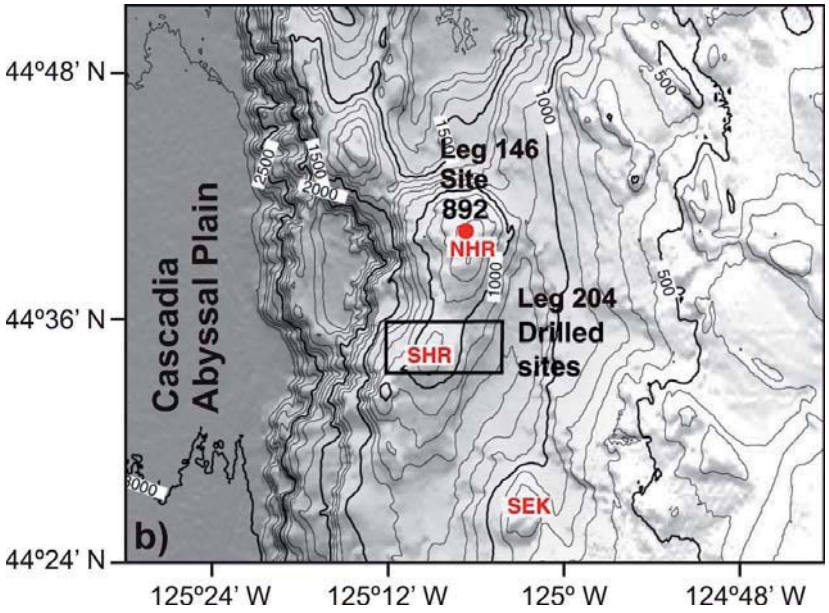

Figure 2.9. Bathymetric map (100 m contour interval) of Hydrate Ridge (NHR= northern Hydrate Ridge; SHR= southern Hydrate Ridge). Outlined box shows the location of the drilled sites during ODP Leg 204. Site 892 was drilled during ODP Leg 146 on SHR. The SEK= South East Knoll fluid venting area is also indicated.

PART II

3. ODP Leg 204

Leg 204 (July-September 2002) was the first ODP cruise exclusively dedicated to the research on gas hydrate processes in accretionary complexes, using the best sampling instrumentation and analytical equipment available. The selected area was southern Hydrate Ridge (Figure 3.1), where the largest volume of gas hydrates was estimated. The sediment measures of the nine drilled Sites carried out onboard included non-destructive physical properties, such as magnetic susceptibility (ring and pointer), gamma-ray, digital image and lightness using different multi-sensor core loggers (MSCL), infrared thermal imagery, chemical composition of interstitial waters (i.e. chlorinity, carbonate, sulphate and barium content), wireline logging (e.g. density, gamma-ray) and logging-while-drilling (LWD) measurements (e.g. porosity, resistivity) (Tréhu et al., 2003; Shipboard Scientific Party, 2003j).

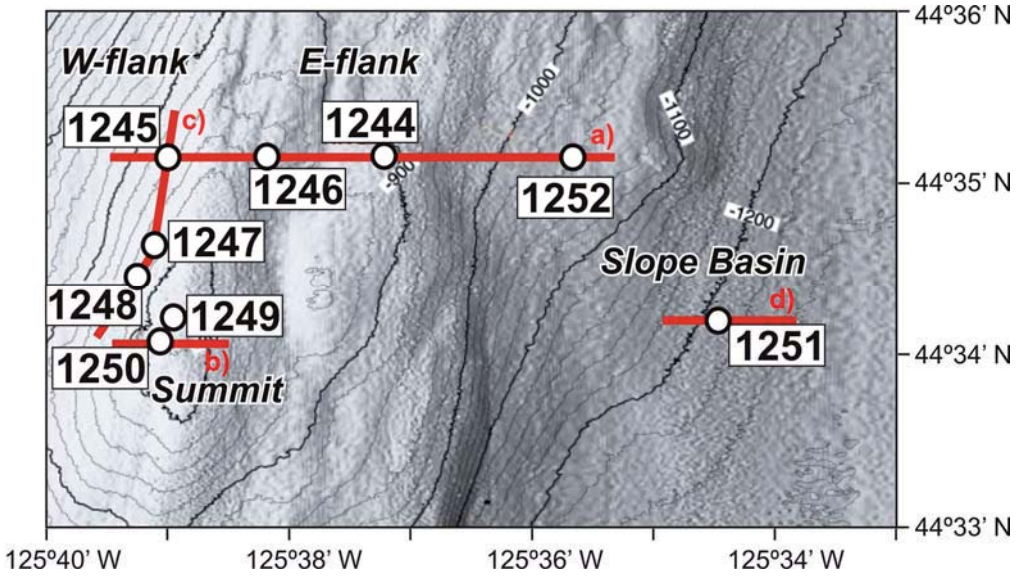

Figure 3.1. Detailed bathymetric map (20 m contour intervals) of southern Hydrate Ridge. Samples analysed in this thesis are from Sites 1244 to 1252 drilled during Ocean Drilling Program Leg 204. Lines a, b, c and d indicate the location of the 3D multi-channel seismic transects presented in Figure 3.3 and Figure 3.16) (modified from Tréhu et al., 2003).

During the ODP Leg 204 onboard the Research Vessel "Joides Resolution" (Figure 3.2), nine Sites (1244 to 1252) were drilled in the southern Hydrate Ridge region, exceeding the depth of the BSR at most sites (~ 100 mbsf) and up to a depth of 550 mbsf at Site 1245 (Figure 3.1). The drilled sites were located in water depths of 780-810 meters at the summit (Sites 1248, 1249 and 1250), 860-900 meters on the eastern flank (Sites 1244 and 1246), 820-860 meters on the western flank (Sites 1245 and 1247) and 1050-1210 meters in the slope basin adjacent to Hydrate Ridge (Sites 1251 and 1252) (Figure 3.1, Table 3.1). At every site, different holes were

made in order to employ different techniques (LWD, coring, etc.) at approximately the same location, ten meters apart.

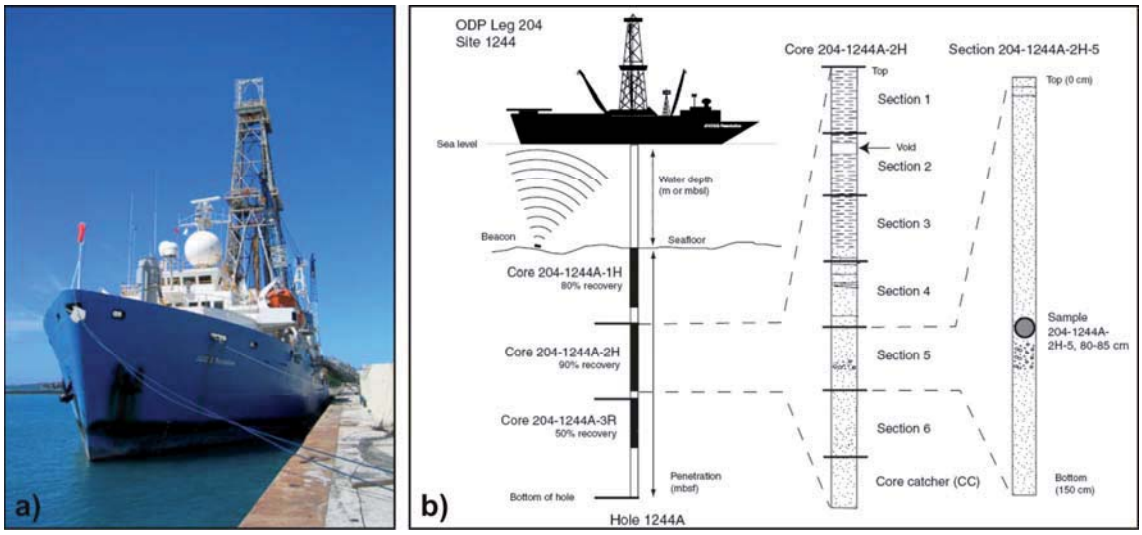

Figure 3.2. A. Image of the research vessel Joides Resolution. The ship is 143 meters long and 21 meters wide. During a leg, the crew positions the ship over the drill site using 12 computer-controlled thrusters as well as the main propulsion system. The rig can suspend as much as 9,150 m of drill pipe to an ocean depth of up to 8,235 m. **B.** Example of coring and sampling for Ocean Drilling Program Leg 204 corresponding to Hole 1244A, core 2H, section 5, sample at 80-85cm depth.

The drilled Sites during ODP Leg 204 are located in a region of 4 km long and 11 km wide, which was selected in accordance with the 3D multichannel seismic data that had been previously acquired from a subseafloor depth of ~1 km (Tréhu et al., 2003). The drilling Sites were located to sample and investigate the physical properties of the bright prominent seismic reflectors, such as the BSR, Horizon A, Horizon B and B' identified in the 3D multichannel seismic data, and to determine the role of these horizons in methane-rich fluids circulation at Hydrate Ridge (Figure 3.3).

Area	Hole	Latitude	Longitude	Seafloor depth (m)	BSR depth (mbsf)	Drilled depth (mbsf)
Summit	1248C	44º 34.45'N	125º 9.1499'W	841.0	115	149
	1249C	44º 34.2368'N	125º 8.841'W	788.5	115	88.5
	1250C	44º 34.1273'N	125º 9.0178'W	807.0	114	143.0
E. Flank	1244E	44º 35.1709'N	125º 7.1719'W	906.0	127-129	135.8
	1246B	44º 35.1644'N	125º 8.1235'W	860.8	114	136.7
W. flank	1245B-E	44º 35.1587'N	125º 8.9455'W	880.0	134	540.3
	1247B	44º 34.6589'N	125º 9.0766'W	845.9	129-134	217.0
Slope basin	1251B	44º 34.2191'N	125º 4.4375'W	1221.4	193	442.1
	1252A	44º 35.1671'N	125º 45.5691'W	1051.0	(170)	259.8

Table 3.1. Location of Ocean Drilling Program Leg 204 Holes at southern Hydrate Ridge, depth of the bottom simulating reflector (BSR) and drilled depth for each analysed Hole. The depth of the BSR was onboard calculated from the vertical seismic profile, electrical resistivity from logging while drilling (LWD) and wireline sonic log. The BSR depth at Site 1252, in brackets, is projected from nearby BSR measurement in the multichannel seismic data; mbsf= meter below sea floor (Tréhu et al., 2003).

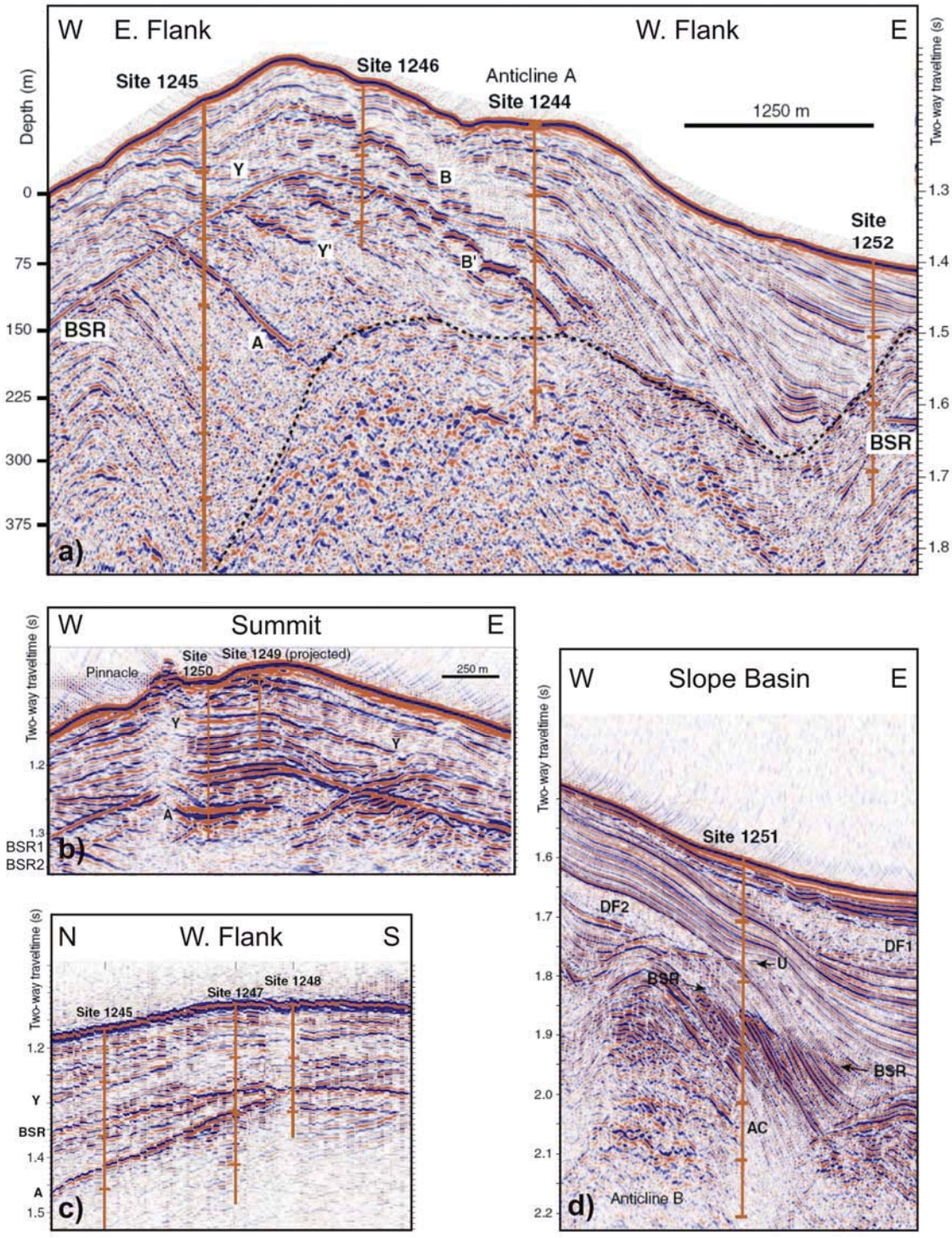

Figure 3.3. Seismic sections from the multichannel seismic survey across southern Hydrate Ridge showing the main horizons and structural features identified. Location and depth of the drilled sites during Ocean Drilling Program Leg 204 are presented. The length of the lines indicates maximum depth of penetration at each site, and horizontal ticks are every 75 m. In the slope basin sequence, an unconformity (U) and two chaotic units interpreted as debris flow deposits (DF1 and DF2) are included, which can be traced throughout the slope basin. AC is the unconformity that limits the top of older (>1.6 Ma) fractured sediments of the accretionary complex. Location of profiles a, b, c and d are in Figure 3.1. BSR = bottom simulating reflector (modified from Tréhu et al., 2003).

Horizon A has an amplitude ~10 times higher than that of adjacent stratigraphic events and the BSR. Horizon A gets shallower and brighter towards the southern summit of Hydrate Ridge (Figure 3.3). Speculation that this horizon is a major path transporting methane-rich fluids to the summit of Hydrate Ridge was tested during ODP Leg 204 by drilling at Sites 1245, 1247, 1248 and 1250 (Tréhu et al., 2003). The multichannel seismic data revealed that the western flank of southern Hydrate Ridge (Site 1245 and 1247) is characterized by folded sediments in which faulting is rare (Figure 3.3).

Horizons B and B' are a pair of strong reflections, that appear east of the southern axis of Hydrate Ridge and seems to be associated with an active secondary anticline (Anticline A) (Figure 3.3). These horizons are pervasively faulted, with offsets consistent with tensional cracking in response to uplift and folding. Horizon B and B' downlap with AC, which was interpreted as the top of the accretionary complex material. Sites 1244 and 1246 were planned to ascertain whether these horizons are permeable stratigraphic horizons transporting fluids from deep in the accretionary complex into the GHSZ (Tréhu et al., 2003). Sites 1244 and 1246 were localized on the eastern flank of southern Hydrate Ridge, which is characterized by pervasive faulting (Figure 3.3).

Beneath the summit of southern Hydrate Ridge some venting structures were identified in the seismic sections (Figure 3.3). A chaotic bright reflectivity zone can be observed just beneath the seafloor at the summit, in the area where the gas plumes were acoustically detected (Figure 2.8). Sediments from Sites 1248, 1249 and 1250 were drilled at the southern summit of Hydrate Ridge to find out whether this transparent seismic facies was related to the presence of massive gas hydrates (Figure 3.1). The presence of a double BSR was detected beneath the summit and western flank of southern Hydrate Ridge (Figure 3.3). Site 1250 was drilled exceeding the BSR depth (~143 mbsf) to ascertain whether gas hydrates were present beyond the depth of the second BSR (Table 3.1).

Site 1251 is located in the slope basin east of Hydrate Ridge. Sediments are rapidly accumulated in the slope basin, and the BSR is not so marked as at the summit and on the flanks, where the large amplitudes below the BSR indicate the presence of free gas (Figure 3.3). This Site was selected to study the physical properties of the *debris flow* deposits identified on the seismic profiles (Tréhu et al., 2003). Site 1252 is also located in the slope basin adjacent to southern Hydrate Ridge (Figure 3.3). Drilling was performed here in order to study the sediments underlying Horizon AC, because at this location, the accretionary complex material is less deformed than beneath the crest of southern Hydrate Ridge (Figure 3.3) (Tréhu et al., 2003).

3.1. Principal scientific results of the ODP Leg 204

The most interesting results of the ODP Leg 204 are given below (Tréhu et al., 2003; 2006).

Very high concentrations of gas hydrate from the seafloor to ~30 mbsf are present near the southern summit of Hydrate Ridge. They contain significant amounts of $C_{>1}$ hydrocarbon gases in addition to methane (e.g. propane, ethane; Claypool et al., 2006). High chloride concentrations near the summit indicate that hydrate formation was recent and rapid. The lateral extent of the near-surface gas hydrate deposit at the summit can be mapped based on its backscatter and seismic signature. At some distance from the summit, no gas hydrate was recovered in the upper ~45 mbsf (Tréhu et al., 2006).

Between ~45 mbsf and the base of the GHSZ, gas hydrates are distributed in lenses that are probably controlled by the physical properties of the sediments. In the slope basin east of Hydrate Ridge, gas hydrate concentrations are relatively low, with the probable exception of a 12-m-thick zone of relatively high concentrations near the base of the GHSZ at Site 1251 (Tréhu et al., 2003).

A number of physical and chemical proxies for gas hydrate distribution and concentrations generally give consistent results (e.g. Lee and Collett, 2006; Ussler III et al., 2006; Winters et al., 2006). Thermal anomalies recorded by systematically scanning the cores upon arrival on deck with an IR thermal-imaging camera provide a robust record of gas hydrate distribution (Tréhu et al., 2003; Weinberger et al., 2005). The thermal anomalies can also be calibrated using estimates of in situ gas hydrate concentration derived from pressure core samples and values of chloride concentration.

An unprecedented number of cores recovered at *in situ* pressure using HYACE or HYACINTH instrumentation provided accurate estimates of subsurface methane concentration. Density logs of cores retrieved at *in situ* pressure provide details of the gas hydrate distribution and direct evidence for free gas within the GHSZ and can also be used to study the changes of gas hydrates due to depressurization (Tréhu et al., 2003).

The base of the GHSZ represents a discontinuity in C_1/C_2 and other chemical constituents of pore waters and gas voids, suggesting that gas hydrate formation

has profound geochemical effects (Claypool et al., 2006). Several geochemical mixing and fractionation signals (i.e. isotopic composition of gas and pore water) provide constraints on fluid flow and gas hydrate dynamics (e.g. Borowski, 2006; Torres and Rugh, 2006; Dickens et al., 2006; Tomaru et al., 2006).

Ash-rich layers and thick turbidites, together with other coarse grain intervals and pervasive faulting serve as conduits for fluid flow (e.g. Weinberger and Brown, 2006; Tréhu et al., 2004a, 2004b). Borehole breakouts provide constraints on tectonic forces and possibly on the *in situ* strength of gas hydrate–bearing sediments (Tréhu et al., 2003).

3.1.1. Stratigraphic correlation

Onboard sedimentological studies of the drilled sites showed that lithology at all sites is similar, with abundant turbidites, some debris flows, and several prominent ash layers interbedded with the hemipelagic sediments. Furthermore, based on lithology, physical properties and seismic facies, five sedimentological units (I - V) were defined onboard, ranging from early Pleistocene to Holocene (Figure 3.4).

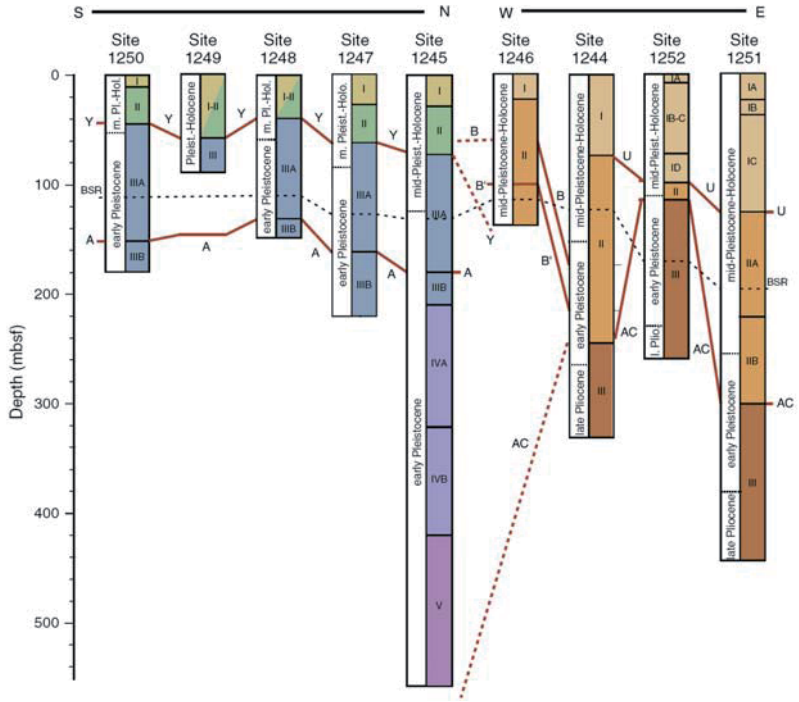

Figure 3.4. Summary of onboard sedimentological units defined during ODP Leg 204 for a South-North transect and an East-West transect across southern Hydrate Ridge. Correlation of seismic horizons A, B, B′ and Y, unconformities (U) and the limit of the accretionary complex material (AC) are also shown. Correlation between both transects was tentative; mbsf= meter below sea floor; BSR=bottom simulating reflector (Tréhu et al., 2003).

Most of the boundaries between these units were established in accordance with the location of the prominent seismic reflectors (i.e. Horizons A, B, B' and Y) identified in the 3D multichannel seismic data (Figure 3.3) or with the relative abundance of mass-transport deposits within the sedimentary sequence. The depositional age of every unit was established based on onboard biostratigraphical results. Subsequently, Chevalier et al. (2006) using a dedicated structural interpretation of the 3D seismic data, proposed a new stratigraphic model with up to seven seismostratigraphic units. These authors suggested a depositional sequence for southern Hydrate Ridge for the last 1.2 Ma (Figure 3.5; Figure 3.6).

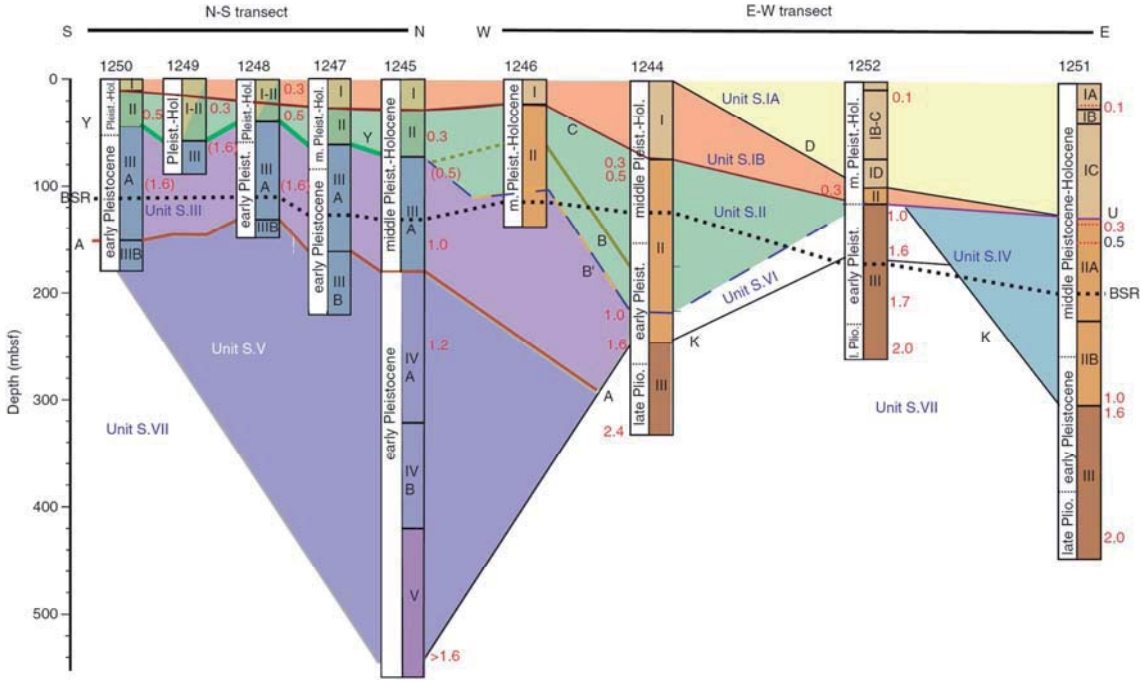

Figure 3.5. Comparison of sedimentological units defined by the shipboard scientific party during Ocean Drilling Program Leg 204 (Tréhu et al., 2003) with the seismostratigraphic units defined by Chevalier et al. (2006). Sedimentological units are shown as columns at each drilled site of southern Hydrate Ridge. Ages, in millions of years, determined by shipboard palaeontologists are shown as red numbers along the sides of the units. Ages in brackets are not compatible with the seismostratigraphic data and are attributed to reworking of older sediments. Seismostratigraphic units represent coherent sedimentary packages that can be mapped between sites and are labelled as Unit S.VII to S.IA. These are separated by the major seismic stratigraphic Horizons (A, B, B′, C, D, and Y) and angular unconformities (K and U). The position of the bottom simulating reflection (BSR) is also shown; mbsf= meter below sea floor (Chevalier et al., 2006).

3.1.2. Depositional sequence of southern Hydrate Ridge

Late Pliocene sediments were originally deposited as part of the deep-sea Astoria abyssal fan (Figure 3.6). Actually, they form Unit S.VII at the core of the Hydrate Ridge dome, which was probably formed at the toe of the accretionary complex overlying a seaward-verging frontal thrust (Johnson et al., 2006). Rapid deposition of Astoria fan sediments at the base of the slope continued during the early Pleistocene with deposition of Unit S.V. Simultaneously, sediments

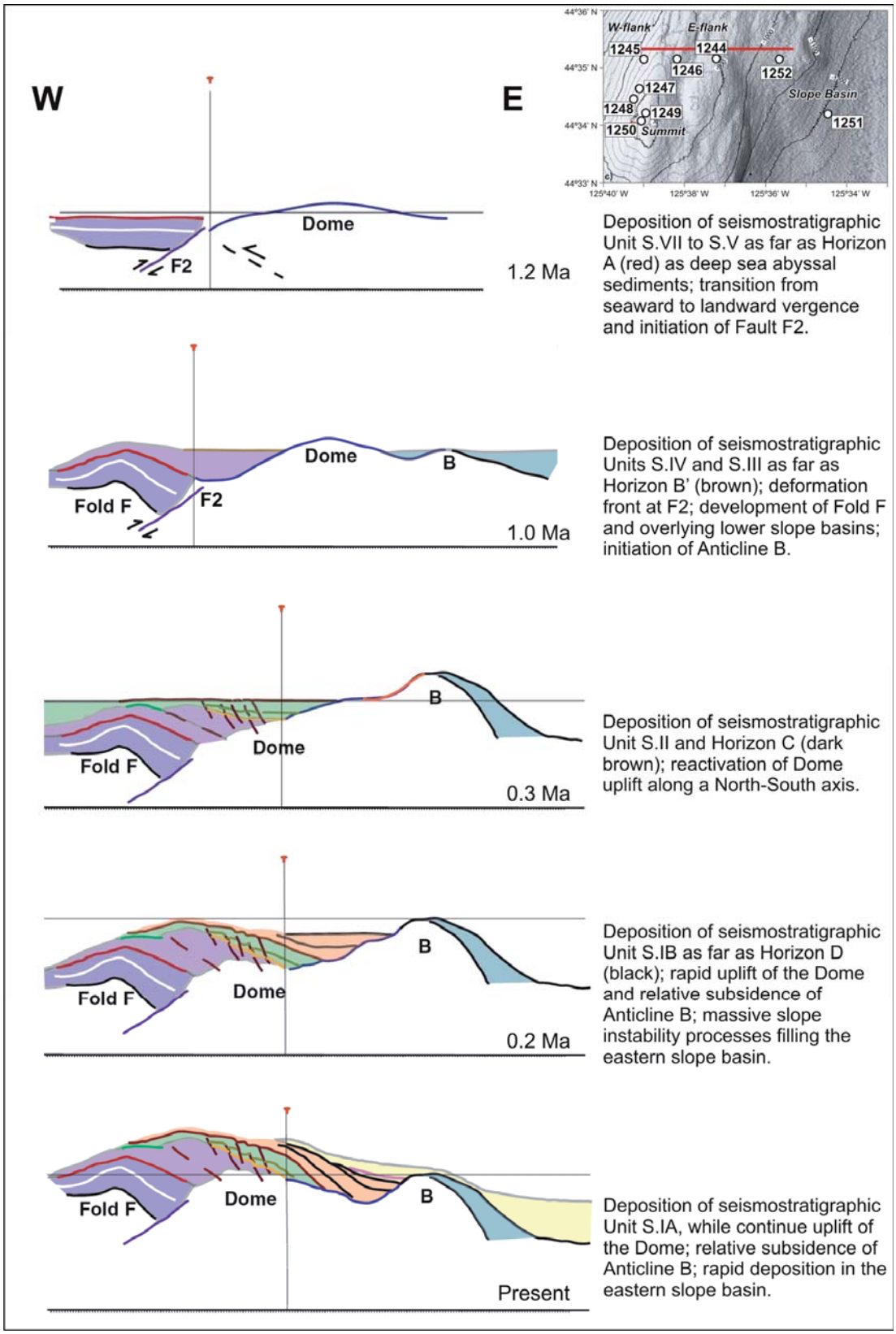

Figure 3.6. Reconstructed sequence of an East-West cross section across southern Hydrate Ridge (Line 230), depicted in red in the inset map. Reconstruction of the strata to their original geometry was achieved using rules of constant length and surface and, vertical and horizontal reference pin lines (marked by black lines and red nail). Colour code and labels for structures are the same as the seismostratigraphic units in Figure 3.5 (modified from Chevalier et al., 2006).

of Unit S.VI were deposited on the lower slope, although at a slow rate (Tréhu et al., 2003). The wavy and chaotic seismic character of Unit S.VI suggests pervasive compressional deformation throughout the proto-dome during this time period (Figure 3.6).

A shift of the frontal thrust form seaward to landward vergence occurred ~1.2 Ma ago. This shift produced the thrusting of abyssal plain deposits (Unit S.V) over the deformed and accreted units that form the older sequences of Hydrate Ridge (Unit S.VII) along fault F2 (Figure 3.6). A drag fold (F) developed during this period, creating a basin that was partially filled by sediments of Unit S.III while the Fold was still active. Other paleobathymetric highs that controlled the distribution of Unit S.III were the Dome and the Anticline A, which generated a series of overlapping slope basins as the depocenters shifted. The shift of the depocenters was produced by the migration of the up-rise movement towards the Northeast. The landward migration of the uplift process can be related to the topographic morphology of the subducting plate, which is now deeply buried beneath the shelf of the North American Plate (Chevalier et al., 2006). During this period of time, sediments from the topographic highs were re-deposited owing to the slope instability. This type of sedimentation continued from ~ 0.5 to ~ 0.3 M.a. with deposition of Unit S.II, which was laterally controlled by the relative uplift of Anticline B. Anticline B has been inactive since ~0.2 Ma as indicated by the onlap of Unit S.IA. At ~ 0.3 Ma, the main uplift movement of Hydrate Ridge shifted westwards to its present position, probably in response to a seaward-vergent frontal thrust and related sediment underplating. An increase in the dip of strata within Unit S.IA over time, the two debris flow deposits, as well as the thinning of the beds against the flanks of the Dome provide evidence for the ongoing relative subsidence of the eastern basin during the deposition of Unit S.IA. This may be caused by the clockwise rotation of Hydrate Ridge during the last 0.1 Ma, as discussed by Johnson et al. (2006).

3.1.3. Double BSR presence beneath southern Hydrate Ridge

Beneath the primary BSR, a second and weaker BSR across the crest of southern Hydrate Ridge was detected in the 3D multichannel seismic reflection data (BSR2 in Figure 3.3). This BSR lays 20-40 meters beneath the primary BSR and is mostly observed on the western flank of southern Hydrate Ridge. The principal BSR lies at the base of the gas hydrate occurrence zone and is in equilibrium with the P/T conditions that define the base of the GHSZ (Bangs et al., 2005), as deduced from the observations of the ODP Leg 204 cruise. The second BSR has been interpreted as representing the disintegrating remnants of a BSR that existed stably for an extended period of time, under past P/T conditions. The most likely cause for the upward migration of the BSR is a change in P/T conditions within the last 18,000 years. According to

the numerical model presented by Bangs et al. (2005), an increase in the bottom water temperatures of 1.75-2.25 ºC combined with a 120 m rise in sea level is the best explanation for the BSR upward shift (Figure 3.7). Furthermore, these estimations coincide with the bottom water temperatures and sea level rise since the Last Glacial Maximum 18,000 years ago (Bangs et al., 2005).

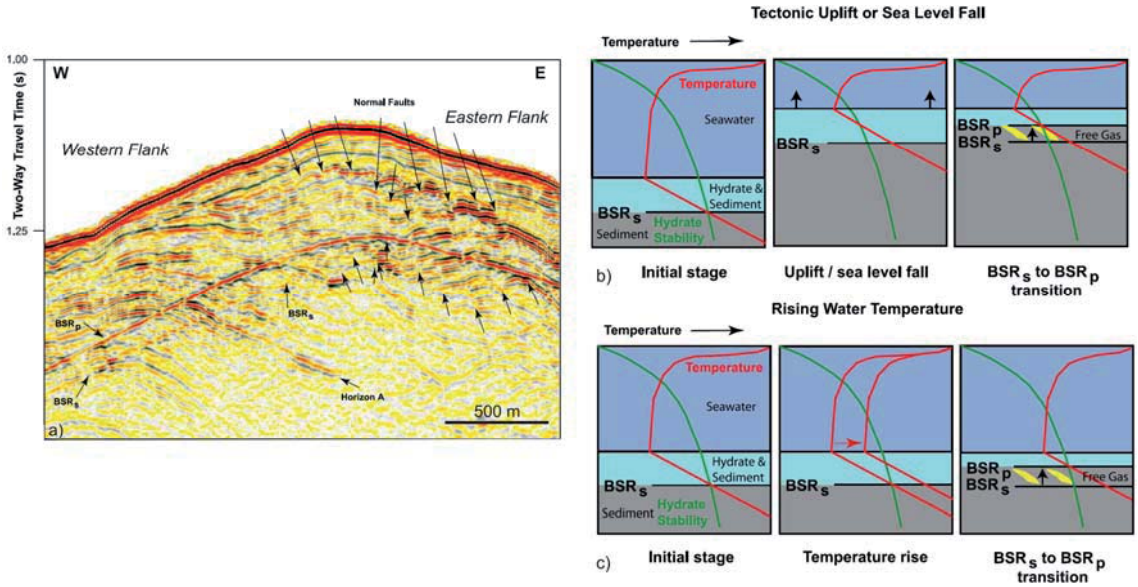

Figure 3.7. Distribution and formation mechanisms for a double bottom simulating reflector (BSR) at southern Hydrate Ridge. **A.** Seismic line 241 showing a coincident relationship between the amplitude of the secondary BSR (BSRs) and the location of numerous normal faults (arrows). **B.** Diagram showing the formation of a double BSR due to a tectonic uplift or a relative decrease in sea level at southern Hydrate Ridge. BSRs at the initial equilibrium stage lies at the intersection of the temperature (red line) and hydrate stability (green line) profiles. Tectonic uplift or sea level fall reduces overburden pressure and shift sediments relative to the gas hydrate stability curve and the temperature profile. The BSRs moves to the principal BSR (BSRp), releasing free gas into sediments (yellow areas) from hydrate dissociation. **C.** Diagram showing the formation of a double BSR due to a rise in the bottom water temperature. The temperature rise is conducted in the sediments, increasing the sediment temperature and maintaining the thermal gradient. Elevated temperature moves the gas hydrate stability boundary upwards and BSRs changes into the BSRp (modified from Bangs et al., 2005).

The double BSR in the southern Hydrate Ridge seismic sections indicates that large amounts of gas were released into seawater from dissociation of gas hydrates during the last thousands of years, and that gas is able to stay in place for long periods due to the slow diffusion along the western flank of southern Hydrate Ridge. On the eastern flank of southern Hydrate Ridge and because of the extensive presence of fractures, permeability is high, contributing to the rapid dispersion of the secondary BSR (Bangs et al., 2005) (Figure 3.7).

3.2. Proxies for gas hydrate detection

Prior to Leg 204, it was already known that methane bubbles were venting at the southern summit of Hydrate Ridge and that massive hydrates were present on the seafloor. However, the rate of hydrate formation and the depth to which massive hydrates were present was still unknown. Seismic reflection data suggested that massive gas hydrates were present up to ~30 mbsf (Tréhu et al., 2002). Multiple geophysical and geochemical indirect proxies were planned and successfully applied during ODP Leg 204 in order to constrain the real extent and concentration of gas hydrates. They also helped to establish the distribution of gas hydrates and the main controlling factors in southern Hydrate Ridge sediments.

3.2.1. Electrical resistivity anomalies measured by logging-while-drilling

During Leg 204, four Anadrill LWD tools, including measurement-while-drilling, were deployed at eight of the nine sites cored and drilled at southern Hydrate Ridge (Sites 1244 to 1251). LWD tools measure *in situ* formation properties and downhole drilling parameters (e.g., weight on bit, torque, etc.) with instruments that are located in the drill collars immediately above the drill bit (Figure 3.8) (e.g. Collett, 2001). Fluid invasion into the borehole wall is reduced because of the short time elapsed between drilling and taking measurements.

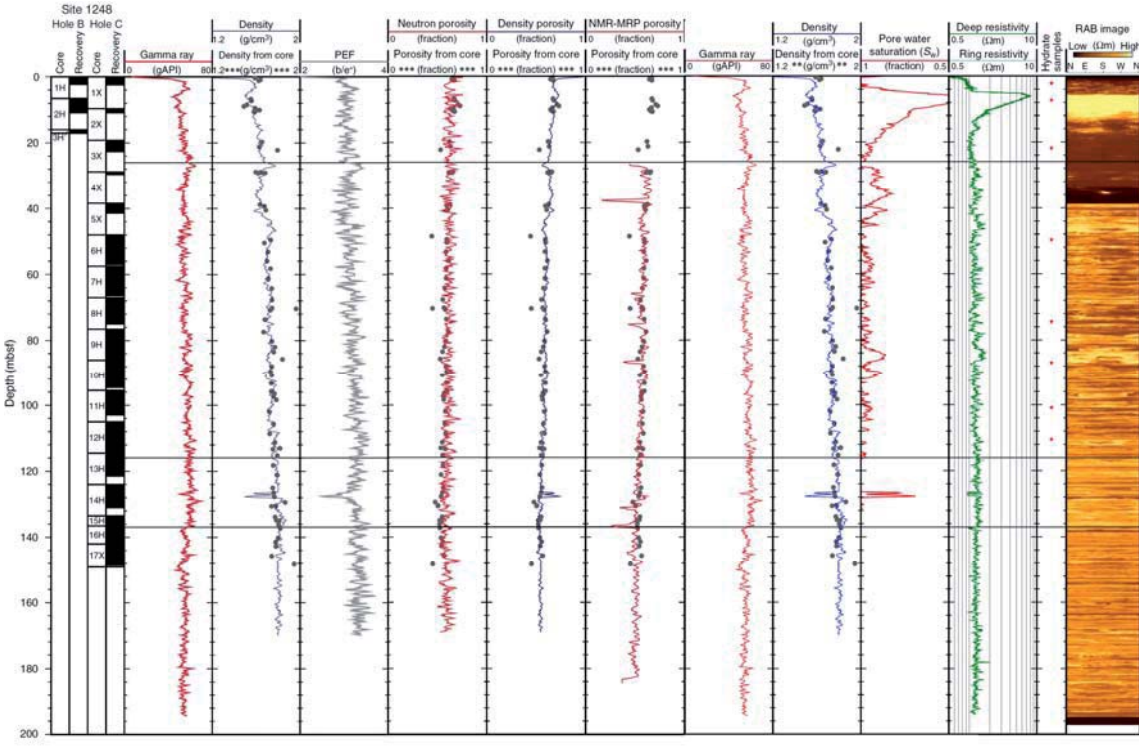

Figure 3.8. Summary of Logging While Drilling (LWD) log data, LWD and core-derived porosities and logging-derived gas hydrate saturation from Hole 1248A obtained during Ocean Drilling Program Leg 204. PEF= Photoelectric effect; TAB = time after bit; RAB = resistivity-at-the-bit; NMR-MRP = Nuclear Magnetic Resonance; gAPI = American Petroleum Institute gamma ray units; mbsf= meter below sea floor (modified from Shipboard Scientific Party, 2003e).

The LWD tools take measurements at evenly spaced time intervals and are synchronized with a system on the drilling rig that monitors time and drilling depth. After drilling, the LWD tools are retrieved and the data are processed in accordance with the synchronization of the uphole and downhole clocks, which allows the transformation of the time-recorded data into depth-measurement data files (Tréhu et al., 2003).

The RAB sensor provides a continuous record of resistivity measurements of the sedimentary formation producing electrical images of the borehole wall with complete coverage with a vertical and horizontal resolution of few centimetres (Figure 3.9). As the electrical resistivity of gas hydrate is higher than that of saturated sediments, RAB was applied during ODP Leg 204 as a proxy for gas and gas hydrate presence. The percentage of gas hydrate in the pore space was estimated by estimating the percentage of pore space filled by water in accordance with Archie's law [5] (Archie, 1942; Collett, 2001). Archie's law relates the *in situ* electrical conductivity of sedimentary rock to its porosity and brine saturation:

[5] $$C_t = C_w \phi^m (S_w)^n$$

where:
C_t = electrical conductivity of the fluid saturated sediment
C_w = electrical conductivity of the brine
ϕ = porosity
m = cementation exponent of the rock (from 1.8 to 2.0)
S_w = brine saturation
n = saturation exponent (usually near 2)

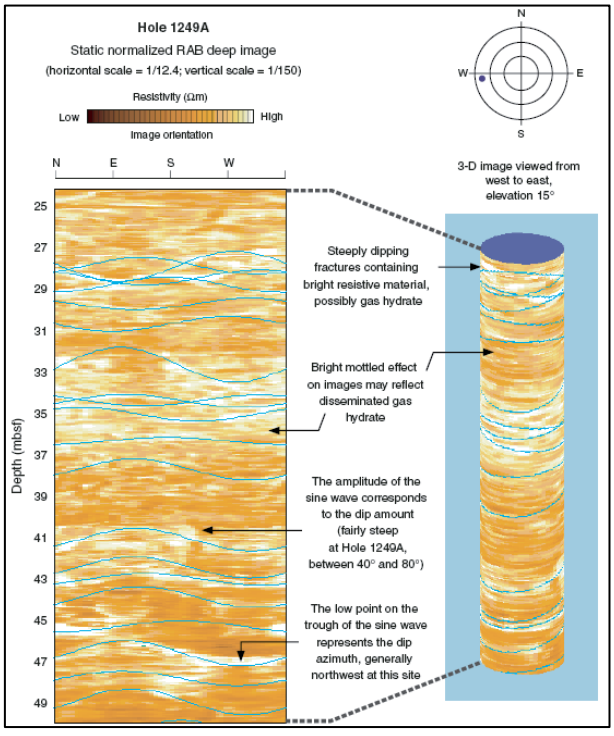

Figure 3.9. Resistivity-at-the-bit (RAB) image showing the possible presence of gas hydrate as bright resistive material occupying low-angle fractures, almost horizontal stratigraphic layers, and disseminated throughout the sedimentary sequence of Hole 1249A; mbsf= meter below sea floor (Tréhu et al., 2003).

In the case of gas hydrate-rich sediments, it is necessary to assume that gas hydrate fills the whole pore space. Given the assumption that all high resistivities are produced by gas hydrates instead of a gas/gas hydrate mixture, an overestimation of the gas hydrate volume is produced by this method (Collett and Ladd, 2000; Tréhu et al., 2004b).

Electrical resistivity anomalies recorded during ODP Leg 204 indicate extremely high resistivities (approximately two orders of magnitude larger than those observed at other legs) from 0 to 40 mbsf at the summit sites of southern Hydrate Ridge (Sites 1248, 1249 and 1250), corroborating the high abundance of gas hydrate in this region previously inferred from the 3D multichannel seismic data.

3.2.2. Chloride concentrations measured in interstitial water

It is well known that the formation and decomposition of gas hydrates lead to changes in the dissolved chloride concentration of marine pore fluids (e.g. Hesse, 2003; Hesse and Harrison, 1981; Ussler and Paull, 2001; Froelich et al., 1995; Kastner et al., 1995; Paull et al., 1996; Torres et al., 2002). Gas hydrates exclude salts from their crystal structure, increasing the salinity of the surrounding water in such a way that the change in the interstitial ion concentration is proportional to the amount of gas hydrate that is formed. Similarly, gas hydrate dissociation due to loss of pressure during core recovery often produces a drop in chloride concentration owing to fresh water release and its dilution effect. Thus, chloride concentration measurements provide robust estimates of hydrate concentration if the background chloride concentration profile can be constrained (Figure 3.10).

Background chloride concentration was well defined during ODP Leg 204, except near the summit because of very rapid hydrate formation (Tréhu et al., 2003). Leg 204 of ODP also demonstrated that it is essential to extend chloride measurements well below the base of the GHSZ in order to estimate possible low chloride concentration diffusion sources at depth. Chloride concentrations were measured on whole-round cores about 10 cm long and systematically sampled at a frequency of two sections per core in the upper 150 m of the sediment section. A lower sampling resolution of one sample per core was applied in the deeper sequences. Measured data indicates chloride background concentrations similar to that in seawater (0.546 mol/kg), except where gas hydrates are found, where numerous low chloride spikes reflect the freshening effect of dissociated hydrates on the interstitial waters composition. A smooth decrease in pore water chloride concentration with depth at the eastern flank Sites 1244 and 1246, as well as in the slope basin Sites 1251 and 1252 is attributed to fresh water released by dehydration reactions deeper in the accretionary complex (Tréhu et al., 2003; MacKay et al., 1994).

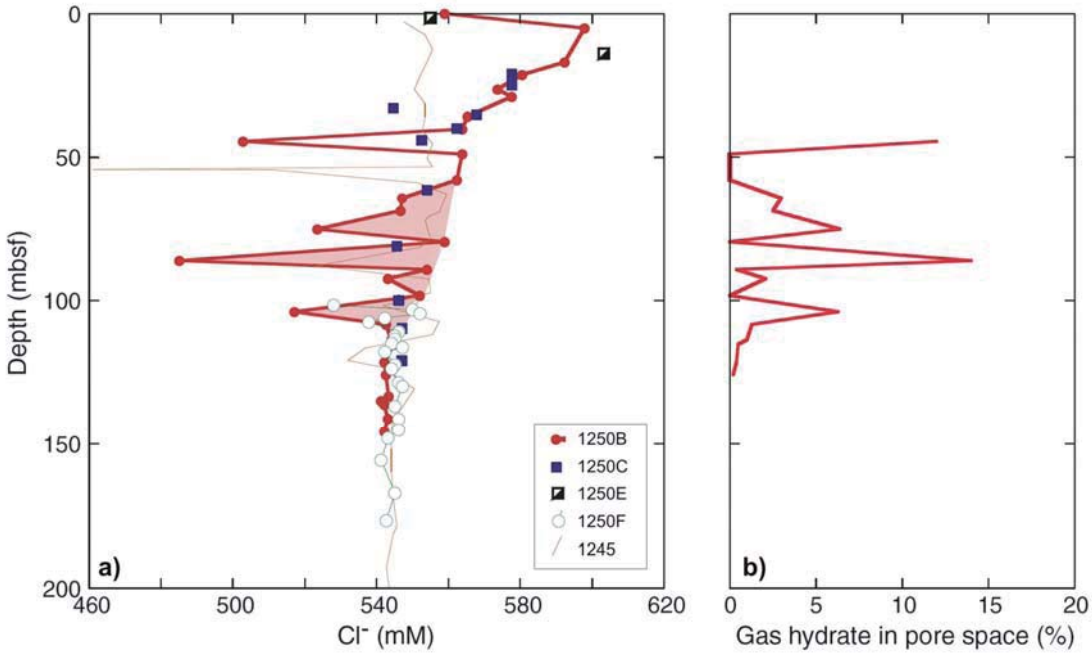

Figure 3.10. Chloride (Cl^-) concentration profiles and gas hydrate estimates based on these chloride data at Ocean Drilling Program Leg 204 Site 1250. **A.** Chloride concentration data from Holes 1250B, 1250C, 1250E**,** and 1250F. For comparison, the chloride profile from Site 1245 is also shown. Note that in the upper 40 mbsf, the chloride concentrations are commonly above seawater values (~560 mM). Below 50 mbsf, the chloride data form a sloping baseline toward slightly fresher values similar to that of Site 1245. There are no anomalies in the chloride concentration below 110 mbsf. **B.** Estimates of the total amount of gas hydrate in sediments at ODP Leg 204 Site 1250; mbsf= meter below sea floor (modified from Tréhu et al., 2003).

One surprising result of Leg 204 was the recovery of pore waters with a chloride concentration that was much higher than seawater near the summit (Milkov et al., 2004) (Figure 3.10). In this region (in the upper 20–40 mbsf at Sites 1249 and 1250), no estimates of gas hydrate content in accordance with the chlorine values were attempted onboard because the baseline of chloride concentration could not be defined. Below 50 mbsf, the establishment of a firm chloride baseline allowed a first-order estimate of gas hydrate amounts that commonly ranged between 0% and 6%, with peaks up to 15% of pore space. Postcruise investigations of the interstitial-brine dataset applying transport-reaction geochemical models and gas hydrate dynamics were presented by Torres et al. (2004). This new approach suggests that methane transported as free gas through the GHSZ is necessary to sustain the formation of the large gas hydrate amount in southern Hydrate Ridge deduced from the chloride enrichment in pore fluids.

3.2.3. Temperature anomalies measured with infrared camera scans

Gas hydrate dissociation is an endothermic reaction with the result that intervals in sediment cores where gas hydrate is dissociating, or has recently dissociated e.g. due to pressure decrease after sediment core recovery are relatively cold. Other processes that produce thermal anomalies in marine sediment cores on a short length scale (less than few meters) include: adiabatic gas

expansion and gas exsolution from pore water (Tréhu et al., 2003). Systematic infrared thermal imaging of the surface of the 10 meter long whole core liner lying on the catwalk was systematically implemented during ODP Leg 204, although the technique was first successfully applied for gas hydrate and void identification during ODP Leg 201 (Ford et al., 2003). The primary benefits of using an infrared camera rather than a hand down sensor include its speedier and simpler use, as well as its higher spatial resolution. Owing to these characteristics, it was possible to identify the thermal anomalies, estimate the hydrate volume in processed images and determine the shape of gas hydrates prior to the core splitting. During Leg 204, it was also demonstrated that most of the negative temperature anomalies developed in response to gas hydrate dissociation after the core arrived on deck (Figure 3.11). Processing of the infrared images produced temperature profiles averaged across the central portion of each drilled core.

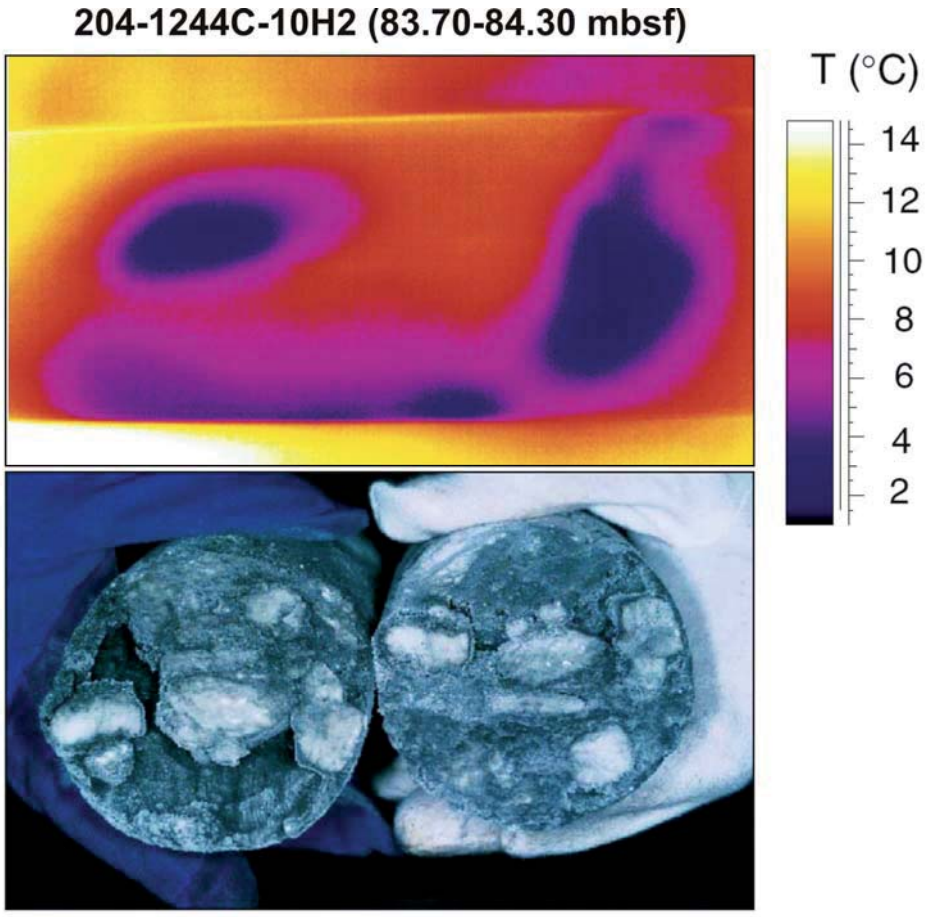

Figure 3.11. Comparison of infrared images of core liners with photograph of the corresponding hydrate occurrence after freezing in liquid nitrogen and extraction of core from the core liner; mbsf= meter below sea floor (modified from Tréhu et al., 2003).

To calibrate the IR data, pore waters at a 2 cm interval frequency were sampled for chloride analyses in selected low temperature sediment intervals. After analyses, a slight difference in depth between the temperature and the chloride anomaly was detected. This difference was

ascribed to core compression caused by the closure of gas voids after scanning the core and before sampling for chloride analyses.

Most of the thermal anomalies described during ODP Leg 204 at southern Hydrate Ridge, are only few centimetres long and their distribution is highly variable and heterogeneous (Tréhu et al., 2003). After these data, the empirical relationship between the hydrate content and the amplitude and depth range of thermal anomalies was calculated and will be presented below (Tréhu et al., 2004b; Weinberger et al., 2005).

3.2.4. Gas volumes measured from pressure core samples

During conventional coring and drilling, substantial volumes of gas escape from the sediments as they are brought to the surface. Pressure core samplers, which recover sediments in an autoclave at *in situ* pressure, provide the only means of retaining all gas that is present at depth. With a successful deployment of these tools, controlled release of pressure enables us to measure the volume of gas stored in an interval of sediment as a direct measurement of *in situ* gas concentration (Figure 3.12). The amount of free gas and gas hydrate can be estimated by comparing the *in situ* gas concentration to the predicted gas solubility. Some uncertainties of this approximation are caused by the inaccuracy of total core recovery, porosity or gas solubility data (Milkov et al., 2003; Schültheiss et al., 2003).

Figure 3.12. Pressure Core Sampler image showing the controlled release of gas in order to measure and analyse its *in situ* concentration.

Two pressure coring systems were used during ODP Leg 204, but restricted to a few times at each site because of logistical limitations. The ODP pressure core sampler (OPCS) permits recovery of a 1-m-long core under *in situ* pressure and provides a measurement of concentration averaged >1 m core length. The new HYACINTH pressure corer also recovers 1 meter length, but provides additional information about centimetre-scale hydrate and free gas distribution in sediments owing to the combination with a density sensor (Tréhu et al., 2003).

3.2.5. Sedimentary disturbance fabrics: mousse-like and soupy

Because of the amount of water contained in clathrate structures, the dissociation of gas hydrate molecules as a result of changes in pressure and/or temperature conditions (natural or during core retrieval) disturbs the sedimentary features of the host sediments. 'Soupy' and 'mousse-like' are the two main fabrics interpreted to result from the process of gas hydrate dissociation (e.g. Kastner et al., 1995; Paull and Ussler III, 2001; Piñero et al., 2007) (Figure 3.13). During ODP Leg 146, the recognition of sediments from Hydrate Ridge showing soupy and mousse-like disturbance fabrics related to gas hydrate dissociation (Westbrook et al., 1994), and the subsequent confirmation of this relationship in ODP Leg 204 during the visual core description soon after sediment retrieval (Tréhu et al., 2003) led to the use of soupy and mousse-like fabrics as a proxy for the presence of gas hydrate.

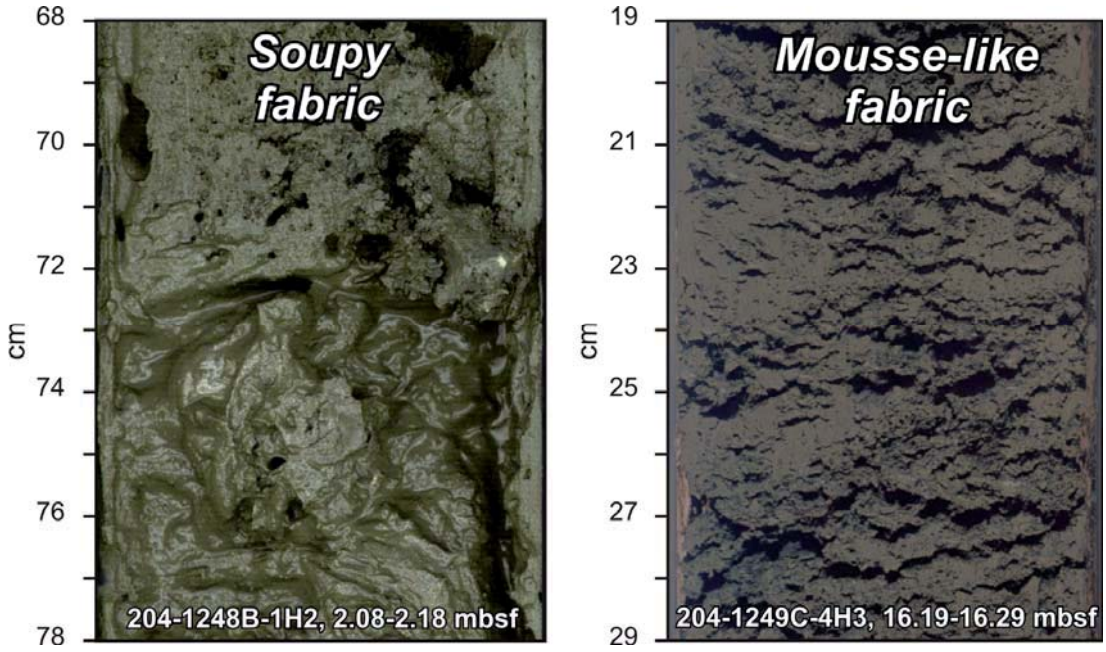

Figure 3.13. Image of sedimentary disturbance fabrics after gas hydrate dissociation: soupy and mousse-like, from southern Hydrate Ridge Ocean Drilling Program Leg 204; mbsf= meter below sea floor (modified from Tréhu et al., 2003).

Soupy sediments are always watery, homogeneous and fluidized. Because of the high water content, they have been related to the dissociation of nodular to massive gas hydrates (Tréhu et

al., 2003). Soupy sediments retain no original sedimentary structures and are able to flow from their original position during core recovery, resulting in void spaces within the cores.

Sediments with mousse-like fabrics can be divided into two types, depending on water content: (1) wet, watery mousse-like sediment that is soft and deforms plastically under slight pressure from a finger; and (2) dry mousse-like sediment that is stiffer and tends to form brittle flakes that break off under the pressure of a finger. These drier, stiffer sediments often appear foliated when split by the core cutter wire. Both types of mousse-like texture contain numerous gas vesicles and obscure primary sedimentary structures. They are thought to result from the dissociation of disseminated gas hydrates in fine grained sediments (Tréhu et al., 2003; Piñero et al., 2007).

3.3. Gas hydrate fabrics in southern Hydrate Ridge sediments

During ODP Leg 204 gas hydrate fabrics were described as: disseminated, veinlets, nodular, and massive (Figure 3.14). After the cruise and based in the shape and orientation of gas hydrates within the sediments, gas hydrate fabrics were re-classified using computer tomographic images (Figure 3.15). Six types of gas hydrate fabrics were defined as: disseminated, veinlet, vein, layer, nodule and massive and are defined as follows (Abegg et al., 2006; 2007):

Figure 3.14. Gas hydrate fabrics identified onboard ODP Leg 204 at southern Hydrate Ridge, corresponding to the intervals: disseminated (ODP Leg 204-1249C-2H1, 108-140); veinlet (ODP Leg 204-1244C-8H1, 47-52); nodular (ODP Leg 204-1244C-10H2, 70-103); and massive (ODP Leg 204-1249C-1H-cc) (modified from Tréhu et al., 2003).

- Disseminated hydrate is formed by small pieces of gas hydrate with grain sizes up to 3 mm, which are disseminated in the sediment in such a way that grains are not connected. Based on their small mass, these grains dissociate very rapidly after recovery.
- Veinlets are thin tabular hydrates, 1 mm thick, with different orientations. This type can also be classified as small or thin form of veins.
- Veins are tabular-shaped hydrates, but thicker than 1 mm and up to 10 cm. Veins, as well as veinlets, are often nonparallel to sediment bedding transecting through it. The dip angles vary from nearly horizontal to vertical.
- Layers of hydrate are considered to be the veins that lie conformably to sediment bedding. They are often intercalated between fine-grained sediments.
- Nodule hydrates are spherical to oblate, typically ranging from one to five cm in diameter.
- Massive gas hydrates are shapes thicker than 10 cm that have less than 25% of sedimentary material intercalated.

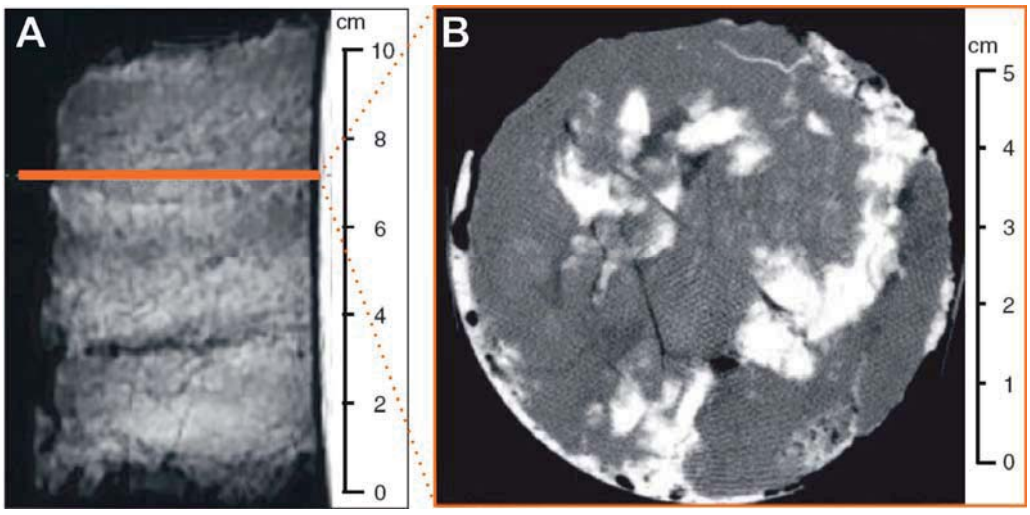

Figure 3.15. Computer tomographic (CT) images of sample ODP Leg 204-1249C-1H1, 0–25 cm, showing gas hydrates (white) and sediments (dark grey). **A.** Two-dimensional vertical CT image showing the extent of gas hydrates and intercalated sediment. **B.** Two-dimensional horizontal image corresponding to a whole round cut of the ~7 cm depth section of image A. Massive gas hydrate fabric predominates with sediment intercalated (modified from Abegg et al., 2006).

3.4. Gas hydrate distribution in southern Hydrate Ridge

Gas hydrates in southern Hydrate Ridge show heterogeneous distribution based on the different proxies used during ODP Leg 204 described above (e.g. chlorinity and RAB data, infrared thermal imagery, disturbance fabrics) (Tréhu et al., 2004b). The various proxies for the presence of gas hydrate measure different length scales and have different sensitivity and resolution to estimate gas hydrate concentration. All these proxies are observed at similar depths

at a given site and on the seafloor at the summit sites (~30–50 mbsf at the sites away from the summit) leading to similar conclusions about the distribution and concentration of gas hydrates beneath Hydrate Ridge. These geochemical and geophysical parameters, however, do not provide a direct measurement of gas hydrate concentration, although it can be estimated through physical models (i.e. Archie's Law for the resistivity data) (Collett and Ladd, 2000).

The gas hydrate content through most of the GHSZ corresponds to less than 2% of the pore space, except near the summit of the ridge (Sites 1249 and 1250), where massive gas hydrates appear in the upper 20-40 mbsf and occupy up to 20%. On both flanks of southern Hydrate Ridge disseminated gas hydrates appear in patchy zones that are structurally and stratigraphically controlled (Tréhu et al., 2004b) (Figure 3.16).

3.4.1. Gas hydrate distribution at the summit of southern Hydrate Ridge

Beneath the summit, all the studied proxies are indicative of very high concentrations of gas hydrates in the upper 20-40 m. Cores obtained during ODP Leg 204 support this idea with recovered hydrate samples as chunks, lenses, nodules and thin plates. The gas hydrate content was estimated at 30-40% in the upper 20-40 m at Site 1249 (Figure 3.16). Below this depth, the presence of gas hydrates was estimated at ~5%, a value resembling those on both flanks of southern Hydrate Ridge. At Sites 1248 and 1250, also located at the summit of the Ridge, similar gas hydrate concentrations were calculated (Tréhu et al., 2004b). The extension of the area of very high gas hydrate concentration was estimated at 300 by 500 m on the basis of the seismic reflection data, which implies an amount of methane stored of 1.5 to 2 $x10^8$ m^3 at standard P/T conditions (Tréhu et al., 2004b).

3.4.2. Gas hydrate distribution on the flanks of southern Hydrate Ridge

On the eastern and western flanks of southern Hydrate Ridge, the mean gas hydrate content of the GHSZ is >5% and 1.7 ±0.2%, respectively (Figure 3.16). At Site 1246, an apparently high concentration of gas hydrate was found in association with seismic Horizon B, which is composed of two coarse-grained layers. At Site 1244 the presence of gas hydrates is related to the presence of pervasive small-offset faults that permit the upward fluid flow migration and gas hydrate distribution in patches along faults and favourable lithologies (Tréhu et al., 2004b).

3.4.3. Gas hydrate distribution in the slope basin adjacent to southern Hydrate Ridge

In the slope basin east of southern Hydrate Ridge, the distribution and extension of gas hydrates is more limited than at the summit and flanks of the ridge (Figure 3.16). The average hydrate content was estimated at less than 1%. Only an area of high gas hydrate concentration in

a patchy fabric was identified immediately above the BSR at Site 1251, which was estimated at ~20% (Tréhu et al., 2004b).

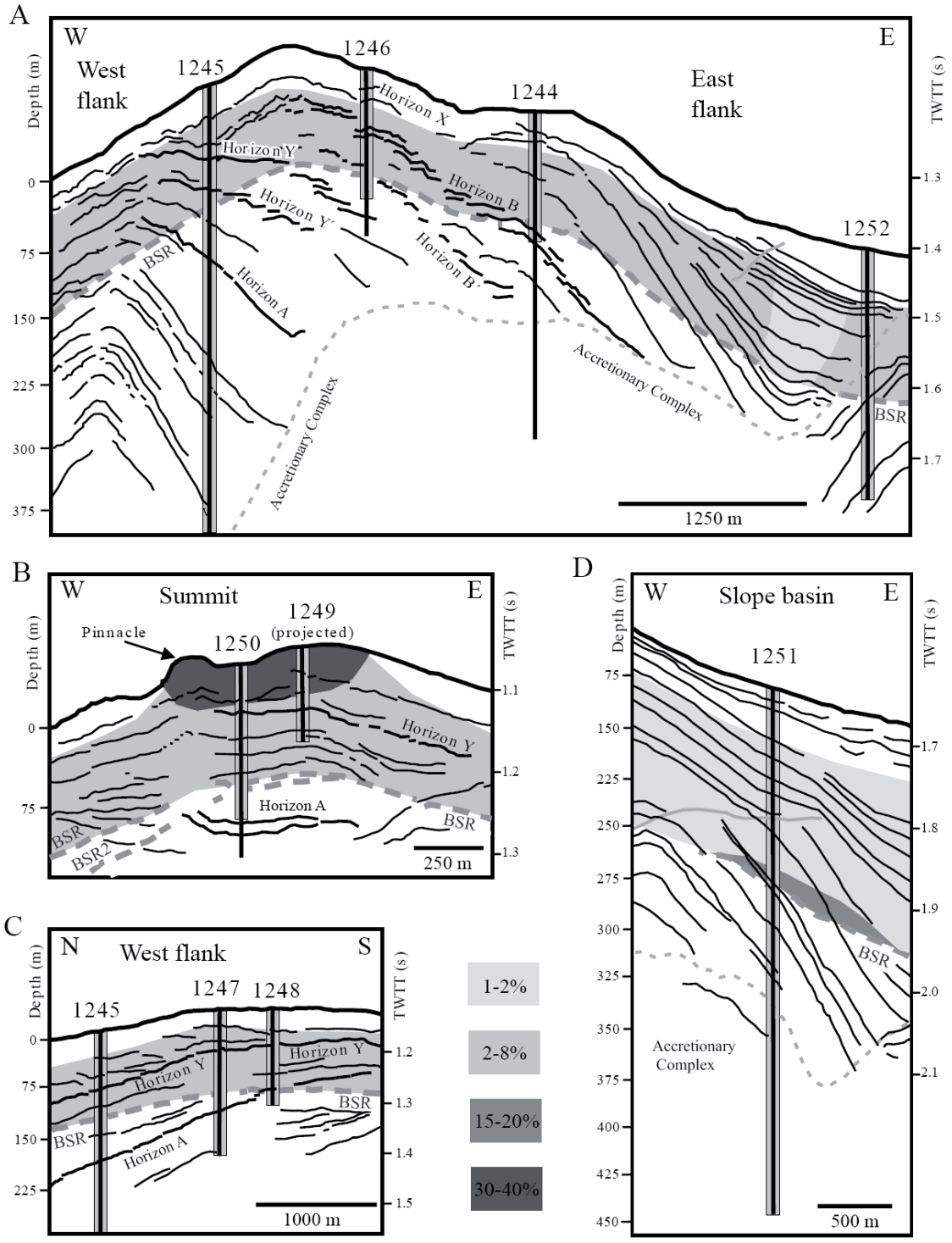

Figure 3.16. Line-drawings of 3D multichannel seismic profiles (Figure 3.3) across different positions of southern Hydrate Ridge. **A)** W-E section across the northern part of southern Hydrate Ridge. **B)** W-E section across the summit of southern Hydrate Ridge. **C)** N-S section along the west flank of southern Hydrate Ridge. **D)** W-E section across the lowermost part of the slope basin east of Hydrate Ridge. The bottom simulating reflector (BSR), main seismic horizons, and Ocean Drilling Program Leg 204 drill sites are indicated. Grey shading indicates zones of different average gas hydrate concentrations (as % of pore space) estimated by Tréhu et al. (2004b). The data presented in this thesis correspond to the stratigraphic intervals marked by the grey shaded box at each site.

The heterogeneous distribution of gas hydrate has been attributed to two distinct regimes of delivery of gas to the GHSZ: the "reaction dominated regime" and the "transport dominated regime" (Tréhu et al., 2003). The "reaction dominated regime" is pervasive throughout southern Hydrate Ridge where methane is produced by *in situ* microbial methanogenesis. Gas hydrate content in sediments is relatively low (2-8% of the pore space) and no gas hydrate is present in the upper 30 mbsf. Superimposed on the reaction regime there is a "transport dominated regime" in which methane is transported as free gas to the structural summit, where active venting is found, resulting in a shallow gas hydrate deposit in which gas hydrate comprises ~25% of the total sediment volume to a depth of 25 mbsf (Tréhu et al., 2003). The isotopic signature of methane suggests that migrated gas includes previously buried microbial methane (~65%) as well as thermogenic hydrocarbons (10-15%). The migration of gas from deep in the accretionary complex material and into the GHSZ takes place through principal stratigraphic horizons described in the multichannel seismic data (Tréhu et al., 2003) (Figure 3.17).

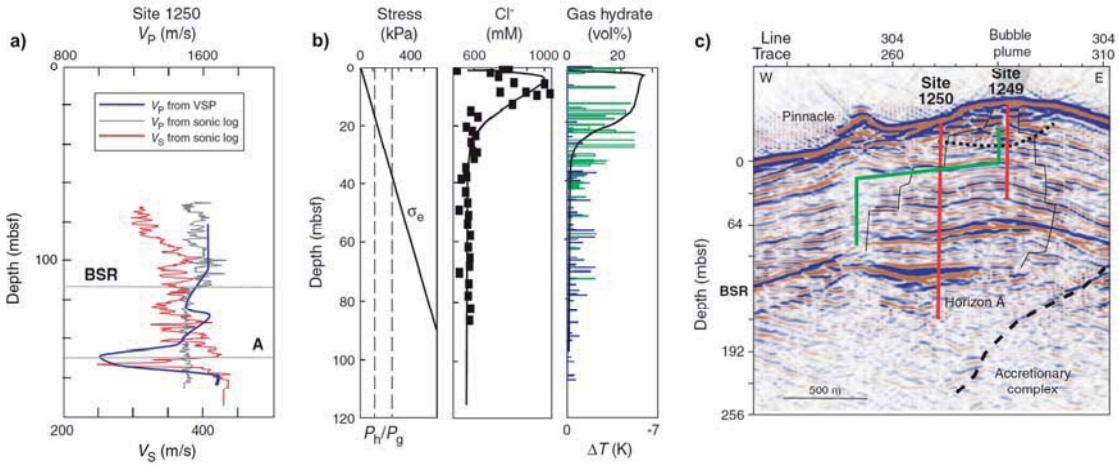

Figure 3.17. Physical and geochemical data corresponding to Horizon A. **A.** *P*- and *S*-wave velocities from sonic logs and a vertical seismic profile (VSP). Horizon A appears as a pronounced low velocity zone in V_S and V_P (VSP only). The absence of a V_P anomaly in the sonic log data may result from intrusion of drilling fluid near the borehole. The V_S anomaly is unexpected, since V_S is not sensitive to whether the pore space is occupied by water or gas, and suggests that overpressures are large enough to affect the sediment shear strength. **B.** Increase in effective stress (σ_e) with depth, as calculated from sediment bulk density at Site 1249 compared to the internal pressures of gas hydrate crystallite (P_h) and gas bubbles (P_g) calculated following Clennell et al. (1999) assuming an average pore radius of 0.5 mm, compared to chlorinity enhancement and gas hydrate saturation predicted by a one-dimensional transport reaction model with enhanced gas dissolution and hydrate precipitation rates in near-surface sediments. Model parameters are described in Torres et al., 2004b. Chlorinity measured at Site 1249 (squares) and IR anomalies at Sites 1249 (green bars) and 1250 (blue bars) are also shown. **C.** Seismic cross section at the summit showing the steady-state gas migration path suggested by Liu and Flemings (2006) and Milkov and Xu (2005) as a green line, compared to two possible paths (from among a wide range of possible paths) in the distributed, temporally variable scenario hypothesized by Tréhu et al. (2004b), Torres et al. (2004), and Weinberger and Brown (2006). mbsf= meter below sea floor (modified from Tréhu et al., 2006).

In this sense, Horizon A has been suggested as the major fluid conduit for gas to the venting area detected on the seafloor at the summit of southern Hydrate Ridge (Tréhu et al., 2004a). This ash-rich layer taps a large reservoir of hydrocarbon-rich fluids derived from the older

accreted and underplated sediments and also draws gas from the surrounding material because of its coarse grain size. Formation of gas hydrate filling the porosity of Horizon A at the GHSZ sealed the conduit, creating a trap. After the increase in gas pressure, fractures were dilated in the summit area, providing a new structural framework for gas migration (Tréhu et al., 2004a) (Figure 3.17).

During ODP Leg 204, numerous gas hydrate samples were recovered and preserved in liquid nitrogen as whole rounds for detailed shored-based studies. X-Ray diffraction analyses of these samples show that only Structure I hydrate is present (Kim et al., 2005; Bohrmann et al., 2007). A complete study by Computerized Tomographic imaging allowed the description of gas hydrates distribution in layers with different dips (Abegg et al., 2006; 2007). Shallow hydrate layers parallel or subparallel to bedding are ascribed to gas bubble injections parallel to the layering of sedimentary deposits. Deeper than 40 mbsf, hydrate layers are characterized by steeper dip angles of 30º-90º, interpreted as open fractures. Thus, free gas migrates through the open fractures and joints, which close as gas hydrate precipitates, leading to the formation of new cracks.

All the estimates for gas hydrate concentration and distribution in southern Hydrate Ridge, discussed above, resemble the estimates made for sediments from the Blake Ridge (2-7%) after ODP Leg 146 (Dickens et al., 1997b; Holbrook et al., 1996). Only the concentrations for the area near the seafloor at the summit of southern Hydrate Ridge (Sites 1248, 1249 and 1250), are significantly higher (20-40%). Previous estimates of the northern Cascadia margin offshore Vancouver (Hyndmann et al., 2001) based only on geophysical and geochemical calculations are much higher (20-35%). The new concentrations presented after ODP Leg 204 suggest that this data would be re-evaluated.

3.5. Integrated Ocean Drilling Program Leg 311

During the Integrated Ocean Drilling Program (IODP) Leg 311, four sites (U1325, U1326, U1327, and U1329) were drilled across the northern Cascadia margin with the aim of study the occurrences and formation of gas hydrate in accretionary complexes (Figure 3.18). In addition to the transect sites, a fifth site (U1328) was established at a cold vent with active fluid and gas flow (Expedition 311 Scientists, 2006). The working area lies across the continental slope off the coast of central Vancouver Island, British Columbia, Canada, with water depths ranging from 2,600 m in the trench to 500 m on the upper slope, where it is well above the minimum depth for gas hydrate stability (Scherwath et al., 2006). The sedimentological and tectonic data acquired during the cruise yielded valuable insights into the northern Cascadia margin (e.g.

Davis and Hyndman, 1989; Carson et al., 1995; Spence et al., 2000; Hyndman et al., 2001; Expedition 311 Scientists, 2006; Riedel et al., 2006a, 2006b, 2006c). Indirect evidence of the presence of gas hydrate included increased electrical resistivities and P-wave velocities on downhole logs, low-salinity anomalies in the interstitial water, numerous infrared cold spots, and decreases in void gas C_1/C_2 ratios, as well as gas hydrate–related sedimentological mousse-like/soupy fabrics in recovered cores. The combined observations show that the occurrence of gas hydrates at these sites mainly appear to be driven by local variation of methane solubility as well as proximity of suitable host sediments: coarser-grained turbidite sands (Expedition 311 Scientists, 2006; Torres et al., 2008).

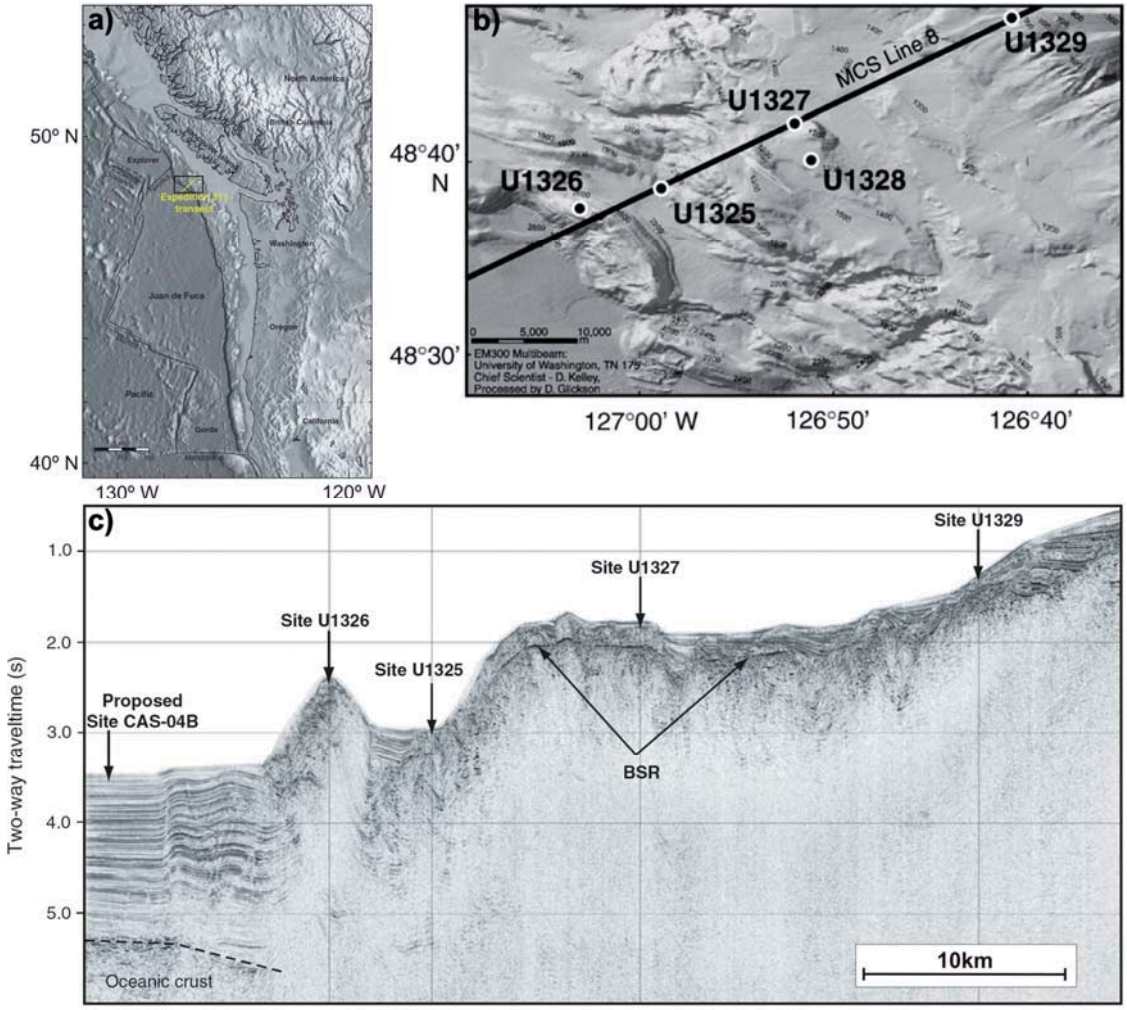

Figure 3.18. A. Map of the study area targeted during Integrated Ocean Drilling Program (IODP) Expedition 311, showing the general location of the drilling transect across the northern Cascadia margin (modified from Riedel et al., 2006b). **B.** Multibeam bathymetry map along the transect in the accretionary prism, showing the location of the drilled sites and of multichannel seismic (MCS) Line 8. The cold vent Site U1328 is ~2 nm southeast of the transect (modified from Torres et al., 2008). **C.** Seismic cross section Line 8 (89-08) across the northern Cascadia margin showing the location of the four drilled sites during Expedition 311 (Sites U1326, U1325, U1327, and U1328) of the IODP as well as proposed basin reference Site CAS-04B. The cold vent Site U1328 is ~2 nmi off this line toward the southeast. The bottom simulating reflector (BSR) is also depicted (modified from Riedel et al., 2006b).

4. Data and methodology

In order to establish the main sedimentological and geochemical properties of the gas hydrate-rich sediments from southern Hydrate Ridge, sediment samples recovered during ODP Leg 204 were analysed for this thesis. Additional pore water geochemical data as well as geophysical data obtained during Leg 204 were also used in order to complete the study.

Grain-size and textural analyses, bulk and clay mineralogy semi-quantifications, geochemical analyses including major and trace elements, and magnetic susceptibility analyses were carried out on 561 samples from nine drilled wells at the summit (Sites 1248, 1249 and 1250), eastern flank (Sites 1244 and 1246), western flank (Sites 1245 and 1247), and in the slope basin (Sites 1251 and 1252) of southern Hydrate Ridge. They are based on regular sampling of two samples per core, except when crossing specific layers (e.g. Horizons A, B, B' and the BSR), which were sampled with a closer spacing of one sample per section (Figure 4.1). From the same stratigraphic intervals, 10 cc tubes for sedimentological and geochemical analyses and 7 cc cubes for rock magnetic measurements were sampled so that the whole dataset is directly comparable (Gràcia et al., 2006; Larrasoaña et al., 2006). In addition, twenty samples stored in liquid nitrogen from four stratigraphic intervals from the western flank and summit of southern Hydrate Ridge were also sampled at the University of Bremen at a resolution of 2 cm for a complete sedimentological, geochemical and magnetic analysis (Bohrmann et al., 2007). These intervals were sampled based on computer tomographic images available at the University of Bremen that suggested gas hydrate-rich contents.

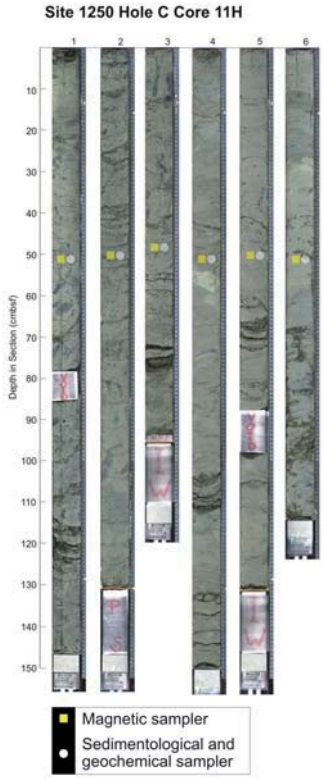

Figure 4.1. Image of Ocean Drilling Program Leg 204 Hole 1250C Core 11H recovered sediment showing sampling depths at each section (1 to 6). Each section was sampled in order to study in more detail the debris flow facies identified in the multi-channel seismic data at this interval; cmbsf= centimeter below sea floor.

4.1. Textural analyses

4.1.1. Grain-size analyses

Grain-size analyses of 385 samples from Sites 1244 to 1250 were performed at the sedimentology laboratory of the *Institut de Ciències del Mar* (CSIC), using a SediGraph 5100 for the < 50 μm diameter particles and a settling tube for the larger ones (Piñero et al., 2004, 2005; Gràcia et al., 2006; Micromeritics, 1978) (Figure 4.2). After a one-week drying procedure at 80ºC and removing the organic matter by a H_2O_2 attack, all samples were wet sieved at 50 μm with a solution of $(NaPO_3)_n$ at 20%. The same grain-size procedure was applied to the twenty hydrate-rich samples from Sites 1245 and 1249, but performing the wet sieving at 63 μm. SediGraph measures the attenuation of X-ray passing through the sediment particles suspended in a solution placed in a transparent cell, determining a vertical profile of intensity that is converted into density and weight on basis of Stoke's Law (McManus, 1988; Bianchi et al., 1999). The coarsest fraction was dry-sieved using a column of 2, 4 and 6 mm mesh sizes. The composition of the coarse silt and sand fraction (50 μm to 2 mm) was determined in a binocular microscope and subsequently, measured in the settling tube. The settling tube measures pressure changes produced while particles fall in water, transforming this information into sediment weight for each grain-size population (Gibbs, 1974). The grain-size data for each sample (including results from the SediGraph and settling tube) were integrated and plotted in a unique cumulative curve using the specific software "Integració" developed in the *Grup de Geologia Marina* of the *Institut de Ciències del Mar* (CSIC).

Figure 4.2. Sedigraph and settling tube of the Institut de Ciències del Mar (CSIC) in Barcelona.

In addition, a subset of 176 samples from Sites 1251 and 1252 located on the slope basin adjacent to southern Hydrate Ridge were analysed for grain size using a Coulter LS 100 at the sedimentology laboratory of the *Departament d'Estratigrafia, Paleontogia i Geociències*

Marines of the *Universitat de Barcelona* (Figure 4.3). Coulter analyses particle grain size by laser diffraction, measuring the scattered light at different angles (Stein, 1985). Textural statistical parameters were calculated using the Coulter processing software. One of the main disadvantages of the Coulter method is its measure-dependence of the geometry of particles.

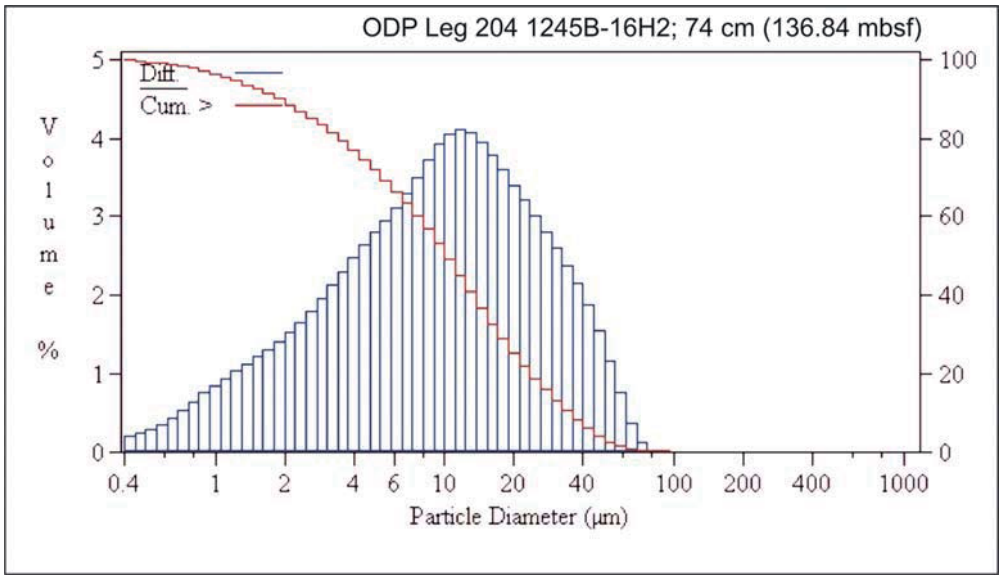

Figure 4.3. Histogram and cumulative curve of sample ODP Leg 204 1251B-16H2; 74cm (136.84 mbsf) obtained by Coulter LS 100; mbsf= meter below sea floor.

The SediGraph / settling tube and Coulter methods are based on different physical laws and, for this reason they give different and not always directly comparable grain-size results (e.g. Stein, 1985; Moreno, 2002; Goosens, 2008; Bianchi et al., 1999). Owing to the discrepancy of results obtained between these two techniques, grain-size data from the slope basin (Sites 1251 and 1252) was only considered to describe general trends, but not as absolute values when comparing to grain-size results from the rest of the studied sites of southern Hydrate Ridge (Sites 1244-1250). To calculate the textural parameters of the sedimentary facies, only the SediGraph / settling tube results were considered.

4.1.2. Statistical textural parameters

Statistical textural parameters (mean, mode, standard deviation (SD), kurtosis and skewness) were calculated using the moment method on sample populations containing one half phi-interval classes in all fractions (Friedman and Sanders, 1978) in all the sediment samples analysed by Sedigraph / settling tube technique. A specific software developed by the *Grup de Geologia Marina* of the *Institut de Ciències del Mar* (CSIC) was used. Statistical textural parameters give information about the energy of the sedimentary regime operating in the area in the time of deposition. Thus, statistical parameters are related to the maximum and averaged energy transporting sediment particles (e.g. mean and mode), and to the oscillations of this

energy regime (e.g. SD). The following ranges of SD were adopted for the classification of sediment into sorting classes (Friedman and Sanders, 1978; Ercilla et al., 1994):

- moderately well sorted sediments 0.50ϕ to 0.80ϕ
- moderately sorted sediments 0.80ϕ to 1.40ϕ
- poorly sorted sediments 1.40ϕ to 2.00ϕ
- very poorly sorted sediments 2.00ϕ to 2.60ϕ

4.1.3. Coarse grain characterization

In order to study the morphology and composition of the coarser grain fraction (> 50 μm) of each sediment sample, a Leica optical microscope (x100) of the *Institut de Ciències del Mar* (CSIC) was used. With the specific software "Compta98" at least 300 grains of each sample were counted and statistical analyses of the grain populations were calculated. The identified components include: biogenic components (as benthic foraminifera, pelagic foraminifera, radiolarians and sponge thorns), light minerals (including quartz, feldspars and micas), heavy minerals, rock fragments and diagenetic minerals (as pyrite, greigite and carbonates). In order to estimate the flux competency, the whole and broken shells of the biogenic components were also quantified.

4.1.4. Carbonate content

Carbonate content was determined by the leaching acid method using a Bernard calcimeter (Figure 4.4) (Milliman, 1974) in the *Institut de Ciències del Mar* (CSIC) on 0.25 g of ground sediment. Its quantification is expressed as % of equivalent $CaCO_3$ with an approximate error of 0.8%.

Figure 4.4. Bernard calcimeter at the *Institut de Ciències del Mar* (CSIC) in Barcelona.

4.2. Mineralogy

4.2.1. X-Ray Diffraction

Bulk and clay mineral compositions were obtained by X-ray diffraction (XRD) in order to study the provenance of the sediments as well as the main processes affecting sediment transport in the area. For bulk mineralogy, samples were air dried, ground in an agate mortar and packed in aluminium sample holders. For clay mineral analyses, the carbonate fraction was removed using acetic acid and the clays were deflocculated by successive washing with demineralised water. The < 2 μm fraction was separated by centrifugation at 900 rpm for 1.3 min, and was smeared onto glass slides. Separation of the clay fraction and preparation of the samples for XRD were performed following the international recommendations compiled by Kisch (1991) (Figure 4.5).

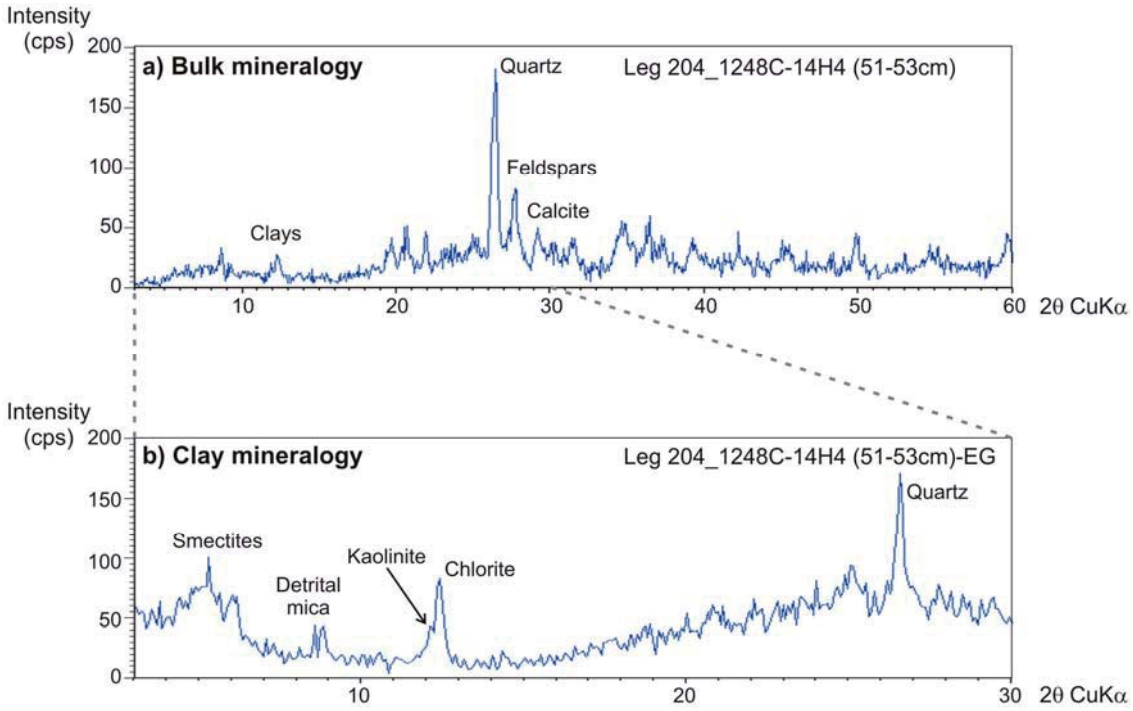

Figure 4.5. X-Ray diffractograms of sample ODP Leg 204 1248C-14H4, 52cm; 127.76 meter below sea floor. **A.** X-Ray diffractogram corresponding to bulk mineralogy (diffraction angle range from 3 to 60º). Main mineral peaks (quartz, feldspars, clays and calcite) are labelled. **B.** Diffractogram of the same sample after a treatment with ethylene-glycol (EG), corresponding to the clay mineralogy range (diffraction angle range from 3 to 30º). The main clay minerals peaks (detrital mica, chlorite, smectites and kaolinite) are labelled. cps= counts per second; 2θ= diffraction angle.

X-ray diffractograms were obtained using a Philips PW 1710 diffractometer with Cu-Kα radiation and automatic slit at the *Instituto Andaluz de Ciencias de la Tierra* (CSIC / *Universidad de Granada*). Scans were run at 2º–64º 2θ for bulk-sample diffractograms and untreated clay preparations, and at 2º–30º 2θ for glycolated clay-fraction samples. Diffractogram interpretations and semiquantitative analyses were performed considering the

integrated peak area using the specific software "X-Powder" (Martin-Ramos, 2004) (Figure 4.5). The clay mineral proportion was estimated from the glycolated diffractograms. The 10 Å peak was used for detrital mica and the 17 Å peak for smectites, the 7 Å peak for the total amount of chlorite+kaolinite, using the peak ratios at 3.54 Å and 3.58 Å, respectively, to differentiate these minerals. The estimated semiquantitative analysis error for absolute values is ± 5%. The estimated semiquantitative analysis error for bulk mineralogy absolute values is < 5% and for clay mineral proportions error is < 10%. Note that the results of semiquantitative analyses presented here will be discussed as changes or gradients in mineral abundances, rather than absolute values. Calcite content data obtained by XRD usually agree with those from carbonates content obtained by the calcimeter method. Nevertheless, some discrepancies are found because only calcite is quantified in the XRD diffractograms, while carbonate content may include some other carbonate phases.

4.2.2. Scanning Electron Microscopy

Scanning electron microscopy (SEM) analyses were conducted on selected samples with a LEO (Carl Zeiss) mod GEMINI-1530 in the *Centro de Instrumentación Científica* of the *Universidad de Granada*. An energy dispersive X-ray analysis (EDAX) was used in order to check the mineralogical composition of selected mineral grains (e.g. sulphur minerals, barite and clays) (Figure 4.6).

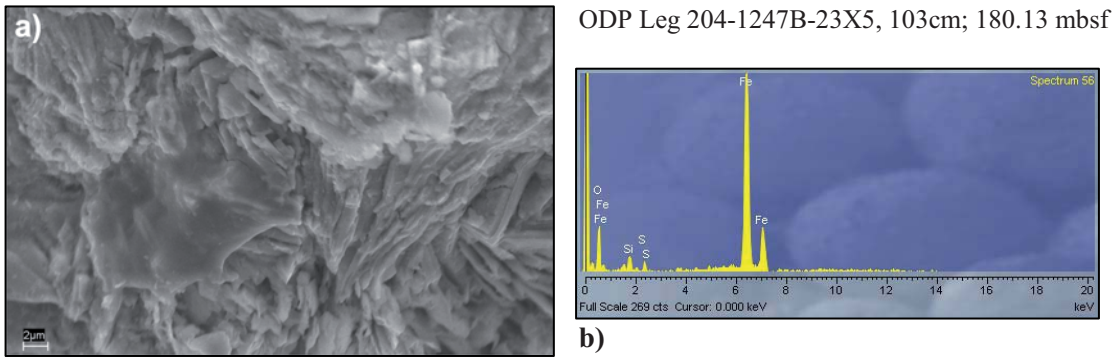

Figure 4.6. A. Scanning electron microscopy image and **B.** energy dispersive X-ray analysis of a coarse grain on sample ODP Leg 204-1247B-23X5, 103cm. mbsf= meter below sea floor.

4.3. Physical properties

4.3.1. Magnetic Susceptibility

Magnetic susceptibility was measured at the *Laboratori de Paleomagnetisme* of the *Institut de Ciències de la Terra "Jaume Almera"* (CSIC / UB) (Larrasoaña et al., 2006). The low field

magnetic susceptibility data was acquired on single samples with a KLY-2 susceptibility bridge using a field of 0.1 mT at a frequency of 470 Hz and was normalized by the dry weight of each sample. Magnetic susceptibility is a measure of the ease with which particular sediments are magnetized when subjected to a magnetic field. The ease of magnetization is ultimately related to the concentration and composition (size, shape and mineralogy) of magnetizable material contained within the sample. Magnetizable minerals include the ferromagnetic minerals (strongly magnetizable) and any of the paramagnetic (moderately magnetizable) minerals and other substances. The former include magnetite, hematite, iron titanium oxides, pyrrhotite, maghemite, greigite and goethite, minerals capable of acquiring remnant magnetization and therefore useful for paleomagnetic studies. The latter include a broad array of substances all of which contain Fe^{2+}, Fe^{3+}, or Mn^{2+} ions. These paramagnetic minerals may include clay minerals (chlorite, smectite and glauconite), iron and manganese carbonates (siderite, rhodochrosite), ferromagnesian silicates (olivine, amphiboles, pyroxenes, etc.) as well as a variety of ferric-oxyhydroxide mineraloids.

4.4. Sediment geochemistry

4.4.1. Total Organic Carbon

Total organic carbon (TOC) content was measured on 0.2 g of sediment samples from both flanks and summit of southern Hydrate Ridge (Sites 1244 to 1250). After an acid attack with 2-3 ml of HCl at 7% during 12 hours, pH neutralization by successive deionised water rinses and freeze drying the sample residue, the analyses of C content were performed on an Elemental Auto-analyzer 1106 at the *Servei de Microanàlisi Elemental of the Institut d'Investigacions Químiques i Ambientals de Barcelona* (CID-CSIC). TOC content was calculated after the measured carbon content, the initial weight of sample and the mass of eliminated sample during the acid attack.

[6] $$TOC = C_M \cdot W_F / W_I$$

where:

TOC is the Total Organic Carbon content of the sediment sample, in weight %

C_M is the measured C content, in weight %

W_F is the final weight of sample after the acid attack

W_I is the initial weight of sample

4.4.2. Trace and major element composition

Analyses of trace elements, including Ba, in bulk samples were performed by inductively coupled plasma-mass spectrometry (ICP-MS) after HNO_3 + HF digestion of 0.1 g of sample powdered in a teflon-lined vessel for 150 min at high temperature and pressure, evaporation to dryness, and subsequent dissolution in 100 ml of 4 vol % HNO_3. Measurements were performed in triplicate using a Perkin Elmer-Sciex Elam 5000 spectrometer (*Centro de Instrumentación Científica* of the *Universidad de Granada*), with Re and Rh as internal standards. The analysed elements are Li, Rb, Cs, Be, Sr, Ba, Sc, V, Cr, Co, Ni, Cu, Zn, Ga, Y, Nb, Ta, Zr, Hf, Mo, Sn, Tl, Pb, U, Th, La, Ce, Pr, Nd, Sm, Eu, Gd, Tb, Dy, Ho, Er, Tm, Yb and Ly. Coefficients of variation calculated by dissolution and subsequent analyses of 10 replicates of powdered samples were better than 3% and 8% (relative %) for concentrations of 50 and 5 ppm, respectively (Bea, 1996).

Analyses of major elementary composition (Al, Ca, K, Mg, Fe and Mn) on bulk sediment samples were performed by Atomic Absorption Spectrometry (AAS), using a Perkin Elmer 5100 at the *Centro de Instrumentación Científica* of the *Universidad de Granada*. Injected samples were digested using the same solution as for determination of trace elements in the ICP-MS and, thus, the sample preparation procedure explained above also applies to this methodology. The analytical error is approximately 2% and the detection limit is 0.1 ppm.

4.4.3. Barite sequential extraction

Barite mineral particles were separated in order to determine qualitatively if barium enrichments derived from barite mineral. The sequential leaching procedure described by Paytan et al. (1993, 1996) and Eagle et al. (2003) was applied on selected bulk samples from barium rich intervals from Sites 1244, 1246 and 1252 in the Geochemistry Laboratory of the *Instituto Andaluz de Ciencias de la Tierra* (CSIC / *Universidad de Granada*), with a recovery yield of around 90%. On a 5-10 gr sediment sample, the acid attack sequence includes:

- 250 ml of acetic acid 4N at room temperature for ~12 h to dissolve carbonates,
- 250 ml sodium hypochlorite 5% for ~12h to decompose organic matter,
- hydroxylamine hydrochloride at 0.2% in a 25% by volume acetic acid solution to remove iron and manganese oxyhydroxides,
- 30 ml nitric acid 0.1 N and 15 ml fluorhidric acid attack at room temperature for 12 h to remove silicates,
- 20 ml nitric acid 0.1 N and 20 ml fluorhidric acid attack at room temperature for 12 h to remove silicates,

- 20 ml nitric acid 0.1 N and 10 ml fluorhidric acid attack at room temperature for 12 h to remove silicates,
- Rinses of 4N nitric acid in order to remove CaF that might have precipitated during previous steps.

After every attack step, a centrifuge and a washing procedure in 3 times with deionised distilled water (DDW) were run. Thereafter, the samples were filtered, ashed (1 hour at 700 ºC) and the barite residue was weighed. The barium content in the leaching residue of the acetic acid step was analysed by ICP-MS in the *Serveis Cientifico Tècnics* of the *Universitat de Barcelona*, after a 100 dilution, on 20 selected samples in order to check whether witherite (barium carbonate mineral $BaCO_3$) was present in the sediment samples. Subsequently, the morphology of the barite crystals was studied by SEM in order to infer their origin (Paytan et al., 2002).

4.4.4. Column Transport Modelling

The modelling software CoTReM (Column Transport and Reaction Model) was adapted and applied to data from ODP Leg 204 Sites 1244 and 1246 from the eastern flank of southern Hydrate Ridge and 1245 and 1247 from the western flank in order to exemplify barite dissolution and re-precipitation processes during early diagenesis in a marine anoxic environment (Adler et al., 2000, Riedinger et al., 2006). In CoTReM, the transport method for sediments and interstitial water is burial and it is controlled by the sedimentation rate, whereas ions in interstitial waters are transported by molecular diffusion (Table 4.1). The diffusive flux of methane was defined as a fixed concentration through the whole sequence. The model was applied to the upper 50 mbsf of sediment, in cells of 25 cm thickness. The time step was set to 1 year. As upper boundary condition sulphate concentration in ocean seawater was established at $2.82 \cdot 10^{-2}$ mmol/l (Morris and Riley, 1966). The lower modelling boundary (50 mbsf) was defined as an open boundary (i.i. allowing diffusion through it).

[7] $$\Delta C_{s,d} = R_{s,d} \cdot dt_{num} \cdot SC_{s,d}$$

where:

$\Delta C_{s,d}$ = change in concentration at a specific depth

$R_{s,d}$ = reaction rate

dt_{num} = time step

$SC_{s,d}$ = stoichiometric factor

Chemical data of interstitial water (including sulphate, alkalinity and dissolved Ba^{2+}), collected onboard during ODP Leg 204, were used in order to establish the environmental

chemical conditions in the sediment column. Data of porosity and sedimentation rate from the Leg 204 Initial Reports Volume (Tréhu et al., 2003) were used as control values for the CoTReM modelling program (Table 4.2). Methane concentration in interstitial waters was interpolated for every calculation point after the onboard analyses of core-headspaces, which were analysed following the standard ODP procedures. Protocols for sampling and analysis of pore waters are detailed in the "Explanatory Notes" chapter of the Leg 204 Initial Reports volume (Tréhu et al., 2003, Claypool et al., 2006). Assuming that a degassing is produced during core retrieval, these data can be considered as minimum values (Snyder el al., 2007).

General characteristics::	
Mechanism of sediment transport	Sedimentation rate
Mechanism for solutes transport	Molecular diffusion
Model area	25 – 50 m
Thickness of the vertical cells	25 cm
Time step	1 year
Upper boundary conditions:	
SO_4^{2-} concentration on seafloor	2.82 $\cdot 10^{-2}$ mol/l (Morris and Riley, 1966)
CH_4 concentration on seafloor	0 nmol/l
Barite that reaches the seafloor	1 $\cdot 10^{-3}$ mol/kg (Church and Wolgemuth, 1972)
Lower boundary conditions:	Open / transmissive boundary
Diffusive flux of methane into the model area from below	constant concentration

Table 4.1. Geochemical parameters used as border conditions of southern Hydrate Ridge sediments for the application of CoTReM numerical modelling.

Applying CoTReM modelling to the background geochemical compositions of sediments, the time needed to form barium enrichments at every site was estimated. On the other hand, by modelling the geochemical composition of sediment obtained in this study, future evolution of sediment composition as well as the interstitial water evolution was obtained.

	Eastern flank		Western flank	
Site	1244	1246	1245	1247
Porosity (%)	60	62	62	60
Sedimentation Rate (cm/yr)	2.7 $\cdot 10^{-02}$	3.1 $\cdot 10^{-02}$	2.3 $\cdot 10^{-02}$	1.3 $\cdot 10^{-02}$

Table 4.2. Sedimentary parameters used as condition values at every modelled Site of southern Hydrate Ridge for the application of CoTReM numerical software (data from Tréhu et al., 2003).

PART III

5. Sedimentology and mineralogy of sediments from southern Hydrate Ridge: Implications for provenance, depositional environment and gas hydrate distribution

There are many variables that control the sedimentation patterns in deep-marine clastic systems. Invariably, these controls are interactive, and comprise: sediment type and grain-size; eustatic and local sea-level changes; tectonics; rates of sediment supply and accumulation; geometry and size of the receiving basin; and ocean current circulation patterns in the area (e.g. Stow and Piper, 1984; Pickering et al., 1989). Thus, in areas where clay transformation is expected to be minimal after burial, provenance can be traced through the regional pattern of terrigenous mineralogy and grain-size distribution (Karlin, 1980; Krissek, 1982; Moore and Reynolds, 1989; Petschick et al., 1996).

In this chapter, the sedimentological results obtained after the textural, physical properties and mineral composition analyses of sediment samples from southern Hydrate Ridge will be presented. The role of different variables affecting the sediment distribution patterns in the Oregon continental margin over time will be discussed below.

5.1. Texture, physical properties and bulk and clay mineralogy of southern Hydrate Ridge sediments

We present the results of grain size, mineral particle identification, magnetic susceptibility, carbonate content, bulk and clay mineralogy of the more than 560 analysed samples, from the three main depositional settings at southern Hydrate Ridge: summit, ridge flanks and slope basin (Figure 3.1).

5.1.1. Summit of southern Hydrate Ridge

Three sites were drilled at the summit of southern Hydrate Ridge: 1248, 1249 and 1250 (Figure 3.1). Sediments from Site 1248 can be classified as silty-clays (average of mean grain-size diameter 8.3ϕ), with an averaged textural distribution of 55% clay, 41% silt and 4% sand (Figure 5.1). Their magnetic susceptibility is relatively low ($1.6 \cdot 10^{-7}$ m^3/kg) with no significant downcore changes. Carbonate content analysed by the calcimeter method ranges from 3 to 17% (averaging 6%) at this site with the highest value at 96 mbsf, and a relative increasing carbonate trend downwards from this depth. As for bulk mineralogy analyses of the sediments obtained by XRD, these are composed of quartz (45-50%), clays (25-30%), feldspars (15-20%) and calcite

(5-10%). Clay mineral assemblages of Site 1248 are mostly composed of detrital mica (average 40-50%), smectites (20-30%), chlorites (15-25%) and kaolinite (5-15%).

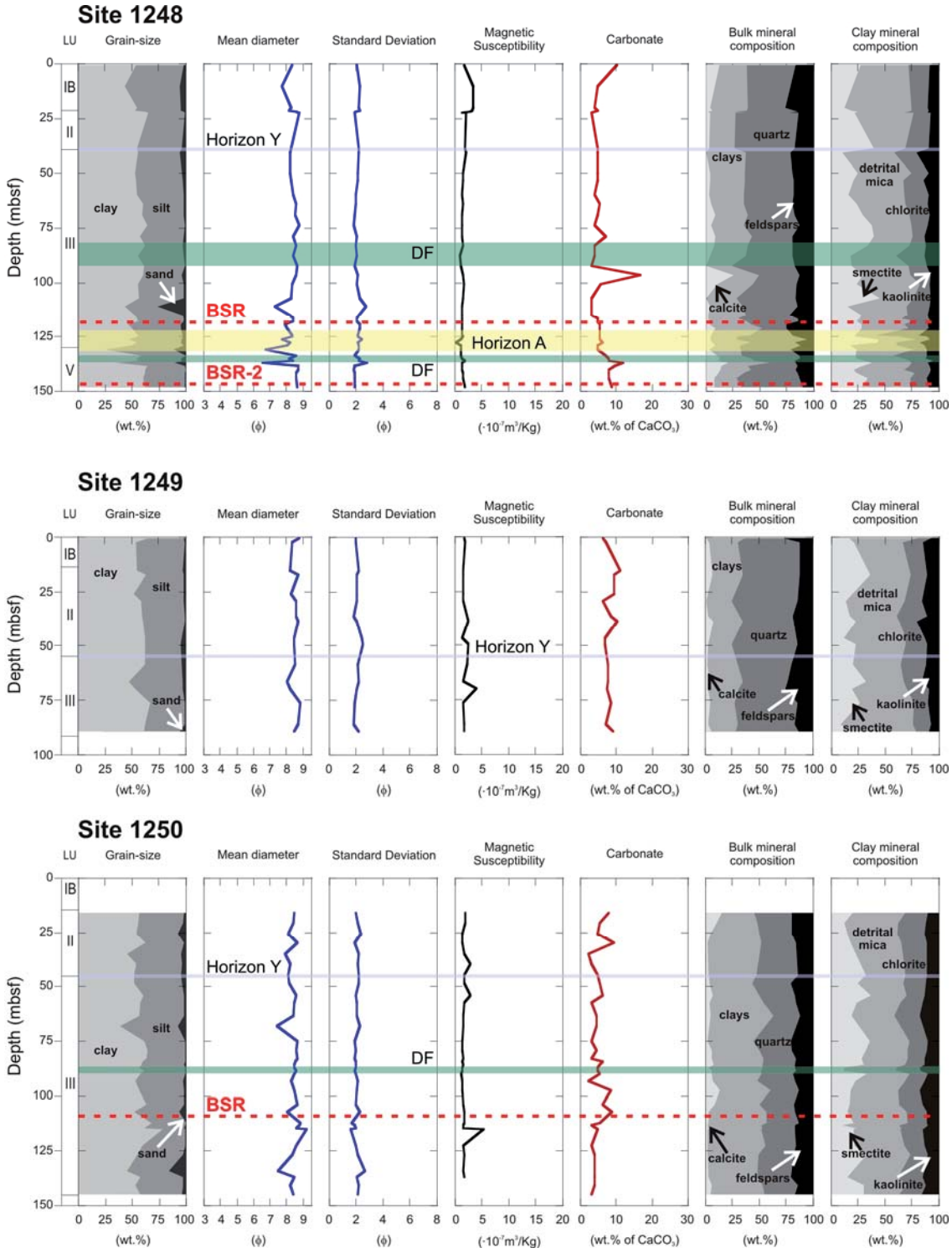

Figure 5.1. Downhole variations of grain-size, textural statistical parameters (mean diameter and standard deviation), magnetic susceptibility, carbonate content, bulk and clay mineral composition from the summit of southern Hydrate Ridge (Sites 1248, 1249 and 1250); wt.% = weight percentages; ϕ=phi. Lithostratigraphic units (LU), main seismic horizons (BSR= bottom simulating reflector) and major debris flow deposits (DF) are also labelled; mbsf= meter below sea floor.

Textural results from Site 1248 present large downcore variability below 100 mbsf, where several coarse-grained layers were identified, with sand contents reaching up to 26.7% at 111 mbsf. This variability is also found in the chlorite and detrital mica contents. From 83 to 92 mbsf, a mud clasts-rich interval is found. These sediments are characterised by the presence of soft-deformation structures and the absence of significant textural changes. Another similar, albeit thinner, interval was observed at 136 mbsf. At 111 mbsf, a coarser grain layer is found (mean diameter 7.3ϕ). Although it shows no significant change in its magnetic susceptibility value, the textural characteristics and grain-size distribution of this sample suggest that it corresponds to a mass-transport deposit (turbidite). From 127 to 130 mbsf an interval of silty-clays with several coarser-grain layers is found, characterized by abundant volcanic ash and glass particles in their coarse silt and sand fractions (Figure 5.2). The depth of this interval corresponds to the position of Horizon A at this Site (127-129 mbsf) (Shipboard Scientific Party, 2003e).

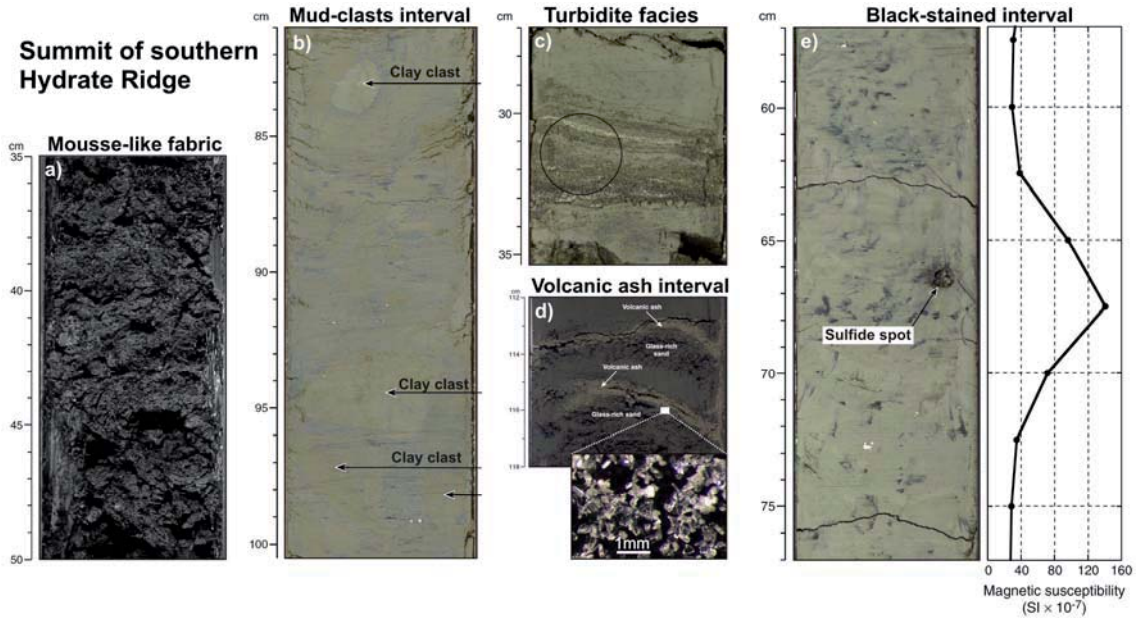

Figure 5.2. Examples of sedimentary fabrics and facies from the summit of southern Hydrate Ridge. **A.** Mousse-like fabric corresponding to interval Leg 204-1249F-3H1, 35–50 cm; 9.35-9.50 mbsf. **B.** Mud clasts –rich interval corresponding to section Leg 204-1250C-10H1, 81–101 cm; 73.81-74.01 mbsf. **C.** Turbidite facies corresponding to sample Leg 204-1250C-17H2, 27–36 cm; 133.77-133.86 mbsf. **D.** Volcanic ash facies corresponding to interval Leg 204-1248C-14H3, 112–118 cm; 126.89-126.95 mbsf. Inset image shows an optical microscope view of the ash particles sampled at 126.93 mbsf corresponding to Horizon A. **E.** Black stained –rich interval corresponding to section Leg 204-1250C-8H6, 57-77 cm; 69.57-69.77 mbsf. The correlation with the magnetic susceptibility data obtained onboard during Ocean Drilling Program Leg 204 by multi-sensor core logger is shown for comparison. mbsf = meters below sea floor (core images from Tréhu et al., 2003).

Only sixteen samples from the 90 m deep hole (1249C) were analysed at Site 1249 (Figure 5.1). They show homogeneous textural results with mean diameters ranging from 8 to 9ϕ (average 8.5ϕ), which indicates that sediments from this site are relatively fine. Magnetic susceptibility is lower than in other environments, with values ranging from 1.4 to 1.7 $\cdot 10^{-7}$

m^3/kg. Background carbonate contents are relatively high (average 8%) and constant with depth, which indicates that the conditions forming the carbonates near the surface have been stable over time in this area. As regards mineral composition, sediments are composed of quartz (45-55%), clays (25-35%), feldspars (10-20%) and calcite (0-5%). Clay minerals are distributed as 45-55% detrital mica, 15-25% smectites, 10-20% chlorite and 5-15% kaolinite. The position of Horizon Y in the 3D multichannel seismic data was located at about 60 mbsf (Shipboard Scientific Party, 2003f) and does not correlate with any significant textural feature.

The averaged mean diameter of sediments from Site 1250 is 8.4ϕ, corresponding to silty-clays (Figure 5.1). The average of their granulometric distributions is 57% clay, 40% silt and 3% sand. As for their magnetic susceptibility, they show values between 1 and 2 $\cdot 10^{-7}$ m^3/kg, with only 3 higher values (2.8 $\cdot 10^{-7}$ m^3/kg at 40 and 54 mbsf and 5 $\cdot 10^{-7}$ m^3/kg at 115 mbsf). Their carbonate content, analysed by the calcimeter method, ranges from 2 to 9.5%, with an average of 5%. Sediments from this site are mainly composed of clays (averaged 46%), quartz (31%), feldspars (17%) and calcite (5%). Their averaged clay assemblage is 44% detrital mica, 23% smectites, 21% chlorites and 13% kaolinite. At Site 1250 three coarse grained layers can be found at 68, 107 and 134 mbsf (sand contents of 8, 7 and 16% respectively). These coarse-grained layers do not correlate with high magnetic susceptibility values, but reveal homogeneous results with the exception of a peak of 5 $\cdot 10^{-7}$ m^3/kg at 115 mbsf. This peak correlates with the presence of black-stained intervals detailed onboard during the visual core description (Tréhu et al., 2002; Shipboard Scientific Party, 2003g). The black-stained intervals have been identified as magnetic iron sulphide-rich sediments (Larrasoaña et al. 2006, 2007) (Figure 5.2). A peak in the kaolinite content of up to 18% is present at 87-89 mbsf, which correlates with the presence of mud clasts and soft deformation features (Figure 5.2).

5.1.2. Western flank of southern Hydrate Ridge

Two sites (1245 and 1247) were drilled during ODP Leg 204 on the western flank of southern Hydrate Ridge (Figure 3.1). Samples up to 475 mbsf were analysed at Site 1245 (Figure 5.3). Sediments from Site 1245 are formed by silty-clays, with an average mean diameter of 8.4ϕ. Most of the granulometric distributions are formed by clays and silts, with minor amounts of sand particles, averaged 56%, 41% and 3%, respectively. Magnetic susceptibility values at this site are relatively low (average 1.9 $\cdot 10^{-7}$ m^3/kg) with only two values higher than 5 $\cdot 10^{-7}$ m^3/kg at 239 and 270 mbsf. Carbonate content analysed by the calcimeter method ranges from 4 to 11%, showing high values near the seafloor (e.g. 10% at 2 mbsf, 11% at 16 mbsf) but also at depth (e.g. 9% at 138 mbsf; 11% at 200 mbsf). The mineral composition of sediments from Site 1245, analysed by XRD, is made up of quartz (average 51%), clays (28%), feldspars (15%) and calcite (6%). As regards clay composition, samples are mostly

composed of detrital mica (average 45%) and smectites (26%), with minor amounts of chlorites (20%) and kaolinite (10%). At 123 mbsf, mud clasts and deformation structures were described at core 204-1245B-14H1. A sample from this section does not show significant changes in texture but a relatively lower content of smectite mica (13%). This suggests that the interval would correspond to a detrital event (i.e. debris flow). An interval with numerous coarse-grained (sand content up to 24%) ash-rich layers is observed between 178 and 181 mbsf, coinciding with the position of Horizon A at this Site (Shipboard Scientific Party, 2003b).

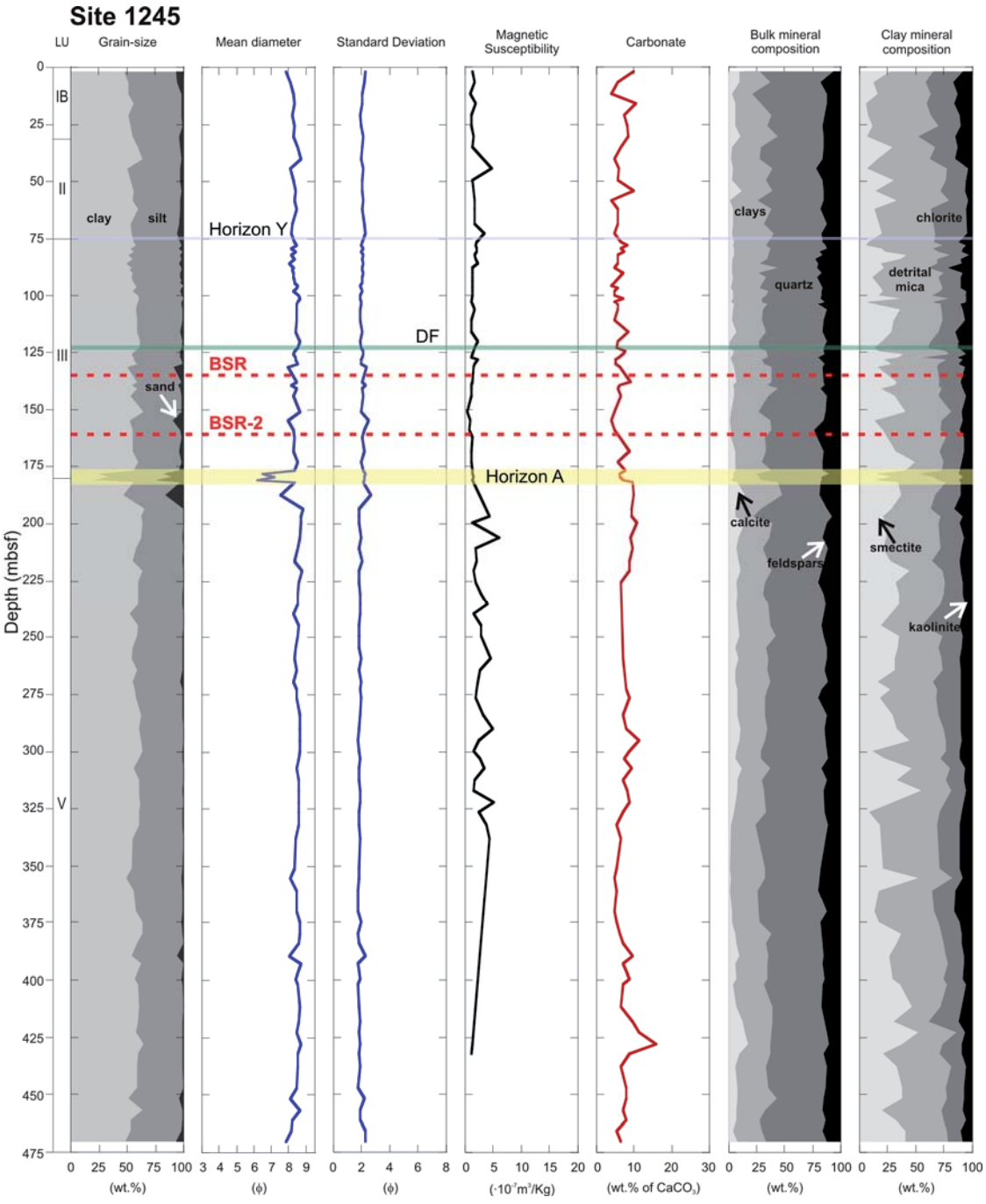

(Continue on next page)

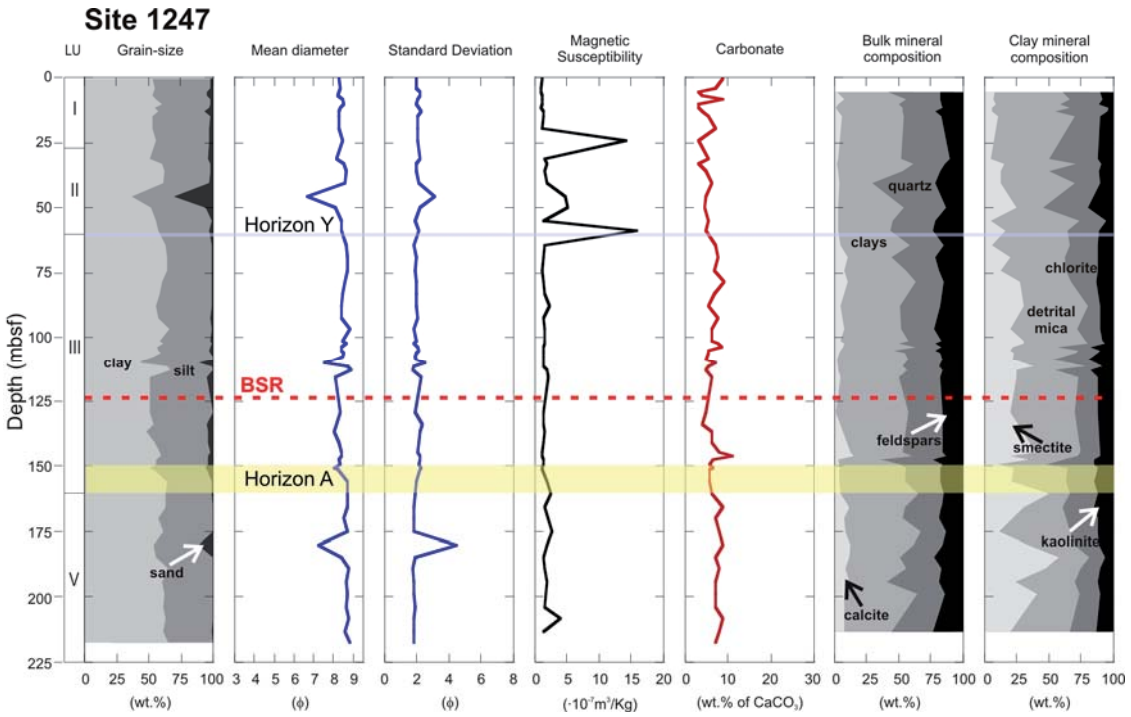

Figure 5.3. Downhole variations of grain-size, textural statistical parameters (mean diameter and standard deviation), magnetic susceptibility, carbonate content and bulk and clay mineral composition from the western flank of southern Hydrate Ridge (Sites 1245 and 1247); wt.% = weight percentages; ϕ=phi. Lithostratigraphic units (LU), main seismic horizons (BSR= bottom simulating reflector) and major debris flow deposits (DF) are also labelled; mbsf= meter below sea floor.

Sediments at Site 1247 are greenish-grey silty-clays (average of mean diameter 8.4ϕ) (Figure 5.3). Numerous black-colour stained intervals are observed at this site, related to the presence of magnetic iron-sulphides (greigite and pyrrhotite) (Figure 5.4) (Larrasoaña et al., 2006, 2007). Grain-size distributions at Site 1247 average 57% clay, 40% silt and 3% sand. Magnetic susceptibility values are relatively high (between 2 and 5 $\cdot 10^{-7}$ m^3/kg), with two very high values of 14 and 16 $\cdot 10^{-7}$ m^3/kg at 24 and 58 mbsf, respectively. Carbonate content at this site ranges from 3 to 11%, with high values from 7 to 8.7% in the first ten meters below the seafloor. As for their mineral composition, sediments from Site 1247 are mainly composed of clays (45-50%), with different amounts of quartz (25-30%), feldspars (15-20%) and calcite (2-7%). Their clay mineral assemblage is formed by detrital micas (40-50%), chlorites (15-25%) and smectites (15-25%) and small amounts of kaolinite (10-20%). At this site, three coarse grained layers are found at 45, 110 and 180 mbsf (with sand contents of 30, 10 and 12%, respectively). Only the shallowest layer shows a relatively high magnetic susceptibility (5 $\cdot 10^{-7}$ m^3/kg). The two deeper layers are characterized by a large amount of foraminifera shells in their sand fraction. Biogenic components represent 15% and 9%, respectively (Figure 5.4). Two samples with high magnetic susceptibility (14 and 16 $\cdot 10^{-7}$ m^3/kg) were analysed from 24 and 58 mbsf. They are not related to coarser-grained layers but to the presence of black-stained intervals and iron-sulphide minerals (greigite and pyrrhotite) (Larrasoaña et al., 2006; 2007).

Coarser-grained layers have been locally identified between 150 and 160 m depth. They correlate with the position of Horizon A at Site 1247, which dips to the East at this flank of southern Hydrate Ridge (Shipboard Scientific Party, 2003d).

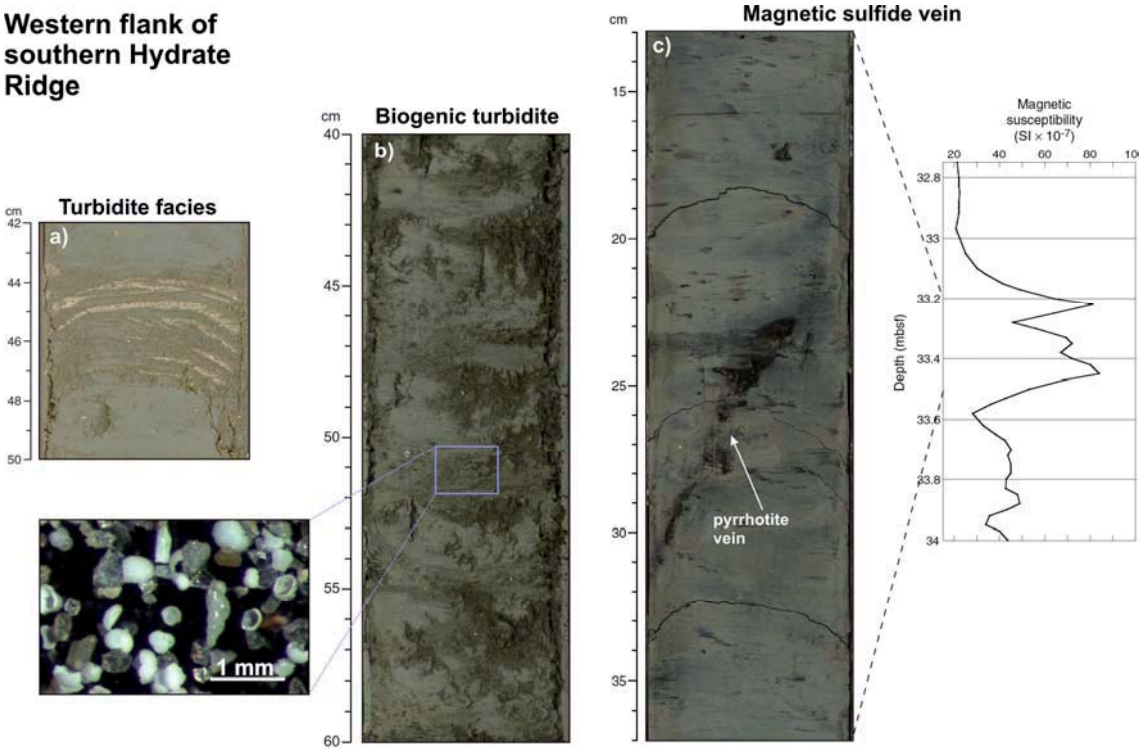

Figure 5.4. Examples of sedimentary fabrics and facies from the western flank of southern Hydrate Ridge. **A.** Turbidite facies corresponding to section 204-1245B-8H7, 42–50 cm; 75.75-75.83 mbsf. **B.** Biogenic turbidite facies corresponding to section 204-1247B-20X2, 40-60 cm; 146.10-146.30 mbsf. Inset image show an optical microscope view of the biogenic and lithogenic particles sampled at 146.21 mbsf with numerous planktonic and benthic foraminifera shells. **C.** Black stained –rich interval corresponding to section 204-1247B-5H6, 13-37 cm; 33.17-33.41 mbsf containing a sulphide vein. X-ray diffraction analyses confirmed the pyrrhotite presence. The correlation with the magnetic susceptibility data obtained onboard during Ocean Drilling Program Leg 204 by multi-sensor core logger is shown for comparison. mbsf = meters below sea floor (core images from Tréhu et al., 2003).

5.1.3. Eastern flank of southern Hydrate Ridge

Samples from Site 1244 are relatively homogeneous, dominated by a silty-clay composition (average of mean grain-size 8.4ϕ) and with a coarser grained interval at 126 mbsf (sand content 5.5%) (Figure 5.5). As regards magnetic susceptibility, the samples show a constant trend with depth (ca. $1.5 \cdot 10^{-7}$ m^3/kg), with a prominent magnetic susceptibility peak observed at 20.7 mbsf (up to $10 \cdot 10^{-7}$ m^3/kg). Carbonate content ranges from 4 to 11%, with the highest values near the seafloor (e.g. 11% at 2.6 mbsf; 9.4% at 5.5 mbsf) (Figure 5.6). The mineralogical composition of Site 1244 samples analysed by XRD show that they are mostly composed of clays (45-50%), quartz (28-33%) and feldspars (18-23%), with minor amounts of calcite (3-8%). As for their clay mineral association, they are mostly composed of detrital mica (40-50%), smectite (20-

30%), kaolinite (15-25%) and chlorite (10-20%). No significant horizons were drilled at this Site (Shipboard Scientific Party, 2003a).

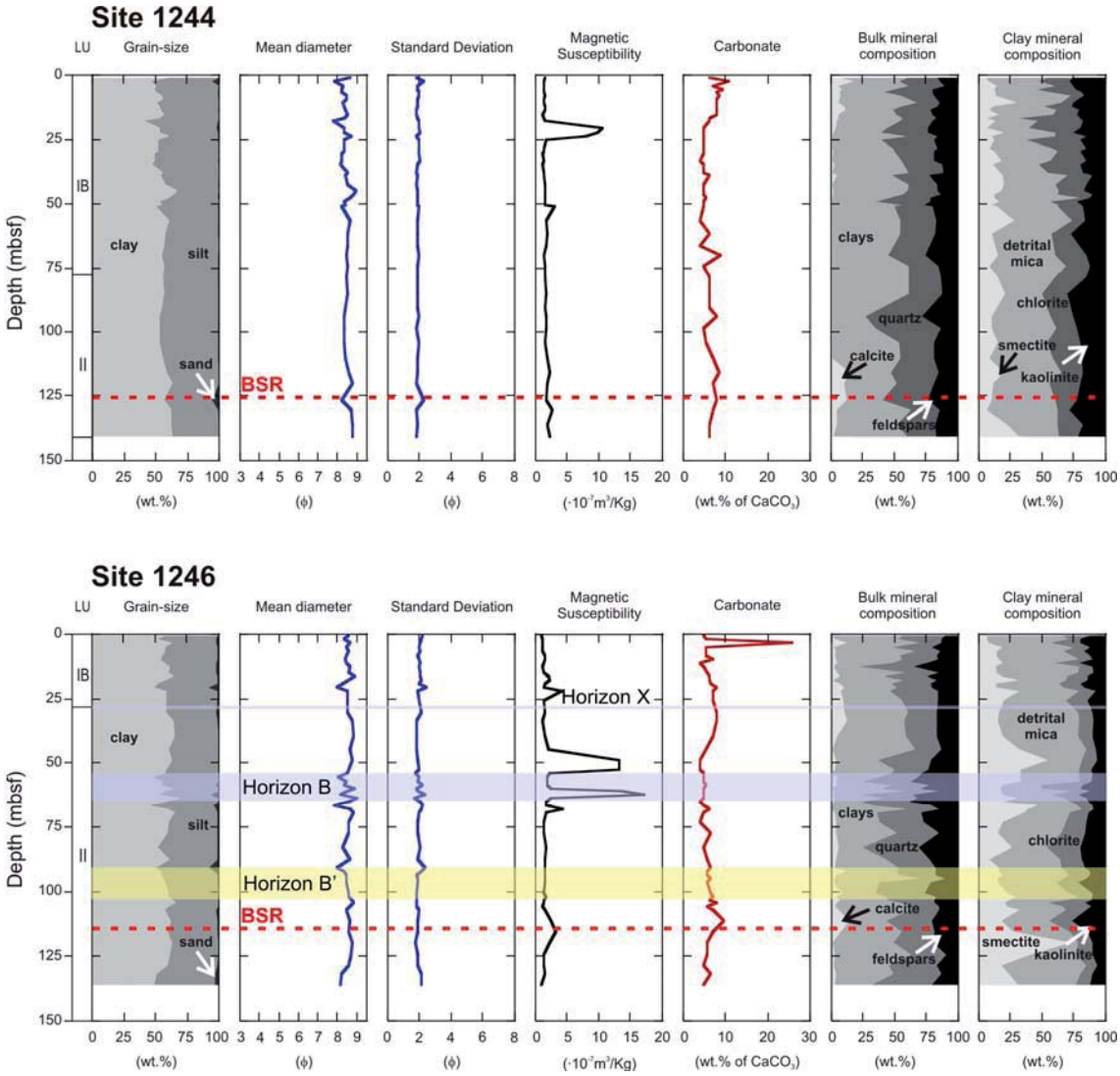

Figure 5.5. Downhole variations of grain-size, textural statistical parameters (mean diameter and standard deviation), magnetic susceptibility, carbonate content, bulk and clay mineral composition from the eastern flank of southern Hydrate Ridge (Sites 1244 and 1246); wt.% = weight percentages; ϕ=phi. Lithostratigraphic units (LU), main seismic horizons (BSR= bottom simulating reflector) and major debris flow deposits (DF) are also labelled; mbsf= meter below sea floor.

Sediments from Site 1246 show higher variability downcore, with grain-size values ranging from very fine silt to clay (7.8ϕ to 9ϕ) with an average texture of silty-clay (8.5ϕ) (Figure 5.5). Magnetic susceptibility shows background values of 1.5-2 $\cdot 10^{-7}$ m^3/kg, with very high values at 50 and 65 mbsf, reaching up to 17 $\cdot 10^{-7}$ m^3/kg. Most of the samples show carbonate contents up to 15%, with only one sample with an extremely high carbonate content (26%), which is found near the surface (3.5 mbsf), probably related to the presence of authigenic carbonate nodules described onboard (Figure 5.6) (Tréhu et al., 2006). The sediments are mainly composed of

clays (44-45%), quartz (28-33%), feldspars (18-23%) and calcite (2-7%). As regards clay assemblage, sediments are mostly composed of detrital mica (40-50%), smectites (18-28%), chlorite (10-20%) and kaolinite (8-18%). Two intervals with very high magnetic susceptibility values (13 and 17 $\cdot 10^{-7}$ m^3/kg) were measured at 50-55 and 65 mbsf, respectively. The first one coincides with a great smectite content interval (up to 55% smectites and 26% detrital mica), whereas the second peak correlates with a relatively coarse-grained interval, with up to 6% sand and with an increase in the content of kaolinite, chlorite and detrital mica. This interval coincides with the position of Horizon B, identified in the 3D multichannel seismic data. An ash-rich interval, relatively coarse-grained (up to 8% sand) and with relatively low magnetic susceptibility values (1.3 $\cdot 10^{-7}$ m^3/kg), is observed at 90-102 mbsf corresponding with the depth of Horizon B' at this Site (Figure 5.6) (Shipboard Scientific Party, 2003c).

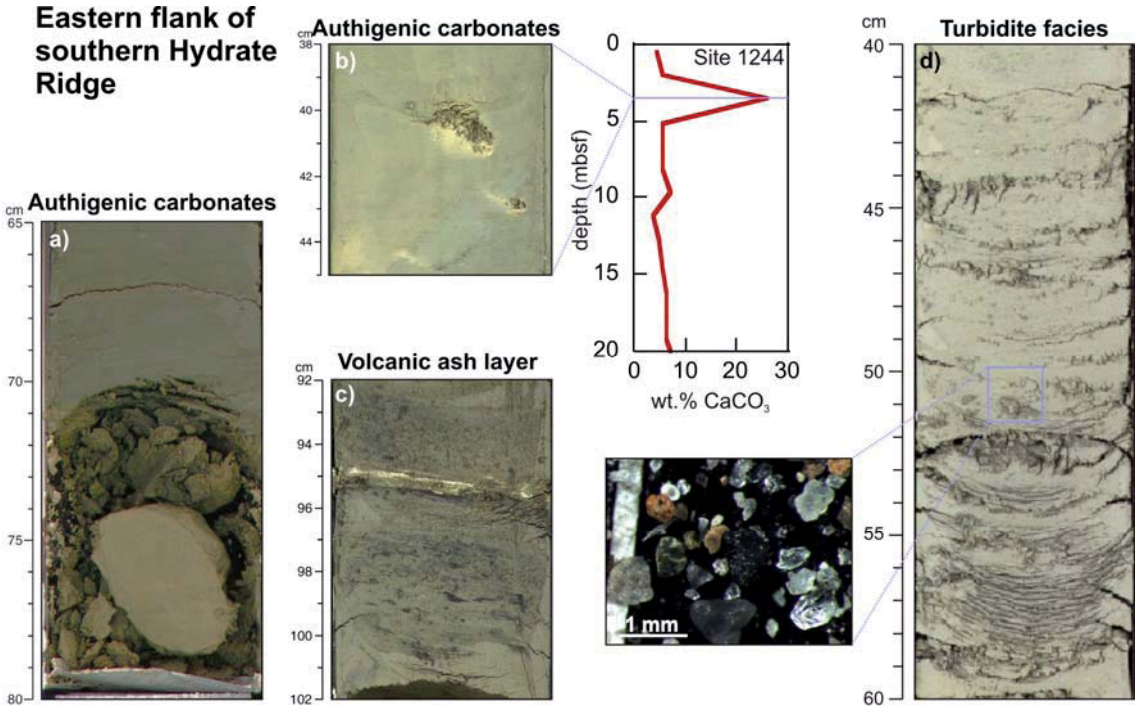

Figure 5.6. Examples of sedimentary fabrics and facies from the eastern flank of southern Hydrate Ridge. **A.** Authigenic carbonate nodule corresponding to section 204-1244B-3H7, 65–80 cm; 25.85-26 mbsf. **B.** Authigenic carbonate nodule corresponding to interval 204-1246B-1H3, 38–45 cm; 3.38-3.45 mbsf. Carbonate content analysed for this thesis by the calcimeter method is shown for reference. **C.** Volcanic ash layer corresponding to interval 204-1246B-11H4, 92–102 cm; 97.99-98.09 mbsf. **D.** Turbidite facies sampled in 204-1246B-8H2, 40-60 cm; 63.50-63.70 mbsf. Inset image shows an optical microscope view of the lithogenic particles sampled at 63.61 mbsf with numerous quartz particles, heavy minerals and rock fragments. mbsf = meters below sea floor (core images from Tréhu et al., 2003).

5.1.4. Slope basin adjacent to southern Hydrate Ridge

Two sites (1251 and 1252) were drilled on the slope basin adjacent to southern Hydrate Ridge (Figure 3.1). Relatively homogenous results have been obtained at Site 1251 (Figure 5.7). It is mainly composed of fine silty sediments (average mean diameter of 6ϕ; see chapter 4 for explanation on Coulter grain-size results) with a downcore increasing trend in the sand content

at units LU IV and VI (up to 22% at 404 mbsf). Magnetic susceptibility data average 1.5 $\cdot 10^{-7}$ m^3/kg and do not show a downcore increase, with only relatively high values of 6.4, 3.4, 2.8 and 8.2 $\cdot 10^{-7}$ m^3/kg at 20, 146, 345 and 440 mbsf, respectively. Carbonate contents at this site are relatively low (average 6%), except at 283 and 312 mbsf, with values of 22 and 11%, respectively. As shown in the XRD results, sediments from Site 1251 are composed of 50-55% clays, 25-30% quartz, 10-15% feldspars and 0-5% calcite. As for their clay mineralogy composition, the sediments are mainly composed of detrital mica (65-75%), smectites (15-25%), kaolinite (10-20%) and low chlorite content (5-15%). No significant reflectors were drilled at Site 1251. Unconformity U does not seem to be related with any textural remarkable feature (Shipboard Scientific Party, 2003h).

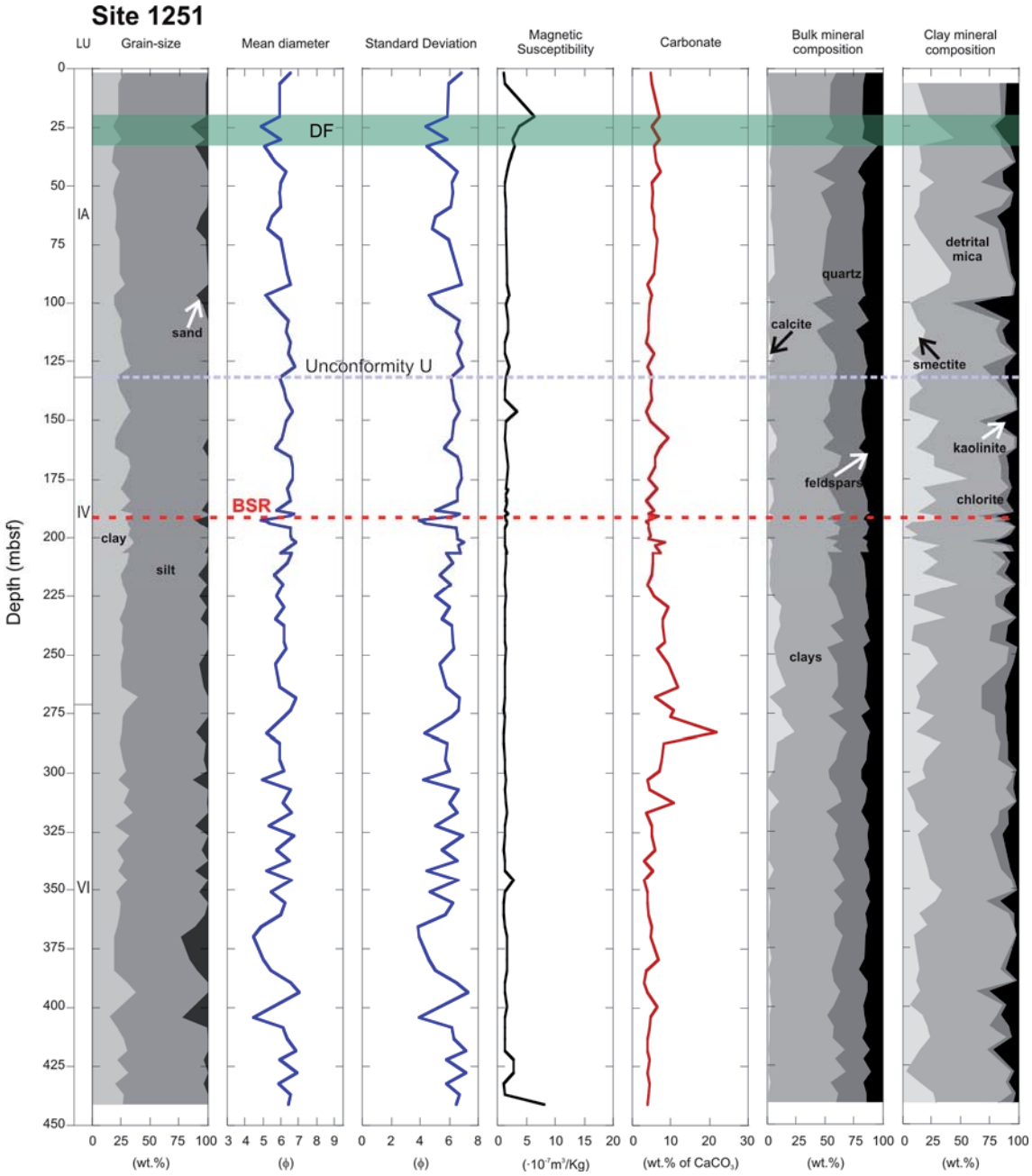

(Continue on next page)

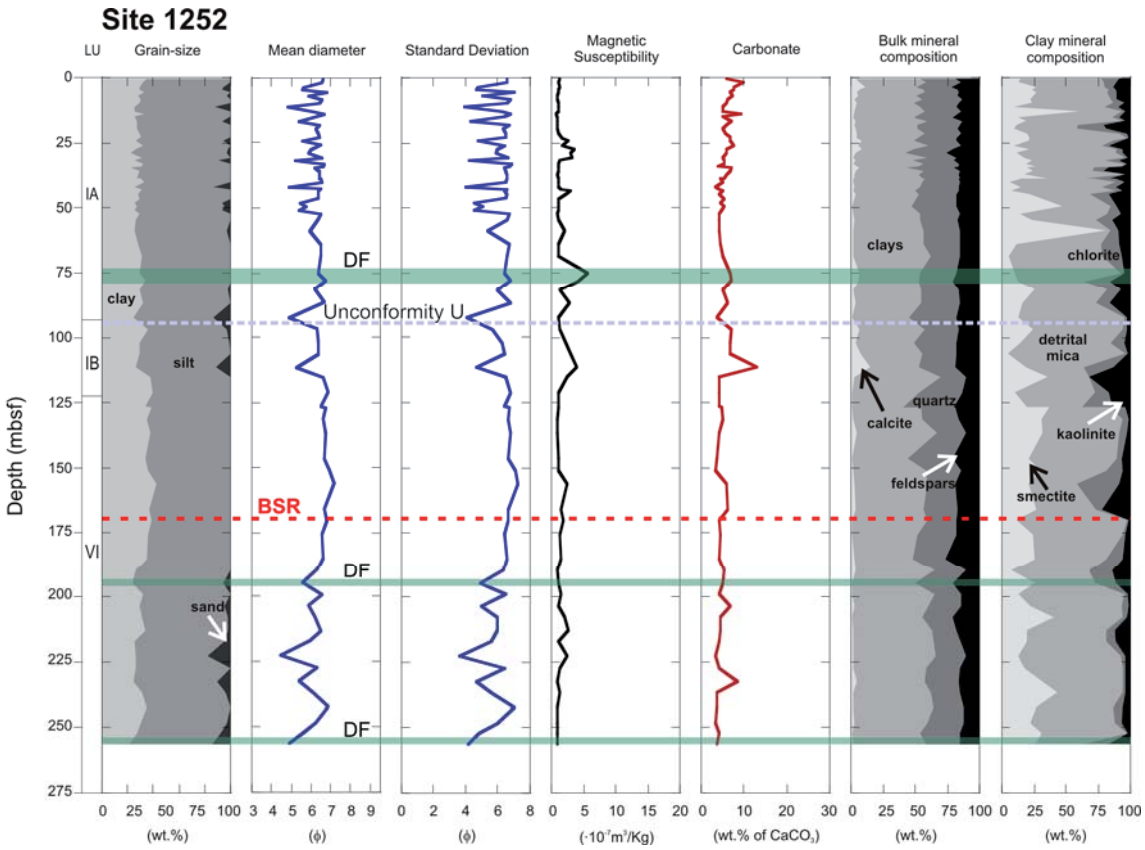

Figure 5.7. Downhole variations of grain-size, textural statistical parameters (mean diameter and standard deviation), magnetic susceptibility, carbonate content, bulk and clay mineral composition from the slope basin adjacent to southern Hydrate Ridge (Sites 1251 and 1252); wt.% = weight percentages; ϕ=phi. Lithostratigraphic units (LU), main seismic horizons (BSR= bottom simulating reflector) and major debris flow deposits (DF) are also labelled; mbsf= meter below sea floor.

The sediments at Site 1252 mainly consist of silts and fine silts (averaged 30% clay, 67.5% silt and 2.5% sand), with an averaged mean diameter of 6.2ϕ (see chapter 4 for explanation on Coulter grain-size results). Magnetic susceptibility values average 1.5 $\cdot 10^{-7}$ m^3/kg, ranging from 0.8 to 5.6 $\cdot 10^{-7}$ m^3/kg (Figure 5.7). Carbonate content at this site averages 5.5%, with a peak of 13% at 111 mbsf, corresponding to the presence of carbonate cements (Figure 5.8). Grain-size results show high textural variability from the surface to about 50 mbsf (note the higher sampling density). Some of the uppermost coarse layers correlate with high magnetic susceptibility values, suggesting that the coarser particles in the sediments include magnetite as detrital component. Downwards, coarse grain-size layers are found at 92, 111, 222, 252 and 256 mbsf (Figure 5.8), with sand contents higher than 10%, also suggesting a downcore trend of increasing grain-size. The averaged mineralogical composition of the sediments is 50-55% clays, 30-35% quartz, 15-20% feldspars and 0-5% calcite. Clay mineralogy composition of the sediments includes detrital mica (65-75%), smectites (15-25%), kaolinite (5-15%) and chlorite (5-15%). Several debris flow deposits were identified during onboard visual core descriptions (Shipboard Scientific Party, 2003i) (Figure 5.8), which can be related to characteristic clay mineralogical assemblages and relatively fine grain-size sediments. Glauconite-rich layers were

onboard described during ODP Leg 204. Nevertheless, no significant glauconite contents were found in the XRD data analyses.

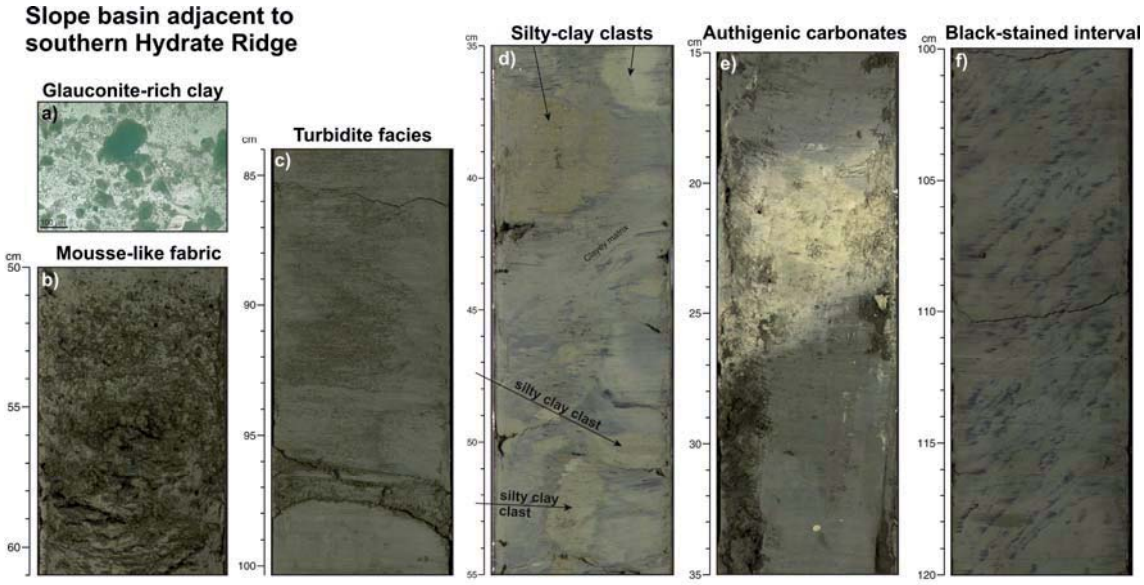

Figure 5.8. Examples of sedimentary fabrics and facies from the slope basin adjacent to southern Hydrate Ridge. **A.** Photomicrograph of glauconite from interval 204-1252A-13H3, 138-148 cm; 113.3 mbsf. **B.** Mousse-like fabric section corresponding to section 204-1252A-15H4, 50–61 cm; 130-130.11 mbsf. **C.** Turbidite facies corresponding to interval 204-1252A-12H5, 84−101 cm; 106.74-106.91 mbsf. **D.** Silty-clay clasts-rich sediment, from the interval 1251B-3H5, 35–55 cm; 24.95-25.15 mbsf. **E.** Authigenic carbonate cement corresponding to sample 204-1252A-19H6, 15–35 cm; 171.45-171.65 mbsf. **F.** Black stained interval sampled at 204-1252A-12H4, 100–120 cm; 105.4-105.6 mbsf. mbsf = meters below sea floor (core images from Tréhu et al., 2003).

5.2. Main lithofacies of southern Hydrate Ridge sediments

In summary, sedimentological and mineralogical analyses of late Pliocene to Holocene-age sediments from southern Hydrate Ridge indicate that they are mainly formed by homogenous sedimentary sequences dominated by greenish-grey silty-clays (average of 57% clay, 41% silt, 2% sand), with an averaged mean diameter of 8.4ϕ, poorly sorted (average of standard deviation 1.9ϕ) and with a skewness value of -0.08ϕ.

Four main lithofacies were characterized in southern Hydrate Ridge sediments on the basis of these sedimentological, mineralogical and magnetic results: hemipelagite, turbidite, debrite, and ash layers (Figure 5.9). Samples of turbidite facies were classified as turbidite tail, turbidite base and biogenic turbidite in accordance with the presence of broken shells, size, shape and composition of detrital particles, and the content of biogenic particles using optical microscopy (Table 5.1). Their magnetic susceptibility, mineralogical proportions and carbonate content as well as the granulometric statistical parameters and core digital images were also taken into account to classify each sample.

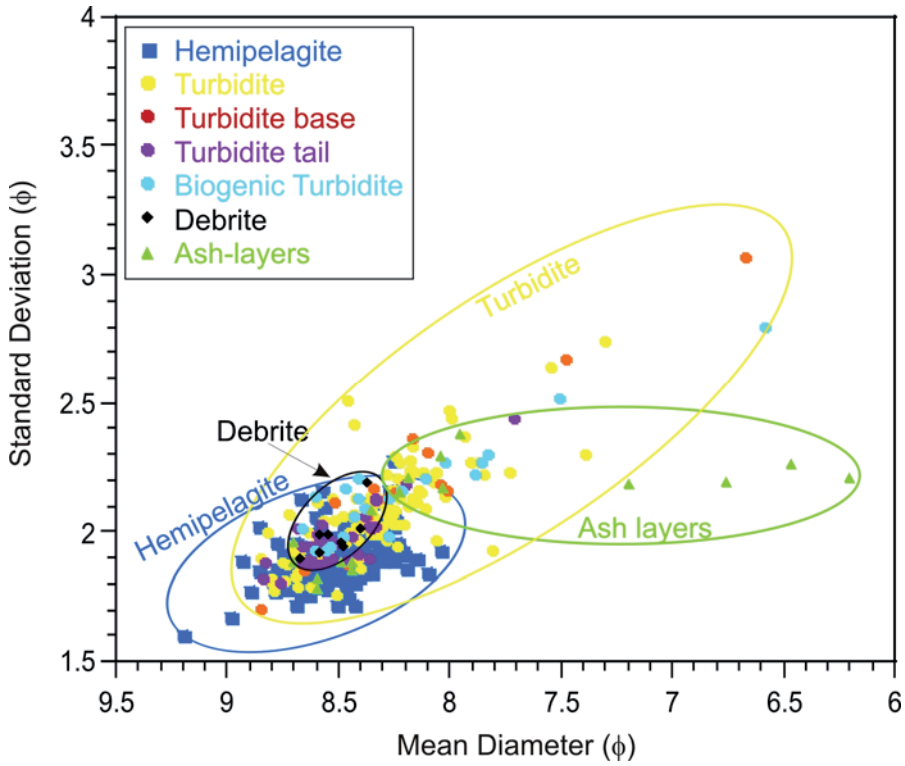

Figure 5.9. Plot of the standard deviation (SD) versus the mean diameter (in ϕ = phi) of the analysed samples from the summit and both flanks of southern Hydrate Ridge (Sites 1244 to 1250). The samples are classified in the four main lithofacies and sub-facies identified in southern Hydrate Ridge sediments.

5.2.1. Hemipelagite

Hemipelagite is the most abundant facies identified in the southern Hydrate Ridge sediments (Figure 5.9). The 162 samples recognized as hemipelagic facies are formed by greenish-grey silty-clay sediments (averaged 58% clay, 41% silt, 1% sand) with minor amounts of sand (up to 3.7%), and an averaged mean diameter of 8.5ϕ (ranging from 8ϕ to 9.2ϕ), and relatively poorly sorted with an averaged SD of 1.9ϕ. Their granulometric curves show an unimodal shape with the mode value between 7ϕ and 8ϕ (Figure 5.10). Sand fraction is largely composed of planktonic foraminifera shells, with variable amounts of benthic shells and terrigenous components (mainly quartz and other light minerals). Magnetic susceptibility of the hemipelagic samples ranges from 0.96 to 13 $\cdot 10^{-7}$ m^3/kg and carbonate content ranges between 3 and 16%, with the highest values corresponding to the uppermost sediments where authigenic carbonates are formed (e.g. 10% in sample 204-1248C-1X1-51cm, 0.51 mbsf). The XRD analyses of the hemipelagic samples show that they are mainly composed of quartz and clays, with an average of 17% feldspars and minor amounts of calcite (6%). As regards the mineralogy of clays, these are mainly formed by an assemblage of detrital mica (averaged 44%), smectites (23%), chlorite (19%) and kaolinite (13%).

	Total	Hemipelagite	Turbidite				Ash layer	Debrite
Granulometric distribution			**Total-turbidites**	**Turbidite-base**	**Turbidite-tail**	**Biogenic turbidite**		
>Sand (wt.%)	(0 – 30.4) 2.3	(0 – 3.7) 0.9	(0.1 – 30.4) 3.2	(0.1 – 30.4) 5.5	(0.5 – 3.8) 1.6	(1.3 – 10.6) 4.2	(0.3 – 24.2) 5.6	(0.8 – 4.1) 1.7
Silt (wt.%)	(21.6 – 63.7) 41.2	(21.6 – 53.6) 40.9	(30 – 59.2) 41.1	(31.2 – 49.5) 40.8	(34.5 – 48.7) 39.7	(33.8 – 54.5) 41.7	(34.4 – 63.7) 45.4	(35.7 – 42.7) 39.4
Clay (wt.%)	(19.3 – 77.9) 56.5	(46 – 77.9) 58.3	(35 – 68.4) 55.7	(37.2 – 68.4) 53.8	(47.5 – 65) 58.7	(35 – 64.2) 54.1	(19.3 – 64.4) 49	(56.1 – 61.9) 58.9
Statistic values								
Mean-diameter (ϕ)	(6.2 – 9.2) 8.4	(8 – 9.2) 8.5	(6.6 – 8.9) 8.2	(6.7 – 8.9) 8.2	(7.7 – 8.8) 8.5	(6.6 – 8.7) 8.2	(6.2 – 8.7) 8	(8.4 – 8.7) 8.5
Standard deviation (ϕ)	(1.6 – 4.4) 2	(1.6 – 2.3) 1.9	(1.7 – 4.4) 2.1	(1.7 – 3.1) 2.2	(1.8 – 2.4) 2	(1.9 – 2.8) 2.2	(1.8 – 2.4) 2.1	(1.9 – 2.2) 2
Skewness	(-2.2 – 0.5) -0.1	(-0.3 – 0.4) 0	(-2.2 – 0.5) -0.2	(-0.6 – 0.1) -0.2	(-0.4 – 0.2) -0.1	(-0.4 – 0.3) -0.2	(-0.3 – 0.5) 0	(-0.4 – 0) -0.1
Kurtosis	(1.8 – 8) 2.6	(2.1 – 3.5) 2.5	(1.8 – 8) 2.7	(2 – 4.6) 2.8	(2.1 – 3.5) 2.6	(1.9 – 3.3) 2.7	(2.4 – 3.2) 2.7	(2.3 – 3.2) 2.7
Median (ϕ)	(6.2 – 9.2) 8.3	(7.8 – 9.2) 8.4	(6.2 – 9) 8.3	(7.1 – 8.8) 8.2	(7.9 – 8.9) 8.5	(6.3 – 8.8) 8.2	(6.2 – 8.7) 7.9	(8.3 – 8.6) 8.5
Carbonate contents								
Carbonate (wt.%)	(2.3 – 25.9) 6.4	(3.1 – 16) 6.7	(2.3 – 25.9) 6.2	(3.9 – 7.8) 5.8	(3.1 – 9.6) 5.9	(2.3 – 25.9) 8.5	(4.7 – 7.2) 6	(3.2 – 7.8) 4.9
Total organic carbon (wt.%)	(0.2 – 2.1) 1.1	(0.5 – 2.1) 1.1	(0.3 – 1.8) 1.1	(0.5 – 1.5) 1.1	(0.9 – 1.4) 1.1	(0.8 – 1.8) 1.2	(0.2 – 1.2) 0.9	(0.9 – 1.3) 1.1
Biogenic component contents								
Total biogenic particles (%)	(0 – 58) 3.6	(0 – 50) 4	(0 – 58) 3.6	(0 – 10) 3.3	(0 – 9.5) 1.5	(5 – 58) 15.4	(0 – 1.6) 0.6	(0 – 15.2) 4.7
Broken foraminifera shells (%)	(0 – 100) 50	(0 – 100) 41	(0-100) 57	(0 – 100) 54	(0 – 100) 58	(31 – 90) 52	(0 – 100) 52	(14 – 100) 51
Magnetic susceptibility								
Magnetic susceptibility ($x10^{-7}$ m^3/kg)	(0.18 – 17.2) 2	(0.96 – 13.5) 2	(0.91 – 17.2) 2.1	(1.26 – 4.8) 1.77	(1.11 – 4.15) 1.58	(1.15 – 2.81) 1.51	(1.82 – 2.55) 1.27	(1 – 1.98) 1.35
Total mineralogical composition								
Calcite (%)	(1 – 25) 5	(1 – 17) 6	(0.5 – 26) 5	(1-10) 4	(1-12) 4	(3 – 26) 11	(1 – 12) 5	(1 – 10) 5
Clays (%)	(16 – 68) 37	(16 – 63) 38	(18 – 65) 37	(21.5 – 65) 41	(24 – 59) 39	(18 – 58) 40	(21 – 68) 39	(23 –50) 36
Quartz (%)	(16 – 70) 40	(18 – 70) 40	(16.5 – 70) 40	(21 – 51) 34	(18 – 65) 39	(16 – 65) 34	(19 – 65) 39	(29 – 59) 41
Feldspars (%)	(7 – 39) 17	(8 – 32) 17	(7 – 39) 18	(13 – 38) 20	(7 – 26) 17	(7 – 20) 15	(10 – 26) 17	(15 – 20) 18
Clay mineral composition								
Detrital mica (%)	(6 – 71) 45	(23 – 68) 44	(6 – 70.5) 46	(22 – 63) 44	(18 – 68) 46	(33 – 61) 43	(16 – 56) 43	(39 – 52) 45
Smectites (%)	(5 – 73) 23	(6 – 58) 23	(5 – 73) 23	(15 – 39) 26	(6 – 49) 23	(8 – 38) 23	(14 – 50) 23	(11 – 34) 21
Kaolinite (%)	(3 – 30) 12	(6 – 30) 13	(3 – 28) 11.5	(5 – 18) 11	(5 – 23) 11	(8 – 28) 13	(9 – 21) 13	(6 – 18) 13
Chlorite (%)	(7 – 48) 20	(7 –48) 19	(7 – 40) 16.5	(7 – 33) 19	(10 – 39) 20	(12 – 26) 20	(11 – 35) 20	(15 – 26) 21

Table 5.1. Averages and ranges (in brackets) of grain-size results, granulometric statistical parameters, total carbonate and total organic carbonate (TOC) contents, biogenic components (total and broken shells) of the coarser fraction (>50 μm), magnetic susceptibility, and total and clay mineral composition of the four lithofacies defined for southern Hydrate Ridge sediments. Samples from the summit and both flanks (Sites 1244 to 1250) were taken into account in this synthesis. ϕ= phi; wt. %= weight percentages.

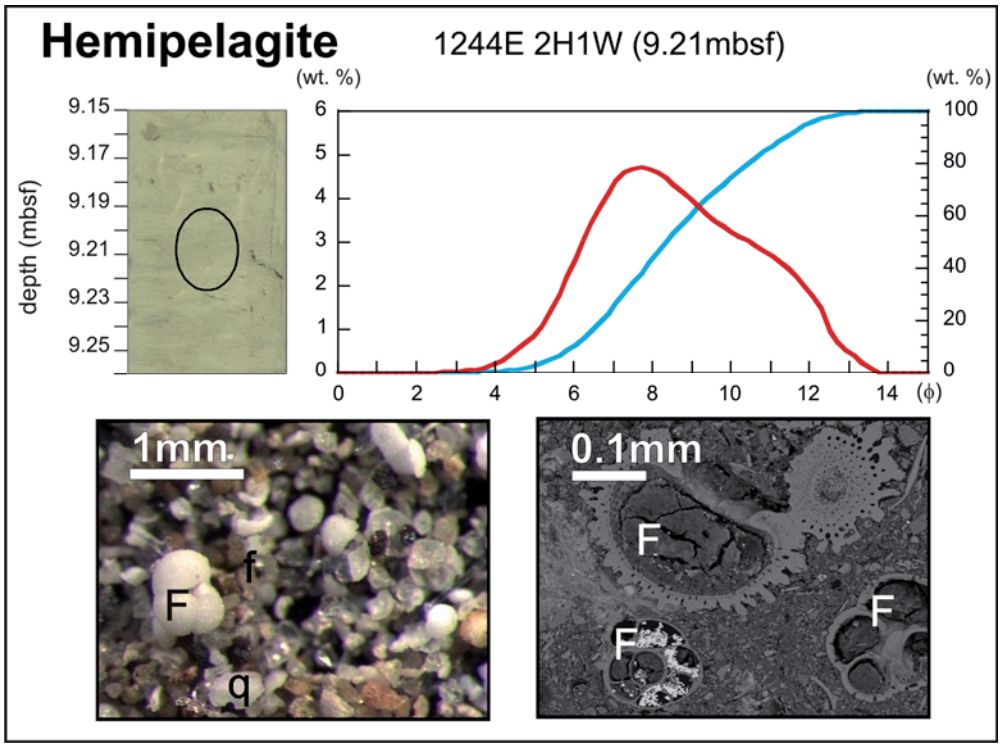

Figure 5.10. Principal textural results of a representative sample of hemipelagite facies defined in southern Hydrate Ridge sediments (ODP Leg 204-1244E-2H1, 9.21 mbsf), including detailed photo of the sampled core section, granulometric distribution curves (histogram in red; cumulative curve in blue), optical microscope image of the coarse silt and sand fraction (>50μm) and scanning electron microscope image. F= foraminifera shell; q= quartz grain; f= feldspar mineral particle; mbsf= meter below sea floor; ϕ= phi; wt. %= weight percentages.

5.2.2. Turbidite

Interbedded with the hemipelagite facies there are numerous coarse-grained intervals, interpreted as turbidite deposits. A total of 190 sediment samples were identified as belonging to this facies, corresponding to different positions in the Bouma sequence (Bouma, 1962), from the base to the tail of the turbidite. In general, turbidite samples are coarser-grained (averaged 56% clay, 41% silt, 3% sand) than hemipelagic background sediments, and have an averaged mean diameter of 8.3ϕ (ranging from 6.6ϕ to 8.9ϕ) (Figure 5.11). Their SD values (averaged 2.1ϕ) indicate that they are very poorly sorted sediments based on Friedman and Sanders classification (1978), and they show bimodal granulometric distribution curves, with modal values at 7-8ϕ and ~3ϕ. As expected, the mean diameter data versus SD data of the turbidite samples show an almost direct relationship, with several values corresponding to the same parameters as the hemipelagic facies (Figure 5.9). The coarser grains (>50 μm) of the turbidite facies samples are largely formed by terrigenous components (quartz, light minerals, rock fragments, micas and heavy minerals), with minor amounts of foraminifera shell fragments. Magnetic susceptibility values are high (up to 17 $\cdot 10^{-7}$ m^3/kg), reflecting a relatively high abundance of magnetic-minerals in the coarse detrital particles. The bulk mineralogy

composition of the turbidite samples is similar to the hemipelagites with only a small increase in feldspar (averaged 18%) and in detrital mica contents (46%). As for the clay mineralogy, a marked decrease in chlorite (17%) and kaolinite (12%) contents was observed.

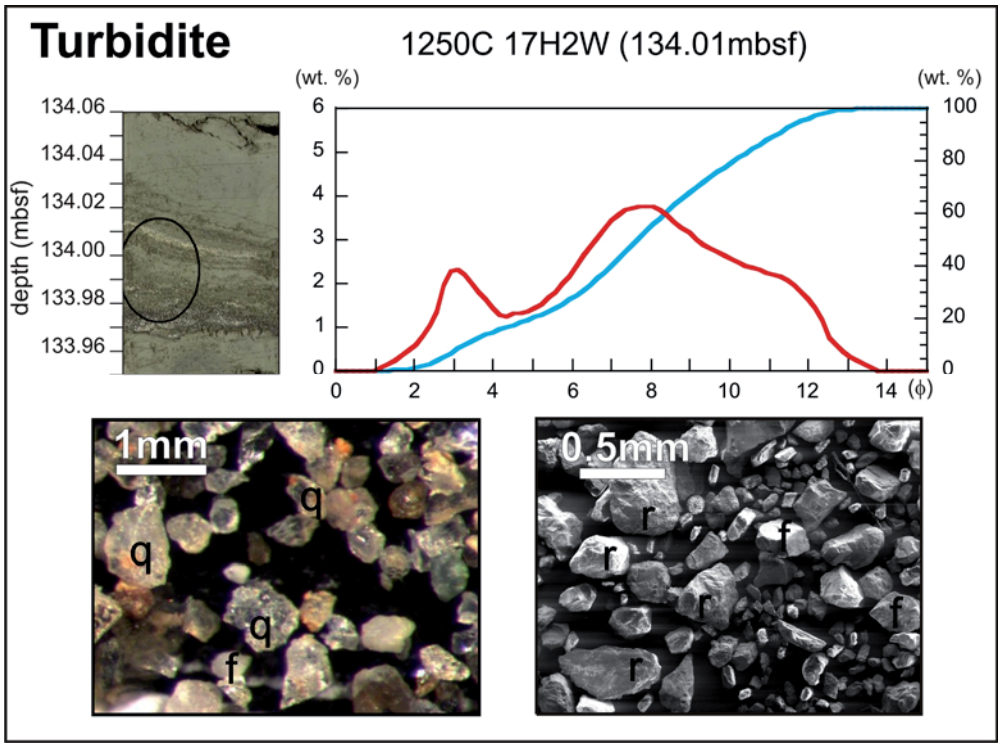

Figure 5.11. Principal textural results of a representative sample of turbidite facies (base) defined at southern Hydrate Ridge (ODP Leg 204-1250C-17H2; 134.01 mbsf), including detailed digital image of the sampled core section, granulometric distribution curves (histogram in red; cumulative curve in blue), and optical microscope and scanning electron microscope images of coarse silt and sand fraction (>50μm). q= quartz grain; f= feldspar mineral particle; r= rock fragment; mbsf= meter below sea floor; ϕ= phi; wt. %= weight percentages.

Of all the analysed turbidite samples, only fifteen correspond to the lower part of the turbidite Bouma sequence (Ta and/or Tb divisions) (Bouma, 1962), and 33 were identified as characteristic of the turbidite tail (Te). The turbidite bases are formed by coarser-grained particles (up to 30.4% sand) with a mean diameter of up to 6.7ϕ Their granulometric distribution parameters are similar to those of the other turbidite samples (Figure 5.9), and the mineralogy of their >50 μm particles is also similar, with only a slight decrease in the content of biogenic particles (up to 10%). Sediment grain-size distributions of the turbidite tail samples (averaged 59% clay, 40% silt and 1.6% sand) are similar to the hemipelagites, but their sand content is slightly higher (up to 4%). The content of biogenic particles is relatively low (up to 9.5% of the coarse fraction), and the magnetic susceptibility values (average $1.6 \cdot 10^{-7}$ m^3/kg) are lower than the samples from other positions in the Bouma sequence (bases and middle positions).

Twenty-one of the total samples classified as turbidite facies contain significant amounts of foraminifera shells (averaged 15% of the total coarse particles identified) and their magnetic susceptibility values are lower than those in detrital turbidites. We classified them as biogenic turbidites, including samples form the turbidite base and tail. Some of these samples, have a high carbonate content (up to 26% in sample 1246B-1H3-51 cm, 3.51 mbsf) versus the 5% average of the rest of turbidite samples (Figure 5.5).

5.2.3. Volcanic ash

Seventeen samples analysed in this study of southern Hydrate Ridge correspond to beige coarse-grained sediments (averaged 49% clay, 45% silt and 6% sand) (Table 5.1). Their mean diameter ranges from 6.2ϕ to 8.7ϕ, with an average of 8ϕ (Figure 5.12). They are very poorly sorted samples (SD averaged 2.1ϕ) (Figure 5.9), with a skewness of up to -0.3ϕ. The SD of volcanic ash samples ranges from 1.8 to 2.4ϕ, which gives rise to an almost horizontal distribution in Figure 5.9.

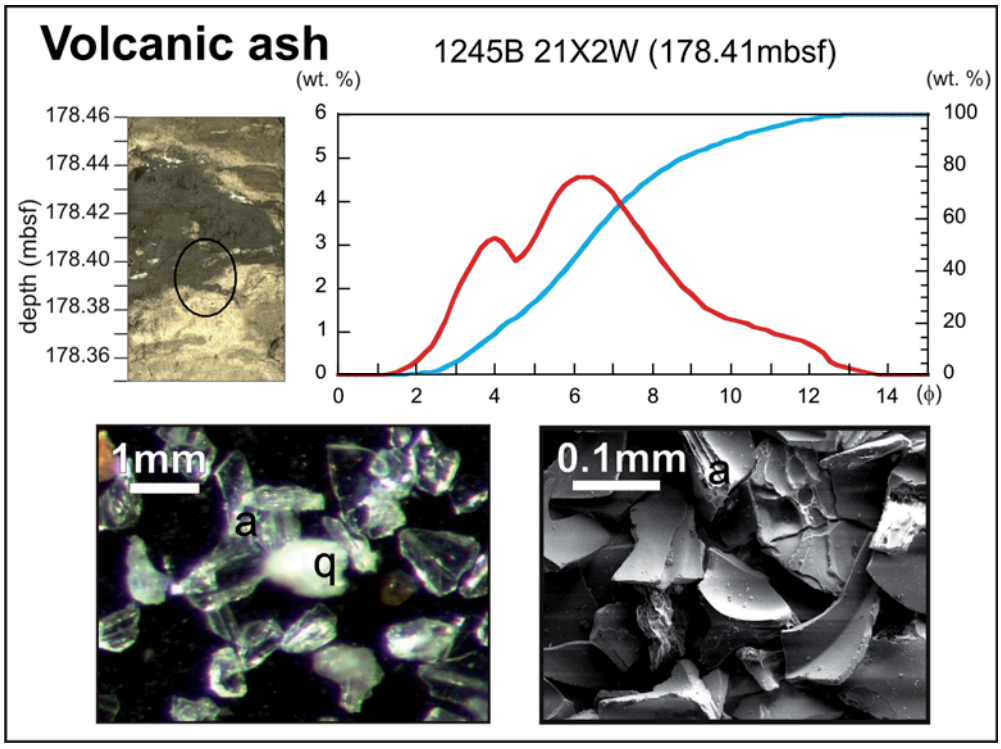

Figure 5.12. Principal textural results of a representative sample of volcanic ash facies defined in southern Hydrate Ridge sediments (ODP Leg 204-1245B-21X2; 178.41 mbsf) including digital image of the sampled core section, granulometric distribution curves (histogram in red; cumulative curve in blue), and optical microscope and scanning electron microscope images of coarse silt and sand fraction (>50μm). q= quartz grain; a= ash particle; mbsf= meter below sea floor; ϕ= phi; wt. %= weight percentages.

All the samples that belong to this facies show a clear bimodal shape in their granulometric distribution curve, with a mode value near 6ϕ and another one at ~4ϕ. Optical microscope

identification and SEM analyses of the coarser particles demonstrate that they are formed by volcanic ash and glass particles, which also explains their low magnetic susceptibility values (averaged 1.3 $\cdot 10^{-7}$ m^3/kg) (Figure 5.12). The mineralogy of the volcanic ash-rich layers is mostly composed of clays (averaged 40%) and quartz (39%), with variable amounts of feldspars (17%) and calcite (5%). The clay mineralogy of these samples is very similar to the hemipelagic facies (averaged 43% detrital mica, 23% smectites, 20% chlorite and 13% kaolinite).

5.2.4. Debrite

Eight of the analysed samples from the summit and western flank of southern Hydrate Ridge were classified as debris flow deposits. They are greenish-grey silty-clays containing greyish mud clasts and showing soft-deformation structures (Figure 5.13).

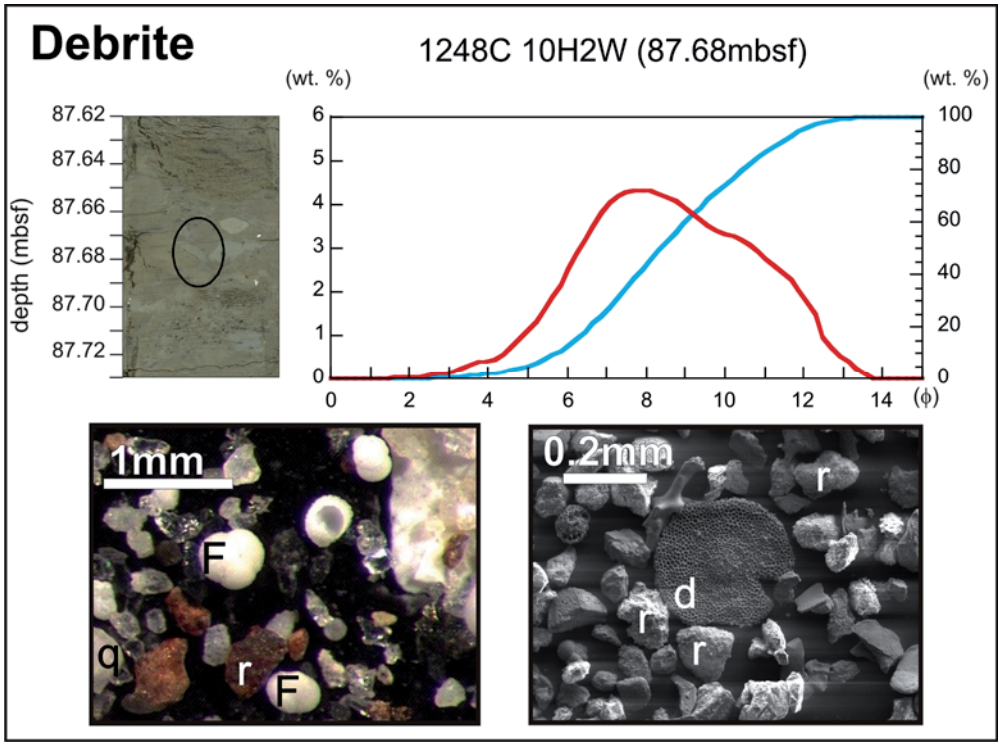

Figure 5.13. Principal textural results of a representative sample of debrite facies defined in southern Hydrate Ridge sediments (ODP Leg 204-1248C-10H2; 87.68 mbsf), including detailed digital image of the sampled core section, granulometric distribution curves (histogram in red; cumulative curve in blue), and optical microscope and scanning electron microscope images of coarse silt and sand fraction (>50μm). q= quartz grain; r= rock fragment particle; F= foraminifera shell; d= diatom; mbsf= meter below sea floor; ϕ= phi; wt. %= weight percentages.

On average, they are composed of 59% clay, 39% silt and <2% sand, with an averaged mean diameter of 8.5ϕ, ranging from 8.3ϕ to 8.7ϕ. Their averaged SD is 2ϕ (Figure 5.9), with a skewness of -0.14ϕ. The sedimentological distribution curves of the debrites are similar to those of the hemipelagite facies samples, with a unimodal shape (mode 7.5ϕ) (Figure 5.13). In general, coarse grain identification yielded similar results for the hemipelagite samples, with

only a relative increase in the broken foraminifera shells content averaged 51% (41% in the hemipelagite facies). As for the bulk mineralogy of the debrites, these are characterized by relatively high contents of quartz (averaged 41%) and feldspars (18%), and lower amounts of clays (36%) and carbonates (5%) with respect to hemipelagites. Mineralogy of clays is composed of 45% detrital mica, 21% smectites, 21% chlorites and 13 % kaolinite (Table 5.1).

5.3. Lithofacies distribution in southern Hydrate Ridge

As stated in Chapter 3, during the ODP Leg 204 cruise, five sedimentological units have been defined onboard using the available seismic data, visual core descriptions, smear slides analyses and physical properties measured by different MSCL (Tréhu et al., 2003) (Figure 3.4). Chevalier et al. (2006) after re-interpreting the multichannel seismic data, defined and modified the southern Hydrate Ridge seismic units, that were increased from five to seven (Units S.VII to S.I) (Figure 3.5). Here, we present a new interpretation of the lithostratigraphic units defined at southern Hydrate Ridge, based on the new textural data presented in this thesis, which includes grain-size, identification of the coarse fraction, magnetic susceptibility and clay and bulk mineralogy. Unit S.VI and VII have been defined as seismically very similar (Chevalier et al., 2006), and given that no sedimentological differences were detected between the two units in this study, we have considered them as a single unit, which is hereafter referred to as Lithostratigraphic Unit (LU) VI (Figure 5.14). The limits between the LU presented here were fixed in accordance with the main seismic reflectors or with significant changes in the lithology of the southern Hydrate Ridge sediments. The position of the boundaries mainly coincides with the limits defined by Chevalier et al. (2006) (Figure 3.5). The main reflectors, identified in the southern Hydrate Ridge multichannel seismic profiles, correspond to changes in the sedimentary facies, e.g. Horizon A and Horizon B', which consist of a number of ash-rich layers interbedded with the hemipelagite facies. Horizons B and Y correspond to turbidite-rich intervals.

The distribution and relative abundance of the defined sedimentary facies in the sedimentary records, and for each LU, of southern Hydrate Ridge was carried out on the basis of their identification in the digital images of the cores, onboard visual core descriptions, density and magnetic susceptibility data measured onboard during the ODP Leg 204 by MSCL at all drilled sites (Sites 1244 to 1252) and the classification of our discrete analysed samples. Especial attention was paid to the identification of gravity flow deposits (turbidites and debrites), which prompted us to pervasively study the abundance and distribution of mass transport deposits in each LU (Table 5.2).

	Summit			W. flank		E. flank		Slope basin		
	Site 1248	Site 1249	Site 1250	Site 1245	Site 1247	Site 1244	Site 1246	Site 1251	Site 1252	
LU IA	-	-	-	-	-	-	-	24 (2)	18 (2)	
LU IB	3	0	0	2	3	5	3	-	24	
LU II	5	0	24	19	43	26	48	-	-	
LU III	27 (10)	11	44 (2)	62 (1)	44	-	0	-	-	
LU IV	-	-	-	-	-	-	-	25	-	
LU V	10	-	-	81 (2)	27 (5)	-	-	-	-	
LU VI	-	-	-	-	-	-	-	25	9 (8)	
Total:	45	11	68	164	117	31	51	74	51	612

Table 5.2. Mass-transport deposits: turbidites and debrites (in brackets) identified in the southern Hydrate Ridge lithostratigraphic units (LU) at each site: Sites 1248 to 1250 at the summit, Sites 1245 and 1247 on the western flank, Sites 1244 and 1246 on the eastern flank and Sites 1251 and 1252 in the slope basin; (see Figure 3.1 for site location). This table integrates data from mass-transport deposits identified during onboard visual core descriptions, digital images of Hydrate Ridge cores and textural results presented in this thesis.

The data presented in this section are new in that the characterization of the sediments from southern Hydrate Ridge was carried out in detail, accurately describing the main sedimentary facies. These sedimentological results allow us to study the horizontal (on space) and vertical (on time) distribution of each lithofacies, presented as a new sedimentological correlation in Figure 5.14. The correlation includes the sedimentological results of the discrete analysed samples as well as the main lithofacies identified in the core digital images. This new correlation is used to assess the parameters that control the distribution of the sedimentary facies over time in the Oregon continental margin. Furthermore, the role of the different horizons and sedimentological facies in the gas-hydrate distribution at southern Hydrate Ridge will be discussed in Chapter 6: "Gas hydrate distribution at southern Hydrate Ridge: relationship with texture and physical properties".

5.3.1. Lithostratigraphic Unit VI

LU VI includes sediments older than 1.6 Ma (late Pliocene to early Pleistocene), and was drilled at Site 1250 at the summit, at Sites 1251 and 1252 in the slope basin as well as at Site 1244 on the eastern flank of southern Hydrate Ridge. The sediments that form LU VI are composed of greenish-grey hemipelagic silty-clays in which a number of mass-transport deposits are intercalated (Figure 5.14; Table 5.2). Mass transport deposits identified in LU VI correspond predominantly to thin turbidite deposits although eight debris flows were also identified at Site 1252 (Table 5.2). LU VI is characterized by a high degree of lithification and micro-fracturing (Shipboard Scientific Party, 2003b, 2003d, 2003e), consistent with its high

compaction at great depths (>300 mbsf). The sedimentological internal structures are poorly preserved in this unit although lamination and soft deformation can still be recognized in most of the mass-transport deposits. Glauconite-rich layers at the top of this sequence were onboard identified at Sites 1250, 1251 and 1252, and where interpreted as an indication of extended periods of exposure on the seafloor and low sedimentation rates near 1.6 Ma ago (Shipboard Scientific Party, 2003b, 2003c, 2003d, 2003e) (Figure 5.8). Nevertheless, there were not found significant glauconite-rich contents in the XRD results of the samples from this LU, probably due to our wide sampling resolution.

5.3.2. Lithostratigraphic Unit V

LU V is a >300 meters thick sequence (e.g. Site 1245, Figure 5.3) composed of greenish-grey hemipelagic sediments that include numerous mass-transport deposits: 10 turbidites were identified in LU V at Site 1248, the summit Site closest to the western flank of southern Hydrate Ridge, and 81 and 27 turbidite facies intervals were identified at Sites 1245 and 1247, respectively on the western flank of southern Hydrate Ridge (note the different thickness of the drilled section at each of these sites; Figure 5.14). A number of intervals with mud clasts and soft deformation structures, corresponding to debris flow deposits, were also recognized in LU V. Debris flow deposits from southern Hydrate Ridge are few meters thick (up to 5 m) and consist of greyish-green clay clasts of centimetric diameter (10-15 cm) included in a greenish muddy matrix with numerous deformational structures. LU V was deposited from 1.6 to 1.0 Ma (early Pleistocene). Horizon A, a 2- to 10-m-thick, coarse-grained, volcanic-ash facies sequence, interpreted as a major fluid flow conduit in the southern Hydrate Ridge region, corresponds to its upper limit (Tréhu et al., 2003).

5.3.3. Lithostratigraphic Unit IV

LU IV is a locally thick deposit (~130 meters) developed in the eastern part of southern Hydrate Ridge, and was only drilled at Site 1251 in the slope basin (Figure 5.14). It consists of greenish-grey hemipelagite sediments, with relatively low content in biogenic particles and high abundance of terrigenous particles (Figure 5.7). It is characterized by a very rapid deposition (~160 cm/ky), with the presence of numerous turbidites (25; Table 5.2). LU IV was deposited from 1 to 0.3 Ma (early to middle Pleistocene), contemporaneously with LU III and II and the compressional phase leading to the formation of Anticline B (Shipboard Scientific Party, 2003h; Figure 3.3).

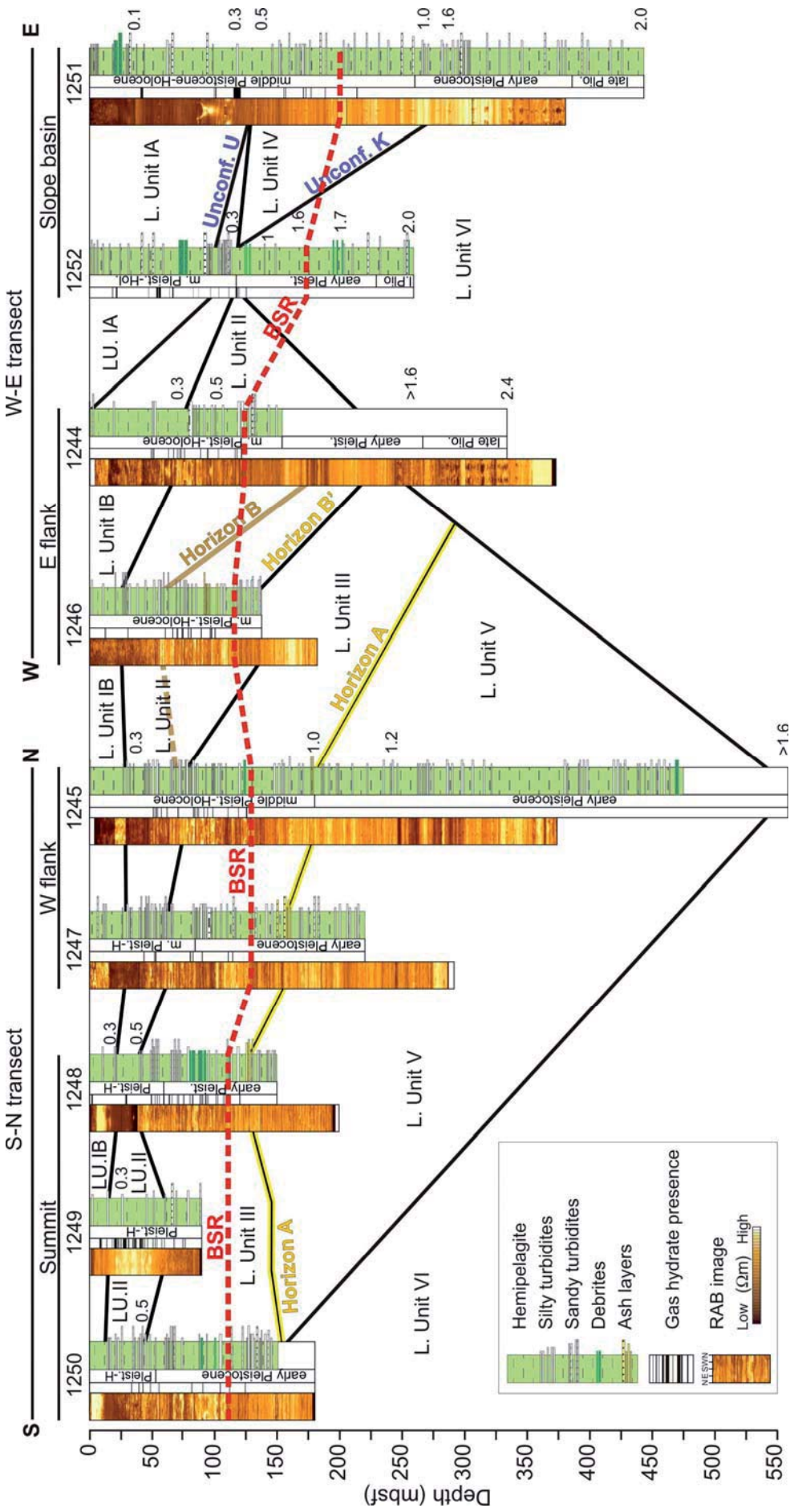

Figure 5.14. Sedimentological correlation of analyzed sediments from southern Hydrate Ridge (Sites 1244 to 1252). Lithostratigraphic units (LU), resistivity at the bit (RAB) images, and gas hydrate presence inferred from infra-red images, chlorinity anomaly data and visual recognition are also shown for each site. Numbers indicate ages in million of years before present inferred from onboard studies of micropaleontology assemblages; mbsf= meter below sea floor (Tréhu et al., 2003).

5.3.4. Lithostratigraphic Unit III

Dark greenish-grey hemipelagite sediments form LU III, with relatively frequent sandy-silt and silty turbidite deposits (Table 5.2), which infer a sedimentation rate of 13 cm/ky to this LU (Shipboard Scientific Party, 2003b, 2003d). Turbidites from this LU are thin sandy silt deposits (up to 40 centimetres thick), with sharp erosional bases and fining upward sequences. Internal sedimentation structures such as cross and parallel lamination are observed in the thickest turbidites. In some intervals, turbidite sequences composed of various pulses show an upward decrease trend in grain-size as well as in thickness (Figure 5.14). LU III lies on top of LU V at the summit and western flank of southern Hydrate Ridge (Sites 1248, 1249, 1250, 1245 and 1247). It is limited by Horizon A at the base. The upper boundary of LU III on the western flank of southern Hydrate Ridge coincides with Horizon Y detected in the seismic data (Figure 5.3; Figure 5.9). Horizon Y is assumed to represent an angular unconformity or a thrust fault (Shipboard Scientific Party, 2003b, 2003d). Deposition of LU III took place from 1 to 0.5 Ma (middle Pleistocene) at the summit and western flank of southern Hydrate Ridge, in a sedimentological ambient of lower slope basin, which was created simultaneously with Fold F (Figure 3.6).

5.3.5. Lithostratigraphic Unit II

LU II consists of dark greenish-grey hemipelagite clays and silty clays commonly interbedded with fine sand turbidite layers. Turbidite deposits at LU II show typical fining upward sequences, cross and parallel lamination and erosional bases. They are turbidite sequences composed of various depositional pulses showing a relative upwards decrease in grain-size as well as in turbidite thickness (Figure 5.14). Turbidites are especially abundant on both flanks of southern Hydrate Ridge (Sites 1244 to 1247) (Figure 5.14), with up to 43 and 48 turbidite intervals identified at Sites 1247 and 1246, respectively (Table 5.2). Horizon Y represents the lower limit of LU II (Figure 5.1; Figure 5.3). Horizon B and B' are two seismic reflectors recognized within LU II, in which gas hydrate or free gas were recovered depending on whether they were sampled within or underneath the GHSZ. Horizon B is a seismic reflector with low content of biogenic components (Shipboard Scientific Party, 2003b), whereas reflector B' is made up of several volcanic glass-rich intervals interbedded with the hemipelagite sequence. LU II was deposited from 0.5 to 0.3 Ma (middle Pleistocene) contemporaneously with the reactivation of the Dome uplift.

5.3.6. Lithostratigraphic Unit I

LU I is divided into LU IB and LU IA. LU IB was identified at all the drilled Sites of this study, while LU IA is only present in the slope basin adjacent to southern Hydrate Ridge

(Figure 5.14). LU IB and IA fill a regional basin that has been deepening to the South over time as southern Hydrate Ridge has being uplifted (Chevalier et al., 2006).

The ages of the youngest turbidite event identified on the sedimentary column have been calculated after the sedimentation rate at each Site (Figure 5.14; Table 5.3). The sedimentation rates were estimated during ODP Leg 204 cruise for each site in basis of the micropaleontology assemblages (Tréhu et al., 2003). The large age uncertainty is due to the difficulty in identifying turbidite deposits in the digital core images. There is also an uncertainty in the calculation of the age of the deposit owing to the consideration of a constant sedimentation rate for the whole unit and the presence of numerous mass-transport deposits and erosional gaps in the sedimentary record.

	Site	LU	Sedimentation rate (cm/k.y.)	Depth of the shallowest turbidite (mbsf)	Estimated turbidite age (k.y.)
Summit	1248	IB	21	10	47
	1249	IB	5	2-3	40-60
	1250	IB	15	15	100
W. flank	1245	IB	23	0-3	<13
	1247	IB	13	6-12	46-92
E. Flank	1244	IB	27	2-3	7.5-11
	1246	IB	31	0-2	<6.5
Slope basin	1251	IA	120	2-6	1.5-6
	1252	IA	28	1-7	3.5-25

Table 5.3. Calculated age of the shallowest turbidite interval identified in the sedimentary sequence of each drilled site from southern Hydrate Ridge. Estimation depends directly on the sedimentation rate onboard calculated for LU IA and IB in basis of their micropalaeontological assemblage; mbsf= meter below sea floor (Shipboard Scientific Party, 2003a to 2003i).

The estimated ages for the youngest turbidite event of each site range from 1.5 to 100 k.y. (Table 5.3). Younger gravity flow deposits were identified on the eastern flank and slope basin of southern Hydrate Ridge, with Holocene values (6.5 to 11 and 1.5 to 25 k.y., respectively), whereas turbidites from the summit and western flank of southern Hydrate Ridge result older (up to 100 years and 92, respectively).

- Lithostratigraphic Unit IB: LU IB lies unconformably on top of LU IV in the slope basin adjacent to southern Hydrate Ridge (Figure 5.14). It is mainly formed by hemipelagic silty-clays, with sparse coarse-grain layers (up to 5 turbidites identified at Site 1244). The limit between LU II and LU IB coincides with Horizon X on the eastern flank of the studied area (Figure 3.16; Figure 5.5), which was identified in the seismic data but did not correspond to any significant textural change. LU IB comprises the time interval from 0.3 to present (middle

Pleistocene to Holocene), during the uplift of the Dome and the relative subsidence of Anticline B. Few turbidite deposits (up to 3 events) are present in the first meters (<15 mbsf) of the sedimentary column at all sites from the summit and the flanks of southern Hydrate Ridge, corresponding to ages ranging from 6.5 to 100 k.y.

- Lithostratigraphic Unit IA: LU IA lies on LU IB and it is located in the slope basin adjacent to southern Hydrate Ridge (Sites 1251 and 1252; Figure 5.14). LU IA contains numerous turbidites (24 and 18 at Site 1251 and 1252, respectively), as well as two debris flow deposits at each Site. The first turbidite event identified at Site 1251 has an approximate age of 1.5 to 6 k.y., whereas at Site 1252 it has an approximate age of 3.5 to 25 k.y. These ages were estimated after the sedimentation rate calculated onboard during ODP Leg 204 (Shipboard Scientific Party, 2003h, 2003i). The lower limit of LU IA coincides with Unconformity U, regionally detected in the seismic profiles (Shipboard Scientific Party, 2003h). LU IA forms in the slope basin of southern Hydrate Ridge (Site 1251 and 1252) probably as sediments from the summit and eastern flank are destabilized, representing the local re-working of sedimentary material (Chevalier et al., 2006). LU IA constitutes the recent sedimentation from 0.2 M.a. to the present (late Pleistocene to Holocene) in the slope basin. This unit grows coevally with the Anticline B subsidence and the tectonic uplift of southern Hydrate Ridge.

5.4. Paleoenvironmental reconstruction of southern Hydrate Ridge

Analysing the downcore distribution of the sedimentary facies at the nine drilled sites of southern Hydrate Ridge (Figure 5.14), two different groups of lithostratigraphic units are differentiated as a function of their sedimentological properties and their depositional environment:

The first group, comprising LU VI and V is characterized by the presence of relatively thin and sparse turbidites interbedded with the hemipelagic sediments (Figure 5.14). The sedimentation rate of these units is moderate, up to 70 cm/ky in LU V (Tréhu et al., 2003). Earlier studies suggested that units coeval with LU VI and V from southern Hydrate Ridge were deposited in a deep-sea fan environment in the Cascadia abyssal plain during the Pliocene-early Pleistocene period before the southern Hydrate Ridge uplift (Camerlenghi et al., 1995).

The second group comprises the uppermost LU IV to I. They consist of abundant turbidites and other mass transport deposits interbedded with the hemipelagic background sediment (Figure 5.14). This uppermost sequence was mainly deposited in a slope basin environment, with very high sedimentation rates, up to 160 cm/ky estimated in LU IV at Site 1251 (Chevalier et al., 2006). The slope instability processes that occurred during the middle Pleistocene to the

present-day period defined a high frequency turbidite record, such as LU III at Sites 1245, 1247, 1248, 1250 from the summit and western flank, with up to 62 events at Site 1245, or LU II at Sites 1245, 1247, 1246, with up to 48 turbidite deposits at Site 1246 (Figure 5.15; Table 5.2). The episodes of high turbidite occurrence have been attributed to periods of reactivation of the tectonic uplift of southern Hydrate Ridge (Figure 3.16) (Chevalier et al., 2006).

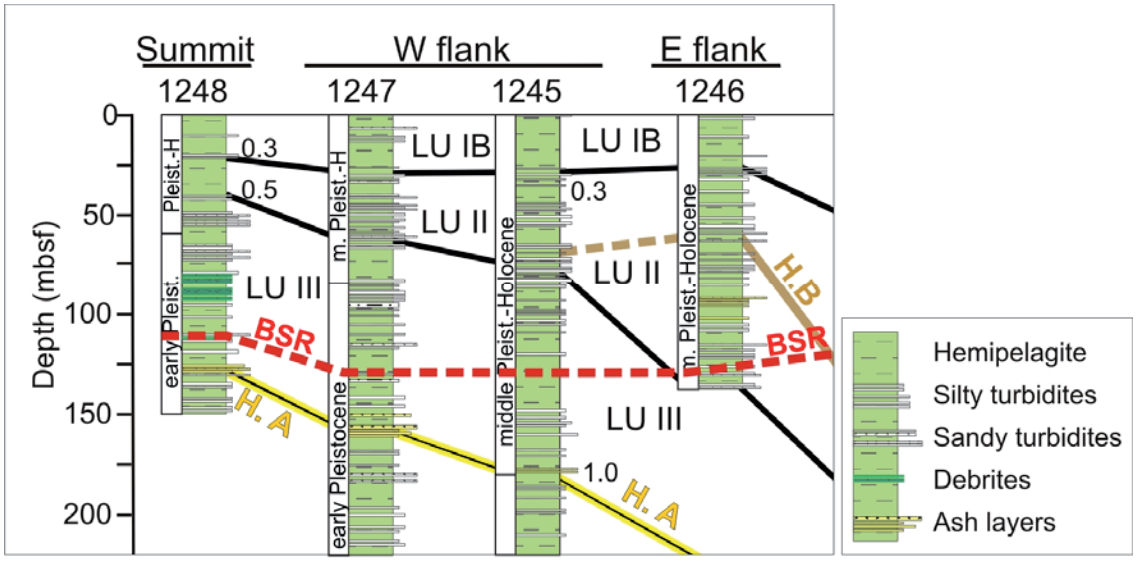

Figure 5.15. Detail of the facies distribution in Lithostratigraphic Unit (LU) II and III at Sites 1248, 1245, 1247, and 1246 at the summit, western and eastern flanks of southern Hydrate Ridge, based on textural analyses of sediment samples and identification of mass-movement deposits in the onboard high resolution images of the cores. Seismic horizons (HA= Horizon A; HB=Horizon B; BSR=Bottom Simulating Reflector) and the main available ages are labelled; mbsf= meter below sea floor.

5.4.1. Provenance and sediment source

Sediments forming southern Hydrate Ridge are mainly made up of hemipelagites, turbidites and debrites. Hemipelagites contain 5-75 volume % of fine particles corresponding to biogenic components, which mainly reach the seafloor by natural settling through the sediment column (Friedman and Sanders, 1978; Encyclopædia Britannica, 2009). They also contain varying amounts of terrigenous components. In this chapter the different processes and parameters that affect the terrigenous material transport and deposition to form hemipelagites, turbidites and debrites will be discussed from the Source-to-Sink point of view. The issues include: the role of changing tectonics, climate and sea level as forcing functions in the production, transport and deposition of sediments; the role of transport in the system altering the sedimentary facies preserved in southern Hydrate Ridge sediments (Margins office, 2003).

As regards the sediment input from the continental shelf area, the primary hydrodynamic processes that govern sediment transport in continental margins affect both suspension transport of fine-grained sediments as well as bedload transport of coarse-grained materials. The main processes affecting weathering and clay-sediment suspended transport from onland continental areas and into the marine continental margins include: surface currents, movement of the near-bottom nepheloid layer by bottom currents, deep water currents along or across submarine canyons, effect of climate change on the balance between chemical and physical weathering, accelerated continental erosion, linkage between submarine canyons and shoreline during eustatic sea-level fluctuations and hyperpycnal discharge from glacial meltwater and river floods (e.g. Pierce, 1976; Pye, 1994). Therefore, the clay mineralogy assemblage of a deep-sea largely depends on climate, relief, lithology of the source area and tectonic activity (e.g. Keller, 1970; Chamley, 1989).

On the other hand, main bedload processes affecting downslope sediment transport include turbidity and other gravity flows through the main canyons, direct sediment supply through the continental slope and local re-working processes (e.g. Duncan and Kulm, 1970). The sedimentary facies produced by these processes include both coarse and fine grained fractions. Thus, the clay mineral association of the coarse materials is also controlled by the source rock, largely depending on the local type of basement, and the paleoflow pattern (Dinis and Soares, 2007).

In the case of the Oregon margin, the sediment supply pathways through rivers, channels and canyons, and the main superficial and deep currents operating in the area are relatively well known (e.g. Nelson, 1976; Karlin, 1980; Duncan and Kulm, 1970; Underwood and Torres, 2006; Herbert et al., 2001; Winograd et al., 2002; Underwood et al., 2005) (Figure 5.16). These studies demonstrate that smectites are the most common clay minerals reaching the Oregon margin from the Columbia River, while chlorites and detrital micas are preferentially directly supplied from the Klamath Mounts (southern Oregon). However, clay mineral distribution patterns also record the dominant dispersal pathways of the region and are strongly influenced by the coastal currents (e.g. Karlin, 1980; Krissek, 1982; Lyle et al., 2000). Herbert (2001) postulated that the extension of the California Current fluctuated during the Pleistocene, as a function of the glacial-interglacial sea-level cycles (Figure 5.17). Unfortunately, the chronostratigraphic model of southern Hydrate Ridge sediments is not accurate enough, making it difficult to evaluate the importance of each individual suspended transport process during each period. This is mainly caused by the high frequency of sea-level fluctuations during the Pleistocene and the limited extension of the studied area. Hence, a simplified view of the sea-level oscillations was considered (Haq et al., 1987) (Figure 5.17).

As regards the bedload transport and sedimentation in the Oregon continental margin the three main processes considered are: a) turbidite events from the Columbia River along the Astoria and Willapa canyons; b) direct sediment supply from the Klamath Mounts; and c) local re-working sedimentary processes (Figure 5.16) (e.g. Sternberg, 1986). Likewise, Krissek (1984) proposed that the Oregon-Washington slope acts as an effective trap for the 2-20μm material (clays to medium silts) for proximal source areas.

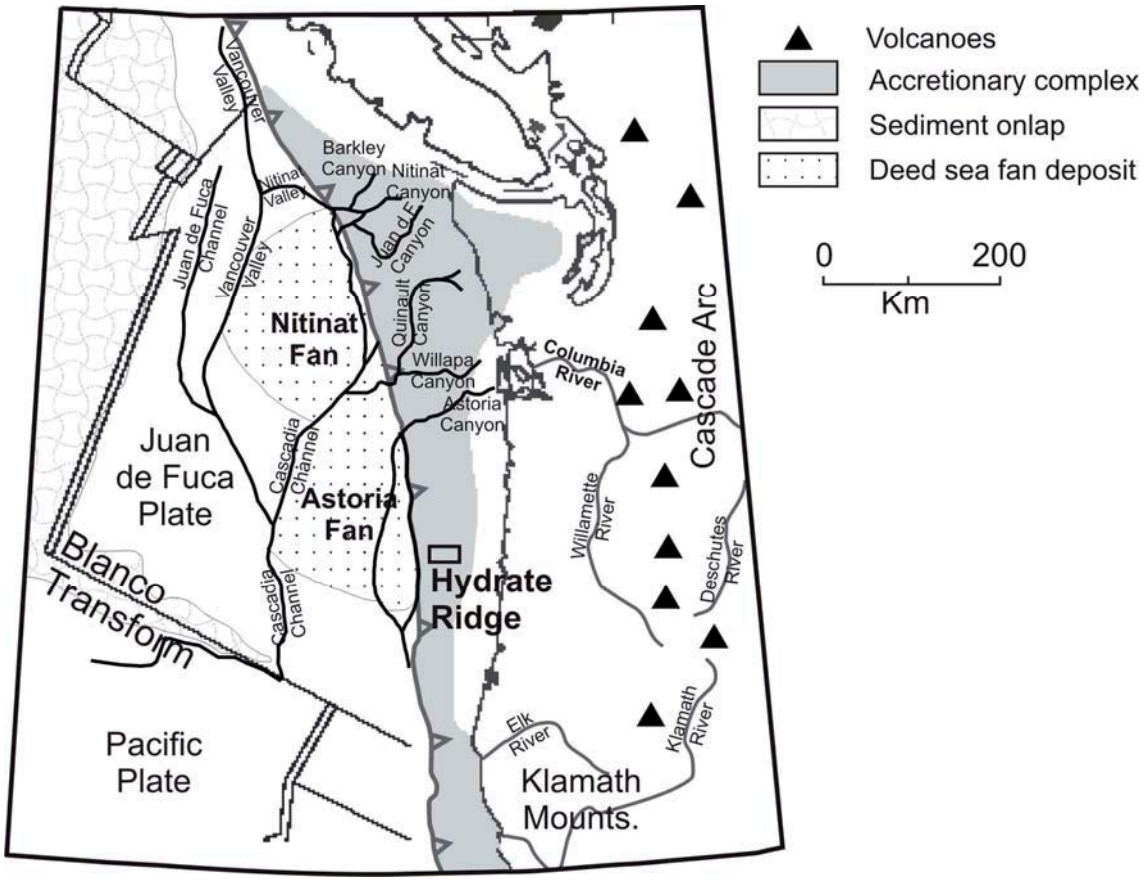

Figure 5.16. Tectonic-morphological map of the main supply areas and sediment transport pathways (rivers, canyons and valleys) in the Oregon - Washington continental margin. Southern Hydrate Ridge, the accretionary complex area and the main onland volcanoes of the region are depicted. Heavy grey line with teeth represents the approximate position of the Cascadia subduction front (modified from Underwood et al., 2005).

5.4.2. Climatic control on southern Hydrate Ridge sedimentation

A decrease in the smectite content over time was detected in some of the analysed sites of southern Hydrate Ridge (Figure 5.3; Figure 5.5). The decreasing trend in the smectite content can be clearly observed at Sites 1245 and 1247 located to the North on the western flank of southern Hydrate Ridge, close to the Columbia River influx. These results suggest that, during the early Pleistocene when LU V was deposited, the suspended transport processes were more effective transporting fine-grained materials southwards from the Columbia River into the

Hydrate Ridge area. The suspended transport reduced its competence during the middle and late Pleistocene as the relative global sea-level decreased.

The main factor affecting the sediment supply input from the Columbia River into the Oregon margin is the onland weathering and the extension of the affected area. Since a decrease in sea level occurred during the Pleistocene, (e.g. Haq et al., 1987; Pazzaglia et al., 2003) (Figure 5.17), the extension of the continental shelf and consequently the weathered area increased, enlarging the weathering importance as a controlling factor for the sediment supply in the Oregon margin. Other factors affecting sediment supply in southern Hydrate Ridge are directly related to transport along the Oregon continental margin, such as the California Current, which is one of the main hydrodynamic processes affecting the southward sediment transport of fine-grained particles. The gradual decrease in smectite content during the Pleistocene discussed above suggests that the California surface current was highly efficient during the early Pleistocene (Figure 2.4), while the Oregon-Washington slope acted as an effective trap for the 2-20μm material (clays to medium silts) (Krissek, 1984) (Figure 5.16). The long distance transport of suspended material from the Columbia River was gradually reduced during the Pleistocene as the global sea level decreased (Figure 5.17), and the California Current reduced its competence.

The sediment material transported in suspension shows a relatively upward decrease (over time) in the sediment column, whereas mass-transport deposits are more abundant at LU II and III at the summit and flanks of southern Hydrate Ridge and in LU IV in the slope basin (e.g. Figure 5.14). The turbidite-enriched record of LU II and III at the summit and on both flanks of southern Hydrate Ridge suggests that bedload sediment transport assumed greater importance during the middle Pleistocene. These turbidites do not show a high smectite content as would be expected if the sediment came from the Columbia River through the Astoria Canyon (Figure 5.16). Therefore, the results suggest that the direct bedload sediment supply from the Klamath Mountains and local re-working processes in the Oregon margin became more prominent during the middle Pleistocene. In this scenario, local re-mobilization of sediments from the flanks and summit of southern Hydrate Ridge would also have been responsible for the mass-transport deposits identified in LU IV in the slope basin of southern Hydrate Ridge (Chevalier et al., 2006). In this regard, the sediment trapped in the continental margin during the early Pleistocene would have also been re-mobilized and re-incorporated into the sedimentary system (Krissek, 1984).

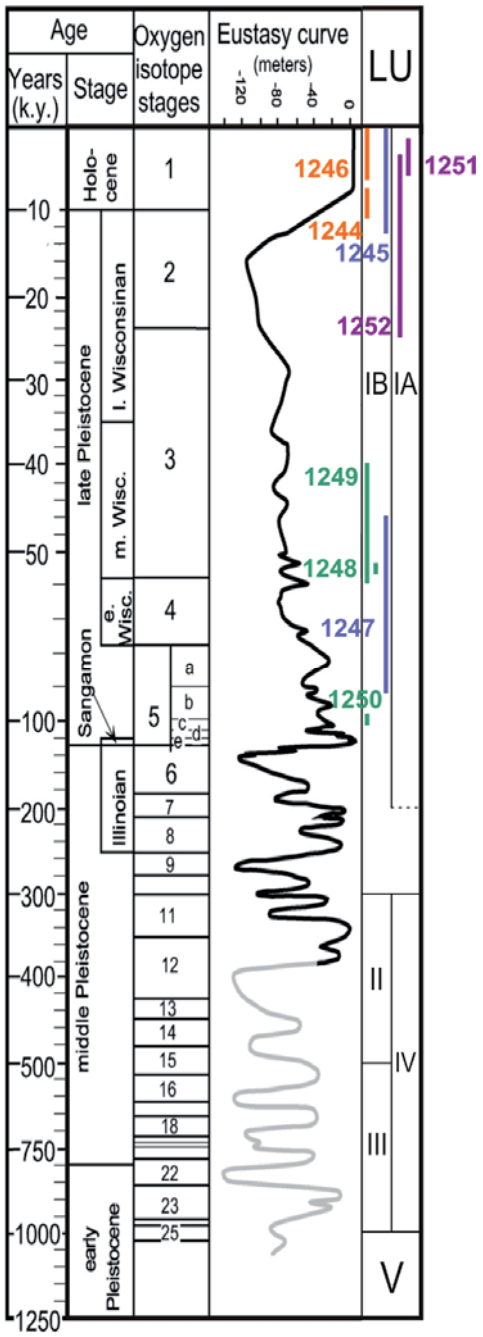

Figure 5.17. Reconstruction of global sea-level changes during the last 1.25 My (Holocene and most Pleistocene). Note the variable scaling in the time axis. The oxygen isotope stages are also labelled from 1 to 25. Note that over most of the Pleistocene history the averaged sea level has been significantly lower than today. Lithostratigraphic units (LU) defined in this thesis are depicted; the youngest turbidite events identified in the sedimentary sequence are depicted for each Site drilled during ODP Leg 204 in different colours: green=summit; blue=western flank; orange=eastern flank; violet=slope basin (modified from Pazzaglia et al., 2003).

5.4.3. Tectonic control on southern Hydrate Ridge sedimentation

The tectonic uplift of Hydrate Ridge has been dated as the late Pleistocene (Chevalier et al., 2006). A number of authors have interpreted the sedimentation at southern Hydrate Ridge during the late Pleistocene as having been controlled by the migrating depocenters sequentially generated during the tectonic events causing the uplift of Hydrate Ridge (Chevalier et al., 2006; Johnson et al., 2006). The tectonic reactivation of the continental margin, the changes in sea level and the subduction movement of the Juan de Fuca plate could be the possible triggering

mechanisms of the frequent slope destabilization movements during the late Pleistocene (i.e. LU IA and IB). The massive dissociation of gas hydrate due to the reduction of the GHSZ as a consequence of the sea-level decrease is another possible triggering mechanism that will be discussed below.

Bedload transport from the Klamath Mounts and from re-worked material became dominant in the entire Oregon continental margin (Duncan and Kulm, 1970) during the Holocene as in the Pliocene (Kulm and von Huene et al., 1973; Scheidegger et al., 1973). In this scenario, the turbidite events described in the last meters of the sedimentary column (i.e. <15 mbsf) at Sites 1244, 1245 and 1252 correspond to the last historical sea-level low-stand period (i.e. last glacial maximum) (Table 5.3; Figure 5.17). On the other hand, mass-transport movements have been described for the Holocene at Sites 1246 and 1252 on the eastern flank and in the slope basin adjacent to southern Hydrate Ridge, providing evidence of the active sedimentation in these areas. At Sites 1248, 1249 and 1250 at the summit of southern Hydrate Ridge, no mass-transport deposits have been described since 40 - 100 k.y., suggesting that erosion due to destabilization of local mass-transport movements has been a major process in this area generated by the recent tectonic reactivation of southern Hydrate Ridge (e.g. Johnson et al., 2003; 2006; Chevalier et al., 2006).

In conclusion, sediments of LU VI and V were deposited during a high sea-level stand period in an abyssal plain environment such as distal parts of the Astoria Fan. These units contain smectite-rich sediments mainly coming from the Columbia River and transported by the California surface current (Figure 5.14). Our data suggest that, mass-transport deposits generated by the local recycling of abyssal plain sediments and sediments coming from Klamath Mounts gradually assumed greater importance during the middle Pleistocene in LU IV to II, as the tectonic events initiated the construction of Hydrate Ridge. The California current lost competence during the late Pleistocene as the sea level decreased towards the last glacial-maximum event, producing a decrease in the smectite content in the sediments. During the Holocene and under conditions of sea-level high-stand, the reactivation of the tectonic uplift of Hydrate Ridge triggered local instability processes that produced erosion at the summit and on the western flank of southern Hydrate Ridge and a number of turbidite events on the eastern flank and in the slope basin. Thus, the data analysed in this thesis supports that the distribution and deposition of Hydrate Ridge sediments have been regionally controlled by a) the growth of the Cascadia accretionary system as the Juan de Fuca plate subducts beneath the North American plate; b) oceanic circulation; and c) sea-level conditions. Locally, sedimentation has been controlled by the tectonic uplift of the different structural highs that form the Oregon margin such as Hydrate Ridge.

5.5. Gravity flow deposits at southern Hydrate Ridge: Triggering mechanisms

Gravity flow deposits (i.e. debrites and turbidites) resulting from mass flows and turbidity currents are commonly found in sediments from southern Hydrate Ridge interbedded with the hemipelagites. Their distribution in the sedimentary register is different in every depositional environment of southern Hydrate Ridge.

The relative abundance of submarine mass-transport deposits in the sedimentary sequence with more than 500 identified events suggests that slope instability has been a recurrent process in the southern Hydrate Ridge region over time (Table 5.2). Other evidence of slope instability includes large erosive scars and seafloor rupture surfaces recognized by their superficial expression in high-resolution bathymetric maps (e.g. Tréhu et al., 1999; Goldfinger et al., 2000; Canals et al., 2004) (Figure 2.5), and stratigraphic unconformities identified in the multichannel seismic record, such as unconformity U, which corresponds to a slope failure occurred during the formation of Anticline B 0.2 Ma ago (Chevalier et al., 2006) (Figure 3.16).

Submarine mass movements are caused either by an increase in the environment loads, a decrease in the strength of the sediment or a combination of both (Locat and Lee, 2002). The processes that could trigger submarine mass movements in continental margins include oversteepening, seismic loading, storm-wave loading, rapid sediment accumulation and under-consolidation, gas charging, gas hydrate dissociation, low tides, seepage, glacial loading and volcanic island processes (Locat and Lee, 2002). Given that the Oregon margin is a seismically active margin (Figure 2.1), most studies based on Holocene sediment cores from this area have focused on earthquakes to account for the main triggering mechanism for turbidity currents and debris flow deposits (e.g. Adams, 1990, Goldfinger et al., 2003; 2006). These studies minimized the importance of gas hydrate dissociation. The turbidite paleoseismology method has been successfully applied to the Quaternary turbidite record of the Oregon margin, obtaining a recurrent rate of about 300 years for large earthquakes. The “confluence test” has been applied to establish the synchronicity of the turbidite events (Goldfinger et al., 2006). Nevertheless, the synchronicity hypothesis cannot be applied in this study because most of the analyzed turbidites are from the Pleistocene, and there are global processes that could generate coeval widespread turbidites during this period (i.i. sea-level changes). Furthermore, turbidites of southern Hydrate Ridge are located on both flanks of a structural high located on the margin slope, which includes a large quantity of gas hydrates (e.g. Tréhu et al., 2004b). In this environment, although we cannot rule out a seismic trigger hypothesis, gas hydrate dissociation produced by a decrease in sea-level together with the tectonic uplift of the ridge seems to be the most likely triggering

mechanism for local mass-transport events especially during the late Pleistocene. Gas hydrate dissociation has been proposed as a major triggering factor for the generation of mass-movements in other margins, such as the Storegga slide in the Norwegian margin (e.g. Bouriak et al., 2000; Reagana dn Moridis, 2007; Sassen et al., 2001).

Paull et al. (1996a) pointed out the direct relationship between slumping frequency and sea-level low-stand in sediments from Blake Ridge, a gas hydrate-bearing submarine area offshore South Carolina. The GHSZ is reduced during sea-level low-stands owing to the lower water column weight (Figure 1.19), whereas pressure is higher during sea-level high-stand, deepening the base of the GHSZ and leading to sediment compaction (e.g. Bangs et al., 2005). Thus, variations in the weight of the water column (due to sea level changes or tectonic uplift) modify the thickness of the GHSZ. Gas hydrates will form only if enough gas and water are available in the GHSZ, resulting in an increase in the sediment cementation and stability of the slope sediments (Sultan et al., 2004a, 2004b).

High frequency distribution of mass-transport deposits in LU III and II of southern Hydrate Ridge sediments coincides with periods of relative sea-level low-stand (middle Pleistocene) (Figure 5.14), suggesting gas hydrate dissociation as a possible triggering mechanism for these processes. The same mechanism can explain the mass-movement deposits during the late Pleistocene (LU IA and IB). As stated above, analogous mechanisms have been described by Bangs et al. (2005) to support an upward shift of the BSR depth, which occurred 18,000 years ago (late Pleistocene). This change in the thickness of the GHSZ took place after the last glacial maximum owing to a temperature increase of 1.75-2.25 ºC in the bottom water, offset by a 120 meter sea level rise (Figure 5.17) (Bangs et la., 2005). The upward shift of the base of the GHSZ could have dissociated gas hydrates, increasing slope instability and producing a number of mass-transport deposits, as observed in the first meters of the sedimentary column of southern Hydrate Ridge sites (e.g. Sites 1244, 1245 and 1252) (Figure 5.14; Figure 5.17). Given that the global sea level has been stable during the Holocene, the tectonic reactivation and uplift of Hydrate Ridge as well as the Juan de Fuca subduction movement seem to be the more plausible triggering mechanisms for sediment mass movements recovered at Sites 1246 and 1251.

6. Gas hydrate distribution at southern Hydrate Ridge: Relationship with texture and physical properties

6.1. Textural results of gas hydrate-rich sediments from southern Hydrate Ridge

In order to establish the relationship between the sedimentological properties and the presence of gas hydrates in sediments from southern Hydrate Ridge, textural analyses of both sediment samples with mousse-like and soupy fabrics and gas hydrate-rich samples were carried out for this thesis. Analyses of grain size, mineral composition, carbonate content, and physical properties such as magnetic susceptibility were integrated with available porosity data onboard measured during ODP Leg 204 by the C method described by Blum (1997) (Shipboard Scientific Party, 2003j).

6.1.1. Textural results of disturbed sediment samples

The soupy and mousse-like samples analyzed from southern Hydrate Ridge show mean grain sizes between 7.7 and 8.8ϕ, sand contents up to 8.9%, and SD ranging from 1.9 to 2.47 (Table 6.1).

Location	Sample Identification	Depth (mbsf)	Sand (wt.%)	Silt (wt.%)	Clay (wt.%)	Mean (ϕ)	SD (ϕ)	Sk	$CaCO_3$ (wt.%)	MS (10^{-7} m^3/kg)	F
Summit	Leg 204-1249C-1H1; 67-69	0.68	1.5	33.2	65.3	8.8	2	-0.3	6.2	1.45	S
Summit	Leg 204-1249C-2H1; 50-52	2.51	1.42	44.3	54.2	8.3	2	0.01	7	1.92	S
Summit	Leg 204-1248C-2X1; 50-52	10.11	5.78	50.6	43.6	7.7	2.2	-0.14	4.8	-	S
Summit	Leg 204-1249C-4H2; 6-8	15.4	3.33	42.1	54.6	8.2	2.2	-0.22	11	1.65	M
Summit	Leg 204-1249C-4H5; 50-52	17.26	1.57	35.3	63.2	8.7	2	-0.3	9.3	1.93	M
Summit	Leg 204-1249C-5H3; 10-12	26.26	1.79	46.5	51.7	8.3	2	0.05	9.4	1.57	M
W flank	Leg 204-1245B-15X1; 50-52	128.3	1.57	42.5	56	8.4	2	-0.06	5.1	1.2	M
W flank	Leg 204-1245B-15X4; 50-52	131.4	8.92	40.7	50.4	7.9	2.4	-0.29	6.3	2.25	M
W flank	Leg 204-1245B-16X1;50-52	138	1.72	40.1	58.2	8.5	2	-0.14	9	1.77	M
W flank	Leg 204-1245B-16X2; 56-58	139.5	4.69	41.4	53.9	8.2	2.2	-0.35	6.2	1.44	M
W flank	Leg 204-1245B-16X3; 50-52	141	3.13	38.2	58.7	8.4	2.1	-0.26	5.8	1.36	M
W flank	Leg 204-1245B-16X5; 50-52	144	2.29	44.8	52.9	8.3	2.1	-0.02	6.4	1.18	M
Average of analyzed disturbed samples			3.14	41.6	55.3	8.3	2.1	-0.17	7.2	1.61	
Average of Leg 204 hemipelagic sediments (124 samples)			0.9	40.9	58.19	8.5	1.9	0.01	6.45	2.0	

Table 6.1. Grain-size results, statistical parameters and magnetic susceptibility values of disturbed sediments from southern Hydrate Ridge. Averaged values of hemipelagic sediments are also known for comparison. mbsf = meter below sea floor; wt.= weight; SD = Standard deviation; Sk = skewness; MS = magnetic susceptibility; F = disturbed fabric: soupy (S) or mousse-like (M) fabric (modified from Piñero et al., 2007).

The mean grain size of samples from the summit of southern Hydrate Ridge (sites 1248 and 1249) averages 8.3ϕ, with values ranging from 7.7 to 8.8ϕ. All the granulometric distribution curves show a bimodal shape, with a significant coarse silt to fine sand content (up to 5.8% sand), with the exception of the two more superficial soupy samples (0.68 and 2.51 mbsf) in which this feature is less marked (Figure 6.1).

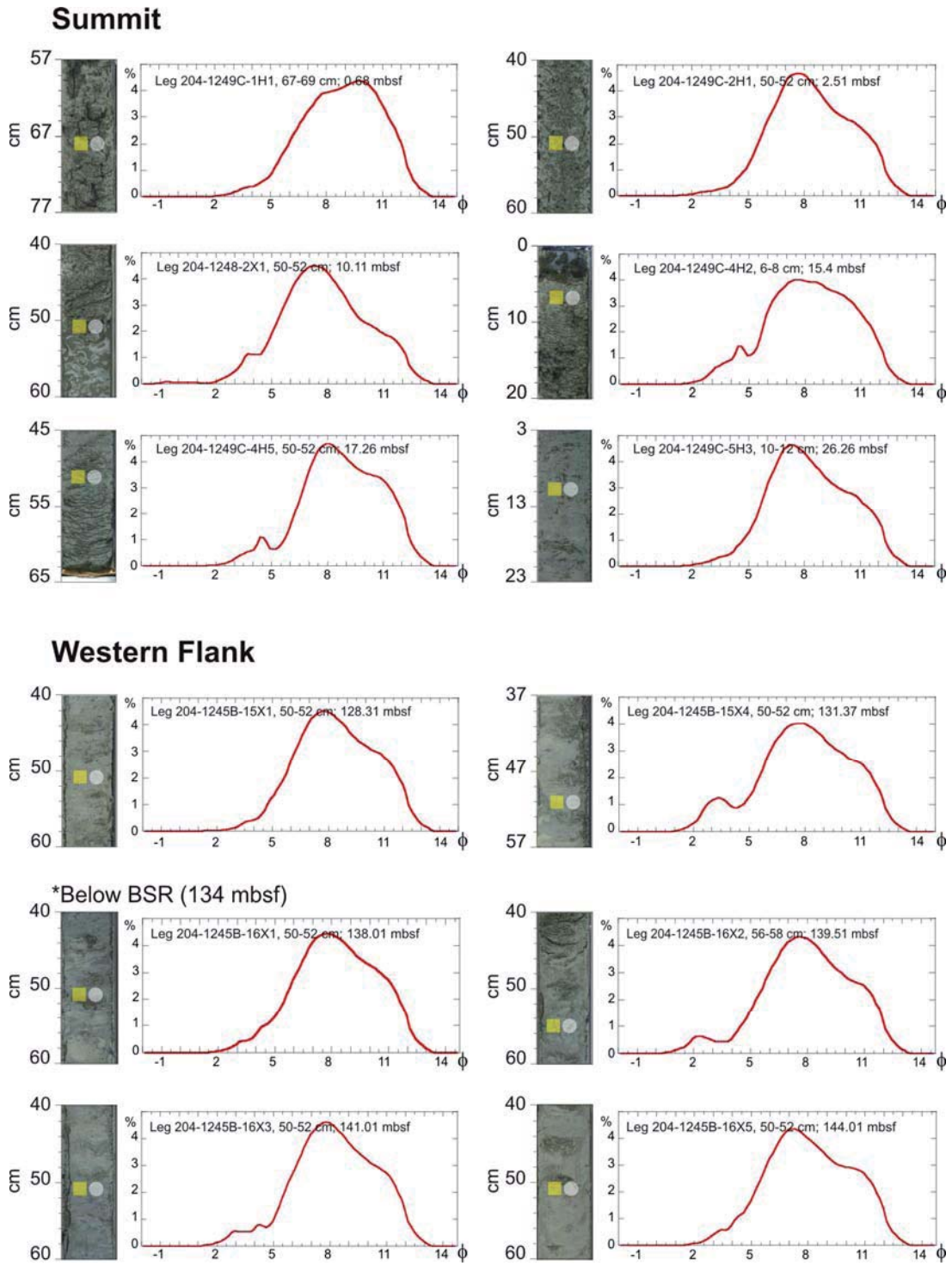

Figure 6.1. Grain-size distribution curves and core photographs of disturbed samples from the summit and the western flank of southern Hydrate Ridge. Squares and circles correspond to the sediment samples analysed for magnetic and textural properties, respectively. mbsf = meter below sea floor (modified from Piñero et al., 2007).

The coarse particle content is superimposed on the clay fraction content, with a mode value of 7.6ϕ in all samples except the first one, where a significant amount of fine clay is also present (mode 9.6ϕ). The magnetic susceptibility values of these samples range from 1.45 to 1.93 $\cdot 10^{-7}$ m^3/kg (Figure 6.2).

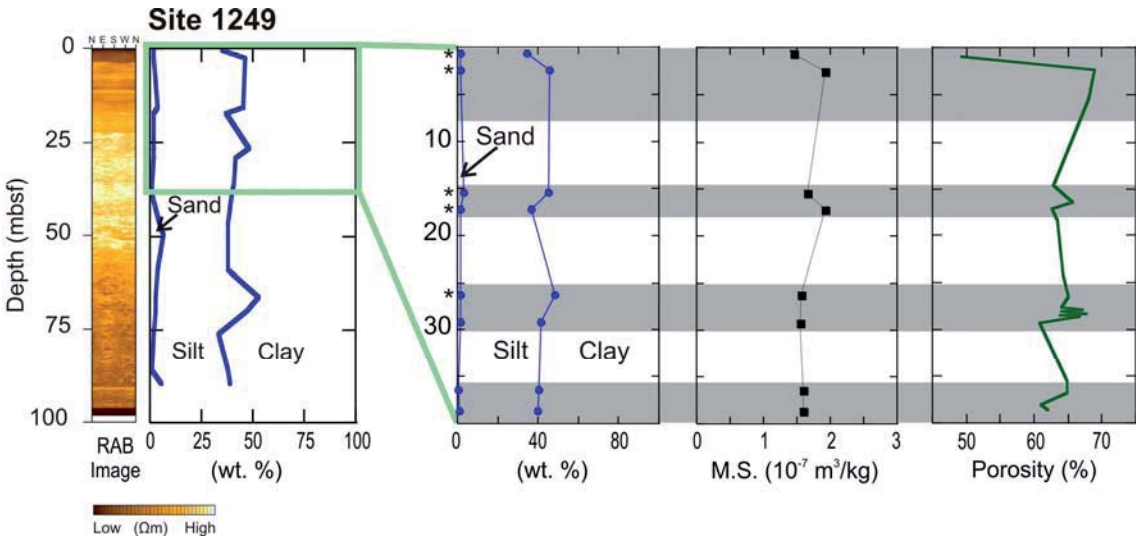

Figure 6.2. Depth variation in sand, silt and clay contents for samples from Site 1249 at the summit of southern Hydrate Ridge. Resistivity at the bit (RAB) image locates areas of high resistivity corresponding to areas rich in gas or gas hydrates (Tréhu et al. 2003). Detailed results of granulometric distributions, magnetic susceptibility (MS) and porosity (%) of disturbed sediments from site 1249 (0–40 mbsf) are also depicted. Shaded areas correspond to gas hydrate-bearing sediment intervals (Tréhu et al. 2004a). mbsf = meter below sea floor; * = location of soupy and mousse-like fabric samples analyzed for this study (Piñero et al., 2007).

The mean diameter of the disturbed samples from the western flank of southern Hydrate Ridge averages 8.5ϕ, ranging from 7.9 to 8.7ϕ. The average sand content is 3.7% with only two samples with contents below 2%, attaining values of 8.9% (Figure 6.3). They also show bimodal shapes in their distribution curves (Figure 6.1), with a modal diameter of 7.6ϕ. Their magnetic susceptibility values range from 1.18 to 2.25 $\cdot 10^{-7}$ m^3/kg (Table 6.1). The samples corresponding to sediments below the depth of the BSR seem to have textural parameters similar to those analyzed from above the BSR (Figure 6.3).

Carbonate contents of the disturbed samples range between 4.8 and 11% (Table 6.1). The highest values are found in the shallower samples from the summit of southern Hydrate Ridge. The carbonate content of the samples form the western flank are lower (5.1–6.4%), with only one sample reaching 9%. As regards the bulk mineralogy, the disturbed sediments from southern Hydrate Ridge analyzed for this study are made up of clays (38–57%), quartz (27–39%) and feldspars (12–18%), with minor amounts of calcite (1– 7%). Only one sample, 204-1249C-1H1, 67–69 cm (0.68 mbsf), has a higher feldspar content (27%) but the mineral

identification of its coarse fraction does not show any atypical features (quartz 70%, feldspars and other light minerals 18%, benthic foraminifera fragments 5%, planktonic foraminifer fragments 3%, planktonic foraminifers 1.8%, and minor contents of rock fragments, micas, sponge spicules and glauconite). All these mineralogical compositions correspond to the characteristic composition of southern Hydrate Ridge sediments (Chapter 5).

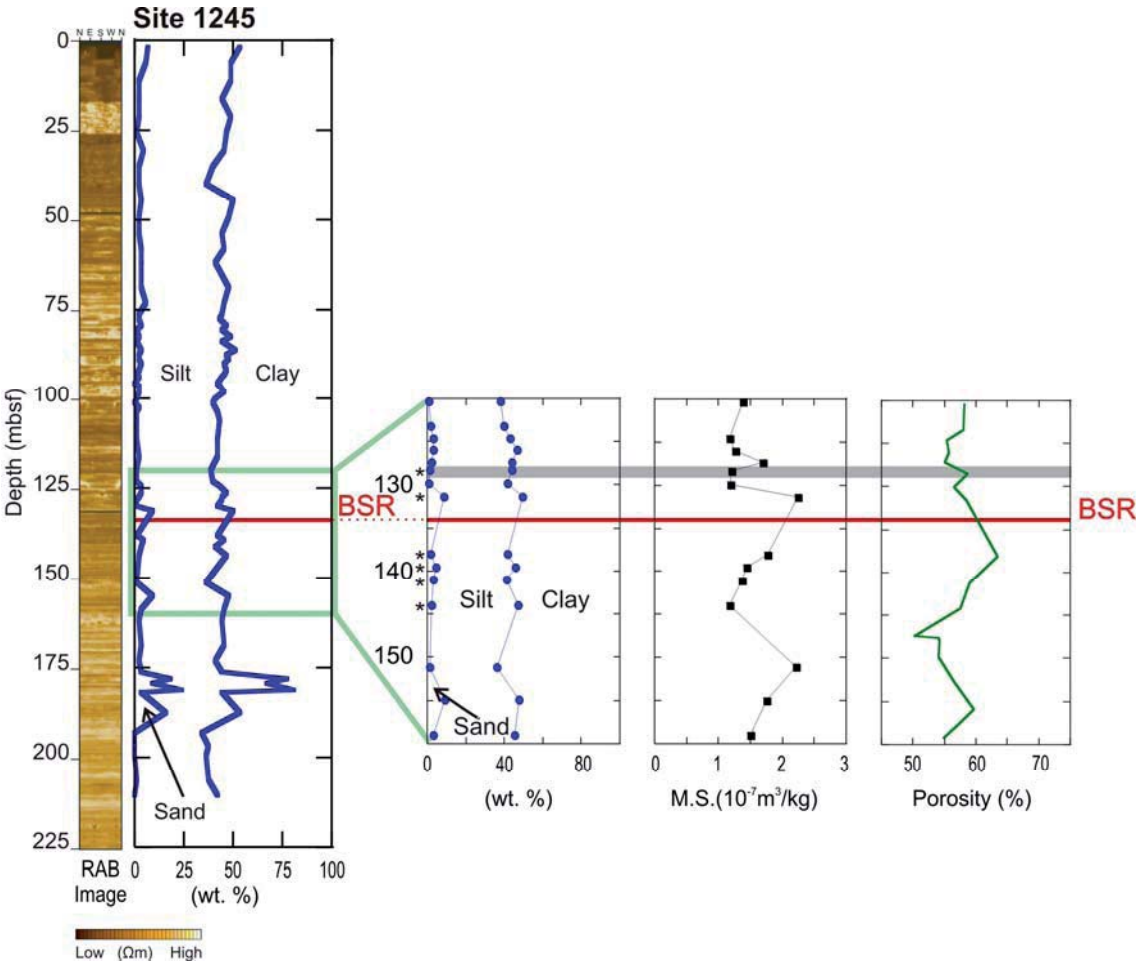

Figure 6.3. Depth variations in sand, silt and clay content for samples from Site 1245 on the western flank of southern Hydrate Ridge. Resistivity at the bit (RAB) image locates areas of high resistivity, corresponding to areas rich in gas or gas hydrate (Tréhu et al. 2003). Detailed results of granulometric distributions, magnetic susceptibility (MS) and porosity (%) of disturbed sediments from site 1245 (120–160 mbsf) are also depicted. Shaded area corresponds to gas hydrate-bearing sediment intervals (Tréhu et al. 2004a). mbsf = meter below sea floor; * = Location of soupy and mousse-like fabric samples analyzed; BSR = bottom simulating reflector (Piñero et al., 2007).

6.1.2. Textural results of gas hydrate-rich samples

Four sediment intervals (A to D) from the western flank and summit of southern Hydrate Ridge were sampled at the University of Bremen for textural and geochemical analyses (Table 6.2) (Chapter 4), according to their high gas hydrate content inferred from computer

tomographic X-ray images (Abegg et al., 2006; 2007). The samples had been stored in liquid Nitrogen (-196 ºC) onboard during ODP Leg 204 in order to preserve their gas hydrate content.

The interval A (Leg 204-1245C-10H1; 57.43 to 57.46 mbsf) was sampled on the western flank of southern Hydrate Ridge, where very little evidence of high gas hydrate content was found (Figure 3.16). After gas hydrate dissociation at ambient conditions (P= 1 atm; T= 21º C), no major disturbance fabric was produced in the sediment structure, confirming its low gas hydrate content, as previously inferred from the computer tomographic image where only little veinlets of gas hydrates were found. The textural analyses of the four samples from this interval show higher sand and silt content than the averaged results of all the hemipelagic samples from southern Hydrate Ridge described in this thesis (Chapter 5). Likewise magnetic susceptibility results are also higher ($2.1 \cdot 10^{-7}$ m^3/kg) than the average of hemipelagic sediments.

	Area	Sample Identification	Depth (mbsf)	Sand (wt%)	Silt (wt%)	Clay (wt%)	MS (10^{-7} m^3/kg)	F (S/M)
A	W flank	Leg 204-1245C-10H1, 0-2.5	57.43	7.02	68.82	24.17	-	-
	W flank	Leg 204-1245C-10H1, 2.5-3.5	57.44	18.78	50.04	31.19	2.18	-
	W flank	Leg 204-1245C-10H1, 3.5-5	57.45	2.76	71.32	25.92	-	-
	W flank	Leg 204-1245C-10H1, 5-7	57.46	2.93	71.84	25.23	2.12	-
B	Summit	Leg 204-1249C-1H1A, 0-3	0.27	4.39	65.14	30.78	2.04	S
	Summit	Leg 204-1249C-1H1A, 3-4	0.29	4.08	65.61	30.50	-	S
	Summit	Leg 204-1249C-1H1A, 4-6	0.30	3.89	65.67	30.90	1.51	S
	Summit	Leg 204-1249C-1H1A, 7-7.5	0.32	3.43	68.98	28.97	-	S
	Summit	Leg 204-1249C-1H1A, 7.5-9.5	0.34	2.05	68.19	27.41	1.44	S
C	Summit	Leg 204-1249B-2A1, 0-3	30.61	1.31	76.28	22.41	1.71	M
	Summit	Leg 204-1249B-2A1, 3-5.5	30.64	1.45	78.11	20.44	1.7	M
	Summit	Leg 204-1249B-2A1, 5.5-8	30.67	1.18	76.09	22.73	1.73	M
	Summit	Leg 204-1249B-2A1, 8-9	30.70	1.22	78.55	20.23	-	M
	Summit	Leg 204-1249B-2A1, 10-12.5	30.71	2.02	72.56	25.41	1.85	M
	Summit	Leg 204-1249B-2A1, 12.5-15	30.73	2.29	75.01	22.70	1.78	M
D	Summit	Leg 204-1249C-7H3, 0-2	37.16	0.71	76.03	23.26	-	M
	Summit	Leg 204-1249C-7H3, 2-4	37.18	0.82	77.79	21.39	1.97	M
	Summit	Leg 204-1249C-7H3, 4-6	37.21	0.79	79.37	19.84	2.14	M
	Summit	Leg 204-1249C-7H3, 6-8	37.23	0.81	78.96	20.22	1.93	M
	Summit	Leg 204-1249C-7H3, 8-9	37.24	1.05	68.19	27.41	1.89	M
Average of analyzed disturbed samples				3.14	41.6	55.3	1.61	
Average of Leg 204 hemipelagic sediments (124 samples)				0.9	40.9	58.19	2.0	

Table 6.2. Grain-size distribution and magnetic susceptibility (MS) results of sediment samples corresponding to selected gas hydrate–rich intervals from southern Hydrate Ridge. mbsf = meter below sea floor; F= disturbance fabric; S= soupy; M= mousse-like. Interval Leg 204-1245C-10H1, after gas hydrate dissociation did not show any disturbance fabric owing to its low gas hydrate content. The average of the same parameters analyzed in all the hemipelagic sediment samples from southern Hydrate Ridge are also shown.

Five samples for textural analyses and three for magnetic analyses were taken in interval B (Leg 204-1249C-1H1A), from the first meter below the summit of southern Hydrate Ridge, where large amounts of gas hydrate were found during the ODP Leg 204 cruise. After gas hydrate dissociation, the interval showed a clear soupy fabric as had been predicted by its computer tomographic analysis (Figure 6.4). Textural results of this interval reveal high sand and silt contents (2 to 4.4 wt.% sand and 65 to 69 wt.% silt) compared with the average of all the hemipelagic samples from southern Hydrate Ridge (1 wt% sand and 49 wt% silt). Magnetic susceptibility results show a high value for the shallower sample (2.04 $\cdot 10^{-7}$ m^3/kg), whereas the two other samples show lower values. Although the main sedimentological features of this interval were destroyed owing to the gas hydrate dissociation, the textural analyses of the five analyzed samples suggest that it corresponds to a turbidite facies interval.

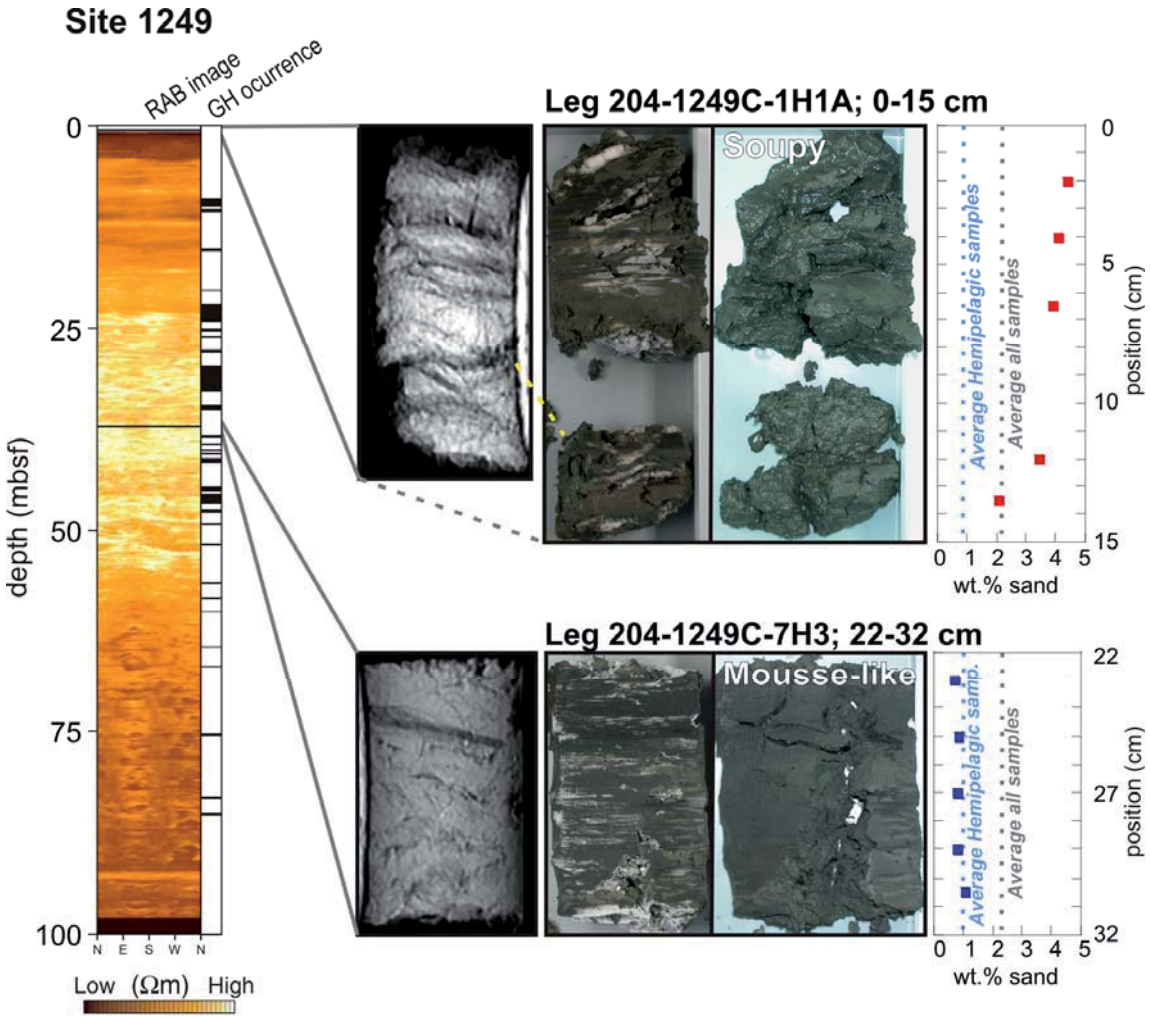

Figure 6.4. Variation in sand content (> 63 µm) of significant gas hydrate-rich intervals from southern Hydrate Ridge. The averaged sand content of all the analysed samples and the hemipelagic samples of this thesis are shown for comparison. Computer tomographic X-Ray images (sediment in white, gas hydrate in dark grey) and core images before and after gas hydrate dissociation (gas hydrates in white) from the same intervals are also shown. Resistivity-at-the-bit (RAB) image as well as the gas hydrate-rich intervals in the whole core are also shown. mbsf = meter below sea floor; wt.= weight.

The six analyzed samples from the interval C (Leg 204 1249B 2A1) range from 30.61 to 30.73 mbsf at the summit of southern Hydrate Ridge. This interval showed low gas hydrate content filling veinlets in the computer tomographic images, and developed a mousse-like fabric after natural gas hydrate dissociation. Textural results show high sand contents and very high silt contents (1.2 to 2.3 wt.% sand and 72.5 to 78.5 wt.% silt) compared with the average of the hemipelagic samples, although they show similar magnetic susceptibility results (1.7 to 1.85 $\cdot 10^{-7}$ m^3/kg).

The last interval D (Leg 204-1249C-7H3; 37.16 to 37.24 mbsf) was divided into five sediment samples. It showed low gas hydrate content in the computer tomographic image (Figure 6.4) and developed a mousse-like fabric after gas hydrate dissociation. Grain-size results of this interval show sand contents similar to the hemipelagic facies (0.7 to 1 wt.%) and silt content relatively higher (68 to 79 wt.%). Magnetic susceptibility results are considerably higher than those of the hemipelagic facies, with values of up to 2.14 $\cdot 10^{-7}$ m^3/kg.

In summary, most of the twenty samples analyzed for this study show grain-size values coarser than the average of the hemipelagic samples of southern Hydrate Ridge. This relationship is especially clear in the richest gas hydrate samples, which developed a soupy fabric after natural gas hydrate dissociation (Figure 6.4), whereas it is not so obvious in the intervals with low gas hydrate content that developed mousse-like fabrics. No evidence of gas hydrate presence was found in the interval Leg 204-1245C-10H1 after gas hydrate dissociation, and the textural results of these samples do not show any significant difference with respect to the hemipelagic samples.

6.2. Sediment texture as a significant factor for gas hydrate distribution at southern Hydrate Ridge

As discussed in the previous section, grain-size distributions supply information on particle size availability to the depositional system, and on the type and competence of the processes operating in the geological area (Friedman and Sanders, 1978). In gas hydrate-rich settings, grain size can also provide valuable information on available pore space and, thereby, on possible fluid flow pathways and distribution of gas hydrate. In this regard, the restriction of gas hydrate to relatively coarse-grained sediments has been proposed in previous works (e.g. Soloviev and Ginsburg, 1997; Clennell et al., 1999; Ginsburg et al., 2000; Weinberger et al., 2005; Su et al., 2006).

Soupy and mousse-like fabrics have been identified in gas hydrate-bearing sediments recovered from several active and passive continental margins, such as the Amazon Fan (e.g. Soh, 1997), Blake Ridge (e.g. Egeberg and Dickens, 1999; Paull et al., 1996b), the Costa Rica accretionary wedge (e.g. Kimura et al., 1997), the Nankai accretionary prism (e.g. Moore et al., 2001), the Congo-Angola Basin (e.g. Charlou et al., 2004) and in the Gulf of Mexico (e.g. Francisca et al., 2005). In other cases, soupy and mousse-like fabrics have been related to the presence of gas hydrates in mud volcano areas such as the Black Sea (e.g. Blinova et al., 2003; Aloisi et al., 2004a), the eastern Mediterranean Sea (e.g. Karisiddaiah, 2000; Cita et al., 1996; Robertson et al., 1998; Aloisi et al., 2004b) and the Gulf of Cadiz (e.g. Pinheiro et al., 2003; Somoza et al., 2003).

Soupy and mousse-like disturbance fabrics were naturally developed in sediment samples where gas hydrate presence had been inferred from computer tomographic X-ray images (Abegg et al., 2006; 2007). The disturbance fabrics form as result of gas hydrate dissociation after increasing the core temperature from -196 ºC (liquid Nitrogen) to ambient conditions (20 ºC) (Figure 6.4). This evidence demonstrates the extended use of the disturbance fabric recognition in the sediment cores as a proxy for the presence of gas hydrates.

Most of our disturbed samples from the near-seafloor sediments at the summit (sites 1248 and 1249) and deep sediments on the western flank of the southern Hydrate Ridge (site 1245) are relatively coarse-grained, compared with hemipelagic sediments that show an average mean grain-size value of 8.57ϕ (Table 6.1). Some of these coarse grained intervals correlate with temperature anomalies in the IR-thermal image data (up to −9.4 °C with respect to background sediment; Tréhu et al., 2003), and also with low chlorinity values (up to −200 mM with respect to background chlorinity; Torres et al., 2004), which are commonly interpreted as proxies of the presence of gas hydrate in marine sediments. We compare this correlation with the RAB data, demonstrating that our disturbed and gas hydrate-rich samples correlate with high resistivity areas that correspond to gas and gas hydrate-rich layers (Figure 6.2; Figure 6.3; Figure 6.4). If we compare these results with onboard porosity calculations determined from moisture and density parameters (porosity (%) = volume pore water/total volume; Tréhu et al. 2003), it can be inferred that gas hydrates form preferentially in sediments with higher porosities (up to 69% at the summit, and up to 63% on the western flank; Figure 6.2, Figure 6.3).

At the same time, a similar approximation can be made on the basis of the textural analyses of gas hydrate-rich samples from the summit of southern Hydrate Ridge with respect to their computer tomographic X-ray images. In this context, sediment samples from the first meters below the seafloor at the summit of southern Hydrate Ridge are coarser than the hemipelagic

sediments and show a large presence of gas hydrate in the computer tomographic X-ray images. On the other hand, samples from intervals with a lower gas hydrate presence from the summit and western flank of southern Hydrate Ridge have a sediment grain size similar to that of the hemipelagic facies (Figure 6.4; Table 6.2).

Only two disturbed samples from the summit of the southern Hydrate Ridge, i.e. 204-1249C-1H1, 67–69 cm (0.68 mbsf), and 204-1249C-4H5, 50–52 cm (17.26 mbsf), show mean grain-size values (in ϕ) higher than the average for hemipelagic sediments and are therefore finer-grained than background hemipelagic samples (Figure 6.5). These samples are located in the zone where the highest concentration of gas hydrates was detected (30–40% of pore space; Figure 3.16; Tréhu et al. 2004a). This suggests that, because of the high gas flux in this area, the large amount of available methane may promote the formation of gas hydrates in fine-grained intervals, despite their lower porosity (Figure 6.2). In this scenario, gas hydrate formation may occur indistinctly in both fine and coarse-grained layers that may continue to act as conduits feeding methane to the seafloor.

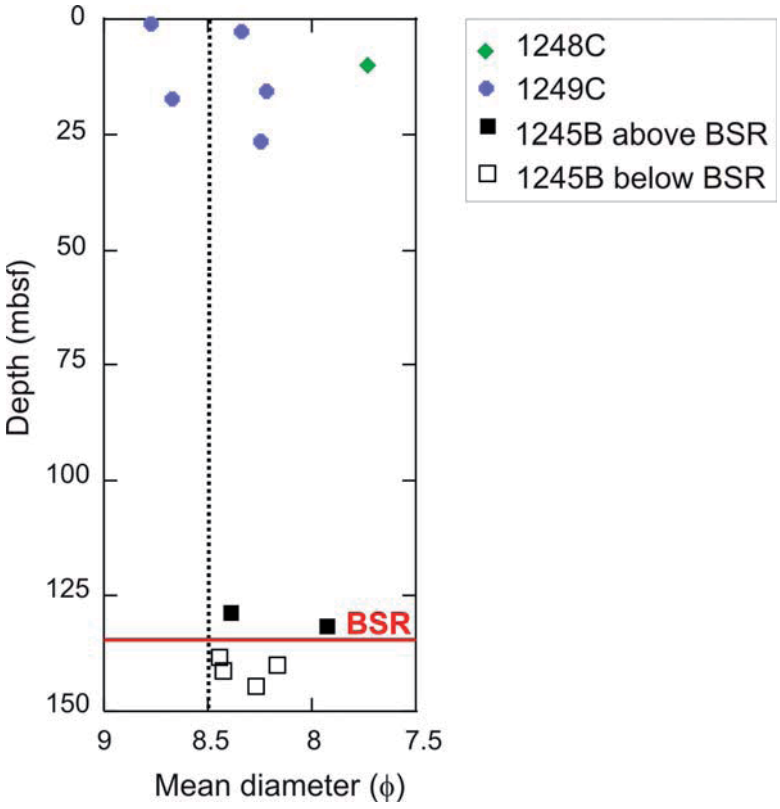

Figure 6.5. Mean diameter of disturbed analysed samples from the summit and the western flank of southern Hydrate Ridge. The average of the mean grain-size diameter of all the hemipelagic sediments analysed for this study is depicted. The depth of the bottom simulating reflector (BSR) at site 1245 is also indicated. mbsf = meter below sea floor; ϕ = phi (Piñero et al., 2007).

Furthermore, mousse-like sediments from site 1245 (core 16), analyzed immediately below the BSR (up to 10 m), are also coarse-grained (Figure 6.2; Figure 6.5). In this case, their disturbance fabric is not clear, although it appears to be very similar to widespread mousse-like patches identified in other core sections (Tréhu et al., 2003). By analogy, the observed disturbance fabric could be produced during gas hydrate dissociation, which might imply an

error in the BSR depth calculation larger than 10 m (7.5%). Another possible explanation for the presence of disturbed samples below the BSR is the gas expansion, due to gas exsolution from gas-rich fluids because of P/T changes occurring during core recovery.

Although the original depositional features of the disturbed sediment samples and the gas hydrate-rich core intervals analyzed in this study cannot be identified owing to gas hydrate dissociation and the consequent disturbance of the sedimentary structure, their coarse grain-size results (Table 6.1; Table 6.2), bimodal granulometric distribution curves (Figure 6.1), sand particle components, and magnetic susceptibility values suggest that the sediments correspond to turbidite facies. Despite high values of standard deviation (2.0–2.47) in some samples (Table 6.1), it should be pointed out that our sampling includes 2 cm of sediment with the result that different parts of the Bouma sequence may be included in each value.

Turbidite deposits have been identified on both flanks and at the summit of southern Hydrate Ridge (Tréhu et al., 2003). It has been suggested that these layers, together with the volcanic ash intervals, act as conduits for methane-rich fluids from deep in the accretionary complex to the GHSZ of southern Hydrate Ridge (Tréhu et al., 2004b). The mineralogical composition of the samples do not show any special characteristics compared with the hemipelagic sediments or other coarser-grained deposits at southern Hydrate Ridge. These sediments are made up of clays, quartz, feldspars and minor amounts of calcite, as are most samples analyzed from this area (Gràcia et al., 2006). The maximum values of total calcium carbonate (11%) are found at the summit sites (Table 5.1) in samples near the sediment surface. This trend is especially evident for samples near a highly reflective active carbonate chemoherm mound known as the Pinnacle (Johnson et al., 2003), and are related to the presence of authigenic carbonate (Teichert et al., 2005a). The high contents of authigenic carbonate suggest a rapid methane flux through the sediments at the summit of southern Hydrate Ridge, which could feed the methanotrophic microbes that form the carbonate near the seafloor. This process was already suggested during ODP Leg 204, and can also be inferred from the transparent facies in the multi-channel seismic profiles near the Pinnacle (Tréhu et al., 2002).

7. Early diagenetic processes: Anaerobic oxidation of methane and authigenic barite fronts

Early diagenesis processes include all the sedimentary changes that take place during the first meters of the burial in the absence of high temperatures or overpressure. In this setting sediment porosity is filled with interstitial water (e.g. Berner, 1980; Emerson and Hedges, 2003). These sedimentological changes include initial compaction, and also different geochemical reactions. In high carbon flux areas such as gas hydrate-rich environments, the hydrocarbon-rich fluxes exert a considerable influence on these reactions. In this regard, AOM is a microbial-mediated reaction that consumes upward migrating methane and downward diffusing sulphate in the upper meters of the sediment column, forming bicarbonate anions (HCO_3^-) that usually precipitate as calcite or aragonite and hydrosulphide anions (HS^-) that can precipitate producing different iron-sulphides (e.g. Neretin et al., 2004; Riedinger et al., 2005; Larrasoaña et al., 2007).

[8] $$CH_4 + SO_4 \rightarrow HCO_3^- + HS^- + H_2O$$

The flux rate and concentration of methane and sulphate, which are the major reactants involved in the AOM reaction, defines the depth where this reaction takes place in the sediment column. This depth is known as the sulphate-methane transition zone (SMT) (Figure 7.1).

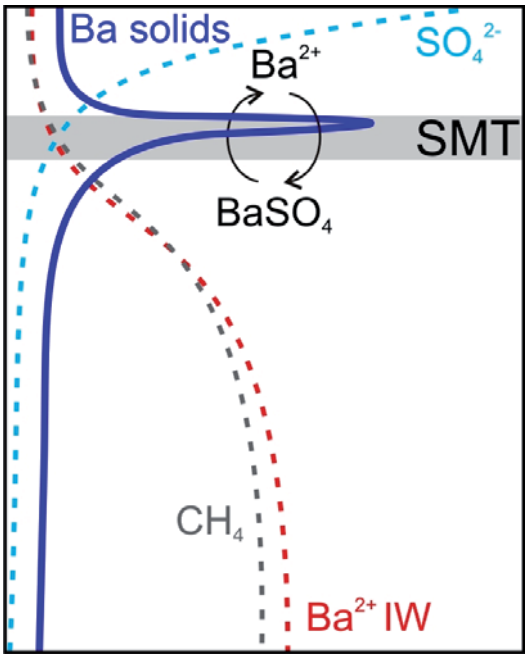

Figure 7.1. Theoretical cycle of Barium in marine sediments. Barite is deposited on the seafloor and is dissolved because of depletion in sulphate concentration at the start of early diagenesis and the burial process. The dissolved Ba^{2+} is diffused upwards and barite precipitates again when it reaches a sulphate-rich interval. A prominent barite front develops near the SMT zone owing to this recycling process. SMT= sulphate methane transition zone (adapted from Torres et al., 1996b).

The oxidation of organic matter is the most usual sulphate-consumer reaction in anoxic marine sediments [9]. As a result of this process, organic matter is oxidized, producing electrons whereas sulphate is reduced acting as the electron acceptor (Tromp et al., 1995).

[9] $2(CH_2O)_{106}(NH_3)_{16}(H_3PO_4) + SO_4^{2-} \rightarrow H_2S + 212\ HCO_3^- + 32\ NH_3 + 2\ H_3PO_4$

Although barite forms part of the sulphur cycle, it is also related to the carbon cycle because of AOM and the oxidation of organic matter (Figure 7.2).

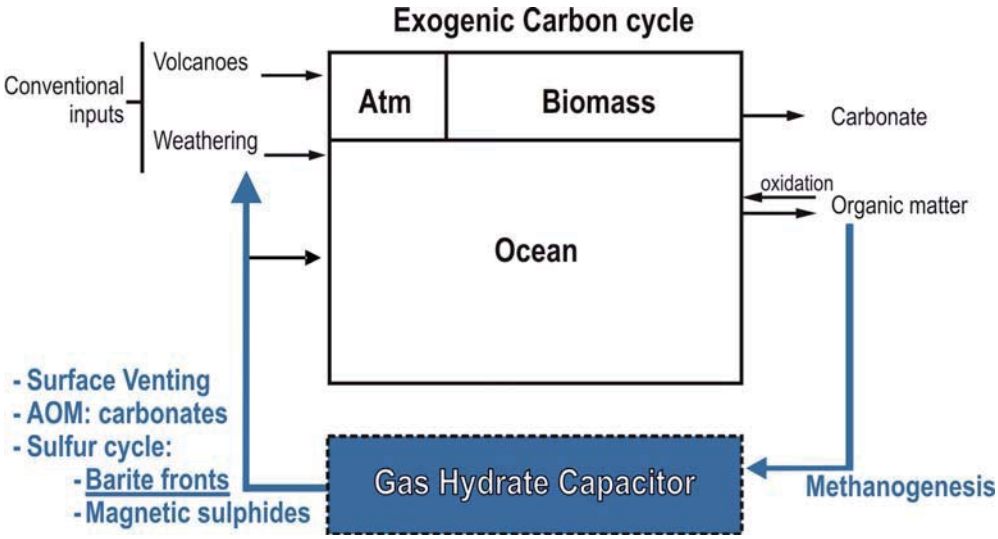

Figure 7.2. Exogenic cycle of carbon, including the gas hydrate capacitor. Methanogenesis is the main methane formation process as result of oxidation of organic matter; whereas surface venting, carbonate precipitation and the relationships with the sulphur cycle are some of the links between the hydrate budget and the other exogenic carbon fields. AOM= anaerobic oxidation of methane; Atm = atmosphere (modified from Dickens, 2003).

Barite forms aggregates in seawater as a result of biological processes (e.g. Kastner, 1999; Chow and Goldberg, 1960; Dehairs et al., 1980) before reaching the seafloor. During sediment burial and because of sulphate depletion in anoxic environments, barite is dissolved as sulphate is consumed by the oxidation of organic matter and by methane oxidation through AOM (Figure 7.1). Subsequently, free Barium is diffused upwards through the sediment column until it reaches a sulphate-rich zone, where barite re-precipitates. This recycling process leads to the formation of a barite front in the sediment column (e.g. Torres et al., 1996b). As Barium and methane are dissolved and diffused as part of the same interstitial fluids, the identification of barite fronts some meters below the seafloor and up to 25 mbsf, has been related to methane flux, which controls the depth where AOM takes place (e.g. Torres et al., 1996b; McManus et al., 1999). Given a constant sedimentation rate, the size of the barite peaks can be used to calculate the duration of AOM at the same depth. This can be related to the duration of the constant flowing out of the methane flux (e.g. Dickens et al., 2000; Torres et al., 1996a).

The formation of barite ($BaSO_4$) in seawater and its subsequent accumulation on the sea floor has been related to the biological activity of the ocean (e.g. Dymond et al., 1992). This has lent support to the widespread use of barite as a paleoproductivity proxy in marine sediments (e.g. Goldberg, 1958; Bishop, 1988; Chow and Goldberg, 1960; Paytan and Kastner, 1996; Dehairs et al., 1987; 2000; Dymond et al., 1992; 1996; Kasten et al., 2001; Paytan et al., 2004; Sanchez-Vidal et al., 2005; Sternberg et al., 2007). Other chemical characteristics supporting barite as a reliable proxy include its extremely low solubility in seawater (Kps $1.5 \cdot 10^{-10}$ Church and Wolgemuth, 1972) as well as its high preservation rate in oxic sediments (Paytan and Griffith, 2007). However, in anoxic marine settings barite suffers chemical recycling processes during early diagenesis (Figure 7.1). This and other causes are currently being investigated as possible processes that may inhibit barite consideration as a paleoproductivity proxy (e.g. van Beek et al., 2003; Fagel et al., 2004).

This chapter focuses on Barium data with respect to other available data such as TOC, Al, sedimentary facies, etc. These new chemical composition data of sediment samples and interstitial waters from southern Hydrate Ridge obtained after ODP Leg 204 are discussed in order to define the Barium-rich intervals and discuss their geochemical significance. SEM images were studied to identify the main Ba-rich mineral phases present at southern Hydrate Ridge and to establish their origin. Finally, the numerical modelling software CoTReM allowed us to calculate the time needed to produce the Barium enrichments near SMT at each site, and to make the preliminary evaluation of the main geochemical processes implied in their preservation over time, as a first attempt to study methane flux evolution over time.

7.1. Barium content in sediments and interstitial waters from southern Hydrate Ridge

Sediments from southern Hydrate Ridge show Barium contents ranging from 454 ppm (sample Leg 204-1244E-1H-5, 38-40 cm; 6.39 mbsf) to 1021 ppm (sample Leg 204-1252A-25X-2, 56-58 cm; 222.97 mbsf), with an average value of 688 ppm. Most of the Barium contents in sediments are lower than 800 ppm with only some higher values. These results are consistent with those previously described by Dickens (2001) (241 to 1407 ppm) for ODP Leg 164 Sites 994, 995 and 997 drilled at Blake Ridge, a well-documented gas hydrate deposit off the South-East of the North American margin (Atlantic Ocean) (e.g. Paull et al., 1996b; 2000). Barium contents in the interstitial waters of southern Hydrate Ridge generally show an increasing trend with depth, with values ranging from 2 to 282 μM. These results are analogous to the findings described in the Peru margin, the Japan Sea and Blake Ridge (Torres et al.,

1996a, 1996b; Snyder et al., 2007). This increasing trend is especially pronounced in the shallowest meters below sea floor of all the non-summit drilled Sites (1244 to 1247, 1251 and 1252).

7.1.1. Summit of southern Hydrate Ridge

The results of Barium concentration analysed in the sediment samples from the summit of southern Hydrate Ridge are homogeneous with depth, with no significant trends in the shallowest meters below sea floor (Figure 7.3). In this environment, only one Barium-rich interval is found from 112 to 127 mbsf at Site 1250, with values up to 958 ppm (e.g. sample Leg 204-1250C-14H1, 130-132 cm; 112.31 mbsf). Similar results are found in the interstitial water analyses at Site 1250, with only slightly higher values of 200 μM in the interval 126 to 145 mbsf. The correspondence between the Barium-high results in sediment and in the interstitial waters suggests that a dissolution process is taking place in this interval.

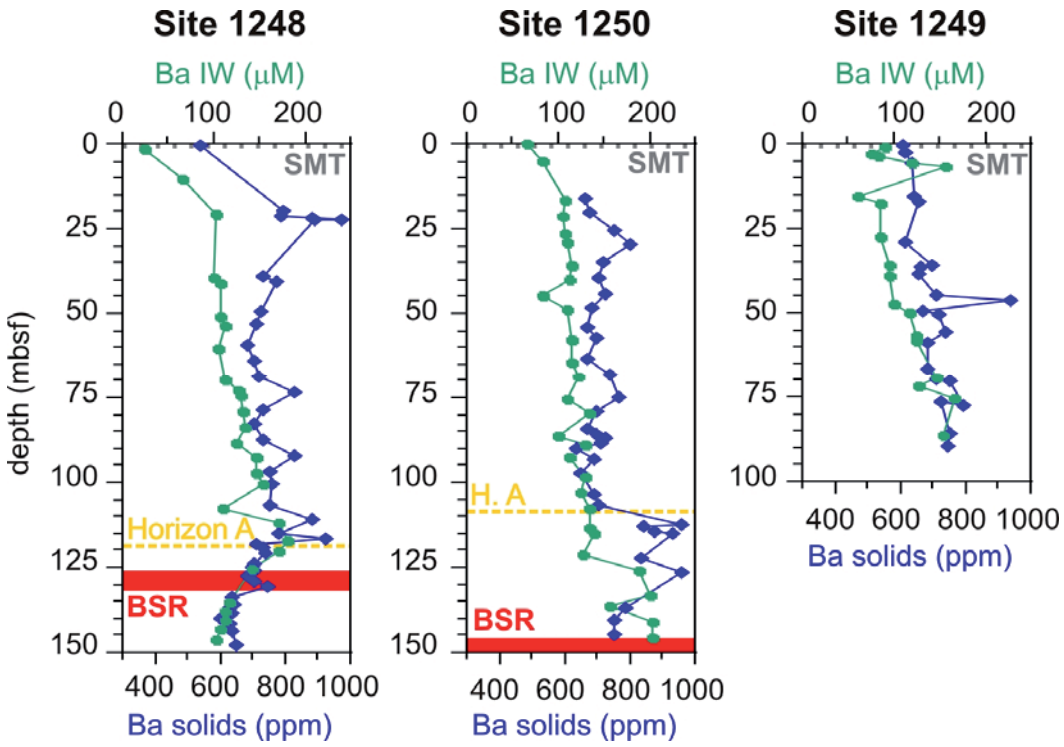

Figure 7.3. Barium variations with depth in solid sediment (blue) and interstitial waters (IW-green) from Sites 1248, 1249 and 1250 at the summit of southern Hydrate Ridge. The sulphate - methane transition zone (SMT), bottom simulating reflector (BSR) and Horizon A (H.A) at each site are also depicted. mbsf= meter below sea floor.

7.1.2. Western flank of southern Hydrate Ridge

The plot of the Barium content in sediment samples from the western flank of southern Hydrate Ridge (Sites 1245 and 1247) shows high values (884 at Site 1245 and 839 ppm at Site 1247) in the shallowest analysed sample below the seafloor (2 and 6 mbsf), and a minimum value (475 and 499 ppm) some meters below it (6.5 and 8.6 mbsf respectively), near the defined SMT depth (Figure 7.4). Some other high values are found deeper in the sediment column, above the BSR at Site 1245, 892 ppm at 151 mbsf (sample Leg 204-1245B-18X2, 50-52 cm), and also below this Horizon at Site 1247 (968 ppm in sample Leg 204-1247B-8H2, 47-49 cm; 55 mbsf, and 949 ppm in sample Leg 204-1247B-18X2, 50-52 cm; 129 mbsf) (Figure 7.4). The Barium content in the interstitial waters of sediments from the western flank shows a general increasing trend with depth, with high-value intervals in the same depths as high Barium contents in the sediments (150 to 182 mbsf at Site 1245 and 130 to 142 mbsf at Site 1247), suggesting that in these intervals a dissolution of Ba-rich minerals is taking place.

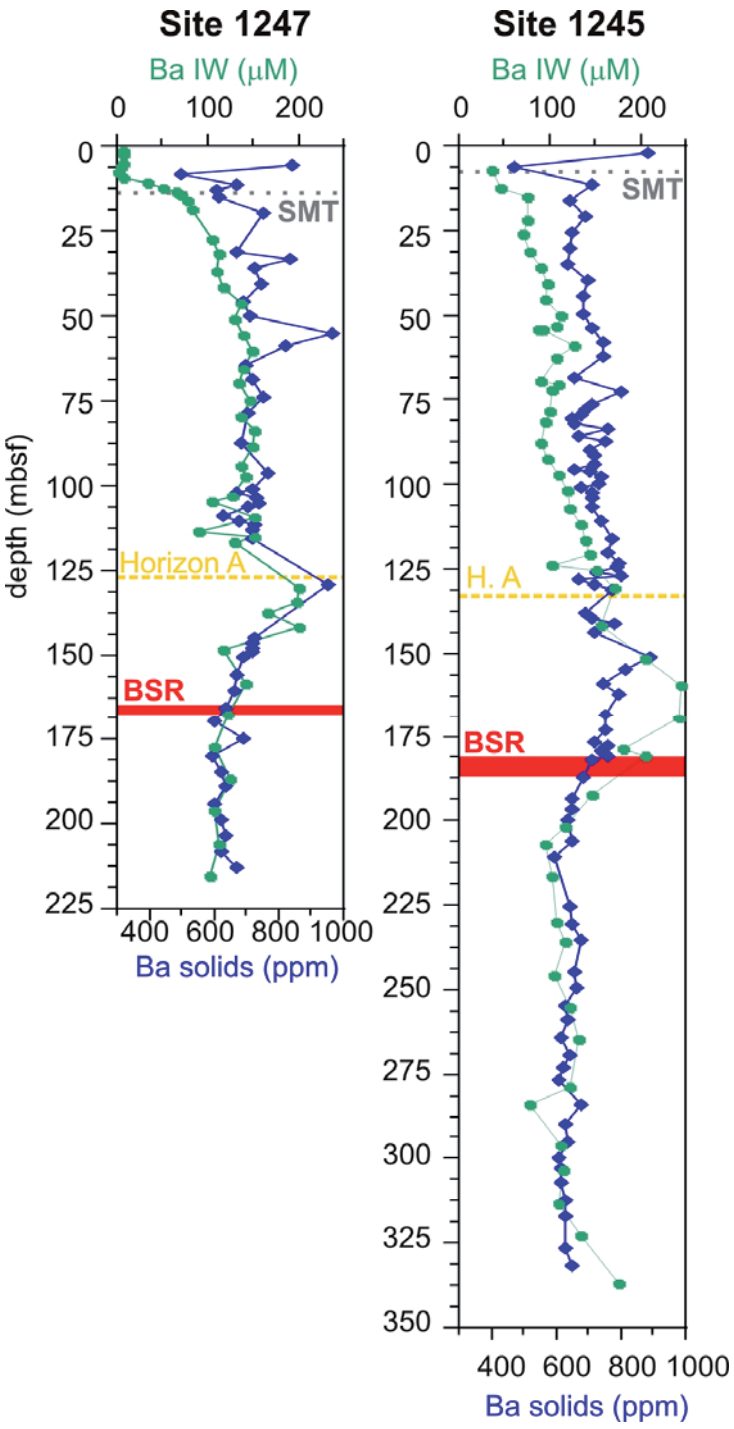

Figure 7.4. Barium variations with depth in solid sediments (blue) and interstitial waters (IW-green) from Sites 1247 and 1245 on the western flank of southern Hydrate Ridge. The sulphate - methane transition zone (SMT), bottom simulating reflector (BSR) and Horizon A (H.A) at each site are also depicted. mbsf= meter below sea floor.

7.1.3. Eastern flank of southern Hydrate Ridge

The plot of the Barium content in sediment samples from the eastern flank of southern Hydrate Ridge (Sites 1244 and 1246) shows the same shape in the first meters below sea floor as the plot of the western flank, with high values (789 at Site 1244 and 974 ppm at Site 1246) in the first analysed sample below the seafloor (samples Leg 204-1244C-1H1, 88-90 cm; 1 mbsf and Leg 204-1246-1H1, 50-52 cm; 2 mbsf), and minimum values (454 and 481 ppm) some meters below it (samples Leg 204-1244C-1H5, 38-40 cm; 6.4mbsf and Leg 204-1246B-2H1, 50-52 cm; 5.2 mbsf) (Figure 7.5). However, the best developed maximum in Barium contents at Sites 1244 and 1246 on the eastern flank occurs some meters below the sea floor in the sediment column, with values of 795 ppm and 809 ppm, respectively (Figure 7.5). The high Barium values form a wide peak in the interval of 20 to 30 mbsf at Site 1244, whereas at Site 1246 this peak is narrower and shallower, located at 10-12 mbsf, both under the calculated SMT depth. In sediments from the eastern flank of southern Hydrate Ridge, other relatively high Barium contents are detected at 70 mbsf at Site 1244 (887 ppm), and at 73 and 129 mbsf at Site 1246 (746 and 837 ppm respectively) (Figure 7.5).

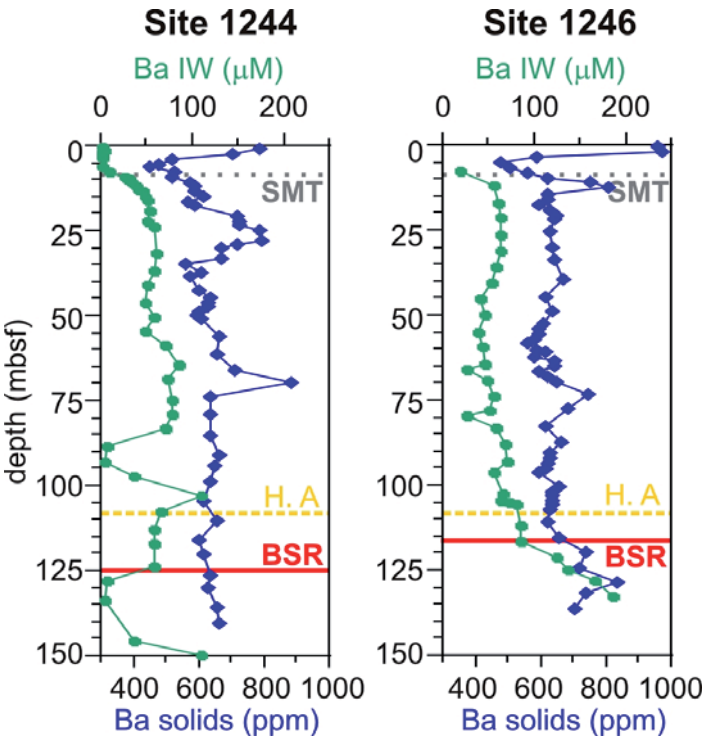

Figure 7.5. Barium variations with depth in solid sediments (blue) and interstitial waters (IW in green) from Sites 1244 and 1246 on the eastern flank of southern Hydrate Ridge. The sulphate - methane transition zone (SMT), the bottom simulating reflector (BSR) and Horizon A (H.A) at each site are also depicted. mbsf= meter below sea floor.

Barium content in interstitial waters on the eastern flank of Southern Hydrate Ridge shows an increasing trend with depth at Site 1246, especially deeper than 115 mbsf. At Site 1244, the Barium content in interstitial waters is more irregular, with two slightly low intervals from 120 to 130 mbsf and at 140 to 150 mbsf.

7.1.4. Slope basin adjacent to southern Hydrate Ridge

In the slope basin adjacent to southern Hydrate Ridge, the Barium content of the sediment samples shows an obvious increasing trend with depth (up to 1021 at 223 mbsf Site 1252) with no significant features near the seafloor (Figure 7.6). Relatively high values (up to 909 ppm at 340 mbsf) were detected below 273 mbsf at Site 1251 and at 64 mbsf (744 ppm) at Site 1252. Relatively low Barium values were found in the deepest analysed sediment samples at Site 1252 (706 ppm at 256 mbsf).

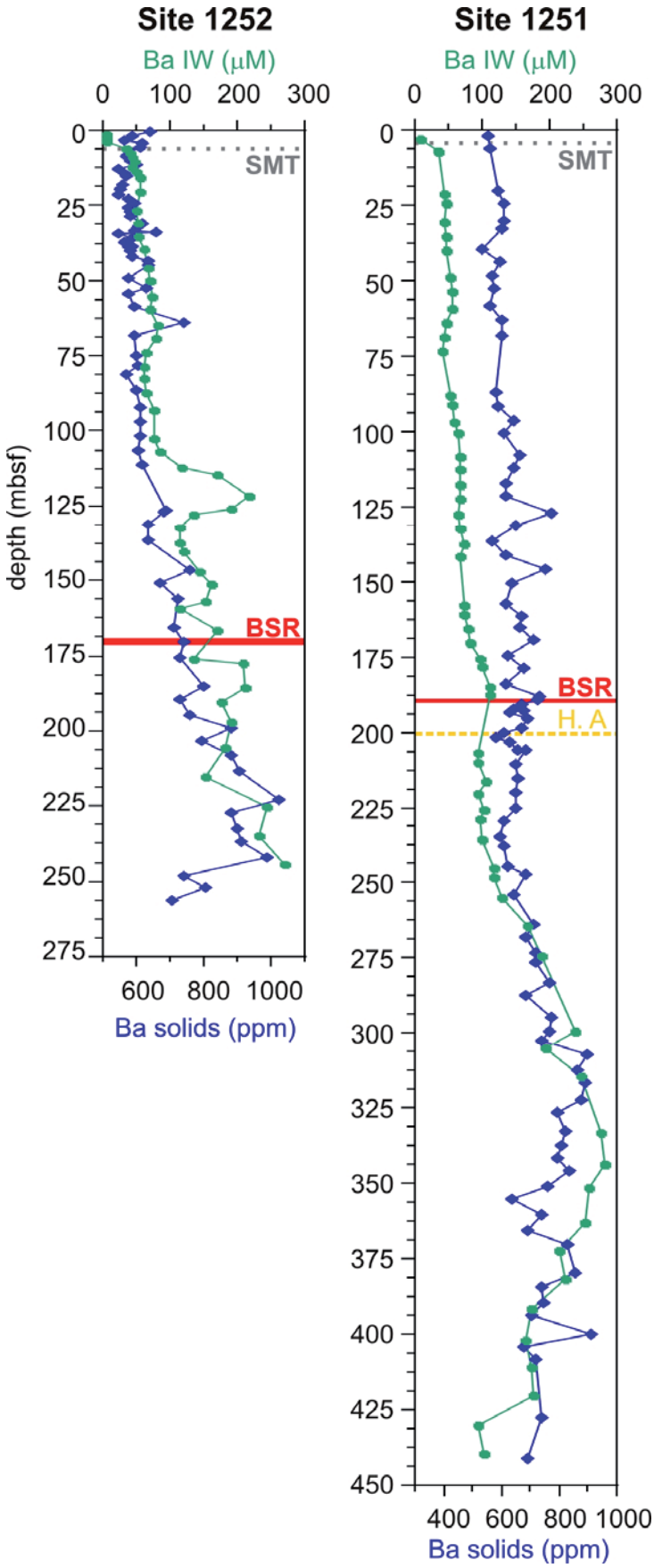

Figure 7.6. Barium variations with depth in solid sediments (blue) and interstitial waters (IW in green) from Sites 1251 and 1252 in the slope basin of southern Hydrate Ridge. The sulphate - methane transition zone (SMT), the bottom simulating reflector (BSR) and Horizon A (H.A) at each Site are also depicted. mbsf= meter below sea floor.

Interstitial water analyses in the slope basin sediments also show increasing trends with depth at both Sites (1251 and 1252), with an obvious Barium-rich interval (up to 215 μM) at 122 mbsf. This interval is located below the position of a debris flow identified in the multi-channel seismic data. The position of the debris flow was confirmed by the visual core description onboard Leg 204 and the sedimentological analyses presented in this thesis (chapter 5).

7.2. Barium, Barium vs. Aluminium and total organic carbon contents in southern Hydrate Ridge sediments

In order to determine whether Barium concentrations in the sediment samples correspond to mineral Barium-rich phases rather than to Barium-rich salts crystallized from the dissolved Barium in interstitial waters, the Ba analysis was repeated in 10 selected samples with different Barium concentrations after applying a washing procedure with deionised water (chapter 4). The difference in Barium content between the bulk sediment samples and the washed samples was in the order of magnitude of the analytical error, and was less than 5% in six of the eight samples (Table 7.1). The difference between both runs was significant in only one sample of the western flank of southern Hydrate Ridge (Leg 204-1247B-23X2, 47-49 cm; 175 mbsf), (9.81%; Table 7.1). Since this sample did not show a significantly high Barium content in the interstitial water analysis (108 μM), this divergence was attributed to an analytical error rather than to the effect of precipitation of Barium from the interstitial water. Given the average porosity for Site 1247 (63%; Shipboard Scientific Party, 2002), the Barium concentration in interstitial water would not be capable of producing such a great Barium deviation in the Barium concentration of the sediment sample.

		Depth (mbsf)	[Ba] in bulk sample (ppm)	[Ba] after washing (ppm)	Difference (%)
Summit	Leg 204-1250C-15H5, 50-52cm	126.57	957.95	923.41	3.74
W. flank	Leg 204-1245B-1H5, 50-52cm	6.51	474.98	452.86	4.89
W. flank	Leg 204-1245B-2H2, 50-52cm	11.51	713.78	719.52	0.80
W. flank	Leg 204-1245B-18X2, 50-52cm	151.11	892.02	845.76	5.47
W. flank	Leg 204-1247B-2H2, 50-52cm	5.61	839.34	821.01	2.23
W. flank	Leg 204-1247B-2H4, 50-52cm	8.61	498.69	486.72	2.46
W. flank	Leg 204-1247B-23X2, 47-49cm	175.08	693.51	631.57	9.81
E. flank	Leg 204-1246B-2H5, 50-52cm	12.71	754.76	722.74	4.43

Table 7.1. Comparison of Barium contents in selected sediment samples from ODP Leg 204 from southern Hydrate Ridge, after applying a rinsing procedure. Results show a minimum importance (< 10%) of the interstitial waters composition, in the Barium analyses of the sediment sample. See text for more details. mbsf= meter below sea floor.

High concentrations of aluminosilicate phases containing Barium in the crystal lattice may increase the Barium content in sediments (Dickens, 2001c). For this reason, the data normalization of Barium to Aluminium is used to minimize the detrital input effect on the diagenetical data (e.g. Dymond, 1981; Walsh et al., 1988; Murray et al., 1992; Saito et al., 1992; Dickens and Owen, 1996). As regards the bulk sediment samples analysed from southern Hydrate Ridge, Ba/Al data show trends similar to those of Barium contents at each drilled site (e.g. Site 1247, Figure 7.7).

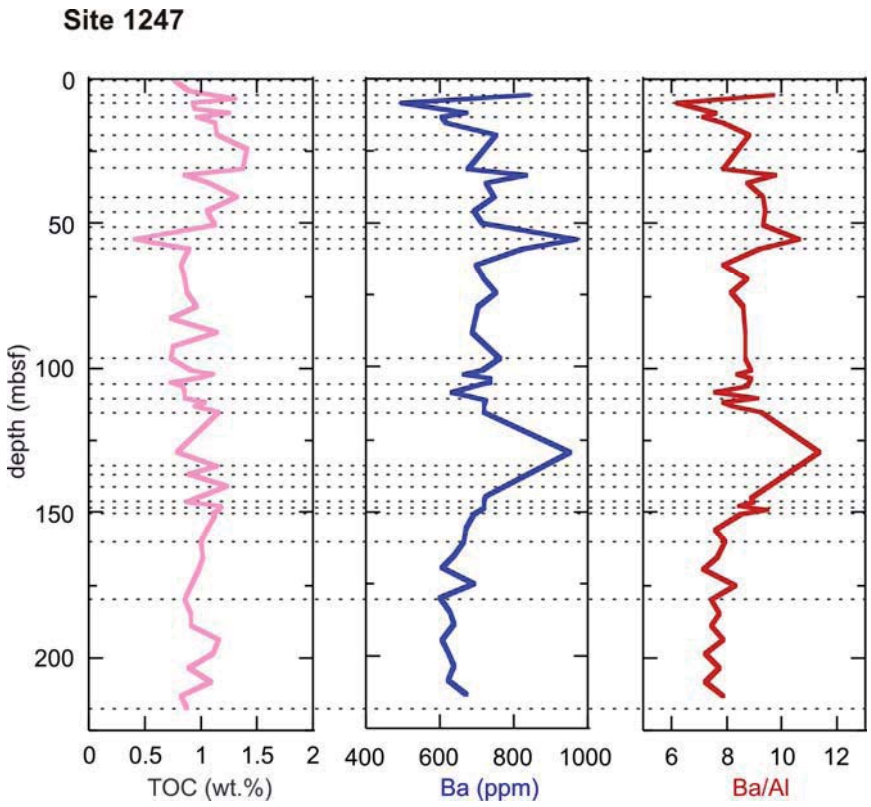

Figure 7.7. Downhole variations of total organic carbon (TOC), Barium (Ba) in sediments and Barium versus Aluminium (Ba/Al) ratios in samples from Site 1247 on the western flank of southern Hydrate Ridge. Turbidite events identified for this thesis are marked as discontinuous lines (Chapter 5). High TOC contents do not correspond to Ba-rich intervals, suggesting that Ba contents are not related to events of high biological productivity. Ba and Ba/Al ratio plots show similar shapes, suggesting that Ba-high values are not related to detrital input events (turbidites). mbsf= meter below sea floor.

TOC data of the Barium-rich samples range from undetectable values (<0.24 wt.%) to 2.1 wt.% in sample Leg 204-1245B-2H2, 50-52 cm; 11.5 mbsf, which represents common organic carbon contents of sediments from southern Hydrate Ridge (Chapter 5). No significant TOC contents were found with respect to the Barium data trends in sediment or interstitial waters (e.g. Site 1247, Figure 7.7).

7.3. Sulphate and methane in interstitial waters

Sulphate and methane contents in interstitial waters were analysed onboard ODP Leg 204, in order to calculate the SMT depth at each drilled site (Tréhu et al., 2003). Sulphate profiles of the three summit Sites (1248, 1249 and 1250) have not been calculated owing to the depletion of the concentration of these anions in the shallowest centimetres below sea floor (Claypool et al., 2006). Sulphate concentrations near the seafloor (2-5 mbsf) at all the analysed sites are greater than seawater (2.82 $\cdot 10^{-2}$ mol/l; Morris and Riley, 1966), subsequently decreasing until complete exhaustion at SMT defined between 5 and 12 mbsf, where sulphate concentration approaches zero (Figure 7.8). Sulphate gradients show curvilinear shapes at most of the analysed sites, especially at the top of the sediment column but also near SMT depth. This trend can be ascribed to the oxidation of organic matter combined with the effect of fluid advection.

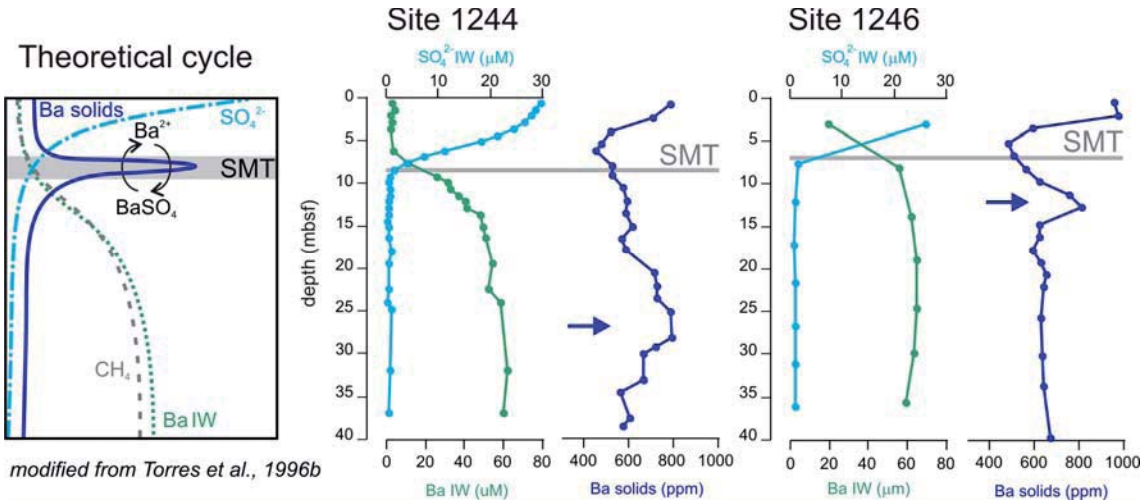

Figure 7.8. Sulphate and Barium data in sediment samples and interstitial waters from Sites 1244 and 1246 on the eastern flank of southern Hydrate Ridge. Sulphate-methane transition zone (SMT) depth at each site was defined on the basis of methane and sulphate data. Well developed Ba-high intervals in sediments are located in the first meters below sea floor (actual Ba – SMT peak) and some meters below it at both analysed sites (blue arrows). mbsf= meter below sea floor.

Analyses performed in the interstitial water from the core-headspaces show methane content ranging from 0 to 14.5 mM, with minimum values in the first meters below seafloor and increasing trends until 5 to 10 mbsf at each non-summit Site. The combination of sulphate and methane profiles at each site was used to calculate the location of the SMT depth (Table 7.2). A well defined SMT occurs at all non-summit Sites (1244 to 1247 and 1251 to 1252), at depths ranging from 4.5 to 11 mbsf. The SMT at the slope basin Sites is more superficial (4.5 and 5 mbsf), whereas SMT at Site 1247 is the deepest one.

		SMT depth (mbsf)
Summit	Site 1248	-
Summit	Site 1249	-
Summit	Site 1250	-
W. flank	Site 1245	7
W. flank	Site 1247	11
E. flank	Site 1244	8.5
E. flank	Site 1246	8
Slope basin	Site 1251	4.5
Slope basin	Site 1252	5

Table 7.2. Sulphate methane transition (SMT) depth at each drilled site of southern Hydrate Ridge (1244 to 1252), defined during ODP Leg 204. mbsf= meter below sea floor.

7.4. Sedimentological and geochemical controls for Barium contents

Downhole Barium distributions analysed in cored sediments from southern Hydrate Ridge show high Barium contents in sediment samples and in the interstitial waters. Some of the high Barium contents in the sediment samples do not correspond to Barium-rich contents in interstitial waters (e.g. Site 1244, 1246, 1247, 1248, 1250) suggesting that Barium-rich mineral (barite) is a stable phase in these intervals. If barite dissolution is taking place, the Barium produced is diffused rapidly, without remaining sufficiently long at this depth to be detected in the interstitial water compositions (Snyder et al., 2007). Some of the Barium peaks can be found several meters below the SMT zone (Figure 7.8), where sulphate is absent and sulphate phases (barite) are assumed to be unstable. This reinforces the idea of the rapid diffusion of fluids at these depths, and will be discussed below. By contrast, some of the Barium-rich intervals in the interstitial water analyses correspond to intervals of normal Barium concentrations in sediments (e.g. Site 1252) suggesting that a Barium-rich fluid is being transported at these depths. Oxygen and sulphate exhaustion at these depths would inhibit precipitation of Barium-rich minerals.

At Sites 1245 and 1247 on the western flank of southern Hydrate Ridge, a Barium enriched interval is found in sediments and interstitial waters results at 150-175 mbsf and 125-135 mbsf, respectively. At Site 1245 this interval coincides with the BSR depth, whereas at Site 1247 it coincides with the depth interval between the BSR and Horizon A (Figure 7.9). Horizon A is an anomalously-bright seismic reflector that was clearly imaged in the multi-channel seismic data from southern Hydrate Ridge (Tréhu et al., 2002). Its negative polarity and extreme brightness suggest that free gas is present in its pore space as has been confirmed by drilling data (Tréhu et al., 2004a). Sedimentological analyses revealed that this 2-4 m thick interval contains several coarse-grained, ash-rich, turbidite beds. Horizon A dips to the northeast from the summit of southern Hydrate Ridge (Site 1248) where it shallows to the BSR depth (110 mbsf) (Figure 7.9).

Gas data collected during ODP Leg 204 on the western flank of southern Hydrate Ridge indicate that the depth interval between Horizon A and the BSR is characterized by an atypical

increase in the ethane/methane (C_1/C_2) ratio (Tréhu et al., 2003), attributed to a rise in ethane concentration. This anomalous distribution of hydrocarbon is due to, at least, two possible mechanisms: a) Ethane recycling after dissociation of gas hydrate which preferentially incorporates ethane; or b) The BSR serves as a barrier to upward fluid flow leading to C_1/C_2 ratios typical of the deep-sourced fluids.

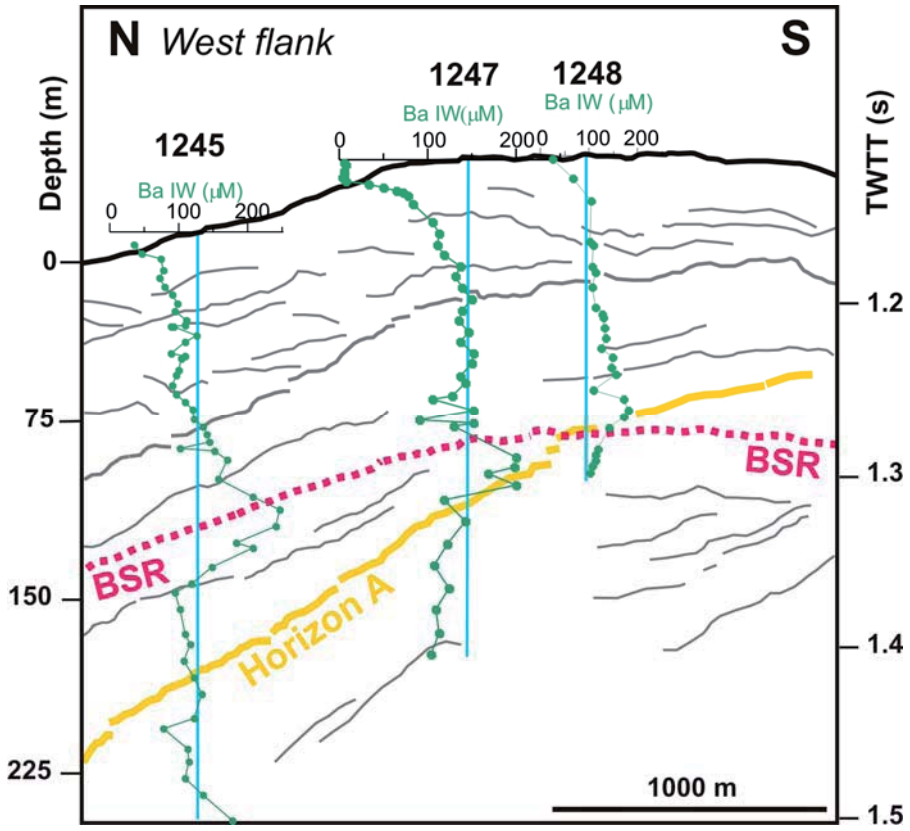

Figure 7.9. Linedrawing of a multi-channel seismic data (Tréhu et al., 2003) along a North-South section on the western flank of southern Hydrate Ridge (Sites 1245, 1247 and 1248). Barium content in interstitial waters (green plots) in relation to the main reflectors identified in the area (e.g. Horizon A, BSR) is superimposed. BSR= bottom simulating reflector; TWTT = two way travel time.

High Barium contents at the deep accretionary complex materials at Sites 1251 and 1252 (Figure 7.6) document the presence of Barium-rich fluids at depth, also supported by the presence of barite at 152 mbsf at Site 1252 (Teichert, personal communication). The Barium enrichment in both pore waters and sediments show an important increase in concentration between Horizon A and the BSR at Sites 1245 and 1247, suggesting migration of Ba-rich fluids along Horizon A and subsequent trapping beneath the impermeable BSR horizon (Figure 7.9). These new data lend support to fluid migration as a cause of the hydrocarbon distribution at southern Hydrate Ridge. Furthermore, the presence of several barite peaks at depth suggests that organic matter oxidation or AOM combined with significant methane fluxes has undergone recurrent processes in southern Hydrate Ridge sediments.

7.5. Barium as diagenetic barite

Barium in marine sediments often forms mineral phases such as sulphate (barite $BaSO_4$), carbonate (witherite $BaCO_3$), Aluminium silicates (e.g. feldspars) oxides and oxyhydroxides (e.g. BaO and $Ba(OH)_2$). The residues of the sequential extraction methodology and their subsequent SEM and EDAX analyses show that at least part of this Barium mostly forms barite mineral at southern Hydrate Ridge (Figure 7.10). It should be noted that barite crystals in the SEM images show euhedral morphologies and sharp edges, providing evidence that they were formed by diagenetic procedures rather than processes associated with biological productivity or detrital input (e.g. Bonny and Jones, 2008; Bertram and Cowen, 1997; Dickens et al., 2003) (Figure 7.11).

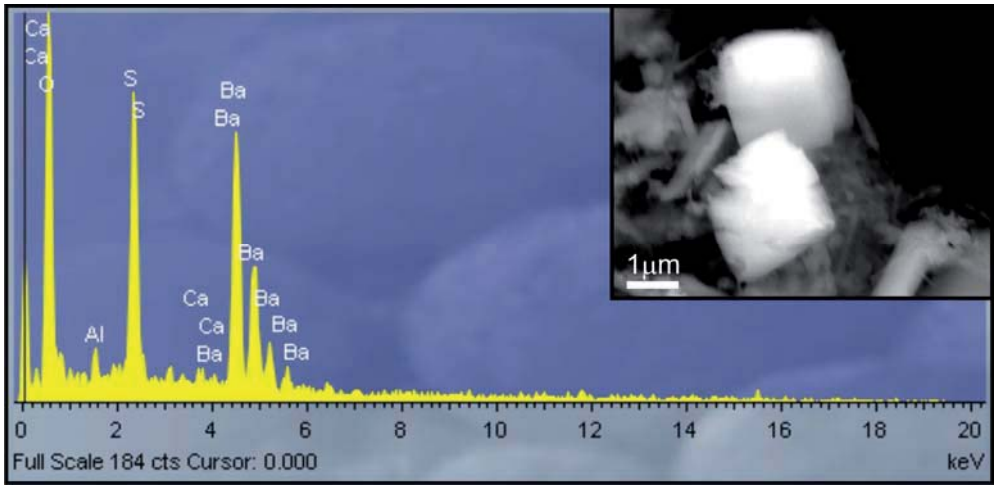

Figure 7.10. EDAX spectrum and scanning electron microscope image of a barite crystal ($BaSO_4$) corresponding to sample Leg 204-1252A-24X2, 50-52 cm; 213.21 meter below sea floor in the slope basin of southern Hydrate Ridge.

Comparison of Ba data with available Ba/Al findings show that Barium peaks are not related to detrital input events (Figure 7.7). Furthermore, comparison with high detrital input events (turbidites and debris flows) in Chapter 5 of this thesis lends support to this idea. Although most of the analysed Sites from southern Hydrate Ridge show several high-Barium contents in the downhole dataset, they cannot be stratigraphically followed from one site to another, even in the same depositional environment (summit, eastern and western flanks or adjacent slope basin) (Figure 7.3 to Figure 7.6). Barium peaks for each site are made up of different lithostratigraphic levels, suggesting that Barium enrichments are not related to sedimentological processes but to post-depositional remobilizations.

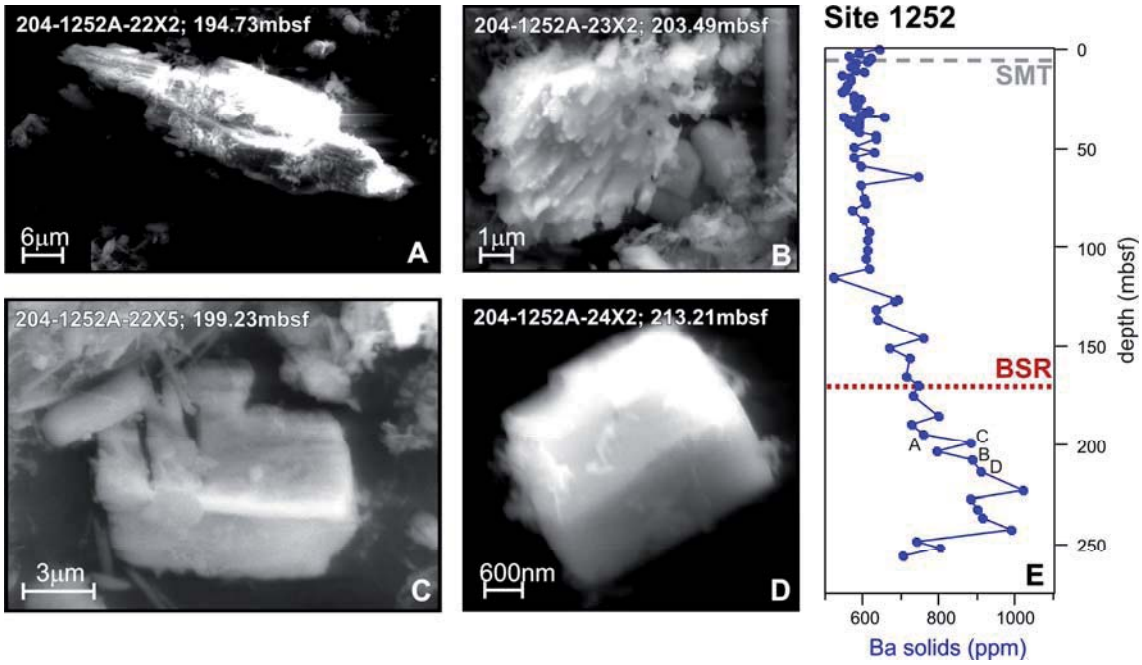

Figure 7.11. A-D. Barite images obtained by scanning electronic microscope after the sequential extraction of barite in selected samples from the slope basin adjacent to southern Hydrate Ridge (Site 1252). **E.** Location of Barium samples in the plot of Barium concentration in sediments at Site 1252. SMT= sulphate methane transition zone; BSR= bottom simulating reflector; mbsf= meter below sea floor.

TOC data can provide information on biological activity. In this regard, barite content has been used before as a proxy for biological productivity studies (e.g. Bishop, 1988; Chow and Goldberg, 1960; Dehairs et al., 1987; 2000; Dymond et al., 1992; 1996; Paytan and Kastner, 1996). In southern Hydrate Ridge sediments, intervals of high Barium content cannot be related to high TOC results (Figure 7.7). Furthermore, Barium-rich peaks do not correspond to the same lithostratigraphic intervals at every analyzed Site (Figure 7.3 to Figure 7.6) and SEM images show that the shapes of the barite particles are not biologically related (Torres et al., 1996a; 1996b). Therefore, Barium contents cannot be related to high biological productivity in southern Hydrate Ridge sediments.

In order to ascertain whether some of the analysed Barium contents were associated with the presence of carbonates, such as the witherite phase, analyses of the Barium content in the acetic acid residue generated during the sequential extraction of barite were performed in fifteen selected samples. The samples were selected on the basis of their Barium, TOC and carbonate contents and their barite abundance. The results confirmed that Barium was not a significant element in the carbonates, with only one value higher than 5 ppm. This finding was regarded as an analytical artefact.

	sample	Total [Ba] ppm	[Carbonate Ba] ppm
Summit	Leg 204-1248C-3X1, 120-122 cm	975	2
	Leg 204-1248C-3X1, 69-71 cm	793	2
W. flank	Leg 204-1245B-1H2, 50-52 cm	884	0.5
	Leg 204-1245B-18X5, 50-52 cm	816	1.7
	Leg 204-1247B-8H2, 47-49 cm	968	3.7
	Leg 204-1247B-3H5, 50-52 cm	750	3
	Leg 204-1247B-19H2, 50-52 cm	806	4
	Leg 204-1247B-8H4, 102-104 cm	821	2.7
E. flank	Leg 204-1244E-4H6, 50-52 cm	795	0.8
	Leg 204-1246B-2H6, 50-52 cm	809	1.3
	Leg 204-1246B-15H5, 54-56 cm	702	4.6
Slope basin	Leg 204-1251B-49X2, 50-52 cm	909	7.3
	Leg 204-1251B-37X5, 50-52 cm	900	1.4
	Leg 204-1252A-22X5, 50-52 cm	678	18.8

Table 7.3. Barium contents analysed on the bulk sample and in the acetic acid residue of the sequential extraction of barite procedure. The analyses show the Barium carbonate content in the sediment samples from southern Hydrate Ridge.

7.6. Time required to form barite fronts

The rate of dissolution and re-precipitation of barite is controlled by the transport of dissolved Barium via molecular diffusion. Thus, the process can be modelled by applying Fick's second law of diffusion provided that the reaction rate at the mineral surface is known (e.g. Berner 1980; Torres et al., 1996a). By applying the modelling software CoTReM to a constant Barium profile with the bounder conditions stated for southern Hydrate Ridge (Chapter 4), an approximation of the maximum time required for the formation of the Barium-rich intervals was obtained (Table 7.4). Initial concentration of Barium in sediments was established for each site on the basis of the measured data presented in this thesis (Figure 7.3 to Figure 7.6).

The time required for the formation of the barite fronts obtained through the CoTReM modelling software ranges from 375 to 1000 years as a function of the modelled Barium value, the Barium background concentration considered, and the sediment porosity for each site. A homogenous porosity was considered at each site, and was calculated as the average of the moisture and density data of the analyses carried out onboard ODP Leg 204 (Shipboard Scientific Party, 2003a; 2003b; 2003c; 2003d). Porosity has been recognized as a substantial influence on the barite-enrichment periods (Riedinger et al., 2006). Therefore, the times presented here should be considered only as an approximation because of the uncertainty of the porosity data (Shipboard Scientific Party, 2002).

	Site	Porosity (%)	$[Ba]_0$ (ppm)	Sample	[Ba] (ppm)	Estimated time (y)
E. flank	1244	60	467	Leg 204-1244C-1H1, 88-90 cm; 0.89 mbsf	789	900
				Leg 204-1244C-10H6, 22-24 cm; 28.21 mbsf	886	1000
E. flank	1246	62	618	Leg 204-1246B-1H2, 50-52 cm; 2 mbsf	973	875
				Leg 204-1246B-2H6, 50-52 cm; 12.7 mbsf	809	600
				Leg 204-1246B-15H5, 54-56 cm; 128.8 mbsf	837	600
W. flank	1245	62	667	Leg 204-1245B-1H2, 50-52 cm; 2 mbsf	884	600
				Leg 204-1245B- 8H5, 50-52 cm; 72.93 mbsf	800	400
				Leg 204-1245B-14H4, 40-42 cm; 127.37 mbsf	802	425
				Leg 204-1245B-18X2, 50-52 cm; 151.11 mbsf	892	625
W. flank	1247	60	698	Leg 204-1247B-2H2, 50-52 cm; 5.6 mbsf	839	380
				Leg 204-1247B-5H6, 127-129 cm; 33.4 mbsf	832	375
				Leg 204-1247B-8H2, 47-49 cm; 55 mbsf	967	700
				Leg 204-1247B-18X2, 50-52 cm; 129.3 mbsf	948	675

Table 7.4. Time required in years (y) for the formation of the analysed Barium-high contents in sediment samples from both flanks of southern Hydrate Ridge calculated through CoTReM modelling software. Porosity data from Shipboard Scientific Party 2002; mbsf= meter below sea floor; [Ba] = Barium concentration in sediments; $[Ba]_0$ = initial Barium concentration in sediments established according to the background values of the results of each site.

The longest times required for barite accumulation were found at Site 1244 and 1246 on the eastern flank of southern Hydrate Ridge (1,000 and 875 respectively), whereas the time required is shorter on the western flank (375 to 625 at Site 1245 and 375 to 700 at Site 1247). The calculated times will be slightly overestimated if we assume a decreasing Barium flux caused by the reduced amount of reactive barite at the deeper Barium fronts, or by a lower dissolution rate under the SMT depth (Riedinger et al., 2006). The calculated times reveal that the SMT depth and the methane flux, which are the most important parameters affecting the formation of diagenetic barite fronts, were constant at these Sites at least during the periods ranging from 375 to 1,000 years.

Recently published studies on Barium-enrichments from the Eastern Cape basin established a formation time of about 14,000 years, for > 4,000 ppm Barium peaks slightly deeper than the SMT (Riedinger et al., 2006). Our study is the first to report the occurrence of preserved barite enrichments in sulphate depleted sediments buried hundred of meters below SMT.

7.7. Shallow barite fronts: Estimated evolution over time

Several Barium peaks have been analysed and modelled from the flanks and slope basin of southern Hydrate Ridge. No shallow Barium peak was observed in the sediments or in the interstitial waters (Figure 7.3) at Sites 1249 and 1250 at the summit of southern Hydrate Ridge.

The SMT at these Sites was not calculated because sulphate gradients at summit Sites (1248, 1249 and 1250) could not be evaluated because the sulphate was apparently depleted in the uppermost 15 cm of sediment beneath the seafloor, a depth interval that is not well sampled in ODP operations (Boetius et al., 2000; Claypool et al., 2006). The sulphate depletion near the sea floor responds to a high methane flux towards the summit through the GHSZ (Tréhu et al., 2006). The methane flux had been previously inferred from the presence of authigenic carbonates and gas vents on the summit of southern Hydrate Ridge (e.g. Suess et al., 2001; Bohrmann et al., 1998) (Figure 2.8). Under these conditions, the high methane flux produces the marine sulphate exhaustion and the subsequent dissolution of barite. The sulphate is then consumed by the methane through AOM in the shallowest sediments at the summit of southern Hydrate Ridge, whereas the released Barium is rapidly diffused through the sedimentary column as part of the migrating fluids (Tréhu et al., 2002). The released Barium would probably have been incorporated into the superficial carbonate crust, but no significant concentrations of Barium have been reported (e.g. Teichert et al., 2005a).

Shallow barite fronts are present in the geochemical data from Sites 1244 to 1247 (Figure 7.4; Figure 7.5). The CoTReM modelling software was applied to these data. The results of modelling barite precipitation and dissolution during early diagenesis show that Barium peaks near the seafloor (2 to 6 mbsf) are currently being dissolved. This indicates that they represent the present interval of direct accumulation of barite (Figure 7.12; Figure 7.13).

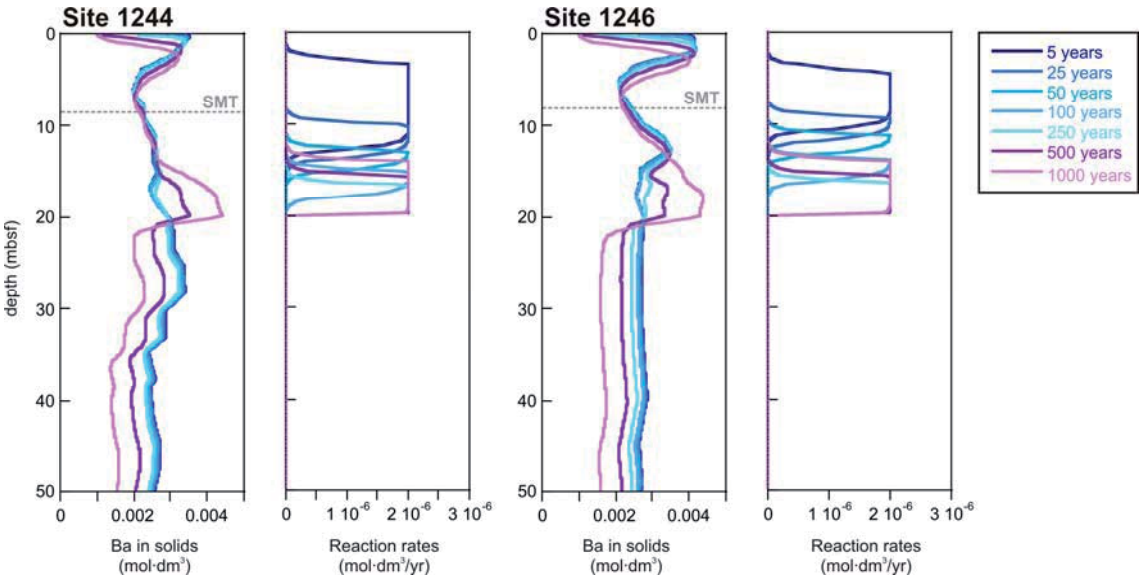

Figure 7.12. Modelling results of Barium concentration and reaction rates over time for Sites 1244 and 1246 on the eastern flank of southern Hydrate Ridge, obtained using CoTReM software in the Barium concentration data analysed in sediment samples recovered during ODP Leg 204. SMT= sulphate methane transition zone; mbsf= meter below sea floor.

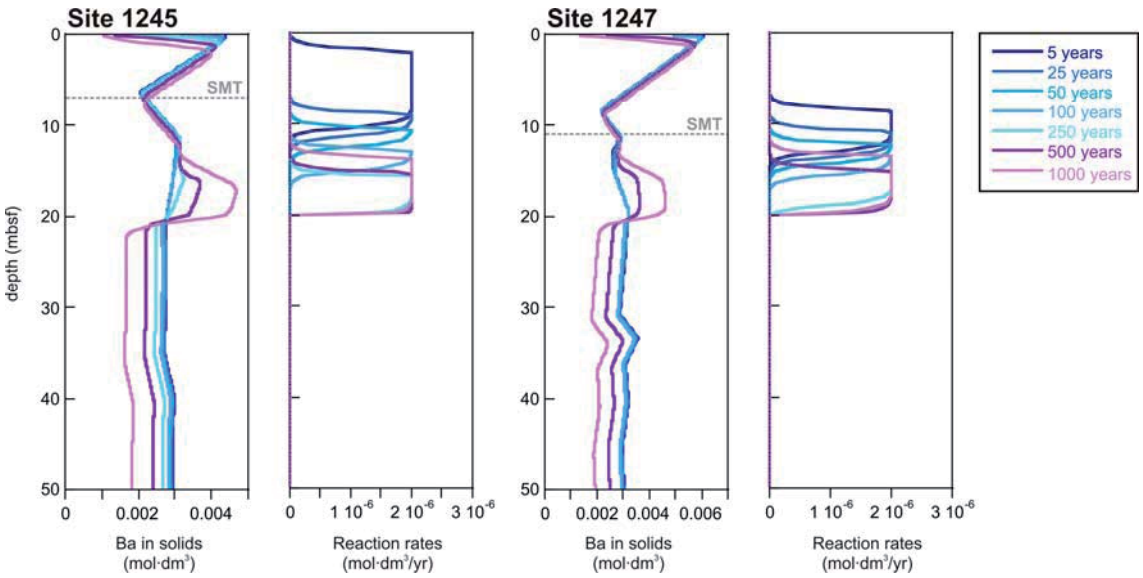

Figure 7.13. Modelling results of Barium concentration and reaction rates over time for Sites 1245 and 1247 on the western flank of southern Hydrate Ridge, obtained by using CoTReM software in the Barium concentration data analysed in sediment samples recovered during ODP Leg 204. SMT= sulphate methane transition zone; mbsf= meter below sea floor.

These Barium-rich intervals are found several meters above SMT, which was defined during the ODP Leg 204 cruise using the methane and sulphate gradients for each site (Table 7.2). A Barium-high content is not observed in the data of the interstitial waters of Sites 1244 to 1247 (Figure 7.4; Figure 7.5), suggesting that a rapid diffusion of the dissolved product is taking place removing all the available Barium. The youngest barite peaks at Sites 1244, 1245, 1246 and 1247 can be ascribed to two different processes (Figure 7.12; Figure 7.13): a) direct accumulation on seafloor of biogenic or terrigenous barite; and b) diagenetical barite recycling in a methane flux environment higher than the present. The estimated times for diagenetic formation of these peaks range from 380 to 900 years. This interpretation is corroborated by the sedimentation rate on both flanks of southern Hydrate Ridge and by the estimated age of the sediments where the peaks are found (ranging from 3 to 72 ky; Table 7.5).

	Site	Depth barite peak (mbsf)	Sedimentation rate (cm/ky)	Estimated age of sediment (y)	Estimated time for peak formation (y)
E. Flank	1244	0.89	27	~3300	900
	1246	2	31	6450	875
W. flank	1245	2	23	4600	600
	1257	5.6	15	72800	380

Table 7.5. Estimated age for shallow sediments containing barite peaks on eastern and western flanks of southern Hydrate Ridge. The estimated times necessary for the barite-enrichment formation are indicated. Sedimentation rates from Tréhu et al., 2003; mbsf= meter below sea floor.

The results of the CoTReM model show that the diagenetic re-precipitation process takes place several meters below the present SMT, and is likely to produce a gradual downward shift of the Barium-rich interval in the next thousand years. At the same time, the initial Barium concentration at >20 mbsf depth is likely to be dissolved owing to the lack of sulphate below SMT. The modelled reaction rates for the next 5 years coincide with the position of the present SMT at each site but with a wider thickness. The maximum reaction rates are also likely to shift downwards in the next thousand years if we consider a constant methane flux.

Our data suggest that, after barite accumulation on the seafloor and during the first stages of burial, barite is currently being dissolved and diffused. The dissolution process will continue for the next thousand years in this interval. Diagenetic barite re-precipitation currently occurs at a wide interval containing SMT, but its position is likely to shift downwards over time. Thus, oxidation of organic matter and AOM in this environment are active processes not only restricted to a narrow interface (SMT) but also active in a wider interval. This interval is represented in the CoTReM results by the high reaction-rate interval (Figure 7.12; Figure 7.13). Similar results have recently been described for the Black Ridge region (Snyder et al., 2007). Some authors have pointed out the possibility of determining the zone where AOM is active after analyzing alkalinity data in interstitial waters (Dickens and Snyder, 2009; Borowski et al., 1996).

Two geochemical processes account for the downward shift in the SMT position: a) a reduction in the methane flux; and b) an increase in the available sulphate that mainly consists of the constant marine water and the dissolved barite sulphate (Riedinger et al., 2006). The CoTReM modelling software considers a constant methane flux from below and a constant sulphate delivery from seawater. Thus, the results of the model suggest that dissolution of the shallowest Barium peak acts as a new sulphate source for the diagenetical processes operating in the system. Nevertheless, a reduction in the methane flux over time could be due to the reduction in the degradation of non-refractive organic matter (methanogenesis) below SMT. This process usually occurs in a large area, affecting several sites of southern Hydrate Ridge. On the other hand, the relatively low TOC values detected in southern Hydrate Ridge sediments contradicts this explanation. Another reason for a downward shift of the SMT depth is a rapid depositional event, such as a gravity mass flow, which will be discussed below.

7.8. Deep Barium peaks: Mechanisms for deep barite formation and preservation

A number of Barium fronts below the SMT depth were analyzed and modelled at Sites 1244, 1245, 1246 and 1247 on both flanks of southern Hydrate Ridge. As discussed above, some barite peaks are conserved several meters below SMT, where barite should not theoretically be preserved due to sulphate exhaustion. Some explanations for barite conservation, which will be discussed below, include a carbonate crust protection for barite particles or episodes of rapid sedimentation. Another topic discussed in this section is the deep preservation of barite fronts as a result of the advection of sulphate-rich fluids from the accretionary complex materials.

Riedinger et al. (2006) suggested a carbonate crust protection for barite fronts from the Eastern Cape basin. This study proposes the dissimilatory reduction of sulphate via the formation of other Barium compounds such as witherite ($BaCO_3$) and the transient species of Barium sulphide (BaS) in a high alkalinity and TOC environment (Baldi et al., 1996). As a result of this process, a sulphur or carbonate coating would individually shield each barite particle from dissolution. Although this process requires further investigation to be elucidated, the low TOC values as well as the low Barium content in the carbonate leaching phase of the barite sequential extraction suggest that this is not a valid explanation for the preservation of barite fronts under SMT at southern Hydrate Ridge. On the other hand, a number of barite particles that form part of the residue of the barite sequential extraction method show relatively high Ca contents in the EDAX analyses. A comprehensive study of the results concerning this topic is currently being carried out.

An abrupt increase in the sedimentation rate has been regarded as a possible cause of a barite front preservation through the sedimentary column (Torres et al., 1996bb; 2003). After a barite front formation near SMT during a period of constant fluid flow and sulphate gradient, a sudden deposition of sediments produced by a single mass-transport deposit or a high depositional period could produce burial of the barite front several meters below SMT. The change in the reduction capacity of sediments over depth is not a well documented issue. Therefore, the geochemical factors that affect the sulphate reduction at depth should be studied in greater detail. Nevertheless, the numerous mass-transport deposits identified at southern Hydrate Ridge (Figure 5.14; Figure 5.15; Table 5.1) suggest that this could be a likely explanation for barite front survival some meters below SMT. Although an accurate age model has not been established, several debris flow deposits identified in the slope basin adjacent to southern Hydrate Ridge could have sealed the barite fronts at Sites 1251 and 1252. Future work

on this hypothesis will include the modelling of the barite peaks at these sites. A comparative study of the time required for the peaks formation with the age of the sediments and the age of the mass-transport deposits identified above them will also be carried out. In this context when the fronts exceed the dissolution depth some meters below SMT, barite could be dissolved owing to the lack of sulphate. The sulphate produced would be consumed and reduced to sulphur, enabling the formation of sulphide minerals. Dissolved Barium diffused upwards until the base of the GHSZ, which acts as a barrier to fluids due to the presence of gas hydrates filling the porosity above it.

Other authors have established that advection of sulphate-bearing fluids from deep within the sedimentary column is a mechanism that can promote large accumulation of Barium sulphates (e.g. Torres et al., 1996b). Large-scale fluxes of fluids within sediment sequences are common occurrences in convergent margin settings, such as the Cascadia margin (Kastner et al., 1995; Kulm and Suess, 1990; Torres et al., 1996b). Horizon A has been identified as one of the main conduits feeding fluids from deep in the accretionary complex into the GHSZ at southern Hydrate Ridge (e.g. Tréhu et al., 2005). Although the plots of Barium concentration in interstitial waters and sediment samples from the accretionary complex at Sites 1251 and 1252 suggest that the dissolution of barite peaks is taking place (Figure 7.6), geochemical data afforded no evidence of a sulphate-rich fluid reaching the summit or the flanks of southern Hydrate Ridge. Furthermore, the relatively high concentration of Barium in interstitial waters at the summit and on both flanks of Hydrate Ridge (Sites 1244 to 1250) suggests that barite is being dissolved at these depths due to sulphate depletion (Figure 7.3; Figure 7.4; Figure 7.5). However, further investigation on this topic is warranted. Recently published studies have highlighted the usefulness of strontium isotopes to trace the origin of fluids in accretionary complex settings such as the Cascadia margin (e.g. Ritger et al., 1987; Sample and Reid, 1998; Teichert et al., 2005b). Research on the isotopic composition of strontium in deep barite crystals could corroborate the hypothesis of barite deep formation at southern Hydrate Ridge.

In conclusion, the Barium data discussed in this thesis account for a complete model of formation and preservation of barite fronts at southern Hydrate Ridge. Barite is deposited on the seafloor as result of biogenic activity or detrital input. During early diagenesis it is dissolved and diffused as a function of methane flux, sulphate availability and sedimentation rate, forming several barite fronts in the shallow sedimentary column. Modelling results suggest that the recycling processes act in a wide interval rather than in a narrow interface. The size of barite peaks indicates a constant methane flux between 400 and 1,000 years. Increases in the sedimentation rates such as sudden large mass-transport deposits could occasionally bury these fronts exceeding the SMT depth, favouring the barite front conservation. Another possible

explanation for the conservation of barite peak is the carbonate or sulphur coating and studies are currently being carried out to elucidate this topic. At great depths, sulphate-rich fluids migrating from the deep accretionary complex material through high-permeability conduits could sustain barite fronts. Nevertheless, the Barium concentration profiles suggest that barite is currently being dissolved at the summit and flanks of southern Hydrate Ridge, and that dissolved Barium is being diffused upwards. This process is taking place below the GHSZ, which acts as an impermeable barrier to fluid flow. The study of the isotope composition of strontium in the deep barite phase would improve our understanding of this process.

8. Discussion and conclusions

In this thesis we presented and interpreted a sedimentological and geochemical study of the southern Hydrate Ridge sediments including the summit, the eastern and western flank and the slope basin. These results were combined with mineralogical and magnetic susceptibility data from the same sediment samples, as well as with physical properties measured onboard during ODP Leg 204. The interpretation of all the obtained results benefited from the fact that all the applied techniques were run on sediments sampled on the same position of the sedimentary column, and thus, sedimentological, mineralogical, magnetic and geochemical datasets can be directly related.

Through all these analyses, we have characterized the sediments that form southern Hydrate Ridge, exploring the relationship between their texture and gas hydrate distribution. As regard to the geochemical characterization of sediments, we focused on the distribution of the Barium composition (in both sediments and pore waters), which has provided a new approach to the reactions that take place in methane-rich areas, such as the marine gas hydrate system of southern Hydrate Ridge.

8.1. Sedimentology and mineralogy of sediments from southern Hydrate Ridge

The textural analyses of 581 Pliocene to Holocene sediment samples have shown that southern Hydrate Ridge is mainly composed of poorly sorted greenish-grey silty-clays (mean diameter averaged 8.4ϕ). As regard to their mineral composition, these sediments are mainly formed of clays (30-60%), quartz (25-40%), feldspars (10-25%) and minor amounts of calcite (usually below 5%). The clay mineral assemblages are composed of detrital mica (45%), smectites (10-30%), chlorite (10-30%) and kaolinite (10-30%); detecting some remarkable trends in their contents (Figures 5.1, 5.3, 5.5 and 5.7). These results coincide with other compositional analyses in the area (e.g. Underwood and Torres, 2006) and have allowed a new and exhaustive description of the main lithofacies identified in the southern Hydrate Ridge sediments, as: hemipelagite, turbidite, debrite and ash layers (Figures 5.10 to 5.13). The study of their distribution in the area permitted the new characterization of six main LU ranging from the Pliocene to the present (Figure 5.14).

The main processes affecting sedimentary transport and deposition in southern Hydrate Ridge have been evaluated, as well as their evolution during the last ~1.5 million of years.

Sediments were transported in the Oregon margin through suspension and bedload processes. Suspension transport of fine-grained particles is basically controlled by the oceanographic currents operating in the Oregon margin. Concerning the bedload transport and sedimentation in the continental margin, the three main processes considered, in accordance with Sternberg (1986), are: a) turbidite events coming from the Columbia River along the Astoria and Willapa canyons; b) direct sediment supply coming from the Klamath Mounts; and c) local re-working sedimentary processes.

Since smectite is the main clay mineral supplied by the Columbia River (e.g. Karlin, 1980), the upwards increase in the smectite content detected at most of the analysed Sites of southern Hydrate Ridge suggests that the California current, the main oceanographic current responsible of the suspended sediment distribution in the southern Cascadia margin, was more effective during the Pliocene and early Pleistocene than during the middle to late Pleistocene. This was probably related to the global sea-level fluctuations, previously suggested by Herbert (2001).

The relative abundance of submarine mass-transport deposits (turbidites and debrites) in each LU suggests that bedload processes were more effective during the middle Pleistocene, resulting from the increase of sediment supplies from the Klamath Mount as well as local re-working processes. The reactivation of the tectonic uplift of Hydrate Ridge during the Holocene, previously inferred by seismic studies (e.g. Chevalier et al., 2006), produced an increase of the local re-working processes, especially in the slope basin adjacent to southern Hydrate Ridge where numerous debris flow were deposited.

The temporal distribution of submarine mass-transport deposits identified in southern Hydrate Ridge, as well as seismic unconformities and seafloor erosive scars, suggests that slope instability has been a recurrent process that is still active. The extensive presence of gas hydrates in the area, as well as the location of mass-transport deposits in the slope basin adjacent to this structural high, suggests that a shift of the base of the GHSZ in relation to sea level changes and subsequent gas hydrate dissociation, should be taken into account as a triggering mechanism for mass transport deposits in marine gas hydrate systems, such as southern Hydrate Ridge. In addition, in a seismically active margin as the Oregon margin, earthquakes mainly generated along the Cascadia subduction zone may also play an important role in triggering gravity flows (e.g. Goldfinger et al., 2003, 2006).

8.2. Gas hydrate presence in southern Hydrate Ridge in relation to sedimentary texture

Mousse-like and soupy fabrics are the main sedimentary disturbance fabrics identified in association with gas hydrate dissociation and produced by changes in the P/T conditions during sediment recovery (Kastner et al., 1995; Piñero et al., 2007; Figure 3.13). The dissociation of gas hydrate was stimulated on four sediment sequences previously stored in conditions of ambient pressure and extremely low temperature (liquid Nitrogen). This dissociation produced soupy and mousse-like fabrics in several of the analyzed sediment intervals, corroborating the use of the sediment disturbance fabric soon after core recovery as a proxy for the presence of gas hydrates.

The accurate sedimentological analyses of eight sediment disturbed core sections, as well as of twenty gas hydrate-rich samples from southern Hydrate Ridge lead to the conclusion that gas hydrates preferentially form in the coarse grain layers, because of their large porosity and permeability. The sediment porosity allows available space for gas hydrates to form and grow, but it is also a preferential pathway for the migration of methane-rich fluids. These results are in accordance to previous studies, in which the presence of gas hydrate was related to layers of higher sandy contents (e.g. Weinberger et al., 2005; Figure 8.1).

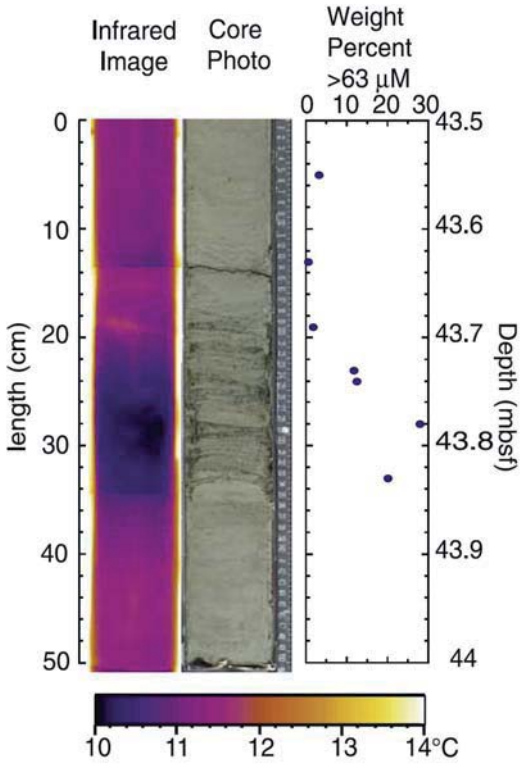

Figure 8.1. Infrared image and core photograph of sample 204-1250C-6H1, 100–150 cm from the summit of southern Hydrate Ridge. The dark blue to black region in the IR image is a negative thermal anomaly associated with gas hydrate. The core photo shows a series of disrupted sand horizons, and the grain size data confirm visual observations of sand horizons. The blue area at 12 cm (43.62 mbsf) is an image edge effect and is not linked to the gas expansion joint in the core at the same depth. mbsf = meter below sea floor (Weinberger et al., 2005).

Although the original depositional features of the disturbed sediment samples and gas hydrate-rich intervals analyzed in this study were not recognizable due to gas hydrate dissociation, textural results suggest that they correspond to turbidite facies. The recognition of their sedimentary texture as corresponding to a turbidite facies reinforced the idea that methane-rich fluids are conducted through the coarse-grained layers within the sedimentary sequence.

8.3. Authigenic barite fronts in southern Hydrate Ridge sediments

Sediments from southern Hydrate Ridge show averaged Barium content of 688 ppm, ranging from 454 to 1021 ppm. The results show several Barium fronts over depth, which generally coincide with high-values of Barium content in the interstitial waters. The maintenance of the concentration-plot features when we normalize Barium to Aluminium content, suggests that Barium enrichments are not related to detrital input events. Furthermore, comparison of the Barium to TOC content suggests that Barium enrichments are not related with events of high biological activity in southern Hydrate Ridge. Thus, the chemical reactions and fluid transport that take place during early diagenesis seem to be the most reliable process producing the Barium-rich fronts.

The mineralogical study by SEM of the Barium-rich phases, subsequently to the barite sequential extraction, has demonstrated that those mainly correspond to barite crystals. In addition, the morphological study of such crystals revealed euhedral morphologies of the particles, which reinforces the idea of the diagenetic origin of the barite grains. During early diagenesis, barite undergoes a recycling process that leads to its accumulation in a single front, in relation with the SMT. The methane flux in the sedimentary column, as well as the available sulphate and the sedimentation rate control the size and position of the barite front. Thus, if the sedimentation rate is well constrained for a given area, the methane flux evolution over time can be deduced studying the Barium peaks downcore.

The application of the CoTReM numerical software on the Barium data from sediments and interstitial waters, together with boundary conditions determined from onboard Leg 204 data, suggests that the barite fronts detected in southern Hydrate Ridge required up to 1,000 years to be formed. This geochemical model allows the recognition of the sediment interval where barite reactions are taking place (i.e. the interval where AOM is active) as a wider interval rather than a narrow interface. The thickness of the area were AOM is active over time, would be future refined through the study of the alkalinity data of the interstitial waters, and its inclusion in the software for geochemical modelling. The results of the CoTReM model suggest that, for a constant methane flux, the barite-rich fronts and the reaction intervals (SMT) will shift their

position downwards during the next thousand years in both flanks of southern Hydrate Ridge (Site 1244 to 1247).

A number of barite fronts are found in the area where sulphate is theoretically exhausted (i.e. below the SMT). In accordance with Riedienger et al. (2006) two mechanisms have been discussed in order to explain the barite conservation over time: a) a carbonate or sulphur coating; and b) a sudden sedimentation event. There is not conclusive evidence for highlighting one of both interpretations, although the low Barium values detected in the leached-carbonate residue suggests that Barium carbonate (witherite) is not a common mineral in southern Hydrate Ridge sediments. On the other hand, some studies have pointed out the relation of methane and gas hydrate presence to the formation of magnetic-sulphur minerals, such as greigite and pyrrhotite, in southern Hydrate Ridge (e.g. Larrasoaña et al., 2007; Figure 8.2).

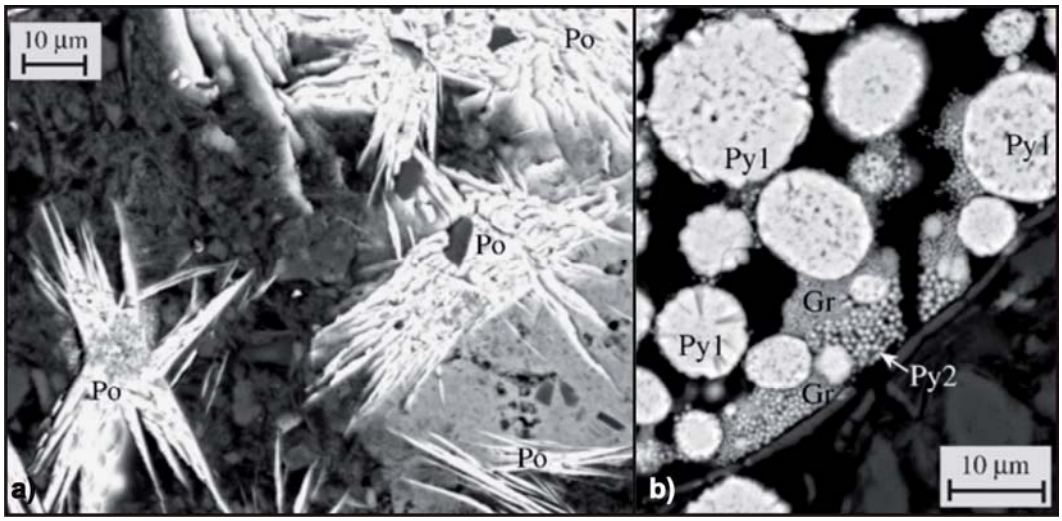

Figure 8.2. Back-scattered scanning electron microscope images of samples 204-1247B 18X5, 50-52 cm (A) and 204-1245E 5R1, 50-52cm (B), with different magnetic properties; showing the formation of magnetic-sulphur minerals in southern Hydrate Ridge. Gr = greigite; Po = pyrrhotite; Py1, Py2 = pyrite (modified from Larrasoaña et al., 2007).

Several authors have pointed out the existence of sulphate-rich fluids in accretionary complex areas, such as the Cascadia margin, which would migrate over long distances through the main permeable conduits (Torres et al., 1996a). These fluids could lead to the formation of barite fronts at great depths, where theoretically a lack of sulphate is expected. However, the Barium data in interstitial waters from southern Hydrate Ridge suggest that barite dissolution is taking place at depth. The dissolved Barium undergoes an upwards diffusion until the GHSZ base, which acts as a barrier for fluids due to the occupancy by gas hydrates of the porosity.

In this thesis, we have presented the lithostratigraphic characterization of southern Hydrate Ridge sediments and a complete study of how sedimentary texture influences gas hydrate distribution. Furthermore, it is discussed how gas hydrate and methane flux produce characteristic geochemical signals, and how they evolve over time due to a number of parameters. Sediment properties influence permeability, which determines the fluid flow pathways and the available methane to form gas hydrates and also to react with other geochemical compounds. These ideas confirm the necessity of applying multidisciplinary approaches in order to understand the evolution of the marine sedimentary gas hydrate systems.

8.4. Conclusions

The main conclusions reached in this thesis include:

- Most of the sediments that form southern Hydrate Ridge correspond to hemipelagites, in which numerous turbidite deposits are interbedded, as well as a number of ash layers and debrites.

- The sedimentation patterns in the Hydrate Ridge region are controlled by climate and tectonic parameters such as the regional intensity of the California Current or the local tectonic movements that lead to the uplift of the Ridge. These parameters mainly control the clay minerals distribution as well as the sedimentary facies that are produced.

- The transport through the California Current of fine sediments in suspension was more effective during the Pliocene and early Pleistocene period. Bedload transport of coarse material from local and distal areas was more effective during the middle Pleistocene and Holocene due to the reactivation of the southern Hydrate Ridge uplift.

- During the late Pleistocene and owing to the pervasive fluctuation of sea-level, gas hydrate dissociation, as well as the seismic movement of the Oregon margin seems to be the most plausible triggering mechanisms for mass-movement deposits in the southern Hydrate Ridge region.

- Mousse-like and soupy sedimentary fabrics are produced after gas hydrate dissociation in a sedimentary core. During visual core description, the accurate identification and logging of soupy and mousse-like sediments is extremely important, especially in gas hydrate-bearing areas such as accretionary ridges, mud volcanoes, and high fluid flow locations.

- Most of the disturbed and gas hydrate-rich sediment samples from southern Hydrate Ridge analyzed for this thesis correspond to coarse-grained layers, presumably turbidites. These coarse layers due to their relatively higher permeability could act as conduits feeding methane-rich fluids into the GHSZ and as preferred intervals for gas hydrate formation in the GHSZ.

- Several barite fronts formed at southern Hydrate Ridge as a result of early diagenetical processes in relation to methane-rich fluids and *in situ* organic matter decomposition. These processes were active for a period of up to one thousand years on the eastern flank of southern Hydrate Ridge.

- The sedimentary texture plays an important role in controlling the major fluid flow pathways at southern Hydrate Ridge. The temporal evolution of the fluid flow can be studied in a given area through the mineral phases that form during early diagenesis.

Nevertheless, a number of interesting questions still need to be solved, and are presented next.

8.5. Perspectives for future research

This thesis corresponds to a multidisciplinary study of a marine gas hydrate system, integrating sedimentological, mineralogical and geochemical approaches. However, there have been some difficulties that need to be pointed out. In this regard, the uncertainty in the sediment age represented a major handicap for this study, specially constraining the temporal evolution of the climatic and tectonic processes that governed the sedimentology at southern Hydrate Ridge (e.g. Figure 5.17).

In addition, there is more work to be done. Here follow some proposals for advances and improvements of forthcoming research.

- Statistical analysis of the data

We have presented the complete textural and geochemical characterization of 561 discrete samples from the nine drilled Sites during ODP Leg 204 on the summit, eastern and western flank and slope basin of southern Hydrate Ridge (Site 1244 to 1252). This data include grain-size distribution, statistical textural parameters, coarse grain quantification, carbonate content, TOC, bulk and clay mineralogy semi-quantifications, magnetic susceptibility and trace and major element composition. Other available data of samples from the same intervals are the complete rock magnetic characterization (low fields magnetic susceptibility, anhysteretic

remanent magnetization and isothermal remanent magnetization at different fields, FORC distributions, etc.) which could be directly related (Larrasoaña et al., 2006; 2007).

However, an accurate statistical analysis of the complete dataset would be of major interest. In this sense, a multivariate statistical model is probably the best option. Specifically, the *principal component analysis* as well as the *correspondent analysis* would help establishing which variables are independent as well as the relationships between them. This approach would help understanding which geological processes affect each sedimentological, mineralogical or geochemical parameter. As regard to the main lithofacies defined in southern Hydrate Ridge, a *recursive portioning model* could be used to numerically evaluate the sample classification presented in this thesis.

- Tectonic and climatic controls in a wider geological context

A complete sedimentological study of the whole Cascadia margin area would provide new insights to establish whether the influence of the climatic and tectonic parameters that control the sediment supply and distribution is regional or local. In this sense, several studies already published have been briefly discussed in this thesis (e.g. Underwood et al., 2006). Nevertheless, a more accurate analysis of the discrete sedimentological and mineralogical data available would be necessary in order to characterize the main parameters that affect sediment distribution in the whole Cascadia margin as well as their evolution over time. In this sense, a comparative study of our mineralogical data with the data obtained during Expedition 311 of the IODP off the Vancouver Island margin is planned. In order to solve the age uncertainty, several techniques could be applied, as the direct determination of the sediment age by the ^{14}C method for ages up to 50,000 years, as well as generating an accurate oxygen isotope curve (^{18}O) or a magnetic paleointensities curve, reaching periods of all the Quaternary and upper Pliocene.

- Geochemical modelling

Concerning the geochemical data presented in this thesis, several tasks have still to be completed, such as the interpretation of most of the trace and major elements analyzed by ICP-MS and AAS (Chapter 4). As regard to the Barium data, further isotope analyses (δSr, δS) of barite crystals would result very useful in order to clarify the main fluid flow pathways from deep in the accretionary complex into the shallow sediments of Hydrate Ridge. An accurate study of the EDAX results on the residue particles of the barite sequential extraction is being carried out in order to investigate if a carbonate or sulphur coating is preserving barite particles from dissolution during sediment burial.

The CoTReM modelling software also needs some adjustments to accurately predict the future evolution of the Barium fronts from the summit of southern Ridge (Sites 1248 to 1250), where the AOM zone is very shallow, reaching the seafloor. The application of this model on the geochemical data from the summit would help quantifying the evolution of the methane flux in the southern Hydrate Ridge area. Applying the model to the geochemical data of the pore waters obtained during Expedition 311 of the IODP will also be taken into consideration.

In addition, geochemical models such as CoTReM could be applied to other mineral reactions that take place during early diagenesis. In this sense, interesting studies have been presented about the formation of magnetic sulphide minerals (greigite and pyrrhotite) in relation to methane hydrate presence in southern Hydrate Ridge (Larrasoaña et al., 2006; 2007). With the aim of completing this work, the application of CoTReM to the sulphide, iron and methane concentration data in the sediment samples and interstitial waters from southern Hydrate Ridge needs to be developed. This new approach would add valuable information concerning the use of mineral fronts, such as barite, greigite and pyrrhotite, in the sedimentary column as proxies to study the temporal evolution of the methane flux in marine sedimentary gas hydrate systems.

PART IV

9. References

Abegg, F., Bohrmann, G., and Kuhs, W., 2006. Data report: Shapes and structures of gas hydrates imaged by computed tomographic analyses, ODP Leg 204, Hydrate Ridge. In: Tréhu, A.M., Bohrmann, G., Torres, M.E., Colwell, F.S. (eds.), Proceedings of the Ocean Drilling Program, Scientific Results, College Station, Texas (Ocean Drilling Program) **204**: 1-11.

Abegg, F., Bohrmann, G., Freitag, J., and Kuhs, W., 2007. Fabric of gas hydrate in sediments from Hydrate Ridge-results from Ocean Drilling Program Leg 204 samples. *Geo-Marine Letters* **27**: 269-277.

Adam, D., 2002. Fire from ice. *Nature* **415**: 913-914.

Adams, J., 1990. Paleoseismicity of the Cascadia subduction zone: evidence from turbidites off the Oregon-Washington margin. *Tectonics* **9**: 569-83.

Adam, J., Klaeschen, D., Kukowski, N., and Flueh, E., 2004. Upward delamination of Cascadia Basin sediment infill with landward frontal accretion thrusting caused by rapid glacial age material flux. Tectonics **23**: TC3009.

Adler, M., Hensen, C., and Schulz, H.D., 2000. CoTReM: Column Transport and ReactionModel;UserGuide,Version2.3.http://www.geochemie.uni-bremen.de/downloads/cotrem/index.htm. (Oct. 2007)

Aloisi, G, Drews, M, Wallmann, K., and Bohrmann, G., 2004a. Fluid expulsion from the Dvurechenskii mud volcano (Black Sea) Part I. Fluid sources and relevance to Li, B, Sr, I and dissolved inorganic nitrogen cycles. *Earth and Planetary Science Letters* **225**: 347-363.

Aloisi, G, Wallmann, K, Haese, R.R., and Saliège, J.F., 2004b. Chemical, biological and hydrological controls on the 14C content of cold seep carbonate crusts: numerical modelling and implications for convection at cold seeps. *Chemical Geology* **213**: 395-383.

Archer, D., 2007. Methane hydrate stability and anthropogenic climate change. *Biogeosciences* **4**: 521-544.

Archie, G.E., 1942. The electrical resistivity log as an aid in determining some reservoir characteristics: Transactions of the American Institute of Mining Metallurgical and Petroleum Engineers **146**: 54–67.

Atwater, B.F., Satoko, M.R., Kenji, S., Yoshinobu, T., Kazue, U., and Yamaguchi, D.K., 2005. The orphan tsunami of 1700: Japanese clues to a parent earthquake in North America. U.S. Geological Survey / University of Washington Press; 144 pp.

Aya, I., Yamane, K., and Nariai, H., 1997. Solubility of CO_2 and density of CO_2 hydrate at 30 MPa. *Energy* **22** (2-3): 263-271.

Baldi, F., Pepi, M., Burrini, D., Kniewald, G., Scali, D., and Lanciotti, E., 1996. Dissolution of barium from barite in sewage sludges and cultures of Desulfovidrio desulfuricans. *Applied and Environmental Microbiology* **62**: 2398-2404.

Bangs, N.L.B., Musgrave, R.J., and Tréhu, A.M., 2005. Upward shifts in the southern Hydrate Ridge gas hydrate stability zone following postglacial warming, offshore Oregon. *Journal of Geophysical Research - Oceans* **110**: B03102.

Barnes, J., 1994. Mother of Storms. Publ. by Tom Doherty Associates, Inc. New York, 432pp.

Barry, J.P., and Kochevar, R.E., 1998. A tale for two clams: Differing chemosynthetic life styles among vesicolmyids in Monterey Bay cold seeps. *Cahiers de Biologie Marine* **39** (3-4): 329-331.

Bea, F., Montero, P., Stroh, A., and Baasner, J., 1996. Microanalysis of minerals by an Excimer UV-LA-ICP-MS system. *Chemical Geology* **133**: 145-156.

Ben-Avraham, Z., Smith, G., Reshef, M. And Junglager, E., 2002. Gas hydrate and mud volcanoes on the southwestern African continental margin off South Africa. *Geology* **30** (10): 927-930.

Berner, R.A., 1980. Early diagenesis: A theoretical approach. Princetown Series in Geochemistry. Princetown University Press, N.J. (USA), 256pp.

Berner, R.A., Lasaga, A.C., and Garrels, R.M., 1983. The carbonate-silicate geochemical cycle and its effect on atmospheric carbon dioxide over the past 100 million years. American *Journal of Science* **283**: 641-683.

Bertram, M. and Cowen, J.P., 1997. Morphological and compositional evidence for biotic precipitation of marine barite. *Journal of Marine Research* **55**: 577-593.

Bianchi, G.G., Hall, I.R., McCave, I.N., and Joseph, 1999. Measurement of the sortable silt current speed proxy using the Sedigraph 5100 and Coulter Multisizer IIe: precision and accuracy. *Sedimentology* **46** (6): 1001-1014.

Bily, C. and Dick, J.W.L., 1974. Naturally occurring gas hydrates in the Mackenzie Delta. *Bulletin of Canadian Petroleum Geology* **22**: 320-352.

Bishop, J.K.B., 1988. The barite-opal-organic carbon association in oceanic particulate matter. *Nature* **332**: 341–343.

Blinova, VN, Ivanov, M.K., and Bohrmann, G., 2003. Hydrocarbon gases in deposits from mud volcanoes in the Sorokin Trough, north-eastern Black Sea. *Geo Marine Letters* **23**: 250-257.

Blum, P., 1997. Physical properties handbook: a guide to the shipboard measurement of physical properties of deep-sea cores. Ocean Drilling Program Technical Note 26. [Online]. Available from World Wide Web: <http://www-odp.tamu.edu/publications/tnotes/tn26/INDEX.HTM>. [Cited 2009-01-29].

Boetius, A., Ravenschlag, K., Schubert, C.J., Rickert, D., Widdel, F., Gieseke, A., Amann, R., Jørgensen, B.B., Wite, U., and Pfannkuche, O., 2000. A marine microbial consortium apparently mediating anaerobic oxidation of methane. *Nature* **407**: 623-626.

Bohannon, J., 2008. Weighing the Climate Risks of an untapped fossil fuel. *Science* **319**: 1753.

Bohrmann, G., Greinert, J., Suess, E. and Torres, M., 1998. Authigenic carbonates from the Cascadia subduction zone and their relation to gas hydrate stability. *Geology* **26**: 647-650.

Bohrmann, G., Heeschen, K., Jung, C., Weinrebe, W., Baranov, B., Cailleau, B., Heath, R., Hühnerbach, V., Hort, M., Masson, D., and Trummer, I., 2002. Widespread fluid expulsion along the seafloor of the Costa Rica convergent margin. *Terra Nova* **14**: 69-79.

Bohrmann, G., Ivanov, M., Foucher, J.-P., Spiess, V., Bialas, J., Greinert, J., Weinrebe, W., Abegg, F., Aloisi, G., Artemov, Y., Blinova, V., Drews, M., Heidersdorf, F., Krabbenhöft, A., Klaucke, I., Krastel, S., Leder, T., Polikarpov, I., Saburova, M., Schmale, O., Seifert, R., Volkonskaya, A., and Zillmer, M., 2003. Mud volcanoes and gas hydrates in the Black Sea: new data from Dvurechenskii and Odessa mud volcanoes. *Geo-Marine Letters* **23**: 239-249.

Bohrmann, G., Kuhs, W.F., Klapp, S.A., Techmer, K.S., Klein, H., Mangir Murshed, M., and Abegg, F., 2007. Apperarance and preservation of natural gas hydrate from Hydrate Ridge sampled during Ocean Drilling Program Leg 204 drilling. *Marine Geology* **244**: 1-14.

Bonny, S.M. and Jones, B., 2008. Experimental precipitation of barite ($BaSO_4$) among streamers of Sulfur-oxidizing bacteria. *Journal of Sedimentary Research* **78** (5): 357-365.

Booth-Rea, G., Klaeschen, D., Grevemeyer, I., and Reston, T., 2008. Heterogeneous deformation in the Cascadia convergent margin and its relation to thermal gradient (Washington, NW USA). *Tectonics* **27**: TC4005.

Borowski, W.S., 2006. Data report: Dissolved sulfide concentration and sulfur isotopic composition of sulphide and sulfate in pore waters, Ocean Drilling Program Leg 204, Hydrate Ridge and vicinity, Cascadia Margin, offshore Oregon. In: Tréhu, A.M., Bohrmann, G., Torres, M.E., and Colwell, F.S. (eds.), Proceedings of the Ocean Drilling Program Scientific Results, College Station, Texas (Ocean Drilling Program) **204**: 1-13.

Borowski, W.S., Paull, C.K. and Ussler, W., 1996. Marine pore-water sulfate profiles indicate in situ methane flux from underlying gas hydrate. *Geology* **24** (7): 655-658.

Borowski, W.S., Paull, C.K., and Ussler, W., 1999. Global and local variations of interstitial sulfate gradients in deep-water, continental margin sediments: sensitivity to underlying methane and gas hydrates. *Marine Geology* **159**: 131-154.

Borowski, W.S., et al., 2000. Significance of Anaerobic Methane Oxidation in Methane-Rich Sediments Overlying the Blake Ridge gas Hydrate Gas Hydrates. Proceedings of the Ocean Drilling Program Scientific Results **164**.

Bouma, A.H., 1962. Sedimentology of some Flysch deposits: A graphic approach to facies interpretation, Elsevier, Amsterdam, 168 pp.

Bouriak, S., Vanneste, M., and Saoutkine, A., 2000. Inferred gas hydrates and clay diapirs near the Storegga Slide on the southern edge of the Vøring Plateau, offshore Norway. *Marine Geology* **163**: 125-148.

Brooks, J.M., II , M.C.K., Fay, R.R., and Mc Donald, T.J., 1984. Thermogenic gas hydrates in the Gulf of Mexico. *Science* **223**: 696-698.

Bryan, G.M., 1974. In situ indications of gas hydrates in I.R. Kaplan (ed). Natural gasses in marine sediments; New York, Plenum: 298-308.

Bryn, P., Berg, K., Forsberg, C.F. et al., 2005. Explaining the Storegga Slide. *Marine and Petroleum Geology* **22** (1-2): 11-19.

Buffet, B. and Archer, D., 2004. Global inventory of methane clathrate: sensivity to changes in the deep ocean. *Earth and Planetary Science Letters* **227**: 185-199.

Bunz, S. and Mienert, J., 2004. Acoustic imaging of gas hydrate and free gas at the Storegga Slide. *Journal of Geophysical Research-Solid Earth* **109** (B4): B44102.

Camerlenghi, A., Lucchi, R.G. and Rothwell, R.G., 1995. 1. Grain-Size analysis and distribution in Cascadia margin sediments, Northeastern Pacific. In: Carson, B., Westbrook, G.K., Musgrave, R.J., Suess, E. (eds.). Proceedings of the Ocean Drilling Program, Scientific Results (1), College Station, TX (Ocean Drilling Program) **146**: 3-31.

Canals, M., Lastras, G., Casamor, J.L., Mienert, J., Cattaneo, A., de Batisi, M., Heflidason, H., Imbo, Y., Laberg, J.S., Locat, J., Long, D., Longva, O., Masson, D.G., Sultan, N., Trincardi, F and Brynm P., 2004. Slope failure dynamics and impacts from seafloor and shallow sub-seafloor geophysical data: case studies from the COSTA Project. *Marine Geology* **213** (1-4): 9-72.

Carlson, P.R. and Nelson, C.H., 1987. Marine geology and resource potential of Cascadia Basin. In: Scholl, D.W., Grantz, A., Vedder, J.G., (eds.). Geology and resource potential of the continental margin of Western North America and adjacent ocean basins-Beaufort Sea to Baja California. Circum-Pacific Council for Energy and Minery Research, Earth Science Service **6**: 523-535.

Carpenter, G., 1981. Coincident sediment slump/clathrate complexes on the U.S. Atlantic continental slope. *Geo-Marine Letters* **1**: 29-32.

Carson, B., Westbrook, G.K., Musgrave, R.J., and Suess, E. (eds.), 1995. Proceedings of the Ocean Drilling Program, Scientific Results **146** (1), 467 pp.

Castellini, D.G., Dickens, G.R., Snyder, G.T., and Ruppel, C.D., 2006. Barium cycling in shallow sediment above active mud volcanoes in the Gulf of Mexico. *Chemical Geology* **226**: 1-30.

Chamley H., 1989. Clay Sedimentology. Springer-Verlag, Berlin,. 623 pp.

Charlou, J.L., Donval, J.P., Bouquet, Y., Ondreas, H., Knoery, J., Cochonat, P., Levaché, D., Poirier, Y., Jean-Baptiste, P., Fourré, E., Chazallon, B., and the ZAIROV Leg 2 Scientific Party, 2004. Physical and chemical characterization of gas hydrates and associated methane plumes in the Congo-Angola Basin. *Chemical Geology* **205**: 405-425.

Chatti, I., Delahaye, A., Fournaison, L. and Petitet, J.P., 2005. Benefits and drawbacks of clathrate hydrates: a review of their areas of interest. Energy Conversion and Management **46** (9-10): 1333-1343.

Chevallier, J., Tréhu, A.M., Bangs, N.L., Johnson, J.E., and Meyer, H.J., 2006. Seismic sequence stratigraphy and tectonic evolution of southern Hydrate Ridge. In: Tréhu, A.M., Bohrmann, G., Torres, M.E., and Colwell, F.S. (eds.), Proceedings of the Ocean Drilling Program, Scientific Results, College Station, Texas (Ocean Drilling Program) **204**: 1-29.

Chow, T.J. and Goldberg, E.D., 1960. On the marine geochemistry of barium. *Geochimica et Cosmochimica Acta* **20**: 192–198.

Church, T.M. and Wogelmuth, K., 1972. Marine barite saturation. *Earth and Planetary Science Letters* **15**: 35-44.

Circone, S., Stern, L.A., Kirby, S.H., Durham, W.B., Chakoumakos, B.C., Rawn, C.J., et al., 2003. CO_2 hydrate: synthesis, composition, structure dissociation behavior, and a comparison to structure I CH_4 hydrate. *Journal of Physical Chemistry* B **107** (23): 5529-5539.

Cita, M.B., Erba, E., Lucchi, R., Pott, M,. van der Meer, R. and Nieto, L., 1996. Stratigraphy and sedimentation in the Mediterranean Ridge diapiric belt. *Marine Geology* **132**: 131-150.

Clague J.J. and Bobrowsky, P.T., 1994. Tsunami deposits beneath tidal marched on Vancouver Island, British Columbia. *Geological Society American Bulletin* **106**: 1293-1303.

Clague, D.A., Maher, N. and Paull, C.K., 2001. High-resolution multibeam survey of Hydrate Ridge, offshore Oregon In: Paull, C.K., and Dillon, W.P. (eds.) Natural Gas Hydrates: Occurrence, Distribution, and Detection. Geophysical Monograph, American Geophysical Union (Publ.) **124**: 297-303.

Claypool, G.W. and Kvenvolden, K.A., 1983. Methane and other hydrocarbon gases in marine sediments. *Annual Reviews of Earth and Planetary Science* **11**: 299-327.

Claypool, G.E., Milkov, A.V., Lee,Y.J., Torres, M.E., Borowski, W.S., and Tomaru, H., 2006. Microbial methane generation and gas transport in shallow sediments of an accretionary complex, southern Hydrate Ridge (ODP Leg 204), offshore Oregon, USA. In: Tréhu, A.M., Bohrmann, G., Torres, M.E., and Colwell, F.S. (eds.), Proceedings of the Ocean Drilling Program Scientific Results, College Station, Texas (Ocean Drilling Program) **204**: 1-52.

Clennell, M.B., Hovland, M., Booth, J.S., Henry, P. and Winters, W.J., 1999. Formation of natural gas hydrates in marine sediments. 1. Conceptual model of gas hydrate growth conditioned by host sediment properties. *Journal of Geophysical Research* **104** (B10): 22985–23004.

Collett, T., 2001. A review of well-log analysis techniques used to assess gas-hydrate-bearing reservoirs. In: Paull, C.K., and Dillon, W.P. (eds.). Natural Gas Hydrates: occurrence, distribution, and detection. Geophysical Monograph **124**, American Geophysical Union (Publ.): 189-210.

Collett, T., 2002. Energy resource potential of natural gas hydrates. *American Association of Petroleum Geologists Bulletin* **86**: 1971-1992.

Collett, T.S. and Ladd, J., 2000. Detection of gas hydrates with downhole logs. In: Paull. C.K., Matsumoto, R., Wallace, P.J., Dillon, W.P. (eds.). Proceedings Ocean Drilling Program, Scientific Results, **164**, Ocean Drilling Program, College Station TX, 179– 191.

Collett, T.S. and Scientific Party N., 2007. Occurrence of marine gas hydrates in the Indian continental margin: Results of the Indian National Gas Hydrate Program (NGHP) Expedition 01. Eos, Transactions, *American Geophysical Union* **88** (52): American Geophysical Union Fall Meeting Abstract OS11C-01.

Dallimore, S.R. and Collett, T.S., 2005. Scientific Results form the Mallik 2002 Gas Hydrate production Research Well Program, Mackenzie Delta, Northwest Territories, Canada. Geological Survey of Canada, Bulletin **585**, 140pp.

Davis, E.E. and Hyndman, R.D., 1989. Accretion and recent deformation of sediments along the northern Cascadia subduction zone. *Geological Society of America Bulletin* **101** (11): 1465–1480.

Davis, E.E., and Villinger, H., 1992. Tectonic and thermal structure of the Middle Valley sedimented rift, northern Juan de Fuca Ridge. In: Davis, E.E., Mottl, M.J., Fisher, A.T., et al. Proceedings Ocean Drilling Program, Initial Reports **139**. Ocean Drilling Program, College Station, TX: 9–41.

Davy, H., 1811. On a combination of oxymuriatic gas and oxygen gas. In: Philosophical transactions of the Royal Society, 155 pp.

Dawson, S. and Smith, D.E., 2000. The sedimentology of Middle Holocene tsunami facies in northern Sutherland, Scotland, UK. *Marine Geology* **170** (1-2): 69-79.

Dawson, A.G. and Stewart, I., 2007. Tsunami deposits in the geological record. *Sedimentary Geology* **200** (3-4): 166-183.

Dawson, A.G., Long, D. and Smith, D.E., 1988. The Storegga Slides: Evidence form eastern Scotland for a possible tsunami. *Marine Geology* **82** (3-4): 271-276.

Dehairs, F., Chesselet, R. and Jedwab, J., 1980. Discrete suspended particles of barite and the barium cycle in the open ocean. *Earth and Planetary Science Letters* **49**: 528–550.

Dehairs, F., Lambert, C.E., Chesselet, R., and Risler, N., 1987. The biological production of marine suspended barite and the barium cycle in the western Mediterranean Sea. *Biogeochemistry* **4**: 119–139.

Dehairs, F., Fagel, N., Antia, A.N., Peinert, R., Elskens, M. and Goeyens, L., 2000. Export production in the Bay of Biscay as estimated from barium–barite in settling material: a comparison with new production. *Deep-Sea Research* **I 47**: 583–601.

DeMets, C., Gordon, R.G. Argus, D.F. and Stein, S., 1990. Current plate motions. *Geophysical Journal International* **101**: 425-478.

Dickens, G.R., 2001a. The potential volume of oceanic methane hydrates with variable external conditions. *Organic Geochemistry* **32**: 1179-1193.

Dickens, G.R., 2001b. Modelling the global Carbon Cycle with a Gas Hydrate capacitor: Significance for the Latest Paleocene Thermal Maximum. In: Paull, C.K., and Dillon, W.P. (Eds.) Natural Gas Hydrates: Occurrence, distribution, and detection. Geophysical Monograph **124**, American Geophysical Union (Publ.): 19-38.

Dickens, G.R., 2001c. Sulfate profiles and barium fronts in sediment on the Blake Ridge: Present and past methane fluxes through a large gas hydrate reservoir. *Geochimica et Cosmochimica Acta* **65** (4): 529-543.

Dickens, G.R., 2003. Rethinking the global carbon cycle with a large, dynamic and microbially mediated gas hydrate capacitor. *Earth and Planetary Science Letters* **213**: 169-183.

Dickens, G.R. and Owen, R.M., 1996. Sediment geochemical evidence for an early-middle Gilbert (early Pliocene) productivity peak in the North Pacific Red Clay Province. *Marine Micropaleontology* **27**: 107–120.

Dickens, G.R., Castillo, M.M., and Walker, J.G.C., 1997a. A blast of gas in the latest Paleocene: simulating first-order effects of massive dissociation of oceanic methane hydrate. *Geology* **25**: 259-262.

Dickens, G.R., Paull, C.K., Wallace, P. and the ODP Leg 164 Scientific Party, 1997b. Direct measurement of in situ methane quantities in a large gas-hydrate reservoir. *Nature* **385**: 426-428.

Dickens, G.R., Wallace, P.J., Paull, C.K., and Borowski, W.S., 2000. Detection of methane gas hydrate in the pressure core sampler (PCS): volume–pressure–time relations during controlled degassing experiments. In: Paull, C.K., Matsumoto, R., Wallace, P.J., Dillon, W.P. (eds.). Proceedings Ocean Drilling Program, Scientific Results, **164**, Ocean Drilling Program, College Station, TX, 2000: 113–126.

Dickens, G.R., Fewless, T., Thomas, E., and Bralower, T.J., 2003. Excess barite accumulation during the Paleocene-Eocene thermal maximum: Massive input of dissolved barium from seafloor gas hydrates reservoirs. In: Wing, S.L., Gingerich, P.D., Schmitz, B., and Thomas, E. (eds.). Causes and consequences of globally warm climates in the early Paleogene: Boulder, Colorado, Geological Society of America Special Paper **369**: 11-23.

Dickens, G.R., Donohue, C.M., and Snyder, G.T., 2006. Dissolved fluoride concentrations in methane-charged sediment sequences. In: Tréhu, A.M., Bohrmann, G., Torres, M.E., and Colwell, F.S. (eds.). Proceedings of the Ocean Drilling Program Scientific Results, College Station, Texas (Ocean Drilling Program) **204**: 1-22.

Dickens G.R. and Snyder, G. T., 2009. Interpreting upward methane flux from marine pore water profiles. *Fire in Ice* (Winter 2009): 7-11.

DingHui, Y., and WenYue, X., 2007. Effects of salinity on methane gas hydrate system. *Science in China Series D: Earth Sciences* **50** (11): 1733-1745.

Dinis, P., and Soares, A.F., 2007. Controlling factors on clay mineral assemblages: insights from facies analysis of Pliocene to Pleistocene coastal margin deposits, western Portugal. *Geologica Acta* **5** (2): 177-192.

Dobrynin, V.M., Korotajev, Y.P., and Plyuschev, D.V., 1981. Gas hydrates-one of the possible energy sources. In: Meyer, R.G., and Olson, J.C. (eds.), Long-Term Energy Resources. Pitman, Boston, MA: 727-729.

Driscoll, N.W., Weissel, J.K. and Goff, J.A., 2000. Potential for large-scale submarine slope failure and tsunami generation along the U.S. Mid Atlantic coast. *Geology* **28**: 407-410.

Dugan, B. and Flemings, P.B., 2000. Overpressure and fluid flow in the New Jersey continental slope: Implications for slope failure and cold seeps. *Science* **289**: 288-291.

Duncan, J.R. and Kulm, L.D., 1970. Mineralogy, provenance and dispersal history of late quaternary deep-sea sands in Cascadia basin and Blanco fracture zone off Oregon. *Journal of Sedimentary Petrology* **40** (3): 874-887.

Dymond, J., 1981. Geochemistry of Nazca plate surface sediments: An evaluation of hydrothermal biogenic, detrital and hydrogenous sources. In: Kulm, L.D., et al. (eds). Nazca Plate: Crustal formation and Andean convergence. Geological Society of America Memoir **154**: 133-173.

Dymond, J. and Collier, R., 1996. Particulate barium fluxes and their relationships to biological productivity. *Deep-Sea Research II* **43**: 1283–1308.

Dymond, J., Suess, E., and Lyle, M., 1992. Barium in deep-sea sediment: a geochemical proxy for productivity. *Paleoceanography* **7** (2): 163-181.

Eagle, M.; Paytan A.; Arrigo, K.R.; van Djiken, G., and Murray, R.W., 2003. A Comparison between excess barium and barite as indicators of carbon export. *Paleoceanography* **18**: 1021-1033.

Egeberg, P.K., and Dickens, G.R., 1999. Thermodynamic and pore water constraints on gas hydrate distribution at ODP Site 997 (Blake Ridge). *Chemical Geology* **153**: 53-79.

Encyclopædia Britannica, 2009. Encyclopædia Britannica Online. 10 Feb. 2009 <http://www.britannica.com/EBchecked/topic/365317/marine-sediment>.

Egorov, A.V., Crane, K., Vogt, P.R., and Rozhkov, A.N., 1999. Gas hydrates that outcrop on the sea floor: stability models. *Geo-Marine Letters* **19**: 68-75.

Ely, LL., Enzel, Y., Cayan, D.R., 1994. Anomalous North Pacific atmospheric circulation and large winter floods in the southwestern United-States. *Journal of Climate* **7** (6): 977-987.

Emerson, S., and Hedges, J., 2003. Sediment diagenesis and benthic flux. In the oceans and marine geochemistry (ed. Elderfield). Vol **6**: Treatise on Geochemistry. In: Holland, H.E., and Turekian, K.K. (eds.). Elsevier-Pergamon, Oxford (UK): 293-320.

Emery, W. and Hamilton, K., 1985. Atmospheric forcing of interannual variability in the Northeast Pacific Ocean: connections with El Niño. *Journal of Geophysical Research* **90** (C1): 857-868.

Ercilla, G., Alonso, B., and Baraza, J., 1994. Post-Calabrian sequence stratigraphy of the northwestern Alboran Sea (Southwestern Mediterranean). *Marine Geology* **120**: 249-265.

Etiope, G., Milkov, A.V., and Derbyshire, E., 2008. Did geologic emissions of methane play any role in Quaternary climate change? *Global and Planetary Change* **61**: 79-88.

Expedition 311 Scientists, 2006. Expedition 311 summary. In Riedel, M., Collett, T.S., Malone, M.J., and the Expedition 311 Scientist Proceedings Integrated Ocean Drilling Program, **311**: Washington, DC (Integrated Ocean Drilling Program Management International, Inc.): 1-68.

Ewing, J.I. and Hollister, C.H., 1972. Regional aspects of deep sea drilling in the western North Atlantic. In: Hollister, C.H., et al. (eds.) Initial reports of the Deep Sea Drilling project 11: Washington D.C., U.S. Government Printing Office: 951-973.

Fagel, N., Dehairs, F., Peinert, R., Antia, A., and André, L., 2004. Reconstructing export production at the NE Atlantic margin: potential and limits of the Ba proxy. *Marine Geology* **204**: 11–25.

Farley, K.A. and Eltgroth, S.F., 2003. An alternative age model for the Paleocene-Eocene thermal maximum using extraterrestrial ^{3}He. *Earth and Planetary Science Letters* **208** (3-4): 135-148.

Fisher, C.R., 1990. Chemoautotrophic and methanotrophic symbioses in marine invertebrates. *Reviews in Aquatic Sciences* **2**: 399-613.

Flueh, E.R., Fisher, M.A., Bialas, J., Childs, J.R., Klaeschen, D., Kukowski, N., Parsons, T., Scholl, D.W., Ten Brink, U., Tréhu, A.M. and Vidal, N., 1998. New seismic images of the Cascadia subduction zone from cruise SO108-ORWELL. *Tectonophysics* **293**: 69-84.

Ford, K.H., Naehr, T.H., Skilbeck, C.G. and Leg 201 Scientific Party, 2003. The use of infrared thermal imaging to identify gas hydrate in sediment cores. In: D'Hondt, S.L., Miller, B.B., Miller, D.J., et al. (eds.). Proceedings Ocean Drilling Program, Initial Reports **201**. Ocean Drilling Program, College Station, TX: 1–20.

Forster, P., Ramaswamy, V., Artaxo, P., Berntsen, T., Betts, R., Fahey, D.W., Haywood, J., Lean, J., Lowe, D.C., Myhre, G., Nganga, J., Prinn, R., Raga, G., Schulz M., and Van Dorland, R., 2007: Changes in Atmospheric constituents and in Radiative Forcing. In: Climate Change 2007: The Physical Science Basis. Contribution of Working Group I to the Fourth Assessment Report of the Intergovernmental Panel on Climate Change. In: Solomon, S., Qin, D., Manning, M., Chen, Z., Marquis, M., Averyt, K.B., Tignor, M., and Miller, H.L. (eds.). Cambridge University Press, Cambridge, United Kingdom and New York, NY, USA.

Fournaison, L., Delahaye, A., Chatti, I., and Petitet, J.P., 2004. CO_2 hydrates in refrigeration processes. *Industrial and Engineering Chemistry Research* **43** (20): 6521-6526.

Francios, R., Honjo, S., Manganini, S. J., and Ravizza, G. E., 1995. Biogenic barium fluxes to the deep sea: Implication for Paleoproductivity Reconstruction. *Global Biogeochemical Cycles* **9**: 289-303.

Francisca, F., Yun, T.S., Ruppel, C., and Santamarina, J.C., 2005. Geophysical and geotechnical properties of near-seafloor sediments in the northern Gulf of Mexico gas hydrate province. *Earth and Planetary Science Letters* **237**: 924-939.

Friedman, G.M., and Sanders J.E., 1978. Principles of Sedimentology. Wiley, cop (ed.), New York, 792 pp.

Froelich, P.N., Kvenvolden, K.A., Torres, M.E., Waseda, A., Didyk, B.M., and Lorenson, T.D., 1995. Geochemical evidence for gas hydrate in sediment near the Chile Triple Junction. In: Lewis, S.D., Behrmann, J.H., Musgrave, R.J., and Cande, S.C. (eds.). Proceedings Ocean Drilling Program, Scientific Results **141**. College Station, TX (Ocean Drilling Program): 279-286.

Gerdom, M., Tréhu, A.M., Flueh, E.R., and Klaeschen, D., 2000. The continental margin off Oregon from seismic investigations. Tectonophysics **329** (1–4): 79–97.

Ginsburg, G.D., and Soloviev, V.A., 1995. Submarine gas hydrates estimation: theoretical and empirical approaches. Proceedings of Offshore Technology Conference, Houston, TX, **1**: 513-518.

Ginsburg G.D., Guseynov, R.A., Dadashev, A.A., Telepnev, E.V., Askeri-Nasirov, P.Y., Yesikov, A.A., Mal'tseva, V.I., Mashiroav, Y.G., and Shabayeba, I.Y., 1992. Gas hydrates on the southern Caspian. *International Geology Review* **43**: 765-782.

Ginsburg, G.D., Soloviev, V.A., Cranston, R.E., Lorenson, T.D., and Kvenvolden, K.A., 1993. Gas hydrates from the continental slope, offshore Sakhalin Island, Okhotsk Sea. *Geo-Marine Letters* **13**: 41-48.

Ginsburg, G., Soloviev, V., Matveeva, T. and Andreeva, I., 2000. Sediment grain-size control on gas hydrate presence, sites 994, 995 and 997. In: Paull C.K., Matsumoto R., Wallace, P.J., Dillon, W.P. (eds.) Proceedings of the Ocean Drilling Program Scientific Results, College Station, Texas (Ocean Drilling Program) **164**: 237-245.

Goldberg, E.D., and Arrhenius, 1958. Chemistry of Pacific pelagic sediments. *Geochimica and Cosmochimica Acta* **13**: 153-212.

Goldfinger, C., Kulm, L.D., Yeats, R.S., Appelgate, B., MacKay, M.E., and Moore, G.F., 1992. Transverse structural trends along the Oregon convergent margin: Implications for Cascadia earthquake potential and crustal rotations. *Geology* **20**: 141-144.

Goldfinger, C., Kulm, L.D., Yeats, R.S., Hummon, C., Huftile, G.J., Niem, A.R., and McNeill, L.C., 1996. Oblique strikeslip faulting of the Cascadia submarine forearc: The Daisy Bank fault zone of central Oregon. In: Bebout, G.E., Scholl, D.W., Kirby, S.H., Platt, J.P (eds.), Subduction: Top to Bottom. AGU Geophysical Monographs **96**: 65-74.

Goldfinger, C., Kulm, L.D., Yeats, R.S., McNeill, L., and Hummon, C., 1997. Oblique strikeslip faulting of the central Cascadia submarine forearc. *Journal of Geophysical Research* **102**: 8217- 8243.

Goldfinger, C., Kulm, L.D., McNeill, L.C., and Watts, P., 2000. Super-scale failure of the southern Oregon Cascadia margin: Pure and Applied Geophysics **157**: 1189-1226.

Goldfinger, C., Nelson, C.H., Johnson, J.E., and Shipboard Scientific Party, 2003. Holocene earthquake record from the Cascadia subduction zone and northern San Andreas fault based on precise dating of offshore Turbidites. *Annual Reviews Earth Planetary Science* **31**: 555-577.

Goldfinger, C., Morey, Nelson, H.C., Gutiérrez-Pastor, J., A.E., Johnson, J.E., Karabanov, E., Chaytor, J.D., Ericsson, A., and Shipboard Scientific party, 2006. Rupture lengths and temporal history of significant earthquakes on the offshore and north coast segments of the northern San Andreas Fault based on turbidite stratigraphy. *Earth and Planetary Science Letters* **254** (1-2): 9-27.

Gonneea, M.E. and Paytan, A., 2006. Phase associations of barium in marine sediments. *Marine Chemistr*y **100**: 124-135.

Gontharet, S. Pierre, C., Blanc-Valleron, M.M., Rouchy, J.M., Fouquet, Y., Bayon, G., Foucher, J.P., Woodside, J., Mascle, J., and the Nautil Scientific Arty, 2007. *Deep-Sea Research Part II* **54**: 1292-1311.

Goosens, D., 2008. Techniques to measure grain-size distributions of loamy sediments: a comparative study of ten instruments for wet analysis. *Sedimentology* **55**: 65-96.

Gornitz, V. and Fung, I., 1994. Potential distribution of methane hydrates in the world's oceans. *Global Biogeochemical Cycles* **8**: 335–347.

Gràcia, E., Martínez-Ruiz, F., Piñero, E., Larrasoaña, J.C., Vizcaino, A., and Ercilla, G., 2006. Data Report: Grain-size, and bulk and clay mineralogy of sediments from the summit and flanks of Southern Hydrate Ridge, Sites 1244 to 1250, Ocean Drilling Program Leg 204. In: Tréhu, A.M., Bohrmann, G., Torres, M.E., Colwell, F.S. (eds.). Proceedings of the Ocean

Drilling Program Scientific Results **204**, College Station, Texas (Ocean Drilling Program): 1-19.

Graue, A., Kvamme, B., Baldwin, B.A., Stevens, J., Howard, J., et al., 2006. Magnetic resonance imaging of methane-carbon dioxide hydrate reactions in sandstone pores. Society of Petroleum Engineers 102915. Presented at 2008 Society of Petroleum Engineers Annual Technical Conference and Exhibition, San Antonio. (Abstract)

Greinert, J., Bohrmann, G., and Suess, E., 2001. Gas hydrate-associated carbonates and methane-venting at Hydrate Ridge: Classification, distribution, and origin of authigenic lithologies. In: Paull, C.K., and Dillon, W.P. (eds.). Natural Gas Hydrates: Occurrence, distribution, and detection. Geophysical Monograph, American Geophysical Union (Publ.) **124**: 99-113.

Griggs, G.B., and Kulm, L.D., 1970. Physiography iof the Cascadia Deep-Sea Channel. *Northwest Science* **44** (2): 82-94.

Gudmundsson, J., Andersson, V., Levik, O. and Mork, M., 2000. Hydrate technology for capturing stranded gas. *Annals of the New York Academy of Sciences* **912**: 403-410.

Gulick, S.P.S., Meltzer, A.S., and Clarke, S.H.Jr., 2002. Effect of the morthward-migrating Mendocino triple junction on the Eel River forearc basin, California: Stratigraphic development. *Geological Society of American Bulletin* **114**: 178-191.

Haflidason H., Sejrup, H.P., Nygård, A., Mienert, J., Bryn, P., Lien, R., Forsberg, C.F., Berg, K., and Masson, D., 2004. The Storegga Slide: architecture, geometry and slide development. *Marine Geology* **213**: 201-234.

Hammerschmidt, E.G., 1934. Formation of gas hydrates in natural gas transmission lines. Industrial and Engineering Chemistry **26**, 851pp.

Haq, B.U., 1998. Natural gas hydrates: searching for the long-term climatic and slope-stability records. In: Henriet, J.P. and Mienert, J (eds.), Gas hydrates: Relevance to World Margin Stability and Climate Change. *Special Publications of the Geological Society* **137**: 303-318.

Haq, B.U., Hardenbol, J., and Vail, P.R., 1987. Chronology of fluctuating sea levels since the Triassic. *Science* **235** (4793): 1156-1167.

Hasselbo, S.P., Grocke, D.R., Jenkyns, H.C., et al., 2000. Massive dissociation of gas hydrate during a Jurassic oceanic anoxic event. *Nature* **406** (6794): 392-395.

Harvey, L.D.D., and Huang, Z., 1995. Evaluation of potential impact of methane clathrate destabilization on future global warming. *Journal of Geophysical Research* **100**: 2905–2926.

Heeschen, K.U., Tréhu, A.M., Collier, R.W., Suess, E., and Rehder, G., 2003. Distribution and height of methane bubble plumes on the Cascadia margin characterized by acoustic imaging. *Geophysical Research Letters* **30**: 1643–1646.

Henriet, J.P., and Mienert, J., eds. 1998. Gas hydrates - Relevance to world margin stability and climatic change. Special Publication of the Geological Society **137**: 1- 338.

Henry, P., Thomas, M., and Clennell, M.B., 1999. Formation of natural gas hydrates in marine sediments 2. Thermodynamic calculations of stanility conditions in porous sediments. *Journal of Geophysical Research* **104** (B10): 23005-23022.

Herbert, T. D., Schuffert, J.D., Andreasen, D., Heusser, L., Lyle, M., Mix, A., Ravelo, A.C., Stott, L.D. and Herguera, J.C., 2001. Collapse of the California current during glacial maxima linked to climate change on land. *Science* **293**: 71-76.

Hesse, R., 2003. Pore-water anomalies of submarine gas-hydrate zones as tool to assess hydrate abundance and distribution in the subsurface: What have we learned in the past decade?, *Earth Sciences Reviews* **61**: 149-179.

Hesse, R., and Harrison, W.E., 1981. Gas hydrates causing pore-water freshening and oxygen isotope fractionation in deep-water sedimentary section of terrigenous continental margins. *Earth and Planetary Science Letters* **55**: 453-462.

Hester K.C., and Brewer, P.G., 2009. Clathrate hydrates in Nature. Annual Review of Marine *Science* **1**: 303-327.

Hickey, B.M., 1979. The California current system-hypotheses and facts. Progress in *Oceanography* **8** (4): 191-279.

Holbrook, W.S., 2001. Seismic studies of the Blake Ridge: implications for Hydrate distribution, methane expulsion, and free gas dynamics, in Paull, C.K., and Dillon, W.P. (Eds.) Natural Gas Hydrates: Occurrence, Distribution, and Detection. Geophysical Monograph, American Geophysical Union (Publ.) **124**: 235-256.

Holbrook, W.S., Hoskins, H., Wood, W.T., Stephen, R.A., Lizarralde D., and Leg 164 Science Party, 1996. Methane hydrate and free gas on the Blake Ridge from vertical seismic profiling. *Science* **273**: 1840– 1843.

Hovland, M., and Gudmestad, O.T., 2001. Potential influence of gas hydrates on seabed installations. In: Paull, C.K., and Dillon, W.P. (eds.) Natural Gas Hydrates: Occurrence, Distribution, and Detection. Geophysical Monograph, American Geophysical Union (Publ.) **124**: 307-315.

Hovland, M., Lysne, D., and Whiticar, M., 1995. Gas hydrate and sediment gas composition, Hole 892A. In: Carson, B., Westbrook, G.K., Musgrave, R.J., and Suess, E. (eds.), Proc. Ocean Drilling Program, Scientific Results, **146** (Pt. 1): College Station, TX (Ocean Drilling Program): 151–161.

Hovland, M., Svensen, H., Forsberg, C.F. et al., 2005. Complex pockmarks with carbonate-ridges off midd-Norway: products of sediment degassing. *Marine Geology* **218** (1-4): 191-206.

Hyndman, R.D. and Davis, E.E., 1992. A mechanism for the formation of methane hydrate and seafloor bottom-simulating reflectors by vertical fluid explusion. *Journal of Geophysical Research* **97**: 7025-7041.

Hyndmann, R.D., and Space, G.D., 1992. A seismic study of methane hydrate marine bottom-simulating-reflectors. *Journal of Geophysical Research* **97**: 6683-6698.

Hyndman, R.D., Spence, G.D., Yuan, T., and Davis, E.E., 1994. Regional geophysics and structural framework of the Vancouver Island Margin Accretionary Prism. In: Westbrook,

G.K., Carson, B., Musgrave, R.J., et al. (eds.). Proceedings Ocean Drilling Program. Initial Reports **146** (Pt. 1): College Station, TX, Ocean Drilling Program: 399-419.

Hyndman, R.D., Spence, G.D., Chapman, R., Riedel, M. and Edwards, R.N., 2001. Geophysical studies of marine gas hydrate in northern Cascadia in Paull, C.K., and Dillon, W.P. (Eds.) Natural Gas Hydrates: Occurrence, distribution, and detection. Geophysical Monograph. American Geophysical Union (Publ.) **124**: 273–295.

Integrating Ocean Drilling Program (IODP) Planning Sub-Committee (IPSC), 2005. Earth, oceans and life. Scientific Investigation of the Earth system using multiple drilling platforms and new technologies. Initial Science Plan **110**, 2003-201.

IPCC, 2001: Climate Change 2001: The Scientific Basis. Contribution of Working Group I to the Third Assessment Report of the Intergovernmental Panel on Climate Change. In: Houghton, J.T., Ding, Y., Griggs, D.J., Noguer, M., van der Linden, P.J., , Dai, X., Maskell, K., and Johnson, C.A. (eds.). Cambridge University Press, Cambridge (United Kingdom) and New York, NY (USA), 881pp.

Irvine, I., 2004. The life lottery. East Roseville, N.S.W., Pocket books, 530pp.

Iversen, N., and Jorgensen, B.B., 1985. Anaerobic methane oxidation rates at the sulfate-methane transition in marinc sediments from Kattegat and Skagerrak (Denmark). *Limnology and Oceanography* **30**: 944-955.

Jenkyns, H.C., 2003. Evidence for rapid climate change in the Mesozoic-Palaeogene greenhouse world. Philosophical Transactions of the Royal Society of London Series a-Mathematical Physical and Engineering Sciences **361** (1810): 1885-1916.

Johnson, H.P., Hutnak, M., Dziak, R.P., Fox, C.G., Urcuyo, I., Cowen, J.P. Nabelek J. and Fisher C.R. , 2000. Earthquake-induced changes in a hydrothermal system on the Juan de Fuca mid-ocean ridge. Nature **407**: 174–177

Johnson, J.E., Goldfinger, C., and Suess, E., 2003. Geophysical constraints on the surface distribution of authigenic carbonates across the Hydrate Ridge region, Cascadia margin. Marine Geology **202**: 79-120.

Johnson, J.E., Goldfinger, C., Tréhu, A.M., Bangs, N.L.B., Torres, M.E., and Chevallier, J., 2006. North-south variability in the history of deformation and fluid venting across Hydrate Ridge, Cascadia margin. In: Tréhu, A.M., Bohrmann, G., Torres, M.E., and Colwell, F.S. (eds.), Proceedings of the Ocean Drilling Program Scientific Results. College Station, Texas (Ocean Drilling Program) **204**: 1-16.

Karisiddaiah, S.M., 2000. Diverse methane concentrations in anoxic brines and underlying sediments, eastern Mediterranean Sea. *Deep-Sea Results I* **47**: 1999-2008.

Karlin, R., 1980. Sediment sources and clay mineral distributions off the Oregon coast. Journal of Sedimentary Petrology **50** (2): 0543-0560.

Karlin, R.E., Holmes, M., Abella, S.E.B., and Sylwester, R., 2004. Holocene landslides and a 3500-year record of Pacific Northwest earthquakes from sediments in Lake Washington. *Geological Society of America Bulletin* **116**: 94-108.

Kasten, S., Haese, R.R., Zabel, M., Rühlemann, C., and Schulz, H.D., 2001. Barium peaks at glacial terminations in sediments of the equatorial Atlantic Ocean – relicts of deglacial productivity pulses? *Chemical Geology* **175**: 635-651.

Kastner, M., 1999. Oceanic minerals: Their origin, nature of their environment, and significance. Proceedings of the National Academy of Sciences of the United States of America **96**: 3380-3387.

Kastner, M., 2001. Gas Hydrates in Convergent Margins: Formation, Occurrence, Geochemistry, and Global Significance. In: Paull, C.K., and Dillon, W.P. (eds.) Natural Gas Hydrates: Occurrence, Distribution, and Detection. Geophysical Monograph **124**, American Geophysical Union (Publ.): 67-86.

Kastner, M., Kvenvolden, K.A., Whiticar, M.J., Camerlenghi, A., and Lorenson, T.D., 1995. 10. Relation between pore fluid chemistry and gas hydrates associated with bottom-simulating reflectors at the Cascadia margin, Sites 889 and 892. In: Carson, B., Westbrook, G.K., Musgrave, R.J., Suess, E. (eds.), 1995. Proceedings of the Ocean Drilling Program, Scientific Results, Vol. **146** (Pt. 1): College Station TX (Ocean Drilling Program): 175-187.

Katz, M.E., Pak, D.K., Dickens, G.R., and Miller, K.G., 1999. The source and fate of massive carbon input during the Latest Pleistocene Thermal Maximum. *Science* **286**: 1531-1533.

Keller, G.V., and Frischknecht, F.C., 1966. Electrical Methods in Geophysical Prospecting. Pergamon Press, Oxford, 1st edition, 519pp.

Kelsey, H.M., Ticknor, R.L., Bockheim, J.G., and Mitchell, E., 1996. Quaternary upper plate deformation in coastal Oregon. *Geological Society of America Bulletin* **108** (7): 843-860.

Kelsey, H.M., Witter, R.C. and Hemphill-Haley, E, 2002. Plate-boundary earthquakes and tsunamis of the past 5500 yr, Sixes River estuary, southern Oregon. Geological Society of America Bulletin **114**: 298-314.

Kelsey, H.M., Nelson, A.R., Hemphill-Haley, E. and Witter, R.C., 2005. Tsunami history of an Oregon coastal lake reveals a 4600 yr record of great earthquakes on the Cascadia subduction zone. Geological Society of America Bulletin **117** (7/8): 1009-1032.

Kennett, J.P., and Stott, L.D., 1991. Abrupt deep sea warming, paleoceanographic changes and benthic extinctions at the end of the Paleocene. *Nature* **353**: 319-322.

Kennett, J., Cannariato, K., Hendy, I., and Behl, R., 2002. Methane hydrates in Quaternary climate change: the clathrate gun hypothesis. American Geophysical Union, 216 pp.

Kerr, R.A., 2004. Gas Hydrate Resource: Smaller but sooner. *Science* **303** (5660): 946-947.

Kim, D.Y., Uhm, T.W., Lee, H., Lee, Y.J., Ryu B.J., and Kim, J.H., 2005. Compositional and structural identification of natural gas hydrates collected at Site 1249 on oceanic drilling program Leg 204. *Korean Journal of Chemical Engineering* **22**: 569–572.

Kimura, G., Silver, E., Blum, P. et al, 1997. Proc. Ocean Drilling Program, Init. Repts., 170 [Online]. Available from World Wide Web: http://www-odp.tamu.edu/publications/170IR/170TOC.HTM. [Cited 2005-10-21]

Kisch, H.J., 1991. Illite crystallinity: recommendations on sample preparation, X-ray diffraction settings and interlaboratory samples. *Journal of Metamorphic Geology* **9**: 665-670.

Klump, J., Hebbeln, D., and Wefer, G., 2000. The Impact of Sediment Provenance on Barium-Based Productivity Estimates. *Marine Geology* **169** (3-4): 259-271.

Krissek, L.A., 1982. Sources, dispersal, and contributions of fine-grained terrigenous sediments on the Oregon and Washington continental slope [Ph.D. dissert.]. Oregon State University, Corvallis.

Krissek, L.A., 1984. Continental source area contributions to fine-grained sediments on the Oregon and Washington continental slope (in Fine-grained sediments; deep-water processes and facies). Geological Society Special Publications **15**: 363-375.

Kulm, L.D., and Fowler, G.A., 1974. Cenozoic sedimentary framework of the Gorda-Juan de Fuca plate and adjacent continental margin—a review. In:,Dott, R.H. Jr., and Shaver, R.H. (eds.). Modern and Ancient Geosynclinal Sedimentation. Society of Economic Paleontologists and Mineralogist (Tulsa, Oklahoma). Special Publication **19**: 212–229.

Kulm, L.D., von Huene, R., et al., 1973. Site 174. In: Initial Reports of the Deep Sea Drilling Project. In: Kulm, L.D., and von Huene, R. (eds.). U.S. Government Printing Office, Washington: 97-167.

Kulm, L.D., Suess, E., Moore, J.C., Carson, B., Lewis, B.T., Ritger, S.D., Kadko, D.C., Thornburg, T.M., Embley, R.W., Rugh, W.D., Massoth, G.J., Langseth, M.G., Cochrane, G.R., and Scamman, R.L., 1986. Oregon Subduction zone: venting, fauna and carbonates. *Science* **231**: 561-566.

Kulm, L.V.D., and Suess, E., 1990. Relationship between carbonate deposits and fluid venting: Oregon accretionary prism. *Journal of Geophysical Research* **95**(B6): 8899–8915.

Kvenvolden, K.A., 1988. Methane hydrate, a major reservoir of carbon in the shallow geosphere? *Chemical Geology* **71**: 41-51.

Kvenvolden, K.A., 1993. Gas hydrates – Geological perspective and global change. *Reviews of Geophysics* **31** (2): 173-187.

Kvenvolden, K.A., 1998. A primer on the geological occurrence of gas hydrate. In Henriet, J.P. and Mienert, J., eds. Gas hydrates: relevance to World Margin Stability and Climate Change. Geological Society. Special Publications **137**: 9-30.

Kvenvolden, K.A., 2002. Methane hydrate in the global organic carbon cycle. *Terra Nova* **14**: 302-306.

Kvenvolden, K.A., and Claypool, G.E., 1988. Gas hydrates in oceanic sediment. U.S. Geological Survey Open-File Report: 88-216.

Kvenvolden, K.A. and Lorenson, T.D., 2001. The global occurrence of Natural Gas Hydrate. In: Paull, C.K., and Dillon, W.P. (eds.) Natural Gas Hydrates: Occurrence, distribution, and detection. Geophysical Monograph **124**, American Geophysical Union (Publ.): 3-18.

Larrasoaña, J.C., Gràcia, E., Garcés, M., Musgrave, R.J., Piñero, E., Martínez-Ruiz, F., and Vega, M.E., 2006. Rock magnetic identification of magnetic iron sulfides and its bearing on the occurrence of gas hydrates, Ocean Drilling Program Leg 204 (Hydrate Ridge). In: Tréhu, A.M., Bohrmann, G., Torres, M.E., and Colwell, F.S. (eds.). Proceedings of the Ocean Drilling Program Scientific Results, College Station, Texas (Ocean Drilling Program) **204**: 1-33.

Larrasoaña, J.C., Roberts, A.P., Musgrave, R.J., Gràcia, E., Piñero, E., Vega, M., and Martínez-Ruiz, F., 2007. Diagenetic formation of greigite and pyrrhotite in gas hydrate marine sedimentary systems: results from ODP Leg 204 (southern Hydrate Ridge). *Earth and Planetary Science Letters* **261** (3-4): 350-366.

Lee, M.W. and Collett, T.S., 2006. Gas hydrate and free gas saturations estimated from velocity logs on Hydrate Ridge, offshore Oregon, USA. In: Tréhu, A.M., Bohrmann, G., Torres, M.E., and Colwell, F.S. (eds.). Proceedings of the Ocean Drilling Program Scientific Results, College Station, Texas (Ocean Drilling Program) **204**: 1-25.

Lee, S., Liang, L., Riestenberg, D., West, O.R., Tsouris, C., and Adams, E., 2003. CO_2 hydrate composite for ocean carbon sequestration. *Environmental Science & Technology* **37**: 3701-3708.

Lorenson, T.D., and Kvenvolden, K.A., 2007. A Global Inventory of Natural Gas Hydrate Occurrence (Map). U.S. Geological Survey, California.

Liu, X., and Flemings, P.B., 2006. Passing gas through the hydrate stability zone at southern Hydrate Ridge, offshore Oregon. *Earth and Planetary Science Letters* **241**(1–2): 211–226.

Locat, J., and Lee, H.J., 2002. Submarine landslides: advances and challenges. *Canadian Geotechnical Journal* **39**: 193-212.

Lyle, M., Koizumi, I., Richter, C., and Moore, T.C., Jr. (eds.), 2000. Proc. ODP, Scientific Results **167**. College Station TX (Ocean Drilling Program).

MacDonald, G.J., 1990. The future of methane as an energy resource. *Annual Review of Energy* **15**: 53–83.

MacKay, M.E., 1995. Structural variation and landware vergence at the toe of the Oregon accretionary prism. *Tectonics* **14** (5): 1309-1320.

MacKay, M.E., Moore, G.F., Cochrane, G.R., Moore, J.C., and Kulm, L.D., 1992. Landward vergence and oblique structural trends in the Oregon margin accretionary prism: implications and effect on fluid flow. *Earth and Planetary Science Letters* **109**: 477-491.

MacKay, M.E., Jarrad, R.D., Westbrook, G.K., Hyndman, R.D., and Leg 146 Shipboard Scientific Party, 1994. Origin of bottom simulating reflectors: geophysical evidence from the Cascadia accretionary complex. *Geology* **22**: 459– 462.

MacLennan, J. and Jones, S.M., 2006. Regional uplift, gas hydrate dissociation and the origins of the Paleocene-Eocene Thermal Maximum, Earth and Planetary Science Letters **245** (1-2): 65-80.

Makogon, Y.F., 1965. Hydrate formation in the gas-bearing beds under permafrost conditions. Gazovaia Promyshlennost **5**: 14-15. (in Russian)

Makogon, Y.F., 1971. Perspectives of development of gas hydrate accumulations. Gasovaya Promyshlennost **3,** 16–18 (in Russian).

Makogon, Y.F., 1981. Hydrates of natural gas. Penn Well Publishing Company, Tulsa, 237 pp.

Makogon, Y.F., 1997. Hydrates of Hydrocarbons. Penn Well Publishing Company, Tulsa, 504 pp.

Mao, W.L., Mao, H.K., Goncharov, A.F., Struzhkin, V.V., Guo, Q.Z., et al., 2002. Hydrogen clusters in clathrate hydrate. *Science* **297**: 2247-2249.

Margins Office (eds.), 2003. NSF Margins Program: Science Plans 2004. Lamont-Doherty Eart Observatory of Columbia University, New York, 170 pp.

Martín Ramos, J.D., 2004. Xpowder, a software package for powder X-Ray diffraction analysis. Legal deposit GR 1001/04 (http://www.xpowder.com).

Masuzawa, T., Handa N., Kitagawa H., and Kusakabe M., 1992. Sulfate reduction using methane in sediments beneath a bathyal "cold seep"giant clam community off Hatsushima Island, Sagami Bay, Japan. *Earth and Planetary Science Letters* **110**: 39–50

Max, M.D., 2006. U.S. Patent no. 6,991,772.

Mazurenko, L.L. and Soloviev, V.A., 2003. Worldwide distribution of deep-water fluid venting and potential occurrences of gas hydrate accumulations. *Geo-Marine Letters* **23**: 162-176.

McIver, R.D., 1977. Hydrates of natural gas -an important agent in geologic processes. Geological Society of America Annual Meeting, Abstract with Programs **9**: 1089-1090.

McIver, R.D., 1981. Gas hydrates. In: Meyer, R.G., and Olson, J.C. (eds.), Long-Term Energy Resources. Pitman, Boston, MA, 713–726.

McManus, J., 1988. Grain-size determination and interpretation. In: J. Tucker (ed.) Techniques in Sedimentology, Blackwell Science Publications: 63-85.

McManus, J., Berelson, W.M., Hammond, D.E., and Klinkhammer, G.P., 1999. Sedimentary Barium Cycling in the North Pacific: Implications for the Utility of Ba as a Paleoproductivity and a Paleoalkalinity Proxy. *Paleoceanography* **14**: 53-61.

McNeill, L.C., Piper, K.A., Coldfinger, C., Kulm, L.D., and Yeats, R.S., 1997. Listric normal faulting on the Cascadia continental margin. Journal of Geophysical Research **102** (B6): 12123-12138.

Micromeritics, 1978. Instruction manual: SediGraph particle size analyser, 122 pp.

Mienert, J., Bünz, S., Guidard, S., Vanneste, M., and Berndt, C., 2005. Ocean bottom seismometer investigations in the Ormen Lange area offshore mid-Norway provide evidence for shallow gas layers in subsurface sediments. *Marine and Petroleum Geology* **22**: 287-297.

Milkov, A.V., 2004. Global estimates of hydrate-bound gas in marine sediments: how much is really out there? *Earth-Science Reviews* **66**: 183-197.

Milkov, A.V., 2005. Molecular and stable isotope compositions of natural gas hydrates: A revised global dataset and basic interpretations in the context of geological settings. *Organic Geochemistry* **36**: 681-702.

Milkov, A.V., and Xu, W., 2005. Comment on "Gas hydrate growth, methane transport, and chloride enrichment at the southern summit of Hydrate Ridge, Cascadia margin off Oregon" by Torres et al. (Earth Planet. Sci. Lett. 226 (2004) 225–241). Earth Planet. Science Letters, **239** (1–2):162–167.

Milkov, A.V., Claypool, G.E., Lee, Y.-J., Dickens, G.R., Xu, W., Borowski, W.S., and the Ocean Drilling Program Leg 204 Scientific Party, 2003. In situ methane concentrations at Hydrate Ridge offshore Oregon: new constraints on the global gas hydrate inventory from an active margin. *Geology* **31** (10): 833-836.

Milkov, A., Dickens, G.R., Claypool, G.E., Lee, Y.J., Borowski, W.S., Torres, M.E., Xu, W., Tomaru, H., Tréhu, A.M., and Schultheiss, P., 2004. Co-existence of gas hydrate free gas, and brine within the regional gas hydrate stability zone at the southern summit of Hydrate Ridge (Oregon margin): evidence from prolonged degassing of a pressurized core. *Earth and Planetary Science Letters* **222**: 829–843.

Milkov, A.V., Claypool, G.E., Lee, Y.J., and Sassen, R., 2005. Gas hydrate systems at Hydrate Ridge offshore Oregon inferred from molecular and isotopic properties of hydrate-bound and void gases. *Geochemica et Cosmochemica Acta* **69** (4): 1007-1026

Milliman, J.D., 1974. Marine Carbonates, second ed. Springer Verlag, New York, 375 pp.

Moreno, A., 2002. Registro de aporte de polvo de origen Sahariando y de la productividad oceánica en la cuenca del Norte de Canarias y en el Mar de Alborán. Respuesta a los últimos 250.000 años de cambio climático. Doctoral Thesis. Universitat de Barcelona, 230 pp.

Moore, D.M., and Reynolds, R.C.Jr., 1989. X-ray diffraction and the identification and analysis of clay minerals. 2nd edition Oxford University Press, New York, NY, 378 pp.

Moore, G.F., Taira, A., Klaus, A., et al., 2001. Proceeding Ocean Drilling Program, Initial Reports., 190 [Online]. Available from World Wide Web: http://www-odp.tamu.edu/publications/190_IR/190ir.htm. [Cited 2005-10-21]

Morris, A.W. and Riley, J.P., 1966. The bromide/chlorinity and sulphate/chlorinity ratio in sea water. *Deep-Sea Research* **13**: 699-705.

Mulder, T. and Cochonat, P., 1996. Classification of offshore mass movements. *Journal of Sedimentary Research* **66**: 43-57.

Murray, R.W., Buchhholtz Ten Brink, M.R., Gerlach, D.C. Russ, G.P.III and Jones, D.L., 1992. Interoceanic variation in the rare earth, major and trace element depositional chemistry of chert. Perspectives grained from DSDP and Ocean Drilling Program record. *Geochimica et Cosmochimica Acta* **56**: 1897-1913.

Nedimović, M.R., Hyndman, R.D., Ramachandran, K., and Spence, G.D., 2003. Reflection signature of seismic and aseismic slip on the northern Cascadia subduction interface. *Nature* **424**: 416-420.

Nelson, C.H., 1976. Late Pleistocene and Holocene depositional trends, processes and history of the Astoria deep-sea fan, northeast Pacific. *Marine Geology* **20**: 129-173.

Nelson, C.H., 1985. Astoria Fan, Pacific Ocean. In: Bouma, A.H., Normark, W.R., and Barnes, N.E. (eds.). Submarine Fans and Related Turbidite Systems, Springer-Verlag, New York, 1985, 45–50.

Nelson, D.C., and Jannasch, H.W., 1983. Chemoautotrophic growth of a marine Beggiatoa in sulphide-gradient cultures. *Archives of Microbiology* **136** (4): 262-269.

Neretin, L.N., Böttcherm M.E., Jørgensen, B.B., Volkov, I.I., Lüschen, H., and Hilgenfeldt, K., 2004. Pyritization processes and greigite formation in the advancing sulfidization front in the Upper Pleistocene sediments of the Black Sea. *Geochimica et Cosmochimica Acta* **68** (9): 2081-2093.

Nisbet, E.G., and Piper, D.J., 1998. Giant submarine landslides. *Nature* **392**: 329-330.

Palin, D.E., and Powell, H.M., 1945. Hydrogen Bond linkng of Quinol Molecules. *Nature* **156:** 334-335.

Palin, D.E., and Powell, H.M., 1947. The structure of Molecular Compounds. Part III. Crystal Structure of Addition complexes of Hydroquinone with Certain Volatile Compounds. *Journal of Chemical Society*: 208-221.

Parkes, R.J., Cragg, B.A., and Wellbury, P., 2000. Recent studies on bacterial populations and processes in marine sediments. *Hydrogeology Reviews* **8**: 11-28.

Paull, C.K., and Ussler III, W., 2001. History and significance of gas sampling during Deep Sea Drilling Project and Ocean Drilling Program drilling associated with gas hydrates. In: Paull, C.K., and Dillon, W.P. (eds.) Natural Gas Hydrates: Occurrence, distribution, and detection. Geophysical Monograph **124**, American Geophysical Union (Publ.): 53-65.

Paull, C.K., Ussler III, W., and Borowski, W., 1994. Sources of biogenic methane to form marine gas hydrates – In situ production of upward migration? *Annals of the NY Academy of Sciences* **715**: 392-409.

Paull, C.K., Buelow, W.J., Ussler III, W., and Boroski, W.S., 1996a. Increased continental-marine slumping frequency during sea-level lowstands above gas hydrate-bearing sediments. *Geology* **24** (2): 143-146.

Paull, C.K., Matsumoto, R., Wallace, P.J., et al., 1996b. Proceedings of the Ocean Drilling Program Initial Reports **164**. College Station, Texas (Ocean Drilling Program), 624 pp.

Paull, C.K., Matsumoto, R., Wallace, P.J., and Dillon, W.P. (eds.), 2000. Proc. Ocean Drilling Program, Scientific Results, 164 [Online]. Available from World Wide Web: <http://www-odp.tamu.edu/publications/164_SR/164TOC.HTM>. [Cited 2009-02-06].

Paytan, A, and Kastner, M., 1996. Bethic Ba fluxes in the central Equatorial Pacific, implications for the oceanic Ba cycle. *Earth and Planetary Science Letters* **142**: 439-450.

Paytan, A., and Griffith, E.M., 2007. Marine barite: recorder of variations in ocean export productivity. *Deep-Sea Research II* **54**: 687-705.

Paytan, A., Kastner, M., Martin, E.E., Macdougall, J.D., and Herbert, T., 1993. Marine barite as a monitor of seawater strontium isotope composition. *Nature* **366**: 445-449.

Paytan, A., Kastner, M., and Chavez, F., 1996. Glacial to Interglacial Fluctuations in Productivity in the Equatorial Pacific as Indicated by Marine Barite. *Science* **274**: 1355-1357.

Paytan, A., Mearon, S., Cobb, K., and Kastner, M., 2002. Origin of Marine Barite Deposits: Sr and S Isotope Characterization. *Geology* **30** (8): 747-750.

Paytan, A., Martinez-Ruiz, F., Eagle, M., Ivy, A. and Wankel, S.D., 2004. Using sulfur isotopes to elucidate the origin of barite associated with high organic matter accumulation events in marine sediments. Geological Society of America Special Paper **379**: 151-160.

Pazzaglia, F.J., Thackray, G.D., Brandon, M.T., Wegmann, K.W., Gosse, J., McDonald, E., Garcia, A.F., and Prothero, D., 2003. Tectonic geomorphology and the record of Quaternary plate boundary deformation in the Olympic Mountains. In: Swanson, T.W., (eds.). Western Cordillera and adjacent areas: Boulder, Colorado. Geological Society of America Field Guide **4**: 37–67.

Pecher, I.A., Kukowski, N., Ranero, C.R., and von Huene, R., 2001. Gas hydrates along the Peru and middle America trench systems. In: Paull, C.K., and Dillon, W.P. (eds.). Natural Gas Hydrates: Occurrence, distribution, and detection. Geophysical Monograph, American Geophysical Union (Publ.) 124: 257-271.

Petschick, R., Kuhn, G., and Gingele, F., 1996. Clay mineral distribution in surface sediments of the South Atlantic: sources, transport, and relation to oceanography. *Marine Geology* **130**: 203–229.

Pickering, K.T., Hiscott, R.N., and Hein, F.J., 1989. Deep-marine environments: clastic sedimentation and tectonics. Unwin Hyman, Inc., London (UK), 416 pp

Pierce, J.W., 1976. Suspended sediment transport at the shelf brak and over the outer margin. In: Stanley, D.J., and Swift, D.J.P. (eds.). Marine sediment transport and environmental managenment. John Willey & Sons, Canada: 437-458.

Pinheiro, L.M., Ivanov, M.K., Sautkin, A., Akhmanov, G., Magalhães, V.H., Volkonskaya, A., Monteiro, J.H., Somoza, L., Gardner, J., Hamouni, N., and Cunha, M.R., 2003. Mud volcanism in the Gulf of Cadiz: results from the TTR-10 cruise. *Marine Geology* **195**: 131-151.

Piñero, E., Gràcia, E., Larrasoaña, J.C., Martínez-Ruiz, F., Ercilla, G., Vizcaino, A. and Garcés, M., 2004. Sedimentología y magnetismo de sedimentos ricos en hidratos de gas de Hydrate Ridge (Margen de Oregon, ODP Leg 204): Aplicación en estudios paleoclimáticos. *Geotemas* **6** (5): 149-152.

Piñero, E., Gràcia, E., Martínez-Ruiz, F., Larrasoaña, J.C., Vizcaino, A., and Ercilla, G., 2005. Sedimentological and mineralogical Characterization of Gas Hydrate Sediments from ODP -Leg 204, Southern Hydrate Ridge (Cascadia Margin). Geophysical Research Abstracts, Volume 7, European Geosciences Union General Assembly, 2005.

Piñero, E., Gràcia, E., Martínez-Ruiz, F., Larrasoaña, J.C., Vizcaino, A., and Ercilla, G., 2007. Gas hydrate disturbance fabrics of southern Hydrate Ridge sediments (ODP Leg 204): Relationship with texture and physical properties. *Geo-Marine Letters* **27**: 279-288.

Pye, K. (ed.), 1994. Sediment transport and depositional processes. Blackwell Scientific Publications, Oxford (UK), 397 pp.

Rath, B.B., 2008. Methane hydrates: An abundance of Clean Energy? *Materials Research Society Bulletin* **33**: 323-325.

Reagan, M.T., and Moridis, G.J., 2007. Oceanic gas hydrate instability and dissociation under climate change scenarios. *Geophysical Research Letters* **34**: L22709.

Riddihough, R.P., 1984. Recent movements of the Juan de Fuca plate system. *Journal of Geophysical Research* **89**: 6980–6994.

Riedel, M., Long, P.E., and Collett, T.S., 2006a. Estimates of in situ gas hydrate concentration from resistivity monitoring of gas hydrate bearing sediments during temperature equilibration. *Marine Geology* **277**: 215-225.

Riedel, M., Willoughby, E.C., Chen, M.A., He, T., Novosel, I., Schwalenberg, K., Hyndman, R.D., Spence, G.D., Chapman, N.R. and Edwards, R.N., 2006b. Gas hydrate on the northern Cascadia margin: regional geophysics and structural framework. In Riedel, M., Collett, T.S., Malone, M.J., and the Expedition **311** Scientists. Proceedings Integrated Ocean Drilling Program, 311: Washington, DC (Integrated Ocean Drilling Program Management International, Inc.).

Riedel, M., Novosel, I., Spence, G.D., Hyndman, R.D., Chapman, R.N., Solem, R.C. and Lewis, T. 2006c. Geophysical and geochemical signatures associated with gas hydrate-related venting in the northern Cascadia margin. *Geological Society of America Bulletin* **118**: 23-38.

Riedinger, N., Pfeifer, K., Kasten, S., Garming, J.F., Vogt, C. and Hensen, C., 2005. Diagenetic Alteration of Magnetic Signals by Anaerobic Oxidation of Methane Related to a Change in Sedimentation Rate. *Geochimica et Cosmochimica Acta* **69** (16): 4117-4126.

Riedinger, N., Franke, C., Pfeifer, K., Kasten, S., and Gröger, J., 2006. Active and Buried Authigenic Barite Fronts in Sediments from the Eastern Cape Basin. *Earth and Planetary Science Letters* **241** (3-4): 876-887.

Ritger, S., Carson, B., and Suess, E., 1987, Methane-derived authigenic carbonates formed by subduction-induced pore-water expulsion along the Oregon/Washington margin: *Geological Society of America Bulletin* **98**: 47–156.

Robertson, A.H.F., Emeis, K.C., Richter, C., and Camerlenghi, A. (eds.), 1998. Proceedings Ocean Drilling Program, Science Results **160** [Online]. Available from World Wide Web: http://www-odp.tamu.edu/publications/160_SR/160TOC.HTM. [Cited 2005-10-21].

Roehl, U., Bralower, T.J., Norris, G., and Wefer, G., 2000. A new chronology for the Paleocene thermal maximum and its environmental implications. *Geology* **28**: 927-930.

Röhl, U., and Abrams, L.J., 2000. high-resolution, downhole, and non-destructive core measurements from Sites 999 and 1001 in the Caribbean Sea: application to the Late Paleocene Thermal Maximum. In: Leckie, R.M., Sigurdsson, H., Acton, G.D., and Draper, G. (eds.). Proceedings of the Ocean Drilling Program, Scientific Results **165**: 191–203.

Sahling, H., Rickert, D., Lee, R.W., Linke, P., and Suess, E., 2002. Macrofaunal community structure and sulphide flux in gas hydrate deposits from the Cascadia convergent margin, NE Pacific. *Marine Ecology Progress Series* **231**: 121-138.

Saito, C., Noriki, S., and Tsunogai, S., 1992. Particulate flux of Al, a component of land origin, in the western North Pacific. *Deep-Sea Reseach* **39**: 1315-1327.

Sample, J.C., and Reid, M.R., 1998. Contrasting hydrogeological regimes along strike-slip and thrust faults in the Oregon convergent margin: Evidence from the chemistry of syntectonic carbonate cements and veins. *Geological Society of American Bulletin* **110** (1): 48-59.

Sanchez-Vidal, A., Collier, R.W., Calafat, A. Fabres, J. and Canals, M., 2005. Particulate barium fluxes on the continental margin: a study from the Alboran Sea (Western Mediterranean). *Marine Chemistry* **93**: 105-117.

Sassen, R., Sweet. S.T., Milkov, A.V., DeFreitas, D.A., Kennicutt II, M.C., and Roberts, H.H., 2001. Stability of Thermogenic Gas Hydrate in the Gulf of Mexico: Constraints on Models of Climate Change. In Natural Gas Hydrates: Occurrence, Distribution, and Detection. Geophysical Monograph **124**: 131-143.

Schätzing, F., 2006. The Swarm: A novel to the Deep. Hodder & Stoughton (eds.), London, 881 pp.

Scheidegger, K.F., Kulm, L.D., and Piper, D.J.W., 1973. Heavy mineralogy of unconsolidated sands in northeastern Pacific sediments: Leg 18, Deep Sea Drilling Project. In: Kulm, L.D., von Huene, R., et al. (eds.). Initial Reports Deep Sea Drilling Project **18**. U.S. Government Printing Office, Washington: 877-888.

Scherwath, M., Riedel, M., Spence, G.D., and Hyndman, R.D., 2006. Data report: seismic structure beneath the north Cascadia drilling transect of Integrated Ocean Drilling Program Expedition 311. In: Riedel, M., Collett, T.S., Malone, M.J., and the Expedition 311 Scientists. Proceeding Integrated Ocean Drilling Program Management International **311**: Washington, DC (Integrated Ocean Drilling Program Management International, Inc.).

Schmidt, G.A., and Shindell, D.T., 2003. Atmospheric composition, radioactive forcing, and climate change as a consequence of a massive methane release from gas hydrates. *Paleoceanography* **18** (1): 1004 pp.

Schultheiss, P.J., Holland, M.E., and ODP Leg 204 Shipboard Scientific Party, 2003. Structure and decomposition of marine gas hydrates recovered at in situ pressures. Geophysical Research Abstracts (European Geophysical Society) **5**: 04375.

Schulz, H.D., and Zabel M. (eds.) ,2006. Marine Geochemistry, 2nd Edition. Springer Verlag, Berlin, Germany, 574 pp.

Seely, D.R., 1977. The significance of landward vergence and oblique structural trends on trench inner slopes. In: Talwani, M. (ed.). Island Arcs, Deep Sea Trenches and Back-Arc Basins. American Geophysical Union, Washington, DC.: 187-198.

Shipboard Scientific Party, 2002. Preliminary Report. Ocean Drilling Program, Preliminary Reports **204**: College Station TX (Ocean Drilling Program): 1-81.

Shipboard Scientific Party, 2003a. Site 1244. In: Tréhu, A.M, Bohrmann, G., Rack, F.R., Torres, M.E., et al. (eds.). Proceedings of the Ocean Drilling Program, Initial Reports **204**: College Station TX (Ocean Drilling Program): 1-132.

Shipboard Scientific Party, 2003b. Site 1245. In: Tréhu, A.M, Bohrmann, G., Rack, F.R., Torres, M.E., et al. (eds.). Proceedings of the Ocean Drilling Program, Initial Reports **204**: College Station TX (Ocean Drilling Program): 1-131.

Shipboard Scientific Party, 2003c. Site 1246. In: Tréhu, A.M, Bohrmann, G., Rack, F.R., Torres, M.E., et al. (eds.). Proceedings of the Ocean Drilling Program, Initial Reports **204**: College Station TX (Ocean Drilling Program): 1-67.

Shipboard Scientific Party, 2003d. Site 1247. In: Tréhu, A.M, Bohrmann, G., Rack, F.R., Torres, M.E., et al. (eds.). Proceedings of the Ocean Drilling Program, Initial Reports **204**: College Station TX (Ocean Drilling Program): 1-84.

Shipboard Scientific Party, 2003e. Site 1248. In: Tréhu, A.M, Bohrmann, G., Rack, F.R., Torres, M.E., et al. (eds.). Proceedings of the Ocean Drilling Program, Initial Reports **204**: College Station TX (Ocean Drilling Program): 1-75.

Shipboard Scientific Party, 2003f. Site 1249. In: Tréhu, A.M, Bohrmann, G., Rack, F.R., Torres, M.E., et al. (eds.). Proceedings of the Ocean Drilling Program, Initial Reports **204**: College Station TX (Ocean Drilling Program): 1-98.

Shipboard Scientific Party, 2003g. Site 1250. In: Tréhu, A.M, Bohrmann, G., Rack, F.R., Torres, M.E., et al. (eds.). Proceedings of the Ocean Drilling Program, Initial Reports, **204**: College Station TX (Ocean Drilling Program): 1-100.

Shipboard Scientific Party, 2003h. Site 1251. In: Tréhu, A.M, Bohrmann, G., Rack, F.R., Torres, M.E., et al. (eds.). Proceedings of the Ocean Drilling Program, Initial Reports, **204**: College Station TX (Ocean Drilling Program): 1-119.

Shipboard Scientific Party, 2003i. Site 1252. In: Tréhu, A.M, Bohrmann, G., Rack, F.R., Torres, M.E., et al. (eds.). Proceedings of the Ocean Drilling Program, Initial Reports, **204**: College Station TX (Ocean Drilling Program): 1-62.

Shipboard Scientific Party, 2003j. Explanatory notes. In: Tréhu, A.M, Bohrmann, G., Rack, F.R., Torres, M.E., et al. (eds.). Proceedings of the Ocean Drilling Program, Initial Reports, **204**: College Station, TX (Ocean Drilling Program): 1-102.

Shipley, T.H., Houston, M.H., Buffler, R.T., Shaub, F.J., McMillen, K.J., Ladd, J.W., and Worzel, J.L., 1979. Seismic evidence for widespread possible gas hydrate horizons on continental slopes and rises. American Association of Petroleum Geologist Bulletin **63**: 2204-2213.

Simpson, J.J, 1983. Large-scale thermal anomalies in the California current during the 1982-1983 El Niño. *Geophysical Research Letters* **10**: 917-940.

Silver E.A., 197. Small plate tectonics in the northeastern Pacific. *Geological Society of America Bulletin* **82**: 3491-3496.

Sloan, E.D.J., 1998. Physical/chemical properties of gas hydrates and application to world margin stability and climatic change. In: Henriet, J.P., and Mienert, J. (eds.). Gas hydrates: Relevance to World Margin Stability and Climate Change. Special Publications, London, Geological Society **137**: 31-50.

Sloan, E.D., 2000. Clathrate hydrates: the other common solid water phase. *Industrial and Engineering Chemistry Research* **39**: 3123-3129.

Sloan, E.D., and Koh, C.A., 2007. Clathrate hydrates of Natural Gases, 3rd Ed. Boca Ratón, FL: CRC Press, 752 pp.

Smith, D.E., Shi, S., Cullingford, R.A., et al., 2004. The Holocene Storegga slide tsunami in the United Kingdom. *Quaternary Science Reviews* **23** (23-24): 2291-2321.

Snyder, G.T., Dickens, G.R., and Castellini, D.G., 2007. Labile barite contents and dissolved barium concentrations on Blake Ridge: New perspectives on barium cycling above gas hydrate systems. *Journal of Geochemical Exploration* **95**: 48-65.

Soh, W., 1997. 28. Computed Tomography Scan Analysis of Site 941 Cores, Western Mass-Transport Deposit, Amazon Fan. In: Flood, R.D., Piper, D.J.W., Klaus, A., and Peterson, L.C. (eds), Proc. Ocean Drilling Program, Scientific Results 155, 3–4 [Online]. Available from World Wide Web: http://www-odp.tamu.edu/publications/155_SR/CHAP_01.PDF. [Cited 2005-10-21]

Solheim, A., Berg, K., Forsberg, C.F.,et al., 2005. The Storegga Slide complex: repetitive large scale sliding with similar cause and development. *Marine and Petroleum Geology* **16** (1): 19-30.

Somoza, L., 2001. Hydrocarbon seeps, gas hydrates, and carbonate chimneys in the Gulf of Cadiz: an example of of the interaction between tectonic and oceanographic controlling factors. In: Natural hydrocarbon seeps, global tectonics and greenhouse gas emissions. In: Van der Meer, F., Scholte, K. (eds.), European Science Foundation - Standing Committee for the Life, Environmental & Earth Sciences exploratory workshop. Delft, The Netherlands: 18-19.

Somoza, L., Díaz-del-Río, V., León, R., Ivanov, M., Fernández-Puga, M.C., Gardner, J.M., Hernández-Molina, F.J., Pinheiro, L.M., Rodero, J., Lobato, A., Maestro, A., Vázquez, J.T., Medialdea, T., and Fernández-Salas, L.M., 2003. Seabed morphology and hydrocarbon seepage in the Gulf of Cádiz mud volcano area: Acoustic imagery, multibeam and ultra-high resolution seismic data. *Marine Geology* **195**: 153-176.

Spence, G.D., Hyndman, R.D., Chapman, N.R., Riedel, M., Edwards, N. and Yuan, J., 2000. Cascadia margin, northeast Pacific Ocean: hydrate distribution from geophysical investigations. In: Max, M.D. (ed.), Natural Gas Hydrate in Ocean and Permafrost Environments: New York (Kluwer Academic Publisher): 183-198.

Stein, R., 1985. Rapid grain-size analysis of clay and silt fraction by Sedigraph 5000D: comparison with Coulter counter and Atterberg methods. *Journal of Sedimentary Petrology* **55** (4): 163-172.

Sternberg, R.W., 1986. Transport and accumulation of river-derived sediment on the Washington continental shelf. *Journal of the Geological Society of London* **143**: 945-956.

Sternberg, E., Jeandel, C., Miquel, JC., Gasser, B., Souhaut, M., Arraes-Mescoff, R., and François, R., 2007. Particulate barium fluxes and export production in the nothwestern Mediterranean. *Marine Chemistry* **105**: 281-295.

Stoll, R.D., Ewing, J.I., and Bryan, G.M., 1971. Anomalous wave velocities in sediments containing gas hydrates. *Journal of Geophysical Research* **76**: 2090-2094.

Stow, D.A.W., and Piper, D.J.W. (eds.), 1984. Fine-grained sediments: deep-water processes and facies. Geological Society (London) Special Publication **15**: 646pp.

Su, X., Song, C.B., and Fang, N.Q., 2006. Relationship between sediment granulometry and the presence of gas hydrate on Hydrate Ridge. In: Tréhu, A.M., Bohrmann, G., Torres, M.E.,

Colwell, F.S. (eds.), Proceedings of the Ocean Drilling Program Scientific Results 204, College Station, Texas (Ocean Drilling Program): 1-30.

Suess, E., Torres, M.E., Bohrmann, G., Collier, R.W., Greinert, J., Linke, P., Rehder, G., Trehu, A., Wallmann, K., Winckler, G., and Zuleger, E., 1999. Gas hydrate destabilization: enhanced dewatering, benthic material turnover, and large methane plumes at the Cascadia convergent margin. *Earth and Planetary Science Letters* **170**: 1-15.

Suess E., Torres, M.E., Bohrmann, G., Collier, R.W., Ricket, D., Goldfinger, C., Linke, P., Heuser, A., Sahling, H., Heeschen, K., Jung, C., Nakamura, K., Greinert, J., Pfannkuche, O., Tréhu, A., Klinkhammer, G., Whiticar, M.C., Eisenhauer, A., Teichert, B. and Elvert, E., 2001. Sea floor methane hydrates at Hydrate Ridge, Cascadia Margin. In: Paull, C.K., and Dillon, W.P. (eds.) Natural Gas Hydrates: Occurrence, Distribution, and Detection. Geophysical Monograph **124**, American Geophysical Union (Publ.): 87-98.

Sultan, N., Cochonat, P., Canals, M., Cattaneo, A., Dennielou, B., Haflidason, H., Laberg, J.S., Long, D., Mienert, J., Trincardi, F., Urgelés, R., Vorren, T.O., and Wilson, C., 2004a. Triggering mechanisms of slope instability processes and sediment failures on continental margins: a geotechnical approach. *Marine Geology* **213**: 291-321.

Sultan, N., Cochonat, P., Foucher, J.P., and Mienert, J., 2004b. Effect of gas hydrates melting on seafloor slope instability. *Marine Geology* **213**: 379-401.

Sundquist, E.T., and W.S. Broecker, 1985. The carbon cycle and atmospheric CO_2: Natural variations Archean to present, in Geophysical Monograph, American Geophysical Union, Washington, DC: 627 pp.

Sundquist, E.T., 1986. Geologic analogs: Their value and limitations in carbon dioxide research, in The Changing Carbon Cycle, A Global Analysis. In: Trabalka, J.R., and Reichle, D.E. Springer-Verlag, New York: 371-402.

Syvitski, J.P.M. (ed.), 1991. Principles, methods and application of particle size analyses. Cambridge University Press: 368 pp.

Takahasi, H., Japan Petroleum Exploration Co., L., Yonezawa, T., Corporation, J.N.O., Takedomi, Y. and Ministry of Economy T.A.I., 2001. Exploration for Natural Gas Hydrate in Nankai-Trough Wells Offshore Japan, Offshore Technology Conference, **13040**, Houston (TX), Offshore Technology Conference.

Teichert, B.M.A., Bohrmann, G., and Suess, E., 2005a. Chemoherms on Hydrate Ridge – Unique microbially-mediated carbonate build-ups growing into the water column. Palaeogeography, Palaeoclimatology, *Palaeoecology* **227**: 67-85.

Teichert, B.M.A., Torres, M.E., Bohrmann, G., and Eisenhauer, A., 2005b. Fluid sources, fluid pathways and diagenetic reactions across as accretionary prism revealed by Sr and B geochemistry. *Earth and Planetary Science Letters* **239** (1-2): 106-121.

Thomas, D.J., Zachos, J.C., Bralower, T.J., et al., 2002. Warming the fuel from the fire: Evidence for the thermal dissociation of methane hydrate during the Paleocene-Eocene thermal maximum. *Geology* **30** (12): 1067-1070.

Tinivella, U., Accaino, F. and Camerlenghi, A., 2002. Gas hydrate And free gas distribution from inversion of seismic data on the South Shetland margin. *Marine Geophysical Researches* **23** (2): 109-123.

Tomaru, H., Matsumoto, R., Torres, M.E., and Borowski, W.S., 2006. Geological and geochemical constraints on the isotopic composition of interstitial waters from the Hydrate Ridge region, Cascadia Continental Margin. In: Tréhu, A.M., Bohrmann, G., Torres, M.E., Colwell, F.S. (eds.). Proceedings of the Ocean Drilling Program Scientific Results **204**, College Station, Texas (Ocean Drilling Program): 1-20.

Torres, M.E. and Rugh, W.D., 2006. Data report: Isotopic characterization of dissolved inorganic carbon in pore waters, Leg 204. In: Tréhu, A.M., Bohrmann, G., Torres, M.E., Colwell, F.S. (eds.). Proceedings of the Ocean Drilling Program Scientific Results **204**, College Station, Texas (Ocean Drilling Program): 1-16.

Torres, M. E., Bohrmann G., and Suess E., 1996a. Authigenic barites and fluxes of barium associated with fluid seeps in the Peru subduction zone. *Earth and Planetary Science Letters* **144**: 469-481.

Torres, M.E., Brumsack, H.J., Bohrmann, G., and Emeis, K.C., 1996b. Barite Fronts in Continental Margin Sediments: A New Look at Barium Remobilization in the Zone of Sulfate Reduction and Formation of Heavy Barites in Diagenetic Fronts. *Chemical Geology* **127**: 125-139.

Torres, M.E., McManus, J., Hammond, D.E., de Angelis, M.A., Heeschen, K.U., Colbert, S.L., Tryon, M.D., Brown, K.M., and Suess, E., 2002. Fluid and chemical fluxes in and out of sediments hosting methane hydrate deposits on Hydrate Ridge, OR I: Hydrological provinces. *Earth and Planetary Science Letters* **201**: 525-540.

Torres, M.E., Bohrmann, G., Dubé, T.E., and Poole, F.G., 2003. Formation of Modern and Paleozoic Strat Form Barite at Cold Methane Seeps on Continental Margins. Geological Society of America **31**(10): 897-900.

Torres, M.E., Wallmann, K., Tréhu, A.M., Bohrmann, G., Borowski, W.S., and Tomaru, H., 2004. Gas Hydrate growth, methane transport, and chloride enrichment at the Southern summit of Hydrate Ridge, Cascadia Oregon. *Earth and Planetary Science Letters* **226**: 225-241.

Torres, M.E., Tréhu, A.M., Cespedes, N., Kastner, M., Wortmann, U.G., Kim, J.H., Long, P., Malinverno, A., Pohlman, J.W., Riedel, M., and Collett, T., 2008. Methane hydrate formation in turbidite sediments of northern Cascadia, IODP Expedition 311. *Earth and Planetary Science Letters* **271**: 170-180.

Tréhu, A.M., and Flueh, E.R., 2001. Estimating the thickness of the free-gas zone beneath Hydrate Ridge, Oregon continental margin, from seismic velocities and attenuation. *Journal of Geophysical Research* **106** (B2): 2035-2045.

Tréhu, A.M., Asudeh,I., Brocher, T.M., Luetgert, J.H., Mooney, W.D., Nabelek, J.L., and Nakamura, Y, 1994. Crustal architecture of the Cascadia forearc. *Science* **266**: 237-242.

Tréhu, A.M., Torres, M.E., Moore, G.F., Suess, E., and Bohrmann, G., 1999. Temporal and spatial evolution of a gas hydrate-bearing accretionary ridge on the Oregon continental margin. *Geology* **27** (10): 939-942.

Tréhu, A.M., Bangs, N.L., Arsenault, M.A., Bohrmann, G., Goldfinger, C., Johnson, J.E., Nakamura, Y., and Torres, M.E., 2002. Complex subsurface plumbing beneath Southern Hydrate Ridge, Oregon continental margin, from High-resolution 3-D seismic reflection and OBS data. Fourth International Confonference of Gas Hydrates: Yokohama, Japan 19023: 90-96.

Tréhu, A.M, Bohrmann, G., Rack, F.R., Torres, M.E. et al., 2003. Proceedings of the Ocean Drilling Program, Initial Reports **204**: College Station TX (Ocean Drilling Program): http://www-odp.tamu.edu/publications/204_IR/204ir.htm. [Cited 2008-10-21]

Tréhu, A.M., Flemings, P.B., Bangs, N.L., Chevallier, J., Gràcia, E., Johnson, J.E., Liu, C.S., Riedel, M.,and Torres, M.E., 2004a. Feeding methane vents and gas hydrate deposits at south Hydrate Ridge. *Geophysical Research Letters* **31**, L23310.

Tréhu, A.M., Long, P.E., Torres, M., Bohrmann, G., Rack, F.R., Collett, T.S., Goldberg, D.S., Milkov, A.V., Riedel, M., Schultheiss, P., Bangs, N.L., Barr, S.R., Borowski, W.S., Claypool, G.E., Delwiche, M.E., Dickens, G.R., Gràcia, E., Guerin, G., Holland, M., Johnson, J.E., Lee, Y.J., Liu, C.S., Su, X., Teichert, B., Tomaru, H., Vanneste, M.E., Watanabe, M., and Weinberger, J.L, 2004b. Three-dimensional distribution of gas hydrate beneath southern Hydrate Ridge: Constraints from ODP Leg 204. *Earth and Planetary Science Letters* **222**: 845-862.

Tréhu, A.M., Torres, M.E., Bormann, G., and Colwell, F.S., 2006. Leg 204 Synthesis: gas hydrate distribution and dynamics in the central Cascadia accretionary complex. In: Tréhu, A.M., Bohrmann, G., Torres, M.E., and Colwell, F.S. (eds.). Proceedings of the Ocean Drilling Program Scientific Results **204**, College Station, Texas (Ocean Drilling Program): 1-40.

Tremolada, F., and Bralower, T.J., 2004. Nannofossil assemblage fluctuations during the Paleocene-Eocene Thermal Maximum at Sites 213 (Indian Ocean) and 401 (North Atlantic Ocean): palaeoceanographic implications. *Marine Micropaleontology* **52**: 107-116.

Trofimuk, A.A., Cherskiy, N.V., and Tsarev, V.P., 1977. The role of continental glaciation and hydrate formation on petroleum occurrences. In: Meyer, R.F. (ed.), Future Supply of Nature-made Petroleum and Gas. Pergamon, New York: 919–926.

Tromp, T.K., VanCapellen, P., and Key, R.M., 1995. A global model for the early diagenesis of organic carbon and organic phosphorous in marine sediments. *Geochimica et Cosmoquimica Acta*, **59**: 1259-1284.

Tucholke, B.E., Bryan, G.M., and Ewing, J.I., 1977. Gas-hydrate horizons detected in seismic-profiler data from the western North Atlantic. *American Association Petroleum Geologists Bulletin* **61**: 698-707.

Uchida, T., Takagi, A., Mae, S., and Kawabata, J., 1997. Dissolution mechanisms of CO_2 molecules in water containing CO_2 hydrates. *Energy Covers Manage* **38**: S307-312.

Underwood, M., and Torres, M., 2006. Data report: composition of clay minerals from hemipelagic sediments at Hydrate Ridge, Cascadia subduction zone. In: Tréhu, A.M., Bohrmann, G., Torres, M.E., Colwell, F.S. (eds.), Proceedings of the Ocean Drilling Program Scientific Results **204**, College Station, Texas (Ocean Drilling Program): 1-15.

Underwood, M.B., Hoke, K.D., Fisher, A.T., Davis, E.E., Giambalvo, E., Zühlsdorff, L., and Spinelli, G.A., 2005. Provenance, Stratigraphic architecture, and hydrogeologic influence of turbidites on the mid-ocean ridge flank of northwestern Cascadia basin, Pacific Ocean. *Journal of Sedimentary Research* **75** (1): 149-164.

Ussler III, W., and Paull, C.K., 2001. Ion exclusion associated with marine gas hydrate deposits. In: Paull, C.K., and Dillon, W.P. (eds.) Natural Gas Hydrates: Occurrence, Distribution, and Detection. Geophysical Monograph **124**, American Geophysical Union (Publ.): 41-51.

Ussler III, W., Paull, C.K., McGill, P., Schroeder, D., and Ferrell, D., 2006. Data report: A test of the temperature, pressure, and conductivity tool prototype at Hydrate Ridge. In: Tréhu, A.M., Bohrmann, G., Torres, M.E., and Colwell, F.S. (eds.), Proceedings of the Ocean Drilling Program Scientific Results 204, College Station, Texas (Ocean Drilling Program): 1-19.

Van Beek, P., Reyss, J.L., Bonte, P., and Schmidt, S., 2003. Sr/Ba in Barite: A proxy of Barite Preservation in Marine Sediments. *Marine Geology* **199**: 205-220.

Wallmann, K., (Coordinator), 2007. Submarine gas hydrate deposits: exploitation, mining and transport (SUGAR project: Submarine Gas Hydrate Reservoirs). [26th november 2008 - http://www.ifm-geomar.de/index.php?id=3563&L=1]

Wallmann, K., Linke, P., Suess, E., Bohrmann, G., Sahlig, H., Schlüter, M., Dählmann, A., Lammers, S., Greinert, J., and von Mirbach, N., 1997. Quantifying fluid flow, solute mixing, and biogeochemical turnover at cold vents of the eastern Aleutian subduction zone. *Geochimica Cosmochimica Acta* **61** (24):5209-5219.

Walsh, I., Dyamond, J., and Collier, R., 1988. Rates of recycling of biogenic components os settling particles in the ocean derived from sediment trap experiments. *Deep Sea Research* **35**: 43-58.

Watkins, J.S., and Moore, J.C. (eds.), 1981. Initial Reports of the Deep Sea Drilling Project **66**, U.S. Government Printing Office, 863 pp.

Weaver, P.P.E., and Thomson, J. (eds.), 1987. Geology and geochemistry of abyssal plains. The Geological Society, Special Publication **31**, 246pp.

Weinberger, J.L., and Brown, K.M., 2006. Fracture Networks and Hydrate Distribution at Hydrate Ridge, OR. *Earth and Planetary Science Letters* **245**: 123-136.

Weinberger, J.L., Brown, K.M. and Long, P.E., 2005. Painting a picture of gas hydrate distribution with thermal images. Geophysical Research Letters **32**: L04609.

Westbrook, G.K., Carson, B., Musgrave, R.J., and Shipboard Scientific Party, 1994. Proceedings of the Ocean Drilling Program Initial Reports **146** (1), College Station, Texas (Ocean Drilling Program), 610 pp.

Wheeler, S.J., 1988a. A conceptual model for soils containing large gas bubbles. *Geotechnique* **38** (3), 389– 397.

Wheeler, S.J., 1988b. The undrained shear strength of soils containing large gas bubbles. *Geotechnique* **38** (3), 399–413.

White, R.S., 1977. Seismic bright spots in the Gulf of Oman. *Earth and Planetary Science Letters* **37**:29-37.

Winograd, I.J., 2002. The California current, Devils hole, and Pleistocene climate. *Science* **296**: 7a.

Winters, W.J., Waite, W.F., Mason, D.H., and Gilbert, L.Y., 2006. Physical properties of repressurized sediment from Hydrate Ridge. In: Tréhu, A.M., Bohrmann, G., Torres, M.E., and Colwell, F.S. (eds.), Proceedings of the Ocean Drilling Program Scientific Results 204, College Station, Texas (Ocean Drilling Program): 1-19.

Witter, R.C., Kelsey, H.M., and Hemphill-Haley, E., 2003. Great Cascadia earthquakes and tsunamis of the past 6700 years, Coquille River estuary, southern coastal Oregon. *Geological Society of American Bulletin* **115:** 1289-1306.

Xu, W., 2004. Modeling dynamic marine gas hydrate systems. American Mineralogists **89**: 1271-1279.

Yang, S.O., Yang, I.M., and Lee, C.S., 2000. Measurement and prediction of phase equilibria for water + CO_2 in hydrate forming conditions. *Fluid Phase Equilibrium* **175** (1-2): 75-89.

Yefremova, O.Y., and Zhizhchenko, B.P., 1974. Occurrence of crystal gas hydrates of gases gases in the sediments of modern marine basins. Doklady Akademii Nauk SSSR **214**: 1179-1181.

Zatsepina, O.Y., and Buffett., 2003. Nucleation of gas hydrate in marine environments. *Geophysical Research Letters* **30** (9): 1451-1454.

Zillmer, M., Flueh, E.R., Petersen, J., et al., 2005a. Seismic investigation of a bottom simulating reflector and quantification of gas hydrate in the Balck Sea. *Geophysical Journal International* **161** (3): 662-678.

Zillmer, M., Reston, T., Leyhaeuser, T., et al., 2005b. Imaging and quantification of gas hydrate and free gas at the Storegga slide offshore Norway. *Geophysical Research Letters* **32** (4): L04308.

Zhou, X., Fan, S., Liang, D, and Du, J., 2008. Replacement of methane from quartz sand-bearing hydrate with carbon dioxide-in-water emulsion. *Energy Fuels* **22** (3): 1759-1764.

Figure Captions

1. Introduction

2. Geological setting

6. Gas hydrate distribution at southern Hydrate Ridge

7. Early diagenetic processes

8. Discussion and conclusions

Table Captions

1. Introduction

3. ODP Leg 204

4. Data and methodology

5. Sedimentology and mineralogy of sediments from southern Hydrate Ridge

6. Gas hydrate distribution at southern Hydrate Ridge

7. Early diagenetic processes

Equations

[1] $CH_4 + 2H_2O \rightarrow CO_2 + 4H_2$

[2] $SO_4^{2-} + 4H_2 + H^+ \rightarrow HS^- + 4H_2O$

[3] $SO_4^{2-} + CH_3COOH + 2H^+ \rightarrow 2CO_2 + H_2S + 4H_2O$

[4] $CH_4 + SO_4^{2-} \rightarrow HCO_3^- + HS^- + H_2O$

[5] $C_t = C_w \phi^m (S_w)^n$ where:

C_t = electrical conductivity of the fluid saturated sediment
C_w = electrical conductivity of the brine
ϕ = porosity
m = cementation exponent of the rock (from 1.8 to 2.0)
S_w = brine saturation
n = saturation exponent (usually near 2)

[6] $TOC\ (\%) = C_M \cdot W_F / W_I$ where:

TOC is the Total Organic Carbon content of the sediment sample, in weight %

C_M is the measured C content, in weight %

W_F is the final weight of sample after the acid attack

W_I is the initial weight of sample

[7] $\Delta C_{s,d} = R_{s,d} \cdot dt_{num} \cdot SC_{s,d}$ where:

$\Delta C_{s,d}$ = change in concentration at a specific depth

$R_{s,d}$ = reaction rate

dt_{num} = time step

$SC_{s,d}$ = stoichiometric factor

[8] $CH_4 + SO_4 \rightarrow HCO_3^- + HS^- + H_2O$

[9] $2(CH_2O)_{106}(NH_3)_{16}(H_3PO_4) + SO_4^{2-} \rightarrow H_2S + 212\ HCO_3^- + 32\ NH_3 + 2\ H_3PO_4$

Acronyms

AAS: Atomic absorption spectrometry	*Espectrometria d'absorció atòmica*
AOM: Anaerobic oxidation of methane	*Oxidació anaeròbica del metà*
BSR: Bottom simulating reflector	*Reflector simulador del fons marí*
CoTReM: Column transport / reaction modelling	*Modelització de transport/reacció en columna*
DF: Debris flow	*Flux de derrubis*
EDAX: Energy dispersive X-ray analysis	*Anàlisi d'energia dispersada de raigs X*
GHSZ: Gas hydrate stability zone	*Zona d'estabilitat dels hidrats de gas*
Gt C: Gigatones (10^{15} tones) of Carbon	*Gigatones (10^{15} tones) de Carboni*
LU: Lithostratigraphic Unit	*Unitat litostratigràfica*
LWD: Logging while drilling	*Mesura- mentre-es-perfora*
mbsf: Meter below sea floor	*Metres sota el fons marí*
MSCL: Multi-sensor core logger	*Mesurador multi-sensor de testimonis*
NGHP: National gas hydrate program (India)	*Programa nacional d'hidrats de gas (Índia)*
ODP: Ocean Drilling Program	*Programa de perforació oceànica*
OPCS: ODP pressure core sampler	*Mostrejador de testimonis a pressió constant d'ODP.*
PDB: Peedee Belemnite	*Peedee Belemnites*
PETM: Palaeocene-Eocene thermal maximum	*Màxim tèrmic del límit Paleocè - Eocè.*
P/T: Pressure and temperature	*Pressió i temperatura*
RAB: Resistivity at the bit	*Resistivitat a la punta*
ROV: Remotely operated vehicle	*Vehicle operat remotament*
SD: Standard deviation	*Desviació estàndard*
SEM: Scanning electron microscopy	*Microscopi electrònic de rastreig / d'escombrada*
SMT: Sulphate – methane transition zone	*Transició sulfat/metà*
TOC: Total organic carbon	*Carboni orgànic total*
XRD: X-ray diffraction	*Difracció de raigs X*